UNIVERSITÀ DEGLI STUDI DELLA BASILICATA

PhD programme

SCIENCES
curriculum: Geo Sciences

Fracture stratigraphy and pore space properties of Mesozoic platform carbonates, Southern Apennines, Italy

Scientific disciplinary sector:
Structural Geology Geo/03

Ph.D Programme Coordinator
Prof.ssa Patrizia Falabella

Advisor
Prof. Fabrizio Agosta

Co-advisor
Prof. Giacomo Prosser

PhD Candidate:
Canio Manniello

Cycle XXXVI

SOMMARIO

ABSTRACT

Fractured reservoir characterization has always had a great relevance for academia and industry, due to the great interest in the resources hosted in the subsurface. It is well known that the behaviour of those reservoirs is due to sub-seismic scale structural discontinuities which cannot be resolved through seismic investigation or well logging. Hence, analogue studies play an important role in filling the resolution gap.

This PhD focuses on the Viggiano Mt. platform carbonates, cropping out in the Agri Valley, in the axial portion of the Southern Apennines fold-and-thrusts belt. The build-up of the Southern Apennines chain occurred since late Oligocene – early Miocene thrusting, with the development of a E to NE-verging multi-duplex structure, formed due to combined thin- and thick-skinned tectonics. Subsequently, during Pliocene, the multi-duplex was dissected by transtensional and extensional faults associated to either the Tyrrhenian Basin opening and/or to the gravitational collapse of the orogen. The Agri Valley formation resulted from the activity of two main sets of regional scale, Quaternary, high-angle, active, transtensional faults that include the NW-SE basin-bounding faults, and the NE-SW faults. Viggiano Mt. forms a Lower Jurassic (Sinemurian-Pleinsbachian-Toarcian) - Cretaceous (Cenomanian) layered carbonate succession that, at sub seismic scale is crosscut by a dense array of pressure solution seams, fractures, and veins, which together form a structural network associated with polyphasic tectonic evolution.

The characterization of rock textures and fossil associations show that the Sinemurian–Pleinsbachian carbonates were originally deposited in a low-energy open lagoon, the Toarcian carbonates in a ramp setting rimmed by sand shoals, and the Cenomanian carbonates in a medium- to high-energy, lagoonal–tidal setting not far form the platform margin. The fracture-density (P20) and intensity (P21) values display similar trends in both Sinemurian–Pleinsbachian and Toarcian carbonates, consistent with the mechanical control of bed and bed-package heterogeneities. Differently, P20 and P21 that characterize Cenomanian carbonates do not show very similar variations, due to pronounced bed amalgamation.

The results of the analyses of the diagenetic processes show that the grain-supported carbonates underwent to cement precipitation during very early diagenesis firstly under

marine phreatic conditions, and then freshwater vadose conditions. During continuous burial of the carbonates, pervasive cementation occurred under freshwater phreatic conditions, with embrittlement of the whole carbonate succession, and formation of laterally continuous, bed parallel wavy-type stylolites and pressure solution seams. Pressure solution continued during thrusting tectonics, due to tectonic burial, forming of bed-parallel seismogram-type stylolites.

Specifically, pressure solution processes were strongly affected by the grain size of single beds. Since early diagenesis, pressure solution localized within the coarser-grained carbonate beds, forming wave-like solution surfaces. During the onset of thrusting tectonics, prior to tectonic burial, small scale thrusting took place by means of shearing of the bed-parallel heterogeneities, and formation of bed-oblique slickolites forming back thrusts characterized by flat-ramp-flat geometries.

The combined results of microstructural observations with those after petrographic and Nuclear Magnetic Resonance (NMR) conducted on bed-perpendicular plugs show that the studied carbonates are characterized by an amount of effective porosity lower than 5%, with mean values of ca. 3%. Focusing on the stylolite related porosity, petrographic analysis shows that in the Lower Jurassic carbonates the secondary pores mainly localize along bed-parallel, seismogram-type stylolites. Differently, in the massive Cretaceous limestones, moldic porosity is due intrafossil and intercrystal micropores. The connectivity in the studied Mesozoic limestones is mainly controlled by the presence of microfractures.

The results reported in this PhD thesis show that the fracture distribution is significantly controlled by the depositional setting and the diagenetic processes that may occur very early during the rock formation. In fact, due to early cementation occurring in grain supported carbonate rocks, the different carbonate lithofacies may develop different mechanical properties during the initial stages of rock formation. Moreover, pressure solution processes can play an important role during the different diagenetic stages and during the tectonic evolution of the multi layer, forming mechanical interfaces capable of compartmentalizing fractures within single mechanical units. Finally, within the rock volumes located far away from large faults, the pressure solution interfaces can also localize significant amounts of porosity, depending upon their morphology. Further permeability measurements may shed lights on the control exerted by those interfaces in the fluid flow/storage properties of the fractured reservoirs hosted in shallow-water carbonates.

CHAPTER 1 – INTRODUCTION

The present PhD Thesis Dissertation focuses on the fracture stratigraphy properties of the Mesozoic succession of shallow-water carbonates cropping out within the axial portion of the Southern Apennines fold-and-thrusts belt. Studying in detail the role of pressure solution processes in the structural evolution of the carbonates during Meso-Cenzoic diagenesis and late Oligocene – Miocene thrusting tectonics, the research work is aimed at improving the knowledge upon the geological processes responsible for the distribution of secondary poristy in fractured carbonate reservoirs. Fractured reservoir characterization has always had a pivotal importance whit respect to resources hosted in the subsurface (Nelson, 2011). In this regard, a great relevance was given in the past to the production of hydrocarbons, but nowadays the efforts are oriented towards the need of decarbonization of the energy industry and to the transition towards more sustainable sources of energy. For example, the characterization of fracture networks in reservoir rocks of the subsurface is widely applied for the study of geothermal systems (Faulkner et al., 2010; Wrage et al., 2017; Smeraglia et al., 2021; 2023), of critical raw materials deposits (Sibson, 1987; Richards, 2013; Wang et al., 2021), and of geological CO_2sequestration (Zweigel et al., 2004; Iding and Ringrose, 2009), and/or H_2 (Safari et al., 2023). Nonetheless, one of the most important applications of the knowledge related to fractured reservoirs concerns the management and preservation of groundwater resources (Strenltsova, 1976; Cooke et al., 2006; Petrella et al., 2015; Corniello et al., 2018).

Depending upon their depositional settings, shallow-water carbonates are well-known for forming either massive or layered successions of tight limestones and/or dolostones (Flugel, 2010). These rock successions are commonly characterized by low to very low values of primary porosity (Lucia, 2001), and for this reason shallow-water carbonates often form type I and II fractured reservoirs. There, fracture porosity forms the greatest amount of the accommodation psace for geofluids (fluid storage properties), and strongly affect the rock permeability (fluid migration properties) due to the geometry, distribution, connectivity, and dimension of the fracture network (Nelson, 2001). Regarding the latter aspect, one of the criticalities associated to the prediction of the fluid storage and migration properties of type I and II fractured carbonate reservoirs is the related to the profound impact that sub-seismic

structural heterogeneities such as stylolites, pressure solution seams, joints, hybrid fractures, general barren fractures, and small faults can have on both fracture porosity and permeability (Agosta and Aydin, 2006; Agosta et al., 20009; Casini et al., 2011; Panza et al., 2016, 2019; Watkins et al., 2018). As a matter of fact, conventional seismic data allows to gain important information about the presence of large faults (>20-100m, depending upon quality of the data), but unfortunately do not provide any information on smaller scale structural elements (<20m). Well data, on the other hand, provide details on m-scale geometry and distribution of the structural heterogeneities, but do not carry any information about the lateral extent, connectivity, and overall nature of these heterogeneities. To fill this resolution gap, numerous studies have pointed out the importance of field analogues due to their 3D exposures, which allows the parametrization of specific fracture attributes such as nature, density, intensity, orientation, connectivity, etc. otherwise not assessed at sub-seismic scale (ie., Agosta et al., 2010; Casini et al., 2011; Panza et al., 2018, Gutmanis et al., 2018; Giuffrida et al., 2019, 2020; Kharrat et al., 2023; Smeraglia et al., 2023).

A further complicating factor that emerges when dealing with shallow-water carbonates pertaining to platform environments regards their textural and composition variations, which might change according to the diagenetic history of the rocks (Tucker and Wright, 1990). In fact, besides the stratigraphic properties associated to the depositional processes, the diagenetic evolution of carbonate rocks includes physical-chemical compaction and cement precipitation (Tucker and Wright, 1990; Lucia, 2001; Flugel, 2004; Lucia, 2007), which can have a profound effect on the failure modes occurring in these rocks (Alvarez et al., 1976; Lamarche et al., 2012; Lavenu et al., 2015; La Bruna et al., 2020). Failure modes within carbonates include opening-mode fracturing (Pollard and Aydin, 1990; Rispoli, 1981; Agosta and Aydin, 2006), pressure solution processes (Alvarez, 1976; Rustichelli et al., 2015), and shear fracturing (Graham et al., 2003; Agosta and Aydin, 2006; Marchegiani et al., 2006; Lavenu et al., 2014). As a result, the complex interactions among the different failure modes, coupled with the mechanical properties of the various types of lithofacies at time of deformation, determine the fracture stratigraphy of the carbonate rocks (Nur and Israel; 1980; Berry et al., 1996; Antonellini er al., 2008; Agosta et al., 2009, 2015). Specifically, the fracture stratigraphy subdivides any rock succession into discrete intervals, according to fractures attributes such as density, intensity, spacing, etc. as first proposed by Laubach et al. (2009) on the basis of the germinal work of Pollard and Aydin, 1990; Dershowitz and Herda, 1992; Gross et al., 1995; Bai and Pollard, 2000, and Bai et al., 2002.

In the present PhD Dissertation, the fracture characteristics exposed along cliffs and pavements of Mesozoic shallow-water carbonates of the Viggiano Mt. are documented in detail. The study area is located along the northern margin of the Agri Valley of the Basilicata region, Italy, along the axial portion of the southern Apennines fold-and-thrust belt (Patacca and Scandone, 2007). This carbonate massif is surrounded by low-permability to impermeable terrigeneous deposits, and hence forms an isolated aquifer in which the large faults are able to control the modalities of meteoric water infilitration forming an equivalent porous medium (Grimaldi, personal communication). Hower, hydrogeological data show that a smaller scales of observation, within the rock volumes bounded by the large faults, the role of the sub-seismic structures is predominant determining a pronounced permeability anisotropy (Abdallah, personal communication). Hence, thanks to the extensive exposure along large cliffs, and to the alternations of various carbonate lithofacies, the Viggiano Mt. massifs represent a great natural laboratory for the fracture stratigraphy analysis at sub-seismic scales, and on the role exerted by pressure solution processes on the time-space evolution of mechanical interfaces inhibiting the vertical growth of opening-mode and shearing-mode fractures.

The carbonate succession exposed at the Viggiano Mt. includes alternations of mud-supported and grain supported carbonates deposited during Pleinsbachian, oolithic grainstones of Toarcian time, and sedimentary breccias, rudstone/floatstones that formed during Cretaceous. The structural setting in which the study area collocates is quite complex, due to a polyphase tectonic activity. The build-up of the Southern Apennines chain occurred since late Oligocene – early Miocene thrusting, with the development of a E to NE-verging multi-duplex structure, formed due to combined thin- and thick-skinned tectonics (Mostardini & Merlini, 1986; Casero et al. 1988, 1991; Monaco et al. 1998; Improta et al. 2000; Noguera & Rea, 2000; Shiner et al. 2004). Subsequently, starting from Pliocene, the multi-duplex was dissected by transtensional and extensional faults associated to either the Tyrrhenian Basin opening and/or to the gravitational collapse of the orogen. (Mostardini & Merlini, 1986; Hippolyte et al. 1995; Giano et al. 2000; Cello et al. 2003; Novellino et al. 2015). Specifically, the Agri Valley formation resulted from the activity of two main sets of regional scale, Quaternary, high-angle, active, transtensional faults that include the NW-SE basin-bounding faults, and the NE-SW faults. In the subsurface, these faults dissect older low angle tectonic structures such as Upper Pliocene low-angle normal faults, and late Oligocene – Miocene thrust faults (Cello and Mazzoli, 1998; Doglioni et al., 1996; Maschio

et al., 2005; Vezzani et al., 2010; Bucci et al., 2012; Novellino et al., 2015, Palladino et al., 2023). Within the large fault-bounded rock volumes forming the studied carbonate outcrops of the Viggiano Mt., the polyphase tectonics activity resulted in a complex mechanical layering due to pressure solution, and multiple high angle fracture sets forming an isotropic network that include both diffuse and localized deformation (Cello and Mazzoli, 1998; Maschio et al., 2005).

According to the aforementioned motivations, the main goals of the PhD research work carried out during the last three years of activity are the following:

(1) Deciphering the role of the depositional architecture on fracture compartmentalization far away from main fault zones.
(2) Diagenetic evolution of the different carbonate lithofacies with respect to the main pressure solution processes
(3) Role of pressure solution processes in the time-dependent evolution of fracture stratigraphy due to bed-parallel and low-angle to bedding mechanical interfaces.
(4) Assessing the control of the pervasive pressure solution processes on the present-day pore space properties.

Each one of the specific points listed above is addressed in a specific chapter of this PhD Thesis Dissertation, which consists of the following:

Chapter 2. Fracture stratigraphy of Mesozoic platform carbonates, Agri Valley, southern Italy.

This chapter was published in the form of research article in the special issue of the Geological Magazine entitled “Faults and Fractures in rocks: mechanics, occurrence, dating, stress history and fluid flow”. The article was published with the title “Fracture stratigraphy of Mesozoic platform carbonates, Agri Valley, southern Italy” in April 2022, and the following author list: C. Manniello, F. Agosta, S. Todaro, F. Cavalcante and G Prosser. The field area was the Viggiano Mt. of Basilicata, southern Italy, the lab activities were carried out at the University of Palermo (petrographic analyses) and CNR IMAA institute of Tito (XRD analyses). The abstract of the published research article is the following:

The Viggiano Mt. platform carbonates form a layered succession crosscut by a dense array of pressure solution seams, and five sets of fractures and veins, which together form a sub-seismic structural network associated with polyphasic tectonic evolution. To assess the influence exerted by depositional and diagenetic heterogeneities on fracture geometry, distribution and multiscale properties, we present the results of stratigraphic, petrographic, mineralogical and mesoscale structural analyses conducted at the Viggiano Mountain, southern Italy. Based on rock textures and fossil associations, we documented that the Sinemurian–Pleinsbachian carbonates were deposited in a low-energy open lagoon, the Toarcian carbonates in a ramp setting rimmed by sand shoals, and the Cenomanian carbonates in a medium- to high-energy, lagoonal–tidal setting. Fracture-density (P20) and intensity (P21) values computed after circular scanline measurements show similar trends in both Sinemurian–Pleinsbachian and Toarcian carbonates, consistent with the bed and bed-package heterogeneities acting as efficient mechanical interfaces during incipient faulting. On the other hand, P20 and P21 do not show very similar variations throughout the Cenomanian carbonates due to pronounced bed amalgamation. Throughout the study area, the aforementioned parameters do not vary in proportion to the bed thickness, and show higher values within the coarse-grained carbonate beds. This conclusion is confirmed by results of linear scanline measurements, which focus on the P10 properties of the most common diffuse fracture set. The original results reported in this work are consistent with burial-related, physical–chemical compaction and cementation processes affecting the fracture stratigraphy of the Mesozoic platform carbonates.

Chapter 3: Diagenetic history and pressure solution-assisted compaction of the Mesozoic shallow-water carbonates exposed along the axial zone of the southern Apennines fold-and-thrust belt, Italy.

This chapter is in preparation for submission in the form of research article to the special issue of Geosciences entitled “Advances in carbonate diagenesis”. The title will be “Diagenetic history and pressure solution-assisted compaction of the Mesozoic shallow-water carbonates exposed along the axial zone of the southern Apennines fold-and-thrust belt, Italy”, and the authors list the following: Todaro S., Manniello C., Pietragalla A., Preto N., Agosta F. The field area was the Viggiano Mt. of Basilicata, southern Italy, the laboratory analyses were carried out at the University of Palermo (petrographic analysis), at the

University of Padova (cathodoluminescence analysis). The abstract of the research article in preparation is the following:

An Integrated petrographic, mineralogical, and microstructural study is carried out on a Jurassic-Cretaceous carbonate platform succession. The goal of this work is the assessment of the main diagenetic processes that took place during burial diagenesis, tectonic burial, and the subsequent uplift and exhumation form depths of ca. 4 km associated to the downfaulting of the southern Apennines fold-and-thrust belt. The results of the analyses show that the grain-supported carbonates underwent to cement precipitation during very early diagenesis under marine phreatic conditions, and then to subsequent cement precipitation under freshwater vadose conditions. These cementation phases determined the early embrittlement of the coarse carbonate beds, with formation of hairline fractures and veins. Then, during continuous burial of the carbonates, pervasive cementation occurred under freshwater phreatic conditions, with embrittlement of the whole carbonate succession, and formation of laterally continuous, bed parallel wavy-type stylolites and pressure solution seams, that initially nucleated at the grain contacts, and dissolved part of the early formed veins. Pressure solution continued during thrusting tectonics, when the stacking of allochthonous units determined a tectonic burial condition, hence forming of bed-parallel seismogram-type stylolites.

Chapter 4: Pressure solution-assisted diagenesis and thrusting-related deformation of Mesozoic platform carbonates.

This chapter was published in the form of research article in the Journal of Structural Geology with the title" Pressure solution-assisted diagenesis and thrusting-related deformation of Mesozoic platform carbonates". The article was published in June 2023 with the following authors list: C. Manniello, I.B. Abdallah, G. Prosser, F. Agosta. The field area was the Viggiano Mt. of Basilicata, southern Italy. The abstract of the published research article is the following:

Depositional and diagenetic processes profoundly control the structural evolution of shallow-water carbonates through time. We focus on the Lower Jurassic platform carbonates pertaining to the southern Apennines fold- and-thrusts belt, Italy, by performing 3D digital outcrop modeling, field structural analysis, and microstructural investigation. Results show

that pressure solution of the platform carbonates was affected by the grain size of single beds. Since early diagenesis, pressure solution localized within the coarser-grained carbonate beds, forming wave-like solution surfaces. Crosscutting relations among blocky cements, bed-parallel solution surfaces and high-angle veins show that pressure solution occurred during burial diagenesis with formation of wave-like solution surfaces, and during Late Miocene tectonic burial with formation of seismogram-like solution surfaces. The tectonic burial postdated the thrusting-related flexural slip folding and small-scale thrusting of the platform carbonates. Small scale thrusting took place by means of shearing of the bed-parallel heterogeneities, and formation of bed-oblique slickolites resulting in the development of back thrusts characterized by flat-ramp-flat geometries. The main results of this work are synthesized in a six-stage synoptic scheme reporting the structural evolution of the platform carbonates. Outcomes are helpful for the better assessment of geofluid production/storage from/in fractured platform carbonates pertaining to fold-and-thrust belts.

Chapter 5: Pore space properties associated with solution surfaces in Mesozoic platform carbonates, southern Italy.

This chapter is in preparation for submission in the form of research article to Marine and Petroleum Geology. The title of the research article will be "Pore space properties associated with solution surfaces in Mesozoic platform carbonates, southern Italy", and the list of authors the following: Manniello, C., La Bruna, V., Bezerra, H. F. R., Morais X. M., Araújo R. E. B., Prosser, G., Agosta, F. The field area was the Viggiano Mt. of southern Italy, the laboratory analyses were conducted at the University of Rio Grande do Norte, Brasil (petrophysical and nuclear magnetic resonance analyses). The abstract of the research article in preparation is the following:

Diagenetic and tectonic processes taking place in platform carbonates produce significant textural and mineralogical modifications through time, influencing the pore space. Focusing on pressure solution processes, this study is conducted on Lower Jurassic, mud- and grain-supported carbonates, and on Cretaceous, grain-supported and bioclastic carbonates currently exposed at the Viggiano Mt. of the southern Apennines. The primary porosity of these rocks was occluded by pervasive blocky cements, which precipitated during burial diagenesis of the carbonates. By integrating field and laboratory analyses, we aim at assessing the role exerted by the bed-parallel and low-angle to bedding solution surfaces on

the pore space geometry and localization within selected rock plugs representative of the study carbonate beds. We combine the results of microstructural observations with those after petrographic and Nuclear Magnetic Resonance (NMR) conducted on bed-perpendicular plugs. All plugs show an amount of effective porosity lower than 5%, with mean values of ca. 3%. Excluding microfractures, results of petrographic analysis show that in the Lower Jurassic carbonates the secondary pores mainly localize along bed-parallel, seismogram-type stylolites. These pores, which were likely due to the non-selective dissolution, now days form a poorly connected vuggy porosity in the Lower Jurassic limestones. Differently, in the massive Cretaceous limestones, moldic porosity due to selective dissolution localize as intrafossil and intercrystal micropores. Overall, the since the seismogram-type stylolite might control the porosity distribution, the connectivity in the studied Mesozoic limestones is mainly controlled by the presence of microfractures. Further permeability analyses will shed light on the fluid flow/storage properties of these carbonates.

Appendix: Permeability measurements in low-porosity, shallow-water carbonates: insights on the effect of pressure solution-related pores on the fluid flow properties of limestone rocks.

This appendix includes the preliminary results of the permeability measurements carried out at both University of Rio Grande do Norte (UFRN), Brazil, and at the University of Liverpool (UOL), UK. Laboratory tests are conducted on samples derived from hand specimens collected from the Viggiano Mt. and the Raparo Mt. of southern Italy. The former site flanks the Agri Valley f the Basilicata Region to NE, and it has been previously studied in terms of its mineralogical and petrographic properties, of its stratigraphic and structural settings, and of the diagenetic and micro- and meso-scale tectonic evolution of the Mesozoic carbonates. There, the shallow-water carbonates are characterized by low values of porosity, which is mainly due to the presence of high-angle barren fractures, seismogram-type stylolites, and sparse moldic pores. Taking advantage of the existing knowledge upon the geometry of pores localized along the seismogram-type-stylolites in samples from the Viggiano Mt., we also selected carbonate samples from the Raparo Mt., which flanks the Agri Valley of the Basilicata Region to the SW, and includes Meso-Cenozoic rocks originally deposited in lagoonal-to-inner lagoonal environments.

Aiming at deciphering the specific role of the seismogram type stylolites on the permeability, after petrographic analysis of the selected samples we first conduct gas permeability measurements at room pressure, and then water permeability measurements at increasing confining pressures (from 5 MPa to 90MPa). The result of petrographic analysis shows that the pore shape associated to seismogram stylolites is significantly different to the pore shape associated to open fractures. In fact, as expected, the fracture-related pores are characterized by very high aspect ratio values. Hence, the higher the aspect ratio, the softer the porosity. The results of permeability measurements at room pressure show that the vertical permeability is generally low with permeability values varying between 10^{-1} and 10^{-3} mDa. The poro/perm relation is non-linear, suggesting that the connectivity operated by microfractures might exert a major control. Then, with the goal of excluding the contribution of open fractures, we then operate at increasing confining pressures. The preliminary results show that, within the samples containing both stylolites and fractures, the permeability decreases of up to one order of magnitude, when a threshold value around 25 MPa of effective pressure is reached. Beyond this threshold value, the permeability remains almost constant. Differently, in the samples containing only stylolites, the decrease of permeability due to the confining pressure is almost negligible. The result of these analyses will shed more lights on the effect of the confining pressure on the different types of pore type, and the depth range at which pore connectivity is affected by open fractures. Further X-ray tomography analyses will shed more lights on the internal structure of the plugs and on the specific structure of the zones where fracture intersect/abut against stylolites, in order to gain more information on the microstructures that the control fluid flow through different structural elements.

During the third year of the PhD work, I spent a total of six months for research activities dealing with petrophysical analyses of selected carbonate rock specimens. Specifically, I spent three months at the University of Rio Grande do Norte, Brasil, where I conducted gas porosimetry and permeametry measurements, NMR (Nuclear Magnetic Resonance) analyses, and micro C/T scan (computed tomography) to decipher the pore space properties of the studied carbonates. There, the laboratory work was carried out under the supervision of the Prof Bezerra F.H.R. and Dr La Bruna V. Then, I spent three more months at the University of Liverpool conducting permeability analyses on similar carbonate samples by means on the PTD (Pulse Transient Decay). In the latter laboratory, named the Rock

Deformation Laboratory, I worked under the supervision of Prof. Faulkner D. and Dr. Emma Michie.

During the three years spent at the University of Basilicata for the PhD research work, I had the opportunity to present my results at several meeting an workshop, the main of which are listed below:

- "Fracture stratigraphy of Mesozoic platform carbonates, Agri Valley, southern Italy", poster presentation presented in 2022 at: AAPG Conference: Carbonate Reservoirs and Sequences… the Challenge Continues, At: Naples, Italy. The author's list is the following: Manniello, C., Agosta, F., Todaro, S., Prosser, G.
- "The role of pressure solution in the evolving fracture stratigraphy properties of Mesozoic platform carbonates", oral presentation held in 2023 at: EGU General Assembly 2023, At: Vienna, Austria. The author's list is the following: Manniello, C., Todaro, S., Abdallah, I. B., Prosser, G., Agosta, F.
- "Origin of bed-parallel mechanical interfaces affecting the fracture stratigraphy properties of Mesozoic platform carbonates, insights from the Viggiano Mt. of southern Italy" oral presentation held at the SGI conference 2023. The author's list is the following: Manniello C., Todaro S., Abdallah I., Prosser G., Agosta F.
- "The role of solution surfaces in the pore space properties of tight platform carbonates" poster presentation at SGI conference 2023. The author's list is the following: Manniello C., La Bruna V., Bezerra F.H.R., Morais X. M., Araùjo R.E.B., Paixão M., Antonino A., Barbosa J.A., Duarte D.A., Prosser G. & Agosta F.

Furthermore, the PhD research work also included both fieldwork and laboratory analyses whose results are not included in the present PhD Thesis Dissertation. These activities allowed me to collaborate with many researchers, and gain a new knowledge on specific methods and field areas. In particular, during the activities carried out in my study area of the Agri Valley of southern Italy I had the opportunity to assist the PhD colleague Ian Bala Abdallah, and elaborate quantitative data that are included in the two following publication:

- "Multiscale structural analyses of Mesozoic shallow-water carbonates, Viggiano Mt., southern Italy." published in October 2023 at Journal of Structural Geology,

with the following authoors list: Abdallah, I. B., Manniello, C., Prosser, G., Agosta, F.

- "DFN modelling of multiscale geo-cellular volumes after field and digital structural analyses on Mesozoic shallow-water carbonates." in preparation for Marine and Petroleum Geology, with the following authoors list: Abdallah, I. B., Manniello, C., Prosser, G., Agosta, F.

During the first year of the PhD work, I joined my tutor and his team in a fieldtrip to peninsular Greece. There, at the Araxos Promontory (Acaia region) I conducted field structural analyses whose results have been published in the following article:

- "Regional scale, fault-related fluid circulation in the Ionian Zone of the External Hellenides fold-and-thrust belt, western Greece: clues for fluid flow in fractured carbonate reservoirs." published in July 2023 in Tectonics, with the following authors list: Smeraglia L., Bernasconi S., Manniello C., Spanos D., Pagoulatos A., Aldega L., Kylander-Clark A., Jaggi M., Agosta F.

Finally, during the tie spent at the University of Rio Grande do Norte, Brazil, I had the opportunity to take part of a fieldtrip to the Chapada Diamantina, state of Bahia, central Brazil, and of a fieldtrip to the Potiguar Basin, state of Rio Grande do Norte, noth-eastern Brazil. There, I joined the local researchers and the team from Parma University led by prof. F. Balsamo, and I helped during structural data acquisition both at surface and within karstic caves. The first results of this work were recently presented at the 2023 meeting of the Italian Geological Society (SGI), which was held in Potenza in the month of September:

- "Mechanical stratigraphy in Mesoproterozoic Morro do Chapeu sandstones combining field data and digital outcrop models in the Ferro Doido waterfall, Bahia, Brazil", abstract submitted at the SGI congress 2023 with the following authors list: Vernazza L., La Bruna V., Balsamo F., Manniello C., Maia R.P., Gomes D.D.M., Tonietto L., Freire J.V. , Da Silveira Jr L.G. & Bezerra F.H.R.
- "Structural and stratigraphic controls on epigenic karst in shallow marine carbonates, Crotes cave, Potiguar basin, Brazil: implications for karstified carbonate reservoirs", abstract submitted at the SGI congress 2023 with the following authors list: Restelli G., Balsamo F., La Bruna V. , Manniello C., Candeloro C., Vernazza L., Maya R., Pinheiro F., Tonietto L., Da Silveira Jr L.G. & Bezerra F.H.R.

- “Reconstruction of 3D fracture pattern, attributes and topology in the Cristal Cave, Brazil, integrating field data with photogrammetric models: implications for karstified carbonate reservoirs”, abstract submitted at the SGI congress 2023 with the following authors list: Candeloro C., Balsamo F., La Bruna V., Restelli G., Manniello C., Vernazza L., Auler A., Maya R., Pereira J., Tonietto L., Silveira L. & Bezerra F.H.R.

CHAPTER 2 - FRACTURE STRATIGRAPHY OF MESOZOIC PLATFORM CARBONATES, AGRI VALLEY, SOUTHERN ITALY

2.1 Introduction

It is well known that platform carbonates deposited in lagoonal/peritidal environments often form well-layered successions (Tucker, 1985), and include low porosity rocks (Lucia, 1983; Lucia & Fogg, 1990; Flügel, 2004) bounded by primary interfaces at the scales of single beds, bed packages, and bed package associations (Moore, 2002; Spalluto, 2008, 2012; Giuffrida *et al*., 2020; La Bruna *et al.*, 2020). Within low-porosity carbonates, typical of Type I fractured reservoirs (Nelson, 2001), the total amount of effective porosity is often enhanced by fractures (Odling, 1999; Korneva *et al*, 2014; Giuffrida et al., 2019). Fractures can occur at both micro and meso scale and might result confined within discrete rock intervals forming single mechanical units (Gross, 1993; Gross *et al.*, 1995; Panza *et al.*, 2016; 2019; Smeraglia *et al.*, 2021a). Bed-parallel pressure solution seams often localize within the primary interfaces (Rustichelli *et al.*,2012, 2015), and act as mechanical boundaries inhibiting the vertical fracture propagation (Nur, 1980; Gross *et al.*, 1995; Wu & Pollard, 1995; Becker *et al.*1996, Gross *et al.*, 1997). The interaction between primary interfaces and facture geometry and distribution is assessed by fracture stratigraphy analysis as first proposed by Berry *et al*. (1996), and subsequently refined by Laubach *et al.* (2009). Accordingly, layered rock successions are subdivided into discrete intervals according to fracture characteristics (i.e. height, spacing, density, intensity), and/or specific failure modes (Pollard & Aydin, 1988; Dershowitz & Herda, 1992; Bai and Pollard, 2000; Antonellini *et al.*, 2008; Agosta *et al.*, 2009, 2015).

In this work, we analyze the fracture characteristics in layered Mesozoic carbonates pertaining to the Apennine Platform exposed along the axial zone of the southern Apennines fold-and-thrust belt, Italy (Patacca & Scandone, 2007; Schettino & Turco, 2011). The Mesozoic carbonates crop out at the Viggiano Mt. area (Figure 2.1). Their polyphasic tectonic evolution caused the formation of multiple fracture sets forming either diffuse and/or localized networks (Cello & Mazzoli, 1998; Maschio *et al.*, 2005). Focusing on carbonate rock volumes mainly crosscut by diffuse fractures, which crop out away from the major fault zones, we apply a variety of methods aiming at unravelling their stratigraphic, petrographic, mineralogical, and structural properties. The results of field stratigraphic logging, and petrographic and mineralogical analyses are discussed to decipher the paleo-depositional environments, diagenetic evolution and overall primary architecture of the

study Mesozoic carbonates. Differently, the results of quantitative field fracture analysis are considered to assess the fracture density and intensity variations throughout the sedimentary succession. We discuss these variations in terms of the geometrical and mechanical control respectively exerted by carbonate bed thickness and carbonate rock texture on the distribution of diffuse high-angle fracture sets. Possible applications of the acquired knowledge span from groundwater management and preservation (Andreo *et al.*, 2008; Marìn *et al.*, 2015; Petrella *et al.*, 2015; Corniello *et al.*, 2018), to geothermal fluid circulation (Bellani *et al.* 2004; Smeraglia *et al*., 2021b) and hydrocarbon production (Mosca & Wavrek, 2002; Shiner *et al.*, 2004).

2.2 Geological Setting

The southern Apennines of Italy extends from the southern Abruzzo-alto Molise area (Ortona-Rocca Monfina tectonic lineament, Patacca *et al.* 1992) to the Calabrian-Lucanian border (Sangineto tectonic lineament, Amodio Morelli *et al.*, 1976). The southern Apennines are bounded westward by the Tyrrhenian back-arc extensional region (Malinverno & Ryan, 1986; Kastens *et al.*, 1990; Patacca *et al.*,1992 a, b), and eastward by the Bradanic Trough including Plio-Pleistocene foredeep basinal sedimentary successions (Patacca *et al.*, 1990; Patacca & Scandone, 2007). The structural setting of the southern Apennines consists of E-to-NE vergent thrust sheets forming a multi-duplex emplaced since late Oligocene – early Miocene due to combined thin- and thick-skinned tectonics (Mostardini & Merlini, 1986; Casero *et al.*, 1988, 1991; Monaco *et al.*, 1998; Menardi Noguera & Rea, 2000; Improta *et al.*, 2000; Shiner *et al.*, 2004;). Since Pliocene, this multi-duplex was dissected by transtensional and extensional faults (Mostardini & Merlini, 1986; Hippolyte *et al.*, 1995; Giano *et al.*, 2000; Cello et al., 2003; Novellino *et al.*, 2015) associated to the Tyrrhenian Basin opening, and/or to the gravitational collapse of the orogen (Cello & Mazzoli, 1998; Doglioni *et al.*, 1996; Scrocca *et al.*, 2005).

At a regional scale, the Apennine carbonate platform now days forms a main thrust sheet encompassed in between upper Ligurian/Sicilian and lower Lagonegro tectonic units (Vezzani *et al.*, 2010, and references therein). During Mesozoic, this carbonate platform developed along the western portion of the Jurassic Ligurian Tethys Ocean (Patacca & Scandone, 2007; Schettino & Turco, 2001), and included the following three main stratigraphic units (Patacca & Scandone, 2007):

(1) Capri-Bulgheria, representing the westernmost portion of the ancient carbonate platform: It included Triassic–Jurassic, shallow-water, internal transitional carbonate facies, and Cretaceous-Miocene marls interbedded with re-sedimented carbonates.

(2) Alburno-Cervati, the ancient platform-interior portion. It contained open Triassic dolomites and dolomitic limestones, Jurassic- Cretaceous shallow-water limestones, and Miocene slope carbonates and terrigenous deposits.

(3) Maddalena Mt., the easternmost portion of the ancient platform. It was made up by transitional facies deposited in between the Alburno-Cervati Unit, to the west, and the Lagonegro Basin, to the east.

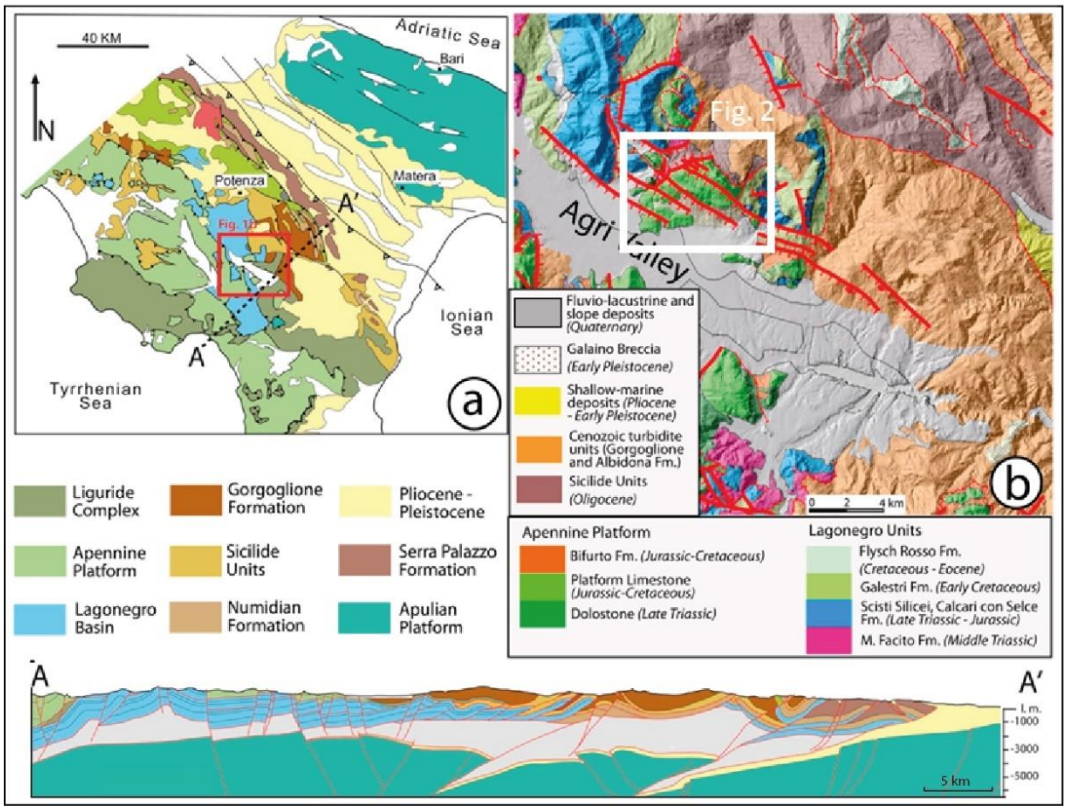

Figure 2. 1 (a) Simplified structural map of the southern Apennines fold-and-thrust belt, Italy (modified after Piedilato & Prosser , 2005); (b) geological map of the High Agri Valley, southern Italy. The white square represents the location of the study Viggiano Mt. area; (c) geological cross-section of the Southern Apennines along the A-A' transect (modified after Prosser *et al.*, 2021)

2.2.1 Viggiano Mt. area

The Viggiano Mt. is located along the NE margin of the High Agri Valley, which is an intra-mountain tectonic basin filled with Quaternary fluvio-lacustrine deposits (Di Niro *et al.*, 1992). The WNW-ESE elongated High Agri Valley basin is bounded by high-angle

transtensional faults forming the East Agri Valley fault system, EAFS (Figure 2.2.1b) and the Monti della Maddalena fault system (Cello & Mazzoli, 1998; Cello *et al.*, 2000, 2003; Maschio *et al.*, 2005; Prosser et al., 2021). The study Mesozoic carbonates of the Viggiano Mt. are crosscut by faults pertaining to EAFS. According to Cello & Mazzoli (1998) and Cello *et al.* (2000), the EAFS includes N120E (left-lateral slip), N30E (right-lateral transtensional slip), N90-110E (left-lateral transtensional slip), and N130-150E (left-lateral transpressional slip) high-angle fault sets. Differently, Maschio *et al.* (2005), documented left-lateral transtensional slip along WNW-ESE striking, left-stepping master faults, and localized dilation within the releasing jogs of interacting WNW-ESE faults due to NE–SW striking normal faults. High-angle faulting involved slope deposits and paleo soils 39 and 18 ka old, respectively (Giano *et al.*, 2000), and caused historical seismicity in the whole Agri Valley area (Mallet, 1862; Cello *et al.*, 2003, Buttinelli *et al.*,2016; Hager *et al.*, 2021).

According to the latest geological map available for the study area (Palladino *et al.*, in preparation), the Viggiano Mt. carbonates are bounded northward and southward by WNW-ESE striking, high-angle transtensional faults, and westward and eastward by NE-SW striking, high-angle extensional faults (Figure 2.2a). The high-angle faults dissect the buried, NE-verging, low-angle thrust juxtaposing the Viggiano carbonates against the Lagonegro II Unit (Patacca & Scandone, 2007; Bruno *et al.*, 2014), and the associated anticline forelimb. The bottom portion of the Viggiano carbonates includes Triassic dolostones, lower Jurassic wackestones and packstones with thick-shelled bivalve (*Lithiotis)*, green algae (*Palaeodasycladus mediterraneus),* and foraminifera (*Siphoalvulina sp, Pseudocyclammina liassica*) marking the Pleinsbachian age (Lechler et al., 2012). These carbonates formed in a subtropical, inner platform depositional environment, and were topped by thick, massive oolites postdating the Early Toarcian Anoxic event (Caruthers *et al.*, 2013; Trecalli *et al.*, 2012; Wignall & Bond, 2008). The upper portion of the Viggiano carbonates consists of Albian-Cenomanian rudstones and grainstones with gastropods, bivalves, rudists (*Radiolitidae)*, and foraminifera (Lechler *et al.*, 2012). The topmost carbonate beds are made up of mudstones-to-rudstones and boundstones (*Lithocodium*) with geopetal structures and rudists (*Conicorbitolina conica*, *Salpingoporella turgida* and *Caprinidae*).

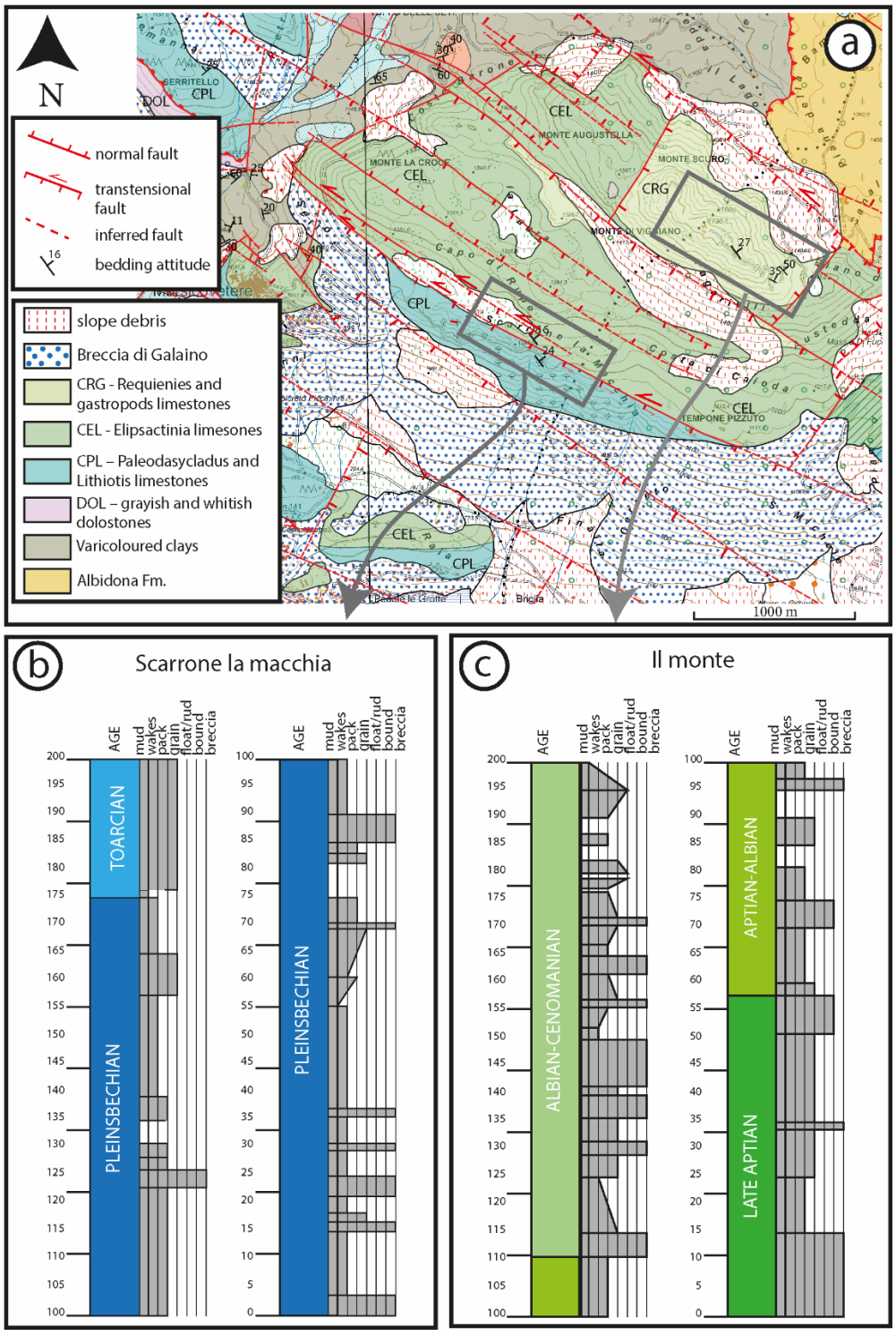

Figure 2. 2 (a) Geological map of the Viggiano Mt. area, located along the northern edge of the High Agri Valley (Palladino *et al.*, in preparation). Location of both "Scarrone la macchia" and "Il monte" study sites is reported; (b), (c) schematic stratigraphic logs of: "Scarrone la macchia", and "Il monte" areas (modified after Lechler *et al.*, 2012), respectively.

2.3 Methods

The present study focuses on the two main sites labelled as "Scarrone la macchia" (40° 22.484'N, 15° 50.383'E) and "Il monte" (40° 22.678'N, 15° 51.693'E), which are respectively

located along the southern cliff (Figure 2.2b) and upper portion of the Viggiano Mt. (Figure 2.2c).

2.3.1 Stratigraphic analysis and rock sampling

Field stratigraphic logging was performed aiming at assessing both bed thickness and carbonate lithofacies (Dunham, 1962). The bed thickness was measured orthogonal to laterally continuous bed interfaces. The carbonate lithofacies were characterized by mean of a portable magnifying lens. A total of 70 samples were collected at the "Scarrone la macchia" site, and 51 samples at the "Il monte" site. Regarding the former ones, 10 samples derive from outcrops exposing the bottommost portion of the oolithic carbonates and the associated primary interfaces.

2.3.2 Petrographic analysis

The analysis was carried out by using an optical microscope (Leitz Laborlux 12 Pol) associated to the Zen software for photomicrograph acquisitions. Microfacies textural classifications after Dunham (1962) and Embry & Klovan (1971). A total of 19 thin sections obtained from samples collected at the "Scarrone la macchia" and 14 at the "Il monte" sites were analyzed. Biostratigraphic analysis of the Lower Jurassic carbonates based on biozonal schemes and chronostratigraphic references related to the Tethyan inner-carbonate platforms (De Castro, 1991; Boufagher-Fadel, 2008, Chiocchini *et al.*, 1994; Barattolo & Romano, 2005). Biostratigraphic analysis of the Cretaceous carbonates after the distribution ranges already described for the Tethyan realm (Di Stefano & Ruberti, 2000; Chiocchini *et al.*, 1994).

2.3.3 Mineralogical analysis

20 powders obtained from the hand samples collected at the bottommost portion of the oolithic carbonates exposed at the "Scarrone la macchia" site was investigated. X-ray Powder Diffraction (XRPD) analysis carried out by mean of the Rigaku D/Max 2200 diffractometer with Θ-Θ Bragg-Bentrano geometry, equipped with CuKα radiation, automatic sample holder spinner, secondary graphite monochromator, and scintillation detector. The following instrumental conditions were adopted: (i) power 40 mA x 30 kV, (ii) step scan 0.02 °2Θ, (iii) speed 3s/step, (iv) divergent slit 1°and receiver slit 0.3 mm. Random

powders and oriented specimens were respectively analyzed in the angular range of 2 - 70 °2Θ and 2 - 32 °2Θ. Mineralogical analyses performed on bulk samples, on their terrigenous components, and on the < 2 μm terrigenous fraction (Table 1).

Hand samples were first crushed. Then, one aliquot was pulverized by friction in a concentric-disk agate mill, whereas another aliquot was treated with diluted HCl to first the carbonates (Cuadros & Altaner, 1998). The remaining silicate component was several times washed with distilled water, and then collected by centrifugation. About 0.5 g of the collected silicates were manually milled by using mortar and pestle, and then used for random specimen analyses by mean of side loading. Differently, ca. 1.5 g of the collected silicates were used for clay fraction (<2μm) separation according to the Stock's law. The clay fraction was then saturated with 1N $MgCl_2$ solution, and finally used for orientated specimen analysis by settling it on a glass slide (Moores & Reynolds, 1997). The oriented specimens were air dried, ethylene glycol solvated, and then heated at 375 °C (Moore & Reynolds, 1997).

Table 1 Sample code, litology, components and fractions determined by XRPD on samples collected from the "Scarrone la Macchia" stratigraphic section. n.d.: not detected because is present in very little amount.

Sample	Litology	Random powder of Bulk sample	Rondom powder of terrigenous component	Oriented specimens (< 2 μm fraction) of the terrigenous component
O-2	cohesive limestone	X	n.d.	n.d.
SC1	interbed with terrigenous component	X	X	X
SC2	interbed with terrigenous component	X	X	X
MC1	cohesive limestone	X	X	X
MC3	cohesive limestone	X	X	n.d.
SL2B-C1	interbed with terrigenous component	X	X	X
SL2B-C2	interbed with terrigenous component	X	X	X
MC4	cohesive limestone	X	X	X
SC3	interbed with terrigenous component	X	X	X
MC5	cohesive limestone	X	n.d.	n.d.
MC6	cohesive limestone	X	X	X
SC4	interbed with terrigenous component	X	X	X

MC7	cohesive limestone	X	X	X
A7	cohesive limestone	X	X	n.d.
SC5	interbed with terrigenous component	X	X	X
C1	cohesive limestone	X	X	n.d.
D5	cohesive limestone	X	X	n.d.
D4	cohesive limestone	X	X	n.d.
SC6	interbed with terrigenous component	X	X	X
D2	cohesive limestone	X	X	X

2.3.4 Structural analysis

Field structural analyses were carried out by mean of circular and linear scanline methods (Priest and Hudson, 1981; Mauldon *et al.*, 2001). The former one consisted of circles drawn on the rock surface delimitating a circular window (symmetric sampling area), in which the number of fracture intersections, n, and the number of fracture endpoints inside the sampling area, m, were measured. All fracture traces longer than 3 cm were considered. Outcrops were chosen based on accessibility, dimensions (width > 10 m), and distance from main fault zones. The measured m and n values were respectively employed for 2D fracture density, P20, and intensity, P21, calculations (Mauldon *et al.*, 2001).

P20 represents the number of fracture trace centers per unit area ($1/m^2$), and it is obtained by applying the following equation:

$$P20=m/2\pi r$$

where "r" is the radius of the circular scan line.

P21 represents the mean total trace length of fractures per unit area (m/m^2), and it is obtained by applying the following equation:

$$P21=n/4r$$

Eighty-five circular scanlines were conducted within single carbonate beds. According to the bed thicknesses, the diameter of circular scanline varied between 15 and 50 cm. In order to obtain representative P20 and P21 estimations, circular scanlines included at least 30 endpoints (Rohrbaugh *et al.*, 2002).

Thirteen linear scanline analyses were performed by considering ideal lines drawn on the rock and measuring both attitude and distance from origin of all surveyed fractures. As a result, true fracture spacing values (S_r) were computed for single fracture sets. Computations performed by applying trigonometric corrections to the apparent spacing values (S_a) in light of the α and β values (α: azimuthal angle formed by fracture strike direction and scanline trend; β: zenithal angle formed by fracture dip angle and scan line plunge).
True fracture spacing is obtained by applying the following equation:

$$S_r=S_a * (\cos\alpha) * (\cos\beta)$$

At both sites, ten of the aforementioned linear scanlines were positioned parallel to carbonate beds, away from mesoscale faults, to measure the 1D fracture intensity, P10, of the high-angle WNW-ESE ("Scarrone la macchia") and WSW-ENE ("Il monte") fracture sets. Differently, the three other linear scanlines, respectively labelled S1 to S3, were performed along orthogonal outcrops of the "Scarrone la macchia" site to assess the multiscale spacing distribution of the outcropping, high-angle fracture sets. Both S1 (N230E/40°) and S3 (N100E/31°) were positioned away from mesoscale faults, whereas the S2 (N180E/25°) was located across a ca. N110E striking, high angle transtensional fault.

2.4 Results

In this chapter, we first present the stratigraphic, petrographic, and mineralogical data. Then, we document the geometry, density, intensity and multiscale spacing distribution of the surveyed fracture sets.

2.4.1 Carbonate stratigraphy

"Scarrone la macchia" site

The ca. 56 m-thick succession includes two informal units (Figure 2.3). The lower one is made up of well-layered carbonates with dark limestones and marly intercalations. The carbonates show a total thickness of about 43 m (Figure 2.3a), and dip NE (Figure 2.3c). They are subdivided into 12 single bed packages, respectively labelled A to N bottom up, whose thickness varies from ca. 13 m (bottom) to ca. 1 m (top) (Figure 2.3b). Single bed packages show fining-upwards carbonate textures, with thick beds of coarse-grained

limestones at the bottom, and thin beds of fine-grained limestones at the top. The bed packages are bounded by laterally continuous, 5-to-10 cm-thick, clay-rich carbonate interfaces including anastomosed pressure solution seams. Single carbonate beds are delimited by mm- to cm-thick bed interfaces, which might include pressure solution seams with siliciclastic films of insoluble material.

The well-layered carbonates are topped by an up to 15 cm-thick, clay-rich carbonate layer including mm- to cm-sized elongated carbonate clasts embedded in a fine-grained matrix. The outcropping 13 m-thick oolithic grainstones above mainly dip NE (Figure 2.3c), forming a large-scale, open syncline. The outcropping oolithic unit at the "Scarrone la macchia" includes four main bed packages, respectively labelled O to R (Figure 2.. 3a, b), delimited by laterally continuous, mm-thick, clay-rich carbonate interfaces. The single 5 to 40 cm-thick carbonate grainstone beds show a pronounced amalgamation, and significant lateral thickness variations. Bed interfaces are marked by localized pressure solution seams. At a close view, the single pressure solution seams do not show any visible insoluble clayish material.

"Il monte" site

The 67 m-thick massive carbonates dip NE, and include 11 bed packages labelled A to M bottom up (Figure 2.. 3d, f). The bed packages are delimited by laterally continuous, erosive surfaces, and show fining upward trends characterized by carbonate breccia and bioclastic rudstone/floatstone at the bottom, and carbonate grainstones and/or mudstone at the top (Figure 2.3e). Single carbonate breccia and rudstone/floatstone beds include rudist fragments. Bed interfaces show a very pronounced amalgamation, and presence of pressure solution seams with tabular shapes.

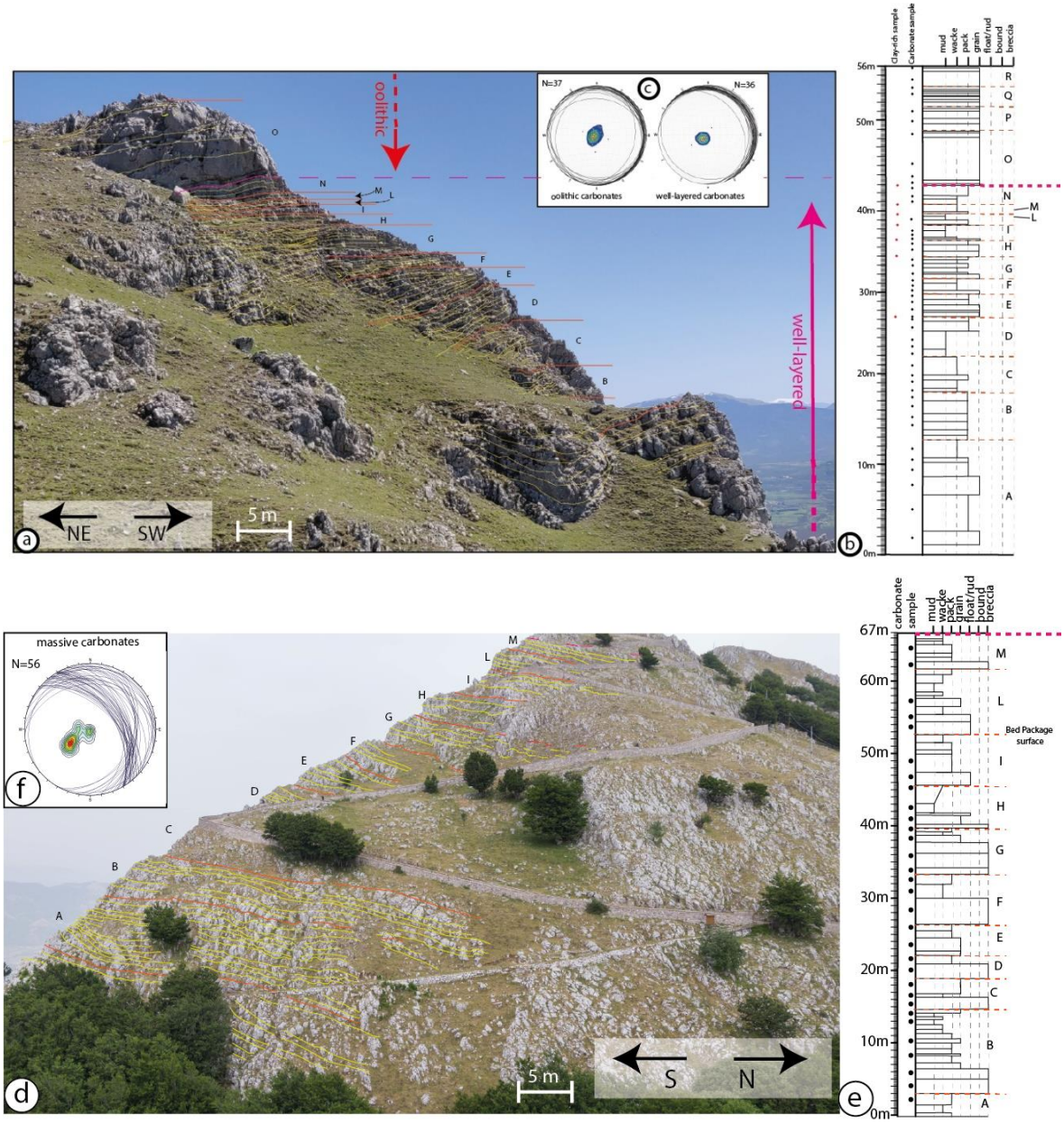

Figure 2. 3 (a) Panoramic view of the "Scarrone la macchia" site. Bedding surfaces (yellow lines), bed packages interfaces (orange lines), and sedimentary unit interfaces (magenta line) are reported; (b) stratigraphic log of the "Scarrone la macchia" site. The aforementioned interfaces are also reported; (c) lower-hemisphere, equal-area stereographic projection of bedding planes measured in well-layered carbonates and oolithic carbonates; (d) panoramic view of the "Il monte" site. Bedding surfaces (yellow dashed lines), bed packages interfaces (orange lines) and sedimentary unit interfaces (magenta line) are highlighted; (e) stratigraphic section of "Il monte" site. The aforementioned interfaces are also reported; (f) lower-hemisphere, equal-area stereographic projection of bedding planes measured in the massive carbonates.

2.4.2 Carbonate petrography

"Scarrone la macchia" site

The well-layered carbonates include abundant benthic foraminifera and calcareous algae (including *Haurania sp., Siphovalvulina sp., Lituosepta sp., Palaeodasycladus*

mediterraneus, the microproblematica Thaumatoporella parvovesiculifera (Figure 2.. 4a-e). Microfractures are partially occluded by blocky cement (Figure 2.4g).

The oolithic limestones are made up ooids with obliteration of the laminae due to intense micritization (Figure 2.4f). However, in some cases, the original fabric consisting of concentric laminae is preserved. Ooids are 500 to 1000 µm in size, cemented with blocky calcite, and consist of alternations of laminae (<1cm thick) including micrite oncoids (> 1 mm). Their nuclei are made up of skeletal grains, peloids, and rare mineral grains. Suture-like contacts among grains are absent, while microfractures are visible (Figure 2.4h).

"Il monte" site

The massive carbonates include rudist fragments, gastropods, algae, and benthic foraminifers (*Orbitolinids*) (Figure 2.. 5a, b, c, e.). Single rudist fragments, up to ca. 5 cm in size, are micritized and affected by both microboring (cf. Figure 2.5b) and pervasive dissolution (Figure 2.. 5e-f). Rare stromatolitic laminae associated with oncoids and ostracods are also documented (Figure 2.5d). Both granular and meniscus cements and isopachous crusts are present (Figure 2.. 5e-f). Intergranular pores are filled with carbonate cements, barren silts, and ostracod-rich sediments (Figure 2.5e-f).

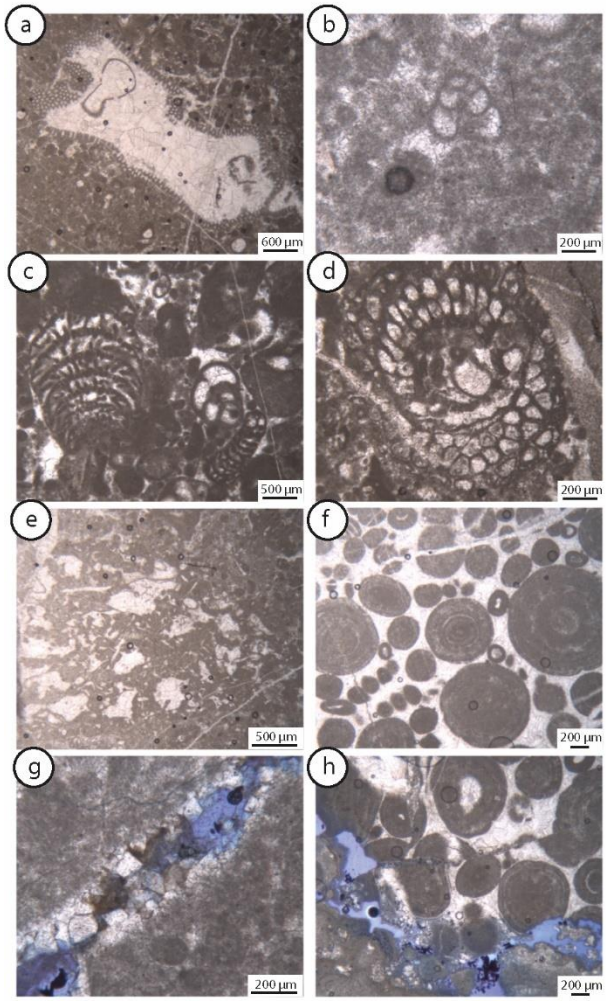

Figure 2. 4 Microfacies of the Scarrone la macchia section (a)-(e): well-layered carbonates, f-h: oolithic carbonates). (a) Packstone with Thaumatoporella parvovesiculifera. (b) grainstone-packstone woth Siphovalvulina sp.; (c) grainstone-pakstone with benthic foraminifera (Siphovalvulina sp., Haurania deserta, Lituosepta sp.); (d) Palaeodasycladus mediterraneus; (e) Bacinella-Lithocodium agregatum; (f) oolithic grainstone; (g) open fractures partially occluded by dolomitic cements; (h) intergranular porosity.

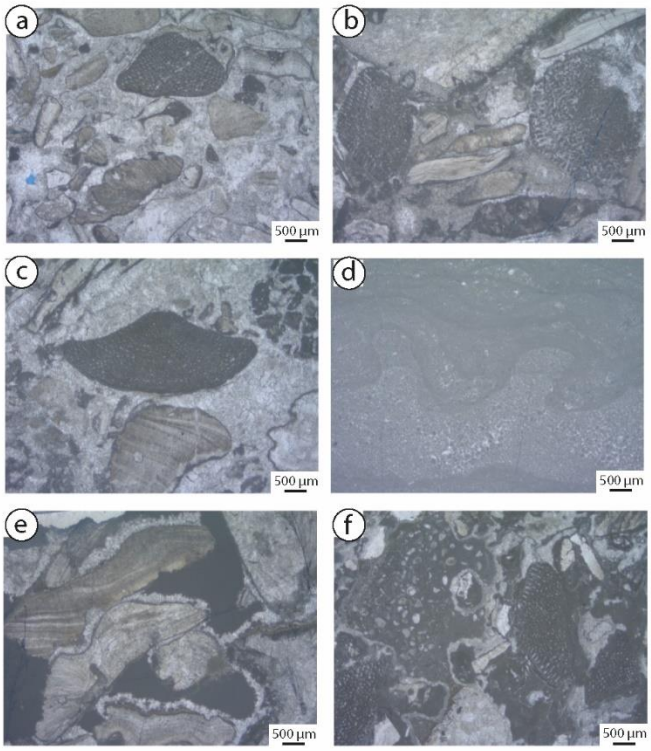

Figure 2. 5 Microfacies of the "Il monte" section. (a), (b) and (c) grainstone to rudstone with fragments of rudists shell, orbitolinids. (d) stromatolitic laminae with peloids. (e) meniscus cements connecting the grains and isopacous cements rims around the rudists fragments. Barren silt filled the residual cavities. (f) meniscus cements connecting the grains. The residual cavity is filled by a silt rich in ostracods.

2.4.3 Mineralogical analysis

The results of the XRPD qualitative analyses are reported in Table 2, and figures 6 and 7. Random powder analysis of the bulk rocks show that all samples mainly include calcite (Figure 2.6a). The silicates include quartz, feldspars (plagioclase), goethite, and clay minerals such as illite, mixed layer illite/smectite (I/S), chlorite, and kaolinite (Figure 2.6b). Mixed-layers show ordered R1 with 80% of illite, and R3 with 90% of illite (Figure 2.7; Table 2).

Table 2 Mineralogical assemblages of the study samples. Cal: calcite; Qtz: quartz; Fs: feldspars; Gth: goethite; I/S: mixed layers illite-smectite; Ill: illite; Chl: chlorite; Kao: kaolinite. X: indicates the presence of mineral phase; n.d.: not detected.

Sample	Random powder analysis of bulk sample and terrigenous component								Oriented specimens (< 2µm)			
	Cal	Qtz	Fs	Gth	I/S	Ill	Chl	Kao	I/S features			
									Ordering, R		Illite percentage	
O-2	X	n.d.	n.d.	n.d.	n.d.	n.d.	n.d.	n.d.	n.d.	n.d.	n.d.	n.d.
SC1	X	n.d.	X	n.d.	X	X	X	n.d.	R1	R3	82	89
SC2	X	n.d.	X	n.d.	X	X	X	n.d.	n.d.	R3	n.d.	87

MC1	X	n.d.	X	n.d.	X	X	X	n.d.	n.d.	R3	n.d.	87
MC3	X	X	X	n.d.	X	X	X	n.d.	n.d.	n.d.	n.d.	n.d.
SL2B-C1	X	X	X	n.d.	X	X	X	n.d.	R1	R3	80	90
SL2B-C2	X	X	X	n.d.	X	X	X	n.d.	R1	R3	78	90
MC4	X	X	X	n.d.	X	X	X	n.d.	n.d.	R3	n.d.	87
SC3	X	n.d.	X	n.d.	X	X	X	X	n.d.	R3	n.d.	86
MC5	X	X	n.d.	n.d.	n.d.	n.d.	n.d.	n.d.	n.d.	n.d.	n.d.	n.d.
MC6	X	X	X	n.d.	X	X	X	X	R1	R3	82	89
SC4	X	n.d.	X	X	X	X	X	n.d.	R1	R3	80	89
MC7	X	X	X	X	X	X	X	n.d.	n.d.	R3	n.d.	85
A7	X	X	X	n.d.	X	X	X	n.d.	n.d.	n.d.	n.d.	n.d.
SC5	X	n.d.	X	X	X	X	X	n.d.	n.d.	n.d.	n.d.	n.d.
C1	X	n.d.	X	n.d.	X	X	X	n.d.	n.d.	n.d.	n.d.	n.d.
D5	X	X	X	n.d.	X	X	X	n.d.	n.d.	n.d.	n.d.	n.d.
D4	X	X	X	n.d.	X	X	X	n.d.	n.d.	n.d.	n.d.	n.d.
SC6	X	X	X	X	X	X	X	n.d.	n.d.	R3	n.d.	86
D2	X	n.d.	X	n.d.	X	X	X	n.d.	n.d.	R3	n.d.	87

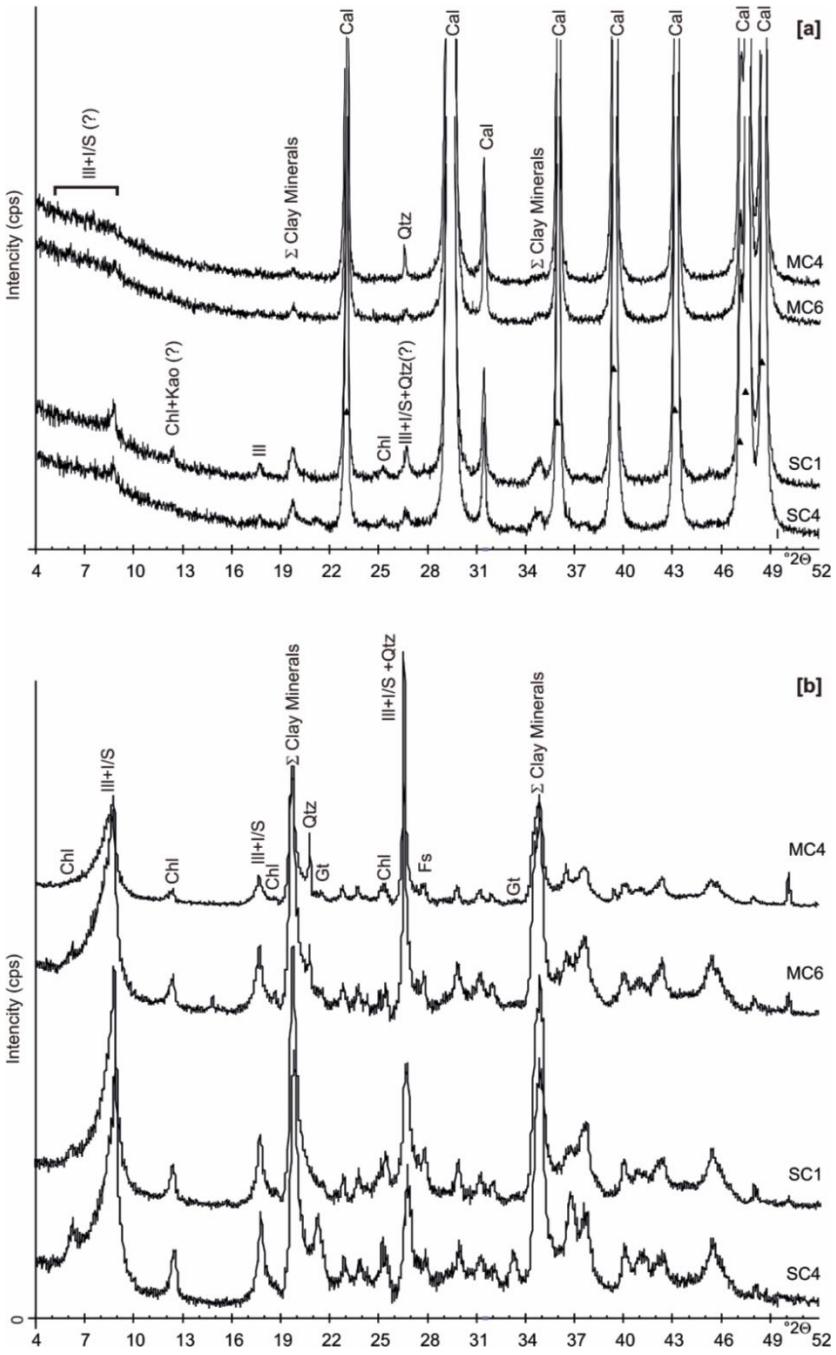

Figure 2. 6 Representative XRD patterns of selected samples. (a) Bulk samples and (b) terrigenous components. Cal=calcite, Qtz=quartz, Fs=feldspars, Gt=goethite, Ill=illite, I/S= mixed layers illite/smectite, Chl=chlorite, Kao=kaolinite; Σ Clay minerals= sum clay minerals.

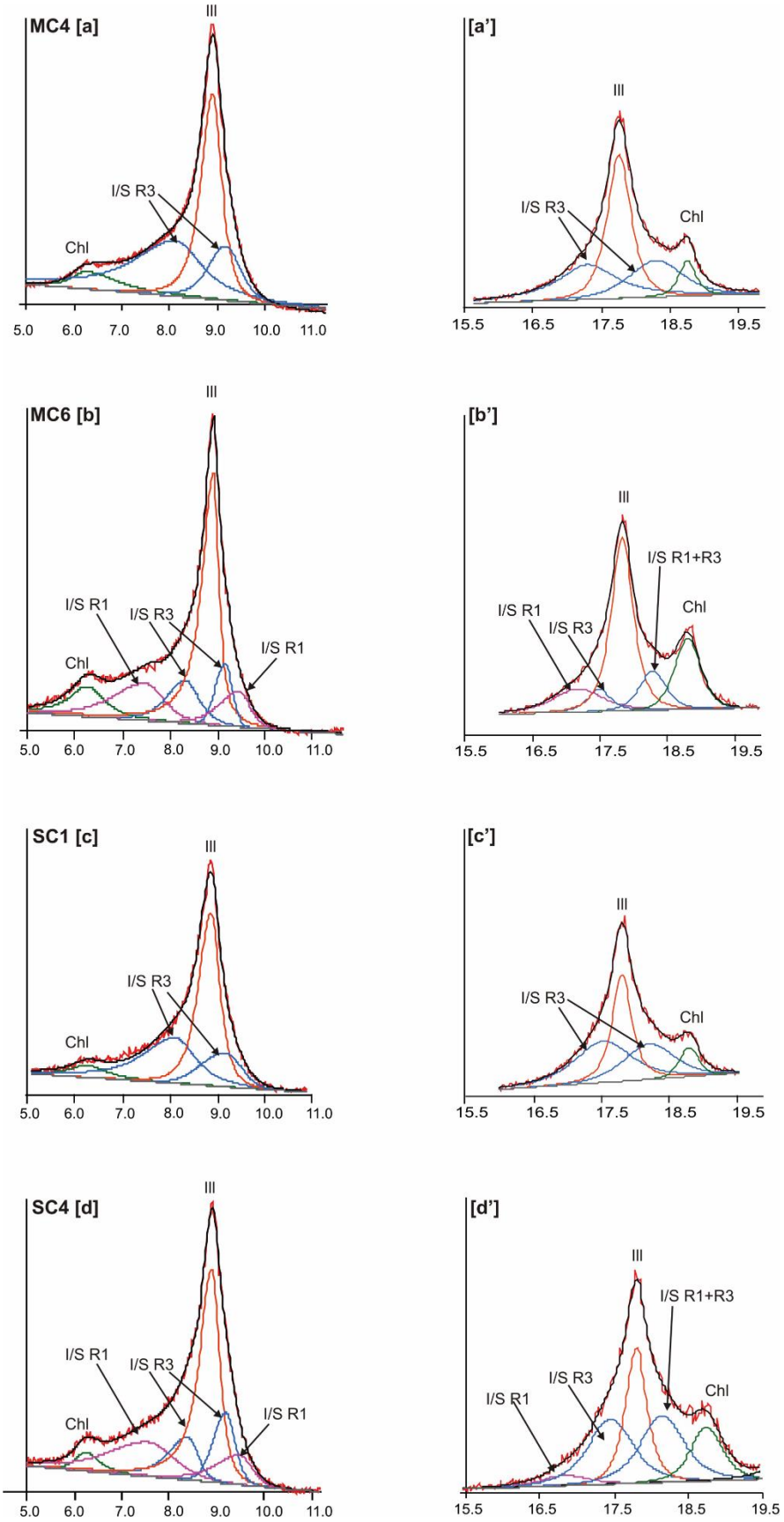

Figure 2. 7 Representative XRD patterns of ethylene glycol solvated clay fraction powders of selected samples. On the left (a, b, c, d) decomposition at low angles; on the right (e,f,g,h) decomposition at higher angles. Ill=illite, I/S= mixed layers illite/smectite, Chl=chlorite.

2.4.4 Structural analysis - fracture orientation

The cumulative plots of fracture poles are shown in equal-area, lower-hemisphere projections (Allmendinger *et al.*, 2011) as present-day data (Figure 2.8a), and after bedding restoration (Figure 2.8b). Fracture data restored by considering the attitude of single carbonate beds. The fracture poles mainly cluster around N199E/06 and N195E/23 (trend/plunge), which are related to ca. WNW-ESE striking fractures respectively dipping 84° and 67°.

In order to precisely document the fracture orientation, the available data are subdivided into three different subsets respectively corresponding to the well-layered, oolithic, and massive carbonates. Five main high-angle sets are shown by both original and restored data (Figure 2.9):

- fractures striking WNW-ESE;
- fractures striking WSW-ENE;
- fractures striking N-S;
- fractures striking NW-SE;
- fractures striking NE-SW.

The WNW-ESE striking fractures show a dense pole cluster in the well-layered carbonates, forming a 68° cut-off angle with bedding. They are also present in the oolithic carbonates, determining a 56° cut-off angle. The WSW-ENE striking fractures are mainly present in the massive carbonates, forming a ca 70° cut-off angle with bedding. The N-S striking fractures are rare in both well-layered and massive carbonates, whereas they form a dense pole cluster in the oolithic carbonates determining a ca. 70° cut-off angle with bedding. The NW-SE striking fractures form low density pole clusters in all study carbonates, with cut-off angles of 74° (well-layered carbonates) to 55° with bedding (both oolithic and massive carbonates). The NE-SW striking fractures form low density pole clusters in all study carbonates, with cut-off angles of 86° (well-layered carbonates), 71° (massive carbonates), and 67° with bedding (oolithic carbonates), respectively.

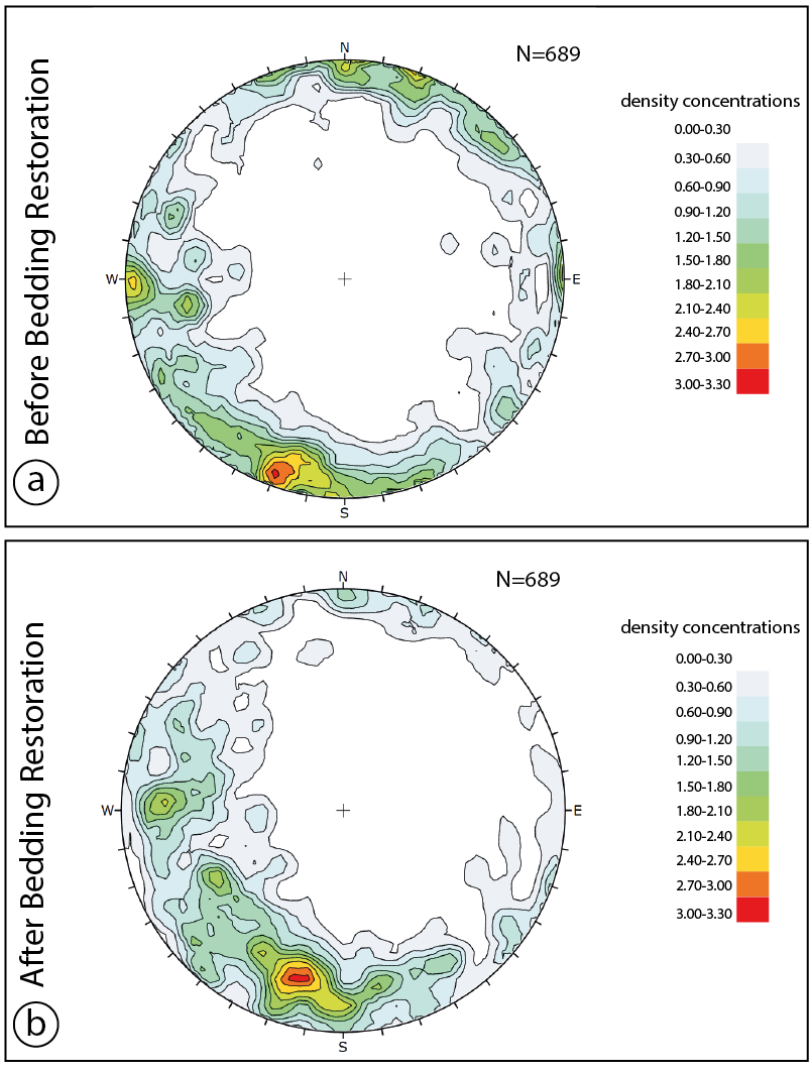

Figure 2. 8 Cumulative lower-hemisphere, equal-area stereographic projection of (a) fracture poles after field measurements and (b) after bedding restoration (right). Fracture data restored considering the attitude of single beds from which data were gathered.

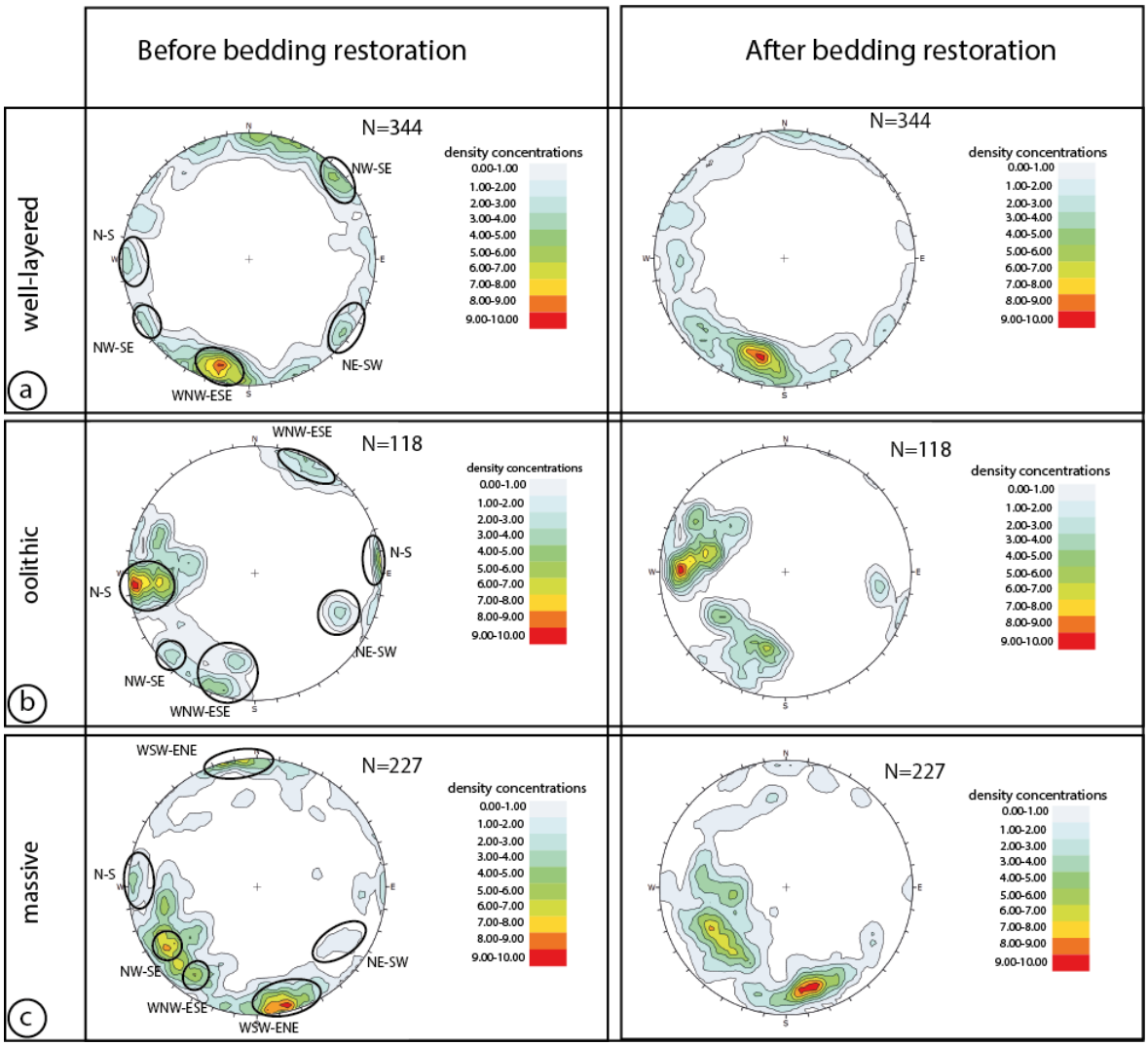

Figure 2. 9 Lower-hemisphere equal-area stereographic projection of fracture poles after field measurements (left) and after bedding restoration (right) subdivided into three subsets, according to the related carbonate units: (a) well-layered carbonates; (b) oolithic carbonates; (c) massive carbonates.

2.4.5 Structural analysis - fracture density and intensity

At the "Scarrone la macchia" site, (Figure 2. 10a, 11) P20 varies from 61 m^{-2} (1 m-thick carbonate wackestone bed, ca. 35 m above the base level) to 552 m^{-2} (40 cm-thick carbonate packstone bed, ca. 14 m above the base level) throughout the well-layered carbonates. There, P20 commonly decreases upward within single bed packages. In the same carbonate unit, P21 varies from 10 m^{-1} (1 m-thick carbonate wackestone bed, ca. 35 m above the base level) to 46.7 m^{-1} (1.6 m-thick carbonate grainstone bed, ca. 7 m above the base level). Similar to fracture density, P21 also decreases upward within single bed packages.

In the oolithic carbonates (Figure 2.10a), P20 varies from 87.6 m^{-2} (90 cm-thick carbonate grainstone bed, ca. 55m above the base level) to 488 m^{-2} (50 cm-thick carbonate grainstone bed, ca. 50 m above the base level). Differently, P21 ranges from 1.0 m^{-1} (90 cm-thick

carbonate grainstone bed, ca. 55 m above the base level) to 47.5 m^{-1} (50 cm-thick carbonate grainstone bed, ca. 50 m above the base level). The highest values of both P20 and P21 characterize the topmost beds of single bed packages.

The P10 values computed for the WNW-ESE and WSW-ENE striking, high-angle fractures respectively associated to the denser pole clusters documented within the well-layered and massive carbonates, are comprised between ca. 0.3 and 1.8 m^{-1} (Table 3).

At the "Il monte" site (Figure 2. 10b, 11), the massive carbonates show P20 varying from 43.3 m^{-2} (20 cm-thick mudstone bed, ca. 14 m above the base level) to 184 m^{-2} (3 m-thick carbonate breccia bed, ca.4 m above the base level). There, P21 ranges from 8 m^{-1} (60 cm-thick carbonate packstone bed, ca. 51m above the base level) to 25 m^{-1} (2 m-thick carbonate breccia bed, ca. 14 m above the base level).

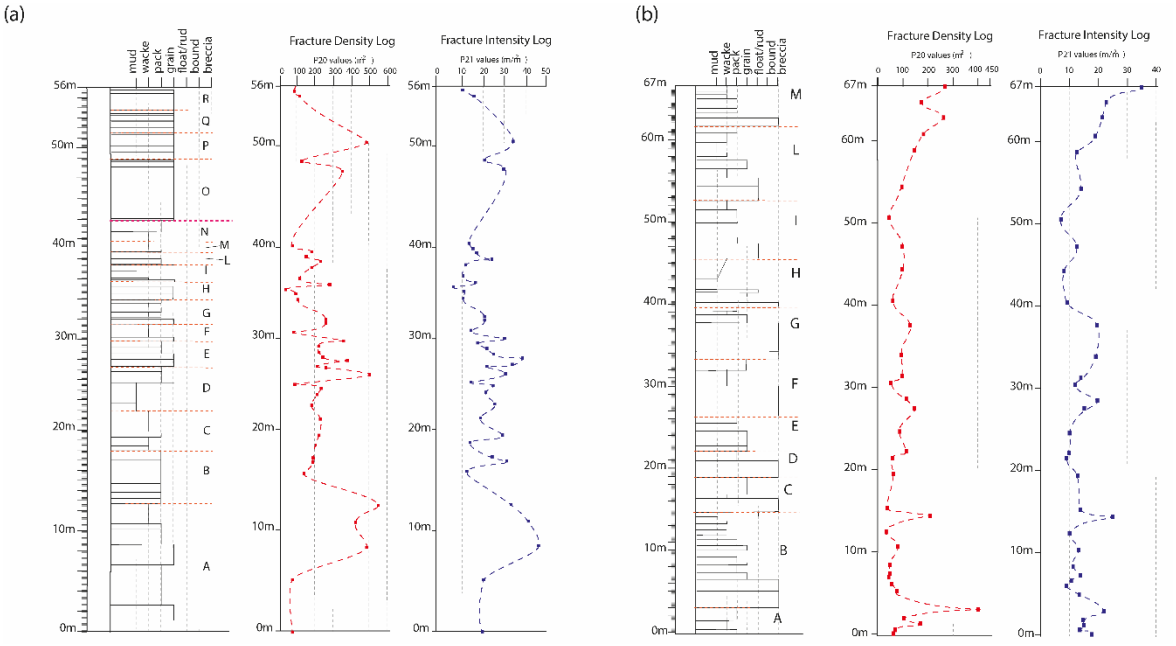

Figure 2. 10 Fracture density (P20) and intensity (P21) logs after field circular scanline measurements conducted across the: (a) well-layered and oolithic carbonates, and (b) massive carbonates.

Table 3 P10 variations for the JV1 fracture set.

Lithofacies	Bed thickness	P10
Grainstone	60 cm	1.79
Grainstone	70 cm	1.26
Wakestone	25 cm	0.85
Wackestone	54 cm	0.3
Grainstone	25 cm	0.86

Oolithic grainstone	55 cm	1.06
Oolithic grainstone	90 cm	0.74
Carbonate breccia	30 cm	1.35
Carbonate breccia	120 cm	0.95
Carbonate breccia	100 cm	0.46

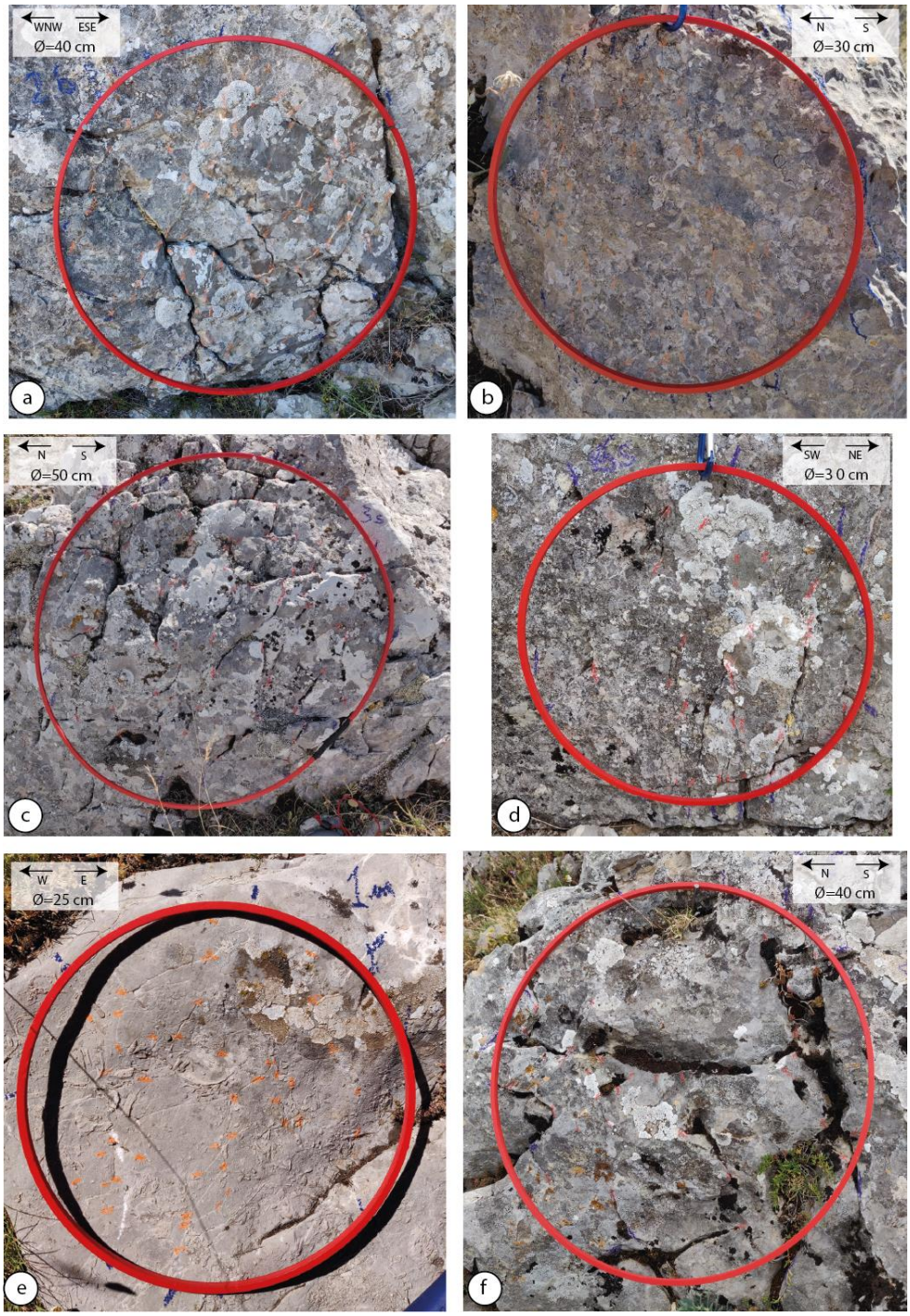

Figure 2. 11 Outcrop images of the investigated carbonate beds by means of circular scan lines: (a), (b) well-layered carbonates; (c), (d) oolithic carbonates; (e), (f) massive carbonates. The right column (a,c,e) shows the beds

characterized by high fracture density and intensity; the left column (b,d,f) shows the beds with high fracture density and intensity.

2.4.6 Structural analysis - multiscale fracture spacing properties

The fracture poles obtained after S1, S2, and S3 linear scanline measurements (Figure 2.12) are reported in equal-area, lower-hemisphere projections (Figure 2. 13a, d, g). Along S1, the two main fracture sets respectively striking N292E and N300E respectively show an exponential best-fit (R^2 = 0.97) and a power law best fit (R^2 = 0.93) in the bi-logarithmic fracture spacing vs. cumulative number plots (Figure 2. 13b, c). Along S2, the two main fracture sets striking N252E and N284E are respectively characterized by power law (R^2 = 0. 96) and exponential (R^2 = 0.93) fracture spacing distributions (Figure 2. 13e, f). Along S3, the two main fracture sets striking N180E and N206E respectively show power law (R^2 = 0.92) and exponential (R^2 = 0.87) fracture spacing distributions (Figure 2. 13h, i).

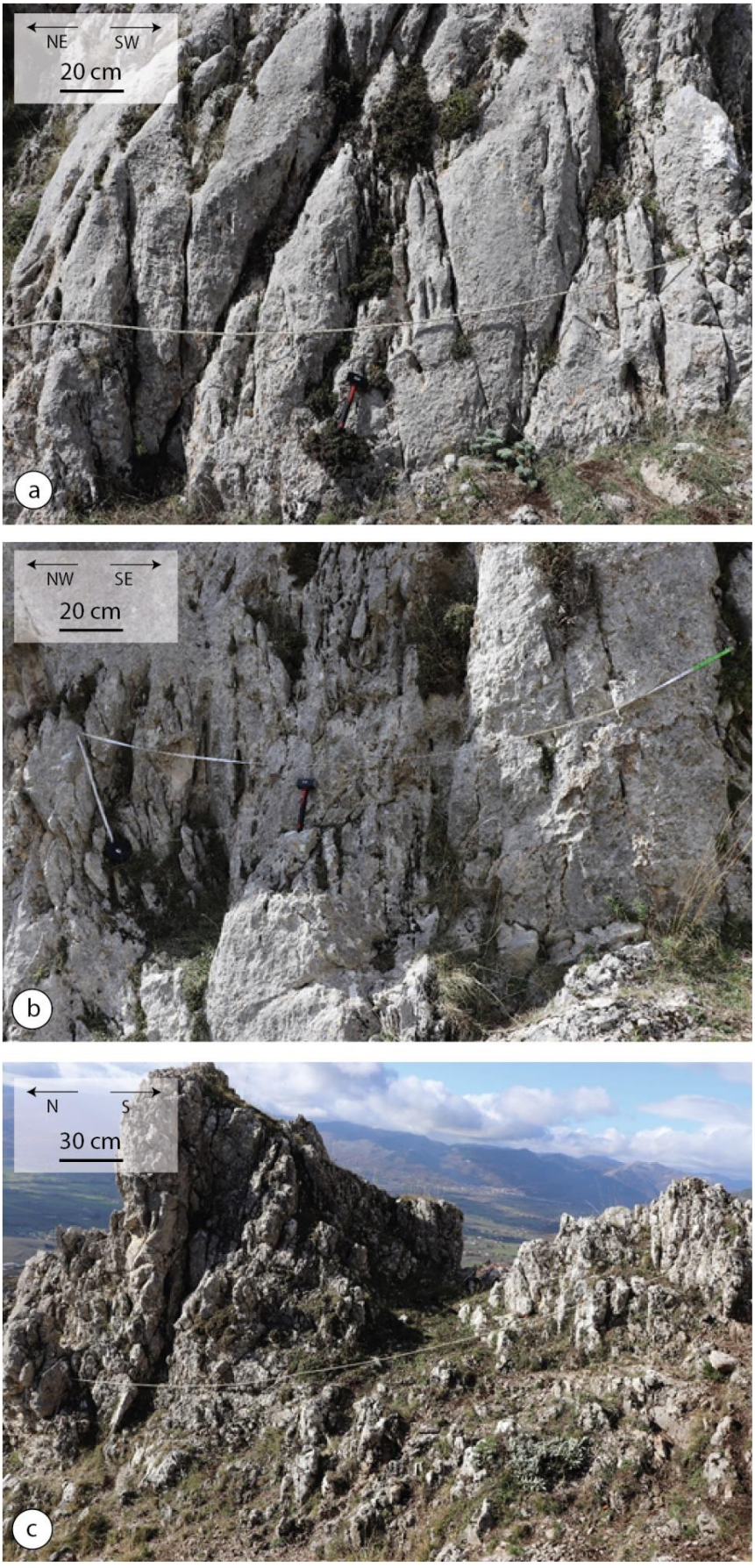

Figure 2. 12 Outcrop images of the (a) S1, (b) S2 and (c) S3 linear scan lines.

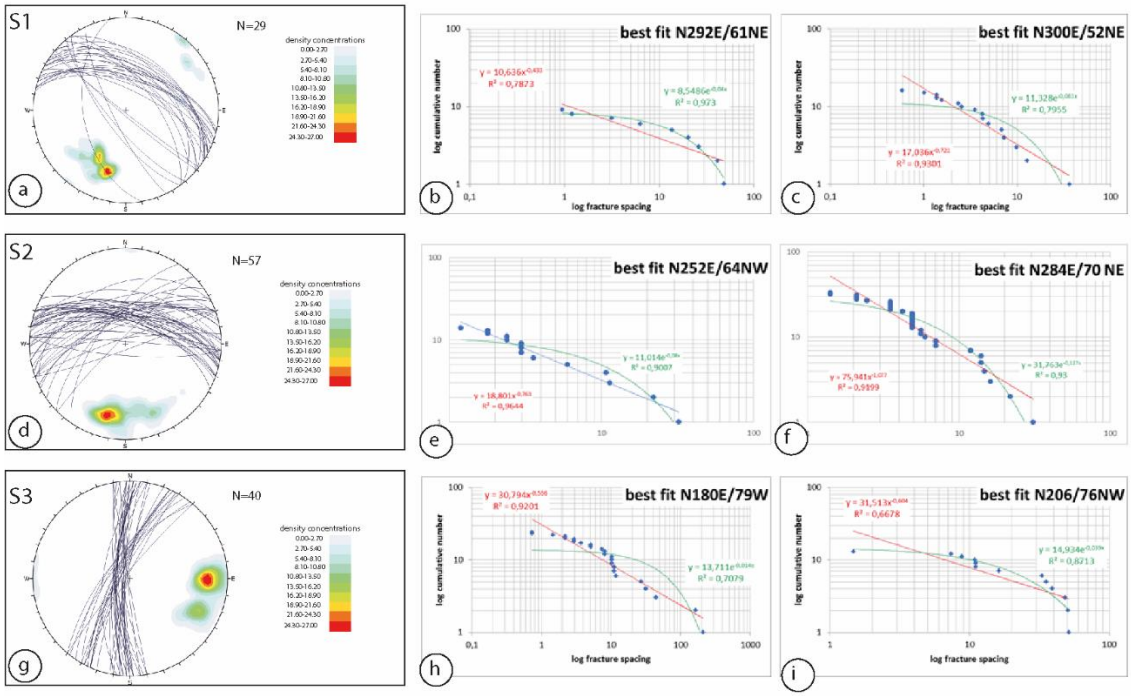

Figure 2. 13 Multiscale fracture spacing distribution. (a) lower-hemisphere, equal-area stereographic projection of fracture poles of the S1 scan line; (b) log cumulative number vs spacing and best fit relative to the N292 striking set; (c) log cumulative number vs spacing and best fit relative to the N300 striking set; (d) lower-hemisphere, equal-area stereographic projection of fracture poles of the S2 scan line; I log cumulative number vs spacing and best fit relative to the N252 striking set; (f) log cumulative number vs spacing and best fit relative to the N284 striking set; (g) lower-hemisphere, equal-area stereographic projection of fracture poles of the S3 scan line; (h) log cumulative number vs spacing and best fit relative to the N180 striking set; (i) log cumulative number vs spacing and best fit relative to the N206 striking set.

2.5. Discussion

In this chapter, we first discuss the results of stratigraphic, petrographic, and mineralogical analyses to assess the paleo depositional environments and diagenetic conditions. Then, the computed P20, P21, and P10 values are considered to unravel the fracture stratigraphy properties of the Mesozoic platform carbonates.

2.5.1 Depositional Setting

The Apennine Platform is considered as part of the bridge that connected the African Plate to the Adria microplate (Zarcone *et al.*, 2010; Randazzo *et al.*, 2021). Its carbonate factory was established during Late Triassic, and lasted until middle Cretaceous (Selli, 1957; Sartoni & Crescenti, 1961, 1962). Previous studies ascribed the Viggiano Mt. carbonates to the Alburno-Cervati Unit (Lechler *et al.*, 2012). In this study, we support this interpretation, and provide further constraints for the assessment of their depositional setting.

According to presence of large benthic foraminifera and algae, the well-layered carbonates formed at tropical and subtropical latitudes within an inner shallow platform environment (Flugel, 2004) characterized by well-oxygenated, warm waters (Fugagnoli, 2004). Furthermore, presence of ooids, irregular clasts, and thick shells of *Lithiotis* bivalves is consistent with occasional turbulent conditions, build-ups, and sand shoals (Clari, 1975; Flugel, 2004; Gale, 2005). Accordingly, we assess that carbonate deposition took place in a lagoonal environment protected by sand shoals. The informal litho-biostratigraphic zonation is mainly based on benthic foraminifers and calcareous algae association. The *Palaeodasycladus mediterraneus* distribution covers the whole Lower Jurassic (Barattolo, 1991); however, presence of this algae with benthic foraminifera such as *Haurania* sp., *Siphovalvulina* sp., *Lituosepta* sp. is consistent with upper Sinemurian-Pliensbachian age (Todaro *et al.*, 2017 and references therein).

The oolithic carbonates formed in high energy water conditions, above fair-weather wave base, within depositional environments characterized by a wide, low-gradient ramp rimmed by sand shoals (Flugel, 2004; Boudager Fadel *et al.*, 2008). Formation of the sandy margin was due to the absence of sponge reefs, as a consequence of the end Triassic mass extinction (Di Stefano *et al.*, 1996, Todaro *et al.*, 2018). The lithofacies transition between well-layered and oolithic carbonates hence marked both relative deepening and landward migration of the depositional setting, similar to other Lower Jurassic carbonate platforms of western Tethys (Mei & Gao, 2012; Ettinger *et al.*, 2021). Accordingly, the Pliensbachian-Toarcian extinction is associated to a sequence boundary related to transgression (Hallam, 1997; Haq, 2017), which drowned the carbonate platform, and therefore affected the carbonate factory.

The massive carbonates formed in a high-energy shelf environment (Flugel, 2004). In detail, the shallow-water biota, rounded skeletal fragments, and/or pristine rudist fossils (*Caprinids* bouquet in growth position, Bentivenga *et al.*, 2017) are consistent with moderate-to-high energy depositional environments close to the platform margin (reef to fore-reef) (Hughes, 2000; Di Stefano & Ruberti, 2000). On the other hand, the stromatolites, ooids, and oncoids are consistent with more internal lagoonal-tidal environments not far from the platform margin, as also documented in northern Sicily (Di Stefano & Ruberti, 2000). Moreover, the stromatolitic laminae and meniscus cements respectively recorded relative sea level oscillations and near surface fluid circulation conditions (Flugel, 2004).

2.5.2 Diagenetic evolution

Clay mineral analysis is useful to assess paleoclimatic conditions and diagenetic rock evolution (Hoffman & Hower, 1979; Chamley, 1989; Cavalcante *et al.*, 2003; 2011; Mazzoli *et al.*, 2008; Waliczek *et al.*, 2021). The very low amount, or absence, of goethite, kaolinite, hematite and boehmite in the study powders suggests the lack of any terrigeneous component associated to possible post-sedimentary reworking processes and/or sub-aerial alteration (Agosta *et al.*, 2021, and references therein). The presence of mixed illite/smectite layers with R1 and R3 ordering with a high percentage of illite are consistent with ca. 130°C thermal maturity, typical of high diagenetic conditions (Merrimman & Peacor, 1999; Cavalcante *et al.*, 2012; Perri *et al.*, 2016; Waliczek *et al.*, 2021). However, since smectite illitization and mixed-layers formation are also time-dependent processes (McCubbin & Patton, 1981; Pollastro, 1993), and function of K-availability (Cavalcante *et al.*, 2007; 2015), we assess 100 to 130° C diagenetic temperature range conditions. Assuming 20-25°C temperature gradients, typical of accretionary wedges (Merriman, 2005), a ca. 4-5 km burial is therefore estimated for the study carbonates. Considering that the overall platform carbonate thickness is lower that 1km (Patacca & Scandone, 2007), the aforementioned diagenetic conditions were likely related to the structural stacking of the Apennines allochthonous units.

2.5.3 Diffuse vs. localized fractures

Within the well-layered carbonates, the exponential fracture spacing distributions assessed for the N292E, N284E, and N206E fracture sets are due to a deformation that took place under uniform, remote stress fields (Dershowitz & Einstein, 1988). Fracturing in this case is hence comparable to a poissonian process (Cruden, 1977), in which the probability that a fracture could enucleate within a given space interval (i.e., single carbonate beds) is constant. The three aforementioned fracture sets therefore form a diffuse fracture network, whose failure modes and relative timing of formation are not yet assessed. Differently, the power-law fracture spacing distributions computed for the N300E, N252E, and N180E fracture sets is due to a deformation that occurred under local stress fields (Bonnet *et al.*, 2001, and references therein). These fracture sets therefore form a localized network and their fractal dimension, D, corresponds the slope of the best fit line (Mandelbrot, 1983). The computed D values for the three aforementioned localized fracture sets are comprised between 0.56

and 0.76, suggesting poorly developed N180E fractures, and moderately developed N300E and N252E fractures, respectively (Gillespie *et al*., 1993). Our results are similar to those gathered by Panza et al. (2016) and Giuffrida et al. (2019), who respectively documented D values comprised between 0.45 and 0.69, and between 0.39 and 0.81 for fractures measured away from major fault zones crosscutting Apulian platform carbonates, Italy. Regarding the study Viggiano Mt. area, Cello *et al.* (2000) also documented a low degree of fracture development within the carbonate fault damage zones, with D values comprised between 1.25 and 1.40 after box counting methodology.

Focusing on the WNW-ESE striking fractures, the most common set within the well-layered carbonates (cf. Figure 2.8), both N284E and N292E striking fractures pertain to the diffuse network, whereas the N300E striking fractures to the localized network. Accordingly, we interpret these results as due to multiple stages of fracture nucleation and subsequent development. Specifically, we propose that the WNW-ESE fractures first nucleated under uniform, remote stress fields likely associated to burial diagenesis (Korneva *et al.*, 2014, Lavenu et al., 2014, 2018; La Bruna et al., 2020; Agosta *et al.*, 2021) and/or paleo foreland bulging of the carbonates (Tavani *et al*., 2015; Corradetti *et al*., 2018). Subsequently, sub-parallel fractures formed under local stress fields associated to mesoscale faulting, as documented for faulted carbonates of the Apulian Platform exposed in the Majella Mt. (Agosta et al., 2010; Volatili et al., 2019; Romano et al., 2021), and Murge Plateau of Italy (Zambrano et al., 2015; Panza et al., 2015, 2016).

2.5.4 Fracture Stratigraphy

Fracture density is related to nucleating fracture networks according to fracture linkage configuration (Myers & Aydin, 2004; Agosta *et al.*, 2006; De Joussineau & Aydin, 2007; Antonellini *et al.,* 2008*;* Agosta *et al.*, 2010*),* and to rock elastic properties (Gross *et al.*, 1995; Agosta *et al.*, 2015, Rustichelli *et al*., 2016). Differently, fracture intensity is associated to well-connected fracture networks, which often localize within fault damage zones (De Joussineau & Aydin, 2007; Aydin et al 2010; Demurtas *et al.*, 2016; Giuffrida *et al.*, 2019; Mercuri *et al.*, 2020; Camanni *et al.*, 2021).

At the Viggiano Mt., both P20 and P21 do not vary proportionally with the bed thickness (Figure 2. 14a, d, e). Such a lack of proportionality is also displayed by the P10 values computed for the WNW-ESE (well-layered) and ENE-WSE (massive carbonates) striking fractures (Figure 2.15), the most common in those sedimentary units. This finding contrasts

with common spacing distributions documented for single fracture sets in layered rock masses (Nur, 1980; Gross *et al.*, 1995; Bai & Pollard, 2000; Schopfer *et al.*, 2011), and can be explained by the structural complexity of the study carbonate outcrops, which expose both diffuse and localized fractures (cf. Ch. 5.c).

The P20 and P21 logs show similar trends in both well-layered and oolithic carbonates (cf. Figure 2.10a). In layered carbonates, this is consistent with not strata-bound fractures forming due to linkage of pre-existing structural elements, and with nucleation of new strata-bound fractures within the narrow process zones that localize at the primary interfaces (Agosta & Aydin, 2006; Antonellini et al., 2008; Agosta *et al.*, 2009). Differently, the P20 and P21 values do not show great similarities in the massive carbonates (cf. Figure 2.10b). Accordingly, we assess that these carbonates with weak primary interfaces were mainly affected by fracture linkage processes, which dominated over fracture nucleation forming well-developed, vertically persistent fractures. The modalities of fracture propagation across the depositional and diagenetic interfaces exposed at the "Scarrone la macchia site" are currently under investigation. The results of this work will likely shed lights into the deformation mechanisms associated to primary interface disruptions.

Focusing on the possible correlations among P20, P21, and carbonate lithology, we document higher values of both fracture density and intensity in the grain-supported carbonate beds (Figure 2. 14b, c, f, g). Accordingly, we interpret such a pervasiveness of diffuse fractures due to the high values of the elastic moduli that characterized the grain-supported carbonates at times of deformation (*sensu* Bai and Pollard, 2000 and references therein). Our interpretation supports previous data published by Wennberg *et al*. (2006) for carbonates with relatively weak bed interfaces, and by Larsen *et al*. (2010) for rock multilayers in which carbonate mudstone beds arrested/deflected a great number of fractures. We further assess that the relatively high values of the elastic moduli characterized the grain-supported carbonate beds due to burial-related physical/chemical compaction (Rustichelli *et al.* 2012, 2015), and/or cementation processes (Eberli *et al.* 2003; Lamarche *et al*., 2012; Lavenu *et al.*, 2014, 2018; La Bruna *et al.*, 2020), as suggested by the high P10 values documented in these rocks for the WNW-ESE and WSW-ESE fractures (cf. Table 3).

Previous studies documented already the control exerted by carbonate lithofacies on fracture intensity. Mercuri *et al*. (2020) investigated a relay ramp zone in Mesozoic platform carbonates of central Italy, and documented lower P10 in carbonate packstones relative to carbonate grainstones and boundstones. At larger scales of observation, Corradetti *et al.* (2018) documented higher P21 in the dolomitic units encompassed by limestone beds

pertaining to Mesozoic platform carbonates exposed in southern Italy. There, diagenetic dolomitization within discrete rock intervals (Vinci *et al.*, 2017 and references therein) was invoked as the driving mechanism for fracture localization within specific carbonate beds and bed packages.

Figure 2. 14) Bed thickness vs P20 and P21 values for (a) well-layered carbonates; (d) oolithic carbonates; (e) massive carbonates. (b) Bed thickness vs P20 for the mud-supported carbonate, in which the grain supported and the mud supported beds are highlighted; (c) bed thickness vs P21 for the mud-supported carbonate, in which the grain supported and the mud supported beds are highlighted; (f) bed thickness vs P20 for the massive carbonate, in which the grain supported and the mud supported beds are highlighted; (g) bed thickness vs P21 for the massive carbonate, in which the grain supported and the mud supported beds are highlighted.

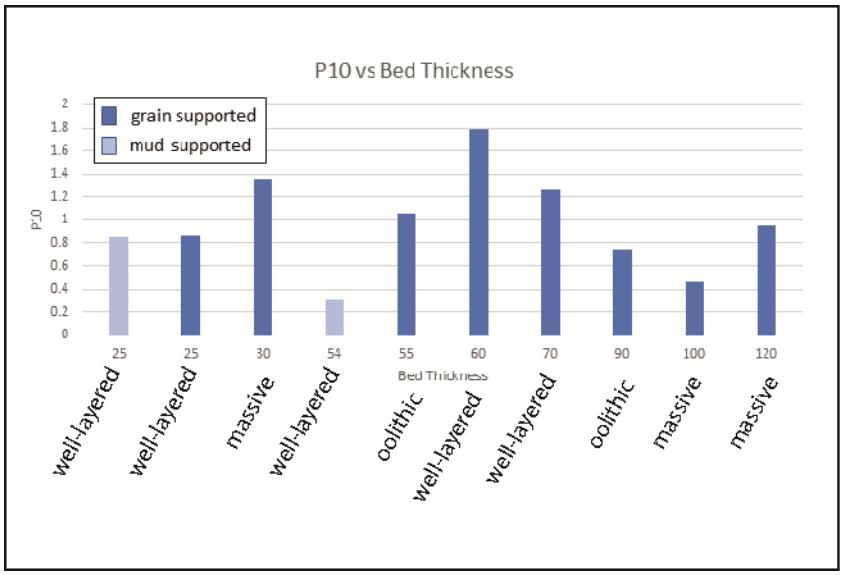

Figure 2. 15 Bed thickness vs P10 values calculated through significant beds in the three carbonate units. The grain supported lithofacies and the mud supported lithofacies are highlighted.

2.6 Conclusions

This work focused on the paleo depositional settings, amount of overburden, and fracture stratigraphy of Mesozoic platform carbonates exposed at the Viggiano Mt. area, southern Italy. In particular, three main depositional units respectively labelled as well-layered, oolithic, and massive carbonates were investigated. The Sinemurian-Pleinsbachian well-layered carbonates formed in a lagoonal environment protected by sand shoals. They include both mm-tick bed interfaces with pressure solution seams and cm-tick bed package interfaces including small amounts of terrigenous material. The Toarcian oolithic carbonates were deposited in a ramp rimmed by sand shoals. The oolithic carbonates contain amalgamated carbonate beds, and bed package interfaces made up of mm-tick terrigenous laminae. A large-scale stratigraphic interface including 10- to 15 cm-thick mixed carbonate-terrigenous rock was documented in between the two aforementioned sedimentary units. Differently, the Cenomanian massive carbonates were deposited in a moderate-to-high energy setting, not far from the platform margin. These rocks are primarily made up of primary breccia and rudist fragments. The well-layered carbonates were subjected to a thermal temperature of 100-130°C, as shown by the R1 and R3 ordering of liilte/smectite documented after XRPD analyses of carbonate powders. Such a temperature was associated to 4-5 km of burial depth associated to the structural stacking of the allochtonous units of the southern Apennines fold-and-thrust belt.

Results of quantitative field structural analysis were consistent with presence of five main sets of high-angle fractures. According to the results of linear scanline measurements, both diffuse and localized fracture networks crosscut the study carbonates. The former network include two orthogonal, high-angle fracture sets striking ca. ESE-WNW and SSW-NNE. Differently, the localized network is made up of ENE-WSW, ESE-WNW, and N-S striking high-angle fractures. According to the computed D values, the localized fracture sets were interpreted as characterized by a low degree of maturity. Results of circular scanline measurements showed similar trends of both P20 and P21 throughout the well-layered and oolithic carbonate successions. Such a similarity was interpreted as due to fault-related fracturing, which mainly localized across primary heterogeneities such as bed and bed-package interfaces. The vertical growth of incipient slip surfaces by linkage of pre-existing structural elements was affected by the mechanical control exerted by the aforementioned interfaces. Differently, P20 and P21 do not show very similar trends throughout the massive carbonates due to pronounced bed amalgamation.

Results of fracture stratigraphy analysis hence showed that the computed P20 and P21 did not vary proportional to bed thickness. These results contrasted with common spacing distributions documented for single fracture sets in layered rock masses and were interpreted in light of the structural complexity of the study carbonate outcrops exposing both diffuse and localized fractures. On the contrary, similar to P10 computed for the most common diffuse fracture sets, both P20 and P21 showed the highest values in correspondence of the coarse-grained carbonate beds. This data was explained by taking the burial-related physical-chemical compaction and/or cementation processes into account. They profoundly affected the mechanical properties of the carbonate multilayers, determining fracture pervasiveness within carbonate beds with the original larger pore space. Further analyses will be required to assess the specific diagenetic mechanisms associated to overburden, which likely played a major role in the fracture stratigraphy of the study Mesozoic carbonates.

CHAPTER 3 - DIAGENETIC HISTORY AND PRESSURE SOLUTION-ASSISTED COMPACTION OF THE MESOZOIC SHALLOW-WATER CARBONATES EXPOSED ALONG THE AXIAL ZONE OF THE SOUTHERN APENNINES FOLD-AND-THRUST BELT, ITALY

3.1 Introduction

Diagenetic processes such as physical and chemical compaction, cement precipitation, and mineral transformation that occur in carbonates at shallow-to-deep burial conditions affect their rock texture and composition (Zhou et al., 2022 and reference therein; Flugel, 2004; Wong and Oldershaw, 1981). Focussing on chemical compaction, according to the classification of pressure-solution features proposed by Choquette and Pray (1987) two main types can be distinguished: i) non-sutured, either as single or as swarms, which form in carbonates with a significant content of insoluble material such as clay, silt, and/or organic matter; ii) sutured, which correspond to stylolites and grain contact sutures that form in carbonates with a low content of insoluble residual material. Bedding parallel stylolites are widespread, cause lithological compaction and extend for great distances within the single units (Laronne Ben-Itzhak et al., 2012). These stylolites, as single and/or network elements, commonly are filled with insoluble materials, and are thought as responsible for porosity and permeability reduction in carbonate rocks. Actually, recent studies outlined the control exerted by stylolites in permeability anisotropy (Carozzi and Vonbergen, 2010; Korneva et al., 2014; Heap et al., 2014, 2018; Rustichelli et al., 2015; Koehn et al., 2016; Humphrey et al., 2019, Araujo et al., 2021).

The pressure solution processes related to chemical compaction are facies-dependent, so the nucleation and development of stylolites have a tight relation with the rock texture. This include the single elements (grain, matrix, cement, and pores) and also the presence of clays and organic matter (Flugel, 2004; Rustichelli et al., 2015; Beaudoin et al., 2016). The identification and characterization of the major depositional and diagenetic processes are therefore important steps to characterize the control exerted by pressure solution elements in the accumulation and migration of geofluids in carbonate rocks. Starting from the above consideration, the results of an integrated sedimentological, petrographic, and mineralogical study carried out in a Jurassic-Cretaceous platform carbonate succession cropping along the axial zone of the southern Apennines fold-and-thrust belt (Patacca and Scandone, 2007) are

reported in this work. The succession has been previously documented in terms of fracture stratigraphy (Manniello et al., 2022) and burial conditions at which the pressure solution processes had taken place (Manniello et al., 2023). According to the former authors, these structures operated a significant mechanical control on vertical fracture growth and propagation. Moreover, according to the latter authors, based on a morphological classification of the pressure solution surfaces(Koehn et al., 2016), and on the relative timing of the different structural elements retrieved from both outcrop and microstructural analyses, the authors recognised two distinct burial stages that resulted into two generations of bed parallel pressure solution surfaces that include sedimentary burial, wave type pressure solution seams, and tectonic burial, seismogram type stylolites.

Aiming at characterizing the diagenetic processes within the different carbonate lithofacies, we focus on the different generations of calcite cements to determine the control exerted by the carbonate texture, and the diagenetic environment at which they formed, and, subsequently, the controls on the formation of bedding parallel stylolites. The relationship between stylolites and tectonic elements (fractures and veins) can be useful to characterize the circulation pattern of the carbonate reservoir for the management of water resources. Focussing on the role exerted by the carbonate texture on formation of bedding parallel stylolites, we study two stratigraphic units respectively comprised of Lower Jurassic and Cretaceous limestone rocks. We first analyse their stratigraphic setting, texture, and mineralogical composition. Then, we investigate the relation between the different dissolution surfaces, classified as bed-parallel and low-angle stylolites, pressure solution seams, and slickolites. Specifically, pressure solution seams are charachterized by smooth morphology and are localized at the grain contancts and/or at single bed interfaces, stylolites are characterized by rougher morphology, displaying a toothed structure, with the teeth oriented perpendicularly to the main surface, slickolites, instead, are characterized by inclined teeth. We also investigate the relation among the different solution surfaces and both the diagenetic elements associated to cements precipitated during continuous burial of the carbonates, and the high-angle fractures and veins that pervasively crosscut the rocks. The information gathered in this work can be useful to characterize the circulation pattern of the carbonate reservoir for the management of water resources, as well as better decipher the role exerted by burial-related and tectonic-related pressure solution on the mechanical layering of carbonate rocks currently exposed along fold-and-thrust belts.

3.2 Geological setting

The southern Apennines fold-and-thrust belt (FTB) started forming since late Oligocene-early Miocene due to collision between Africa and the Eurasian plates, and the intervening Adria-Apulia plate (Vezzani et al., 2010). This deformation determined the progressive involvement of Mesozoic sedimentary units in a compressional tectonic regime, and formation of an east-verging FTB by mean of mixed thin-skinned and thick-skinned tectonics (Shiner et al., 2004). The latter units include the terrigenous and mixed siliciclastic-carbonate infills of the Sicilide-Liguride Basin and of the Lagonegro Basin, the Apenninic platform carbonates, the Apulian platform carbonate, and all the terrigenous syn-orogenic flysch deposited in the foreland and thrust-top basins (Piedilato and Prosser, 2005; Patacca and Scandone, 2007; Vezzani et al., 2010). Tectonic stacking of the aforementioned units caused the sandwiching of the Apenninic Platform in between the overlying Sicilide-Liguride and the underlying Lagonegro units. Altogether, this tectonic wedge overrode the Apulian Platform (Menardi Nouguera and Rea, 2000). Particularly, the basinal Liguride and Sicilide units overthrusted during early Miocene the Apennine Platform; subsequently, the two aforementioned units overthrusted during Tortonian the already duplexed basinal Lagonegro units (Patacca and Scandone 2007; Vezzani et al., 2010). The foredeep and thrust-top basins that formed along the evolving FTB during this time lapse marked the various tectonic stages that characterized the east-directed migration of contractional deformation (Wortel and Spankman, 1992; Patacca et al., 1992; Palladino et al., 2008).

Due to the aperture of the Tyrrhenian back arc basin, and the concomitant gravitational collapse of the collisional belt, starting from late Pliocene the tectonic wedge was subjected to extension (Mostardini & Merlini, 1986; Hippolyte et al. 1995; Cello and Mazzoli, 1998; Doglioni et al., 1996; Giano et al. 2000; Scrocca et al., 2005). At first, the belt was dissected by low-angle normal faults likely due to gravity-driven reactivation of pre-existing thrust faults; then, during Quaternary, the belt was dissected by high angle transtensional faults that caused exhumation of the allochtonous units from depth (Ghisetti and Vezzani, 1999; Agosta and Aydin, 2006; Vezzani et al., 2010; Bucci et al., 2012; Novellino er al., 2015; Ferraro et al., 2018, 2019).

The present study focuses on the carbonates pertaining to the Apenninic Platform, which developed during Mesozoic along the western region of the Tethys Ocean (Patacca and Scandone, 2007; Schettino and Turco, 2011). At a regional scale, three main stratigraphic units were documented within this carbonate succession: (1) Capri-Bulgheria unit, which

includes Triassic to Jurassic shallow-water, transitional carbonate facies, Cretaceous to Miocene marls, and resedimented carbonates deposited along the western margin of the paleo carbonate platform; (2) Alburno-Cervati unit, which includes Upper Triassic to Cretaceous shallow-water limestones, Miocene slope carbonates and Miocene terrigenous deposits, and represents the internal portion of the ancient carbonate platform; (3) Monti della Maddalena unit, which is constituted by transitional carbonate facies deposited along the eastern margin of the ancient carbonate platform.

3.2.1 The Viggiano Mt.

The Viggiano Mt. is located in the High Agri Valley of the Basilicata Region, Italy (Fig 1), which is a tectonic intra-montane basin infilled with Quaternary fluvio-lacustrine sediments. The High Agri Valley basin is bounded by high-angle, WNW-ESE and NW-SE striking transtensional faults forming the East Agr (EAFS) and the Monti della Maddalena (MMFS fault systems (Figure 3. .1a). The Viggiano Mt. is dissected by high-angle faults pertaining to the EAFS, and it is comprised of Apenninic platform carbonates that overrode the Lagonegro II Unit by mean of an east-verging, low-angle thrust fault (Fig 1b). The Viggiano Mt. succession, belonging to the Alburno Cervati unit, consistsof Lower Jurassic wackestones, packstones and grainstones originally deposited in a low-energy lagoonal environment. The latter carbonates include bivalve shells (*Lithiotis*), foraminifera (*Siphovalvulina* sp., *Pseudocyclammina liassica*), and green algae (*Palaeodasycladus mediterraneus*). The low energy carbonates are topped by oolitic grainstones, which were originally deposited in a carbonate ramp rimmed by sand shoals (Lechler et al., 2012; Manniello et al., 2022).

The Upper Jurassic carbonates consist of alternations of depositional breccias and lagoonal mudstones/wakestones. Through the not-brecciated portions green algae (*Thaumatoporella parvovesciculifera, Cayexuia piae*), calcified cyanobacteria (*Lithocondium aggregatum*), gastropods, bivalves, and various foraminifera species (*Miliolidae sp., Conicospirillina basiliensis, Pseudocyclammina lituus)* have been documented (Lechler at al., 2012). The youngest portion of the Viggiano Mt. consist of Cretaceous limestones made up of carbonate grainstones, rudstones, floatstone with rudists fragments, and sporadic mudstones. These rocks were originally deposited during Albian-Cenomanian in a high-energy shelf environment close to the platform margin (Lechler at al., 2012; Manniello et al., 2022). At

the Viggiano Mt., the present work focuses on the carbonated exposed at two sites respectively labelled as Scarrone la Macchia (SLM) and Il Monte (ILM) (Figure 3. 2).

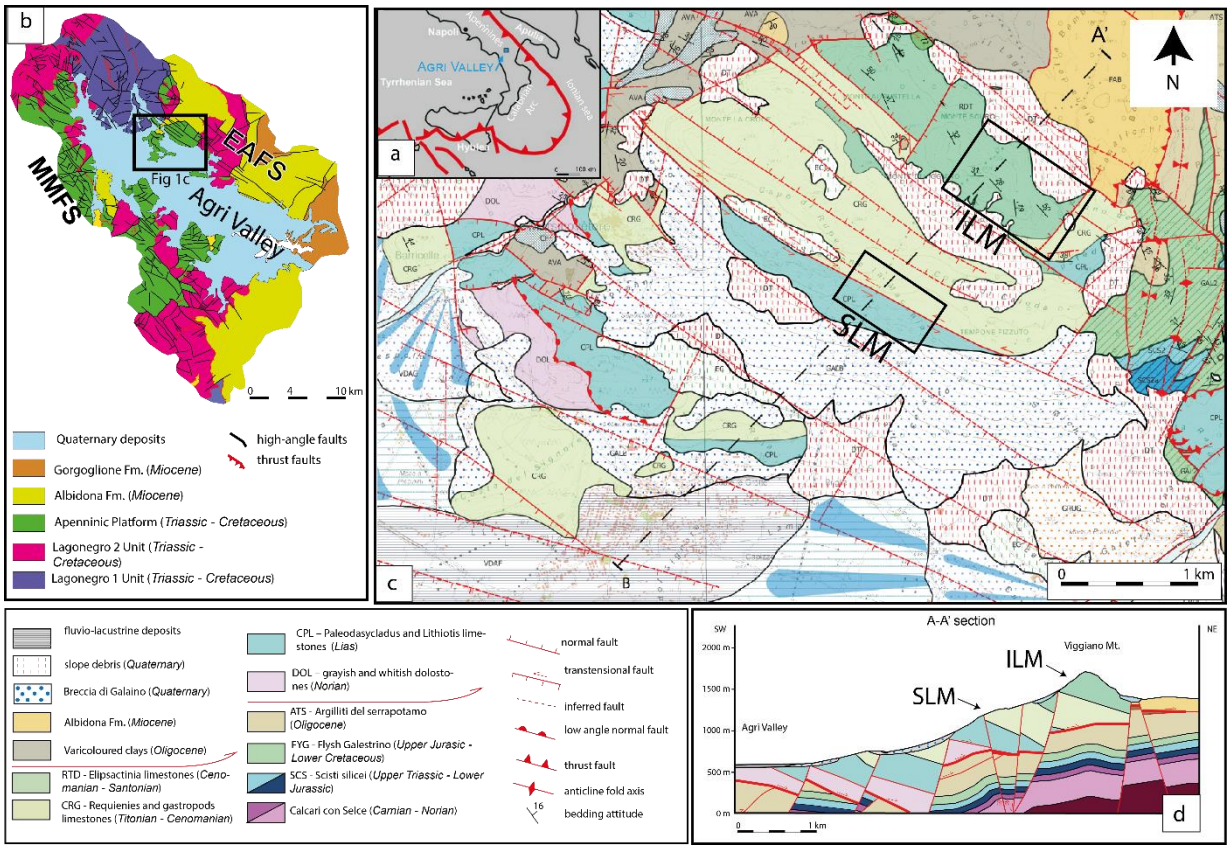

Figure 3. 1: Geological map of the study area. a) schematic map of the southern Apennines FTB, with the Agri Valley location. b) Structural map of the Agri Valley. c) Geological map of the Viggiano Mts. area (Palladino et al., personal communication), with the locations of the SLM (Scarrone la Macchia) and ILM (Il Monte) study sites. d) NE-SW trending geological cross-section of the Viggiano Mts. area.

"Scarrone la Macchia (SLM) site"

On the basis of their lithofacies (Manniello et al., 2022), the exposed carbonates were subdivided into two informal units (Figure 3. 2a). Starting from the base, a well-layered unit consists of shallow-water limestone with marl intercalations. The microfacies analyses showed that the well layered unit is characterized by an alternation of grain supported facies (grainstone-packstone) and mud supported facies (wackestone-mudstone) cyclically arranged. The association of benthic foraminifera (including *Haurania* sp., *Siphovalvulina* sp., *Lituosepta* sp.) and calcareous algae (*Palaeodasycladus mediterraneus* and *Thaumatoporella parvovesiculifera*) was consistent with an upper Sinemurian-Pliensbachian age, in accordance to the biozonal scheme proposed by Chiocchini et al. (1994) and Boudagher-Fadel (2008).

On top of the aforementioned carbonates, a grain-supported unit consisting of oolitic limestones was documented. The results of microfacies analyses showed presence of a

carbonate grainstone and packstone with ooids (500 to 1000 μm in size), oncoids (> 1 mm), and algal lumps. In some cases, the ooids showed an obliteration of the laminae due to intense micritization. Their nuclei are made up of skeletal grains, peloids, and in rare cases of mineral grains.

"Il Monte (ILM) site"

This site exposes massive carbonate rudstones and floatstones, which include fragments of rudist bivalves (Radiolitidae and Caprinae), common larger foraminifera (Orbitolinids), corals and fragments of microbial boundstone (as, e.g., intraclasts made of clotted peloidal micrite). Microbial encrustations were documented as common around skeletal and non-skeletal grains, and many grains are heavily micritized. According to the biozonal schemes proposed by Chiocchini and Mancinelli (1977) and Chiocchini et al. (1994), the benthic foraminifera and rudist associations indicated an Upper cretaceous age for these stratigraphic horizons. Recent studies argue for Albian-Cenomania age due to the association between Radiolitidae, *Concorbitolina conica*, *Salpingoporella turgida* and Caprinidae (Lechler et al., 2012).

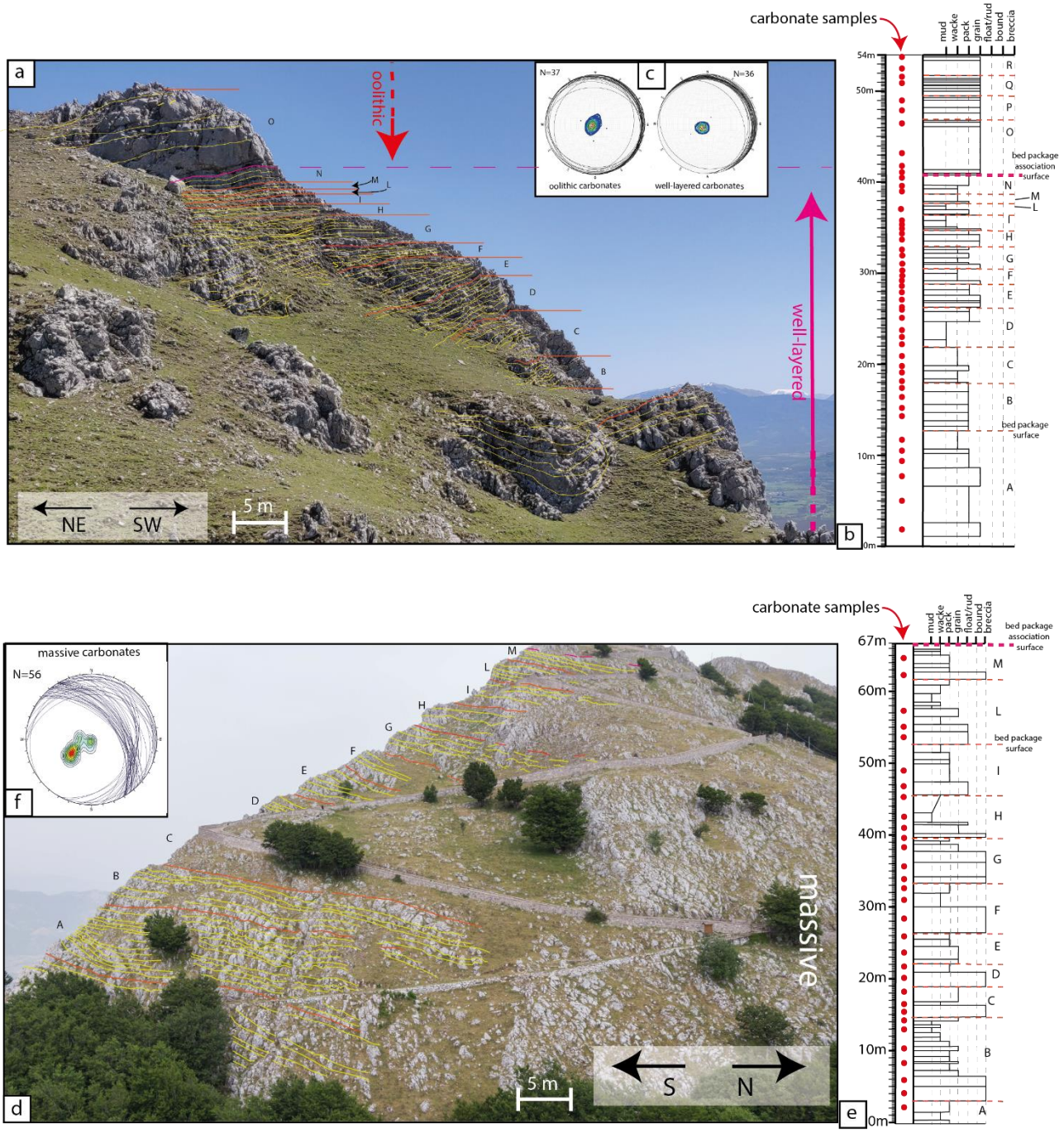

Figure 3. 2: Outcrop views of a) the SLM and f) ILM study sites. The three stratigraphic units are labelled as oolitic, well-layered and massive carbonates, respectively. b) and e) include the stratigraphic logs of SLM and ILM, respectively, with the location of analysed samples. c) and f) include the bedding attitude of SLM and ILM, respectively.

3.3 Methods

The petrographic characterization of the Viggiano limestone was carried out in order to obtain information on the carbonate microfacies, and on the bed-parallel pressure-solution surfaces. The laboratory work followed the field stratigraphic analysis of the carbonates exposed at the two sites, and detailed mesoscale structural analysis of the aforementioned

solution surfaces. The petrographic analysis was conducted by using an optical microscope (Leitz Laborlux 12 Pol) associated to the Zen software for the acquisition of photomicrographs. The textural classifications of microfacies followed Dunham (1962), and Embry and Klovan (1971). The classification of solution surfaces followed Flugel (2004), and Koehn et al. (2016). A cold-stage CL instrument (CITL CCL 8200 Mk3) present at the Department of Geosciences of University of Padua, Italy, was used to obtain data on the several generation of cements and the crosscutting relationship with the pressure-solution features. The CL beam was operated at 20 kV beam energy and 200-300 mA beam current. Images were obtained with a Nikon petrographic microscope.

3.4 Results

The analysis of the diagenetic features present in samples collected from the two sites is meant to assess the relations among textures facies dependent, cementation and pressure-solution processes. In particular, the results of petrographic observations associated with CL analysis allow the distinction of the multiple generations of cements. For the Scarrone la Macchia site, results of field stratigraphic and structural analyses are also reported for the well layered and oolitic unit that are studied in detail.

3.4.1 Scarrone la Macchia (SLM) site

Overall SLM carbonates, an early generation of isopachous rim around major cavities is documented. These rims consist of hundreds of micron thick cements, which are made up of elongated crystals of radiaxial fibrous type. These cements are dark under cathode lights and occur only in the carbonate packstones and wackestone of the well-layered unit (Figure 3. 3a, b). Another early generation of cements occurring only in the carbonate grainstones of both well-layered and oolitic units consist of ca. 50 micron-thick isopachous calcite rims, which localize around intraparticle pore space in between adjacent grains as meniscus cements (Figure 3. 3c, e, f). The latter cements are dark under cathode lights (Figure 3. 3d). A second generation of cements is characterized by blocky calcite, which is often densely twinned and appear either dark or very dull under cathode lights (Figure 3. 3a, b, c, d). These cements may also exhibit rhythmic luminescence. The carbonate cements infilled all primary porosity, and the WNW-ESE high-angle veins.

Focusing on the solution surfaces, the grain-supported facies of both well-layered and oolitic units are characterized by dissolution that localized at the grain contacts and are consequently classified as grain-contact seams (Figure 3. 4). The bedding-parallel stylolites show rough morphologies and are classified as seismogram-type to sharp-peak (Koehn et al., 2016; Zhou et al., 2022) (Figure 3.5 a, b). These stylolites dissolve both carbonate grains and calcite cements (Figure 3. 5a, b). The stylolites are filled with residual material, which consists of clay and/or oxides, and are non-luminescent under CL (Figure 3. 5 b). Occasionally, these features may include a partially preserved porosity (Figure 3. 5b). In the mud-supported carbonates of the well-layered unit, the solution surfaces consist of stylolites with irregular to rough morphologies, which are classified as rectangular to wave-like (Koehn et al., 2016; Zhou et al., 2022). These features either dissolve or abut against the high-angle WNW-ESE veins, and to contain films of brownish-reddish residual material (Figure 3. 5e, 5f).

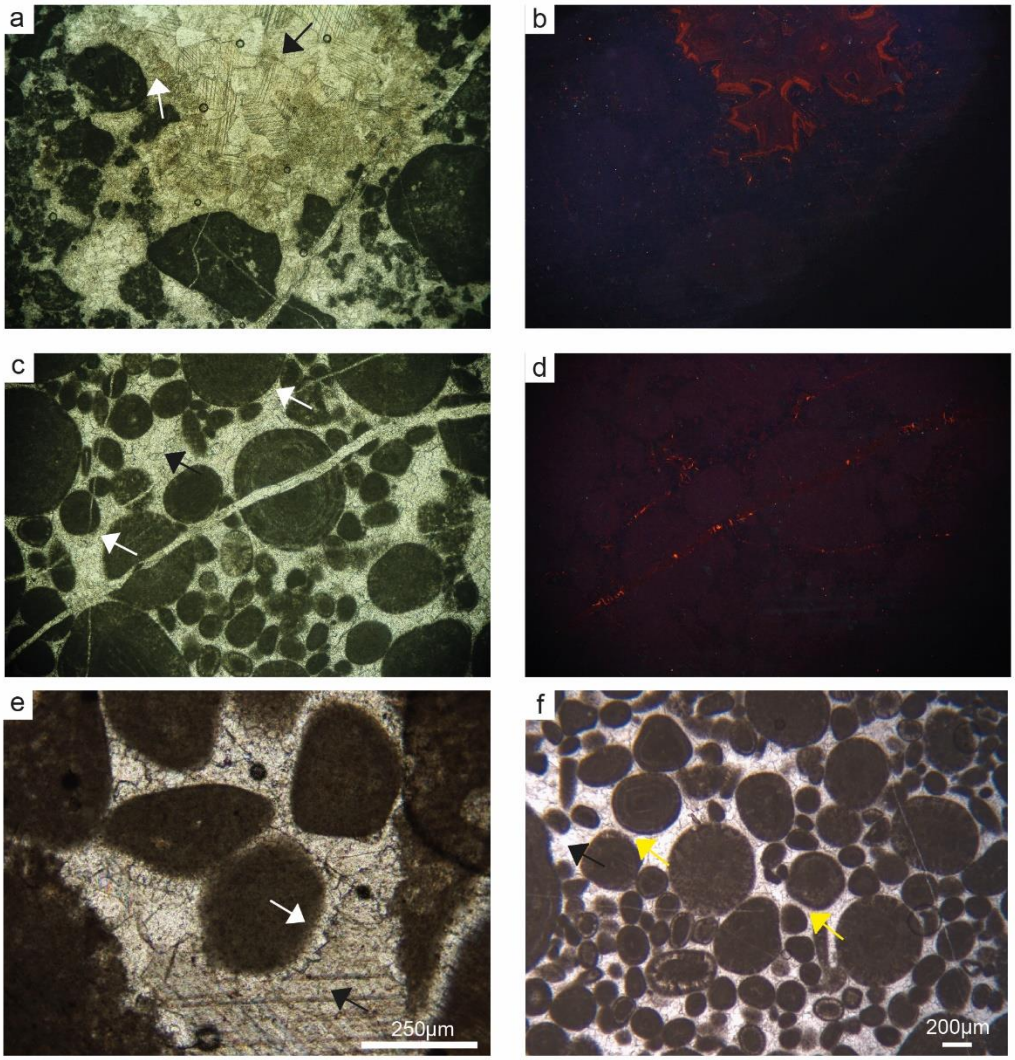

Figure 3. 3 a) polarized images of the well layered unit showing the radiaxial fibrous cements (white arrow) and blocky cements (black arrow) (magnification 4X). b) same image of a) under CL (magnification 4X). c) polarized images of the oolitic unit showing isopachous cements (white arrow) and blocky cements (black arrow) (magnification 10X). d) same image of c) under CL (magnification 10X). e) polarized images of a grain supported facies in the well layered unit showing isopachous cements (white arrow) and blocky cements (black arrow). f) polarized images the oolitic unit showing meniscus cements (yellow arrow) and blocky cements (black arrow).

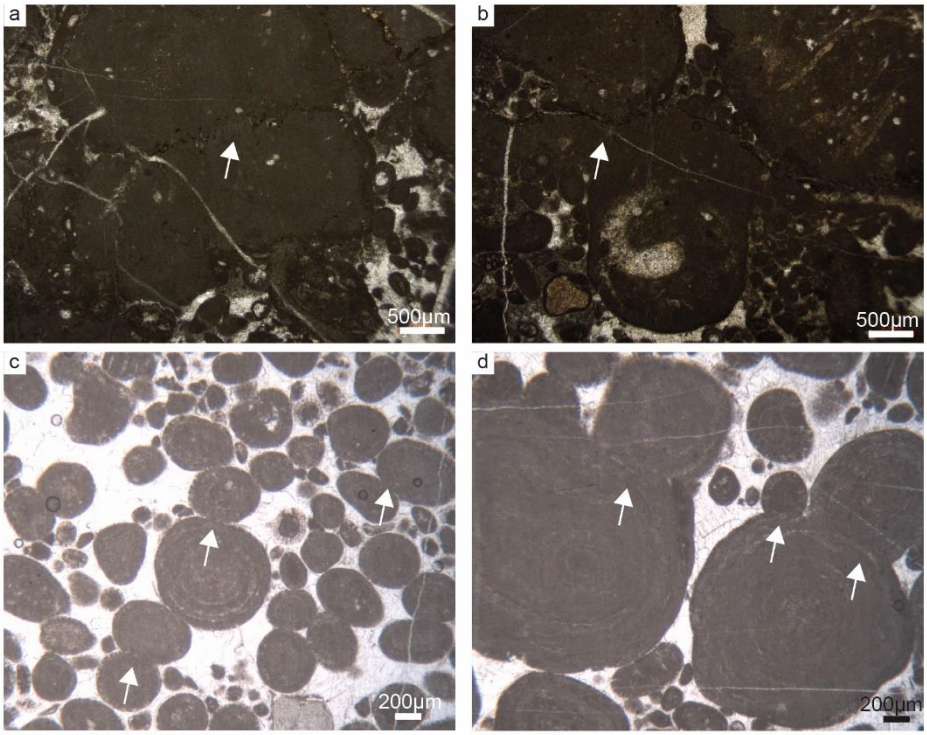

Figure 3. 4: Polarized images showing the grain-contact seams (white arrows) of the grain supported facies in the well layered unit (a, b) and in the oolithic unit (c, d)

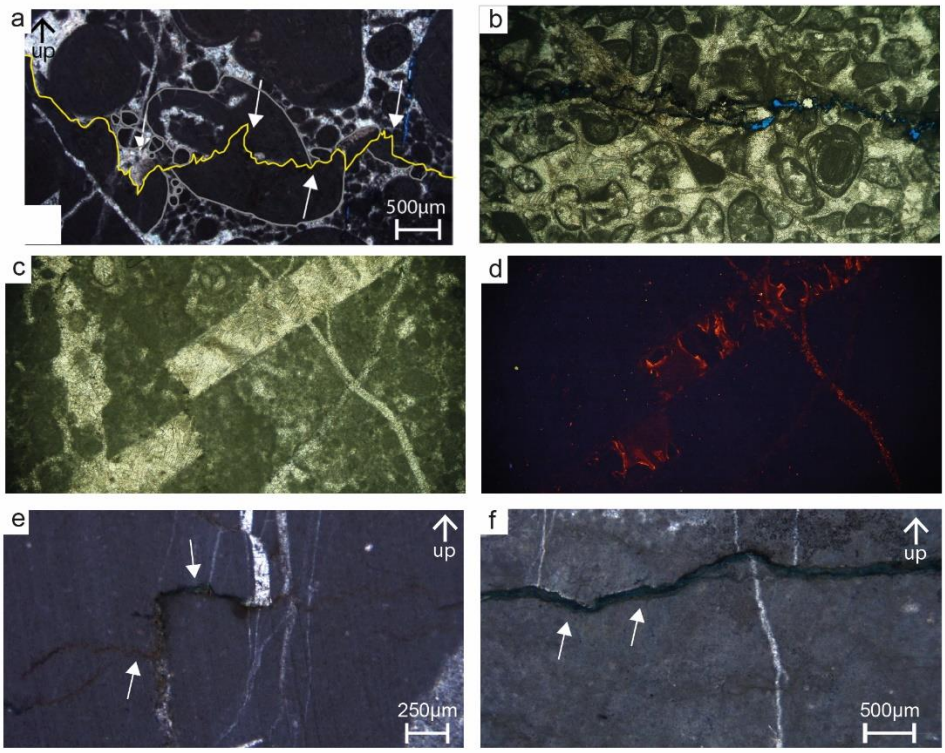

Figure 3. 5: Stylolites filled with residual material (clay or oxides) that under CL are non-luminescent (a, b). Sometimes they have a partially preserved porosity (c, d). e) bed perpendicular WNW-ESE veins dissolved by a seismogram-type stylolite (see white arrows), within mudstone in the well-layered unit. f) bed perpendicular WNW-ESE veins abutting against a wave-type stylolite (see white arrows), within mudstone in the well-layered unit

3.4.2 Il Monte (ILM) site

The diagenetic features consist of an early generation of radiaxial fibrous cements, which are dark under CL but also punctuated by luminescent spots probably due to defects of the crystals (Figure 3. 6a, b). In some cases, a very early generation of cements consist of dog-tooth cements, which are dull under CL (Figure 3. 6c, d). A deposition of fine-grained carbonate sediment within the primary cavities, often forming geopetal partial infills, postdated the aforementioned carbonate cements (Figure 3. 6c, d). The last generation of cements consist of blocky calcites, which infill veins and all primary pores. Under CL, the latter cements show a zonation due to alternations of layers with a dull to bright luminescence (Figure 3. 6e, f). The skeletal grains preserving their original calcite minerals, which mainly consist of bivalve fragments, and the calcitic component of rudists, are fully dark under CL (Figure 3. 6e, f). Differently, the micritic rims and microbial carbonates are instead dull luminescent under CL. The skeletal grains in which the shell-skeleton was substituted by a mosaic of blocky calcite crystals, likely aragonite in origin, are fairly common.

At the microscale, the pressure solution features only include stylolites; the grain-contact seams are not observed. The morphology of stylolites is rough, and for this reason it is classified as sharp peaky type to seismogram-type (Koehn et al., 2016). There, tiny, pinning teeth as high as few 10's μm are documented (Figure 3. 7a, b). Differently, stylolites with teeth as high as 100 - 200 μm are documented within the floatstone carbonate facies (Figure 3. 7c, d). Wave-like stylolites occurred only in those facies that contain micrite (Figure 3. 7 e). The stylolites dissolve the skeletal fragments and the carbonate grains (Figure 3. 7a), the calcite cements (Figure 3. 7b, c), and the WSW-ENE high-angle veins (Figure 3. 7d). The stylolites contain a residual reddish-brownish material, and/or are partially open (Figure 3. 7e, g). Occasionally, under CL the residual sediment appears bright luminescent (Figure 3. 7 f).

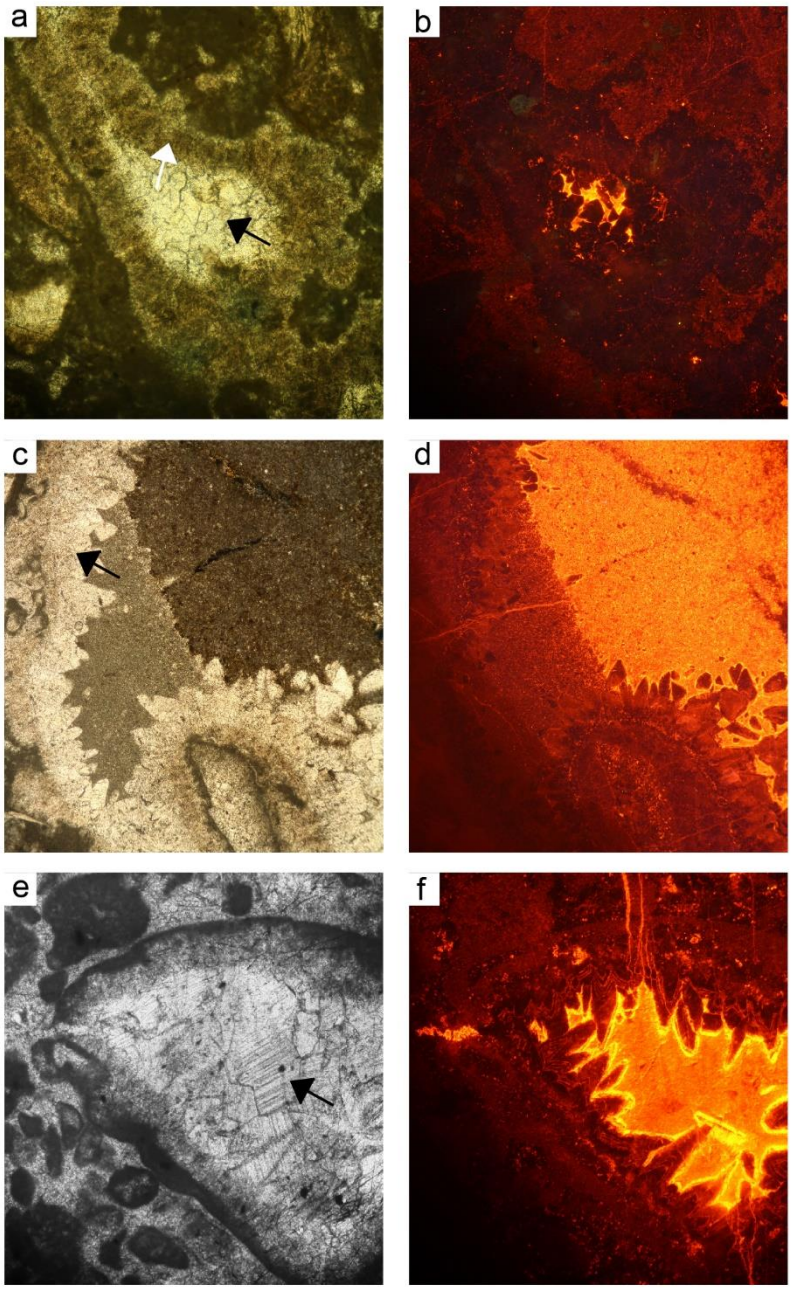

Figure 3. 6: a) polarized images showing the radiaxial fibrous cements (white arrow) and blocky cements (black arrow) (magnification 10X). b) same image of a) under CL. c) polarized images showing dog tooth cements (black arrow) and sediment infill (magnification 4X). d) same image of c) under CL. e) polarized images showing blocky cements (black arrow). f) same image of e) under CL.

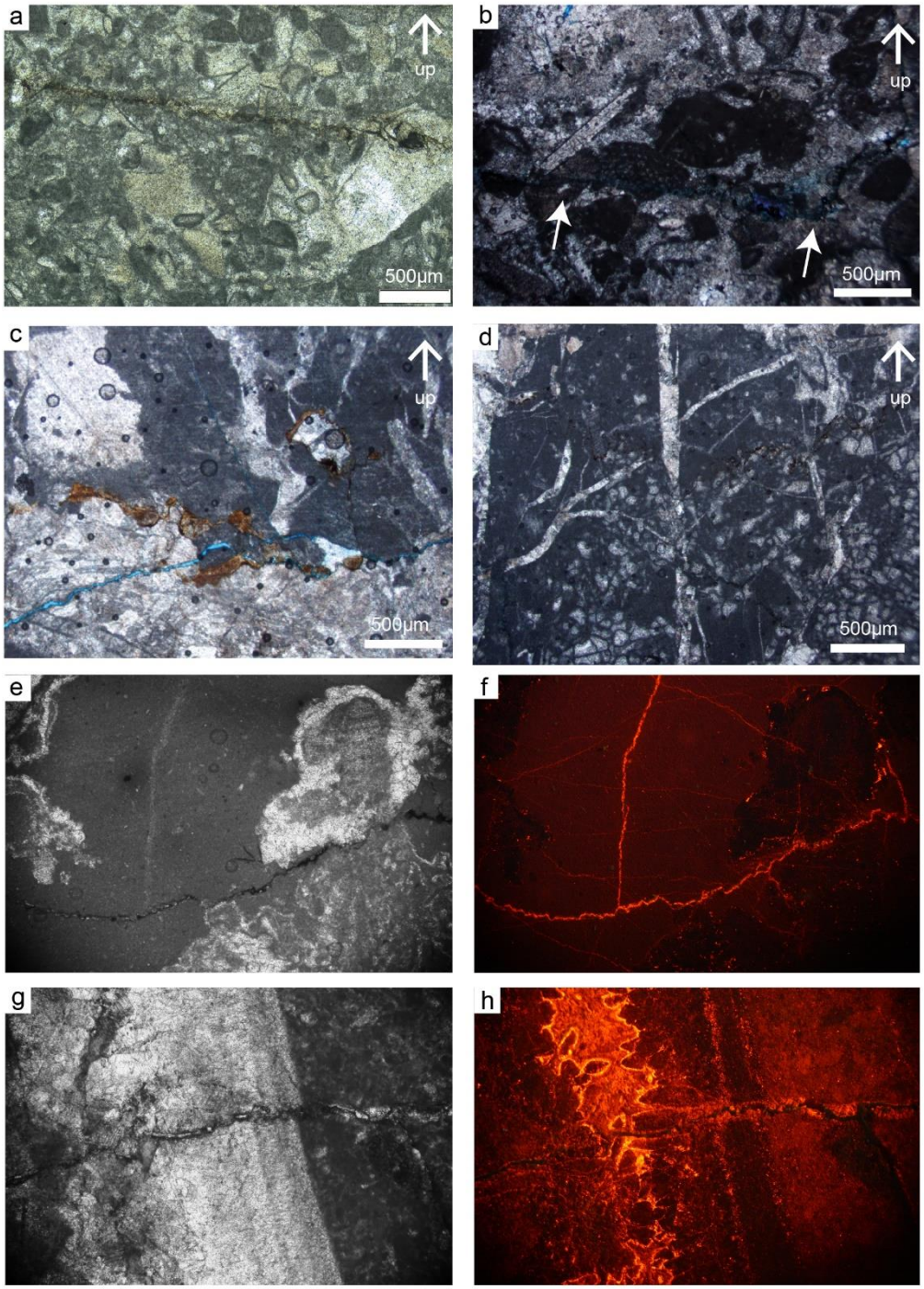

Figure 3. 7: Suture and sharp peak stylolites in floatstone facies containing residual sediment or are partially open. Under CL the residual sediment appears sometimes bright luminescent. (magnification 10X). c) and e) Intrabed stylolite characterized by low roughness that dissolve both carbonate grains/bioclasts and cements, localized within cemented carbonate grainstones; d) and f) Intrabed stylolite, characterized by high roughness and containing undissolved residual material, dissolving both re-crystalized bioclasts and veins (see with arrows in f) localized within muddy carbonate wakestones/packstones.

3.5 Preliminary discussion and conclusions

It is known that chemical compaction is a facies-dependent processes, so that the nucleation and growth of stylolites and pressure solution seams have a tight relation with the texture of carbonate rocks (Flugel, 2004). Starting from this consideration, based on the microfacies characterization of the study carbonates, we assess the main diagenetic processes and burial conditions that occurred during Meso-Cenozoic dissolution of the study rocks.

At the SLM site, the radial fibrous cements of mud-supported facies of the well-layered carbonates are interpreted as precipitated under marine phreatic conditions (Flugel, 2004), as also suggested by non-luminescence under CL documented for these carbonates. Similarly, the isopachous rims of cements documented in the grain-supported carbonates of both well-layered and oolithic units are interpreted as formed in a marine phreatic environment, whereas the meniscus cements documented in the latter carbonates are consistent with a vadose circulation of freshwater fluids. In all the study carbonate lithofacies, a later generation of cements consists of blocky calcite, which is often densely twinned and appears either dark or very dull under cathode lights with a typical rhythmic luminescence. They are interpreted as formed in shallow freshwater phreatic environments. The time-space evolution of the diagenetic environments of cement precipitation is hence the following:

- marine phreatic conditions (non-luminescent, radiaxial fibrous cement in mud-supported carbonates; isopachous rims in grain-supported carbonates);
- freshwater vadose conditions (meniscus cement in grain-supported carbonates)
- freshwater phreatic conditions (densely twinned, dark or very dull blocky cements with typical rhythmic luminescence in all study carbonate rocks)

Focusing on the pressure solution processes, they started during early diagenesis of the Pleinsbachian-Toarcian carbonates with the formation of grain-contact seams, which mainly took place in the grain-supported carbonates pertaining to either well-layered or oolithic units. We note that the early cementation of these grain-supported carbonates facies predated the formation of the bedding parallel stylolites as shown by the systematic dissolution of the latter cements. The morphology of stylolites in mud-supported carbonates changes from wavy to rectangular sharp-peak to seismogram-type, suggesting also that pressure solution processes were generally favoured in the mud-supported carbonate facies during the whole diagenetic history of the study rocks. This interpretation agrees with what it was observed in several limestone successions, which all documented that finer grain sizes favoured pressure

solution processes (Zhou et al., 2022; Beaudoin et al., 2018, Rustichelli et al., 2015; Bruce Railsback and Andrews, 1995). The time-space evolution of pressure solution processes is hence the following:

- Localization of wavy-type pressure solutions seams at grain contacts during Mesozoic times especially within grain supported lithofacies.
- Propagation of those seams forming laterally continuous bed-parallel stylolites after the diffuse formation of blocky calcite cements (those stylolites dissolve the calcite cements, maximum sedimentary burial of ca. 1.6 km of depth, Manniello et al., 2022).
- Formation of sharp-peak seismogram type stylolytes in a subsequent diagenetic stage, occurred due to tectonic burial, involving mainly mud-supported lithofacies (these stylolites systematically dissolve high angle veins formed during the Miocene thrusting tectonics, maximum tectonic burial estimated ca. 4 km, Manniello et al., 2022).

At the ILM site, the diffuse micritization of clasts is interpreted as due to the long-lasting residence time of carbonate sediment at the water-sediment interface (Flugel, 2004). According to the petrographic data and CL observations, the two first generations of cements consisting of radiaxial fibrous and toothed calcite precipitated in a shallow marine diagenetic environment. The time-space evolution of the diagenetic environments of cement precipitation is hence the following:

- meteoric vadose environment with occasional subaerial exposure of the carbonatic sediments (non-luminescent isopachous calcite rims, and deposition of fine carbonate sediments within primary cavities, dull under CL);
- freshwater vadose environment (non-luminescent radiaxial fibrous cement);
- freshwater phreatic conditions (rhythmic dull to bright luminescent blocky cement)

Microstructural analyses show that fractures crosscut the cemented portions, suggesting that they broke the early cemented sediment during early burial, while some primary intergranular pores were still open. Blocky cements fill both the residual primary pores and the moldic pores. We interpret this evidence to be related to an early-intermediate burial, before the inception of pressure solution processes. The development of the laterally continuous bed-parallel stylolites and pressure solution seams occurred when the rock was almost completely cemented, since their cut the blocky cements. The stylolites appear roughly (seismogram-type) while in floatstone have a smooth morphology. The time-space evolution of the pressure solution processes is hence the following:

- during burial diagenesis, the pressure solution processes were not predominant (absence of grain contact pressure solution seams);
- formation of rough, seismogram-type stylolites during tectonic burial associated with Miocene thrusting tectonics; the latter stylolites systematically dissolve the high-angle veins that formed prior to during thrusting tectonics, and the bed-parallel veins associated to thrusting tectonics.

All the calcite cements documented for the study carbonates may be therefore ascribed to diagenetic environments associated to marine phreatic and early-to-intermediate sedimentary burial, which predated the Miocene-Pliocene thrusting tectonics, and the Quaternary exhumation of the southern Apennines FTB. We ascribe to these stages also the formation of the wavy-type pressure solution seams and stylolites documented within the Lower Jurassic carbonates. These data are in accordance with the recent data reported by Manniello et al. (2023), which were interpreted with a sedimentary burial of ca. 1.4 - 1.6 km. Differently, the formation of the more recent, rough seismogram type styololites, is ascribed to a different burial phase, due to the tectonic load occurred during Miocene-Pliocene thrusting tectonics (ca. 4 km), and could result from either reactivation of pre-existing wavy surfaces or as newly formed surfaces.

We also note that formation of some of the stylolites was likely linked to presence residual undissolved material disperse within the original carbonate sediments and took place under low burial condition during the very early in the diagenetic history of the carbonates (Gruzman, 1997). Moreover, according to Beaudoin et al. (2018) nucleation of the bedding parallel stylolites can be useful to estimate the burial depth. In this regard, Zhou et al. (2022) proposed that a quantification of the burial depth can be achieved on the basis of the on the maximum amplitude of the stylolites teeth dissolving carbonate grain-supported rocks. The calculation was derived from the assumption that the tooth length of a stylolite represents the minimum reduction thickness of strata (Park and Schot, 1968). We note that the grain-supported carbonates of the SLM site show height of bedding parallel stylolite teeth ranging from 0.3 to 0.8 mm (Manniello et al. 2023).

CHAPTER 4 - PRESSURE SOLUTION-ASSISTED DIAGENESIS AND THRUSTING-RELATED DEFORMATION OF MESOZOIC PLATFORM CARBONATES

4.1 Introduction

In shallow-water settings, carbonate sediments are commonly subjected to significant textural and architectural modifications due to diagenetic processes involving physical compaction, chemical compaction, and cement precipitation that modify their mechanical properties soon after deposition (Lucia, 2007; Lamarche et al., 2012; Lavenu et al., 2015; La Bruna et al., 2020). These modifications, hence, might also affect the failure modes of the lithifying carbonates. In platform carbonates, these failure modes encompass opening-mode fractures such as joints and veins (Pollard and Aydin, 1990; Rispoli, 1981, Agosta et al., 2006), disjunctive cleavage such as stylolites and pressure solution seams (Alvarez, 1976; Rispoli, 1981; Rustichelli et al., 2012, 2015), and shearing-mode fractures such as hybrid fractures and veins, shear fractures and small-scale faults (Rispoli, 1981; Willemse et al., 1997; Graham et al., 2003; Agosta et al., 2006; Marchegiani et al., 2006; Lavenu et al., 2014). As a result, the interplay among the different failure modes localized within the various lithofacies determines the fracture stratigraphy properties of shallow-water carbonates (Peacock et al., 1995; Cooke and Underwood, 2001; Agosta et al., 2009; Lamarche et al., 2012; Panza et al., 2016; La Bruna et al, 2020; Al-Fahmi et al., 2020). Altogether, diagenetic processes and deformation mechanisms take place during very long time lapses, at different pace, and might affect the degree of fracture connectivity, the values of secondary porosity, and the modalities of fluid flow and mineralization through time (Nelson, 2001; Agosta and Kirschner, 2003; Ehrenberg and Nadeau, 2005; Agosta et al., 2007, 2010; Bense et al., 2013;Ferraro et al., 2019; Giuffrida et al., 2020; Smeraglia et al., 2021; Araujo et al., 2021; Pontes et al., 2023).

Platform carbonates can include well-layered successions of alternating mud- and grain-supported lithofacies, and primary interfaces such as laminations, bedding interfaces, and larger-scale heterogeneities that are often loci of pressure solution (Flugel, 2004; Tucker and Wright, 2009). Pressure solution profoundly impacts the mechanical layering of platform carbonates (Lavenu et al., 2018; Panza et al., 2019; Giuffrida et al., 2019; Humphrey et al., 2019), with the dissolution rates being function of the rock textures (Koehn et al., 2007).

Specifically, platform carbonates are characterized by depositional and diagenetic architectures including single beds and bed packages separated by mechanical interfaces that exert a major control on the modalities of fracture growth (Berry et al., 1996; Laubach et al., 2010). In this work, we analyze the Mesozoic platform carbonates cropping out at the Viggiano Mt. of southern Italy, in an area lying within the axial zone of the southern Apennines fold-and-thrust belt (ftb). These carbonates were subjected to Oligo-Miocene thrusting tectonics, and to a subsequent Plio-Quaternary downfaulting and exhumation from depth (Patacca and Scandone, 2007). A previous work showed that the fracture network crosscutting the Mesozoic platform carbonates formed during the latest tectonic stage, with development of new fracture sets, and reactivation of the pre-existing high-angle fractures (Manniello et al., 2022). In their work, the latter authors interpreted the variations of fracture density and intensity as dependent upon both carbonate lithofacies and primary interfaces, which affected the modalities of vertical fracture growth. In order to gain new insights into the structural architecture that characterized the Mesozoic platform carbonates prior to the Plio-Quaternary downfaulting, we now focus on the deformation mechanisms that occurred during early to burial diagenesis, and subsequent thrusting tectonics. Results of this work are discussed to decipher the time-dependent, pressure solution-assisted deformation of the platform carbonates, and synthesized in a six-stage synoptic scheme. The applications of this knowledge will be beneficial for a more precise assessment of geofluid production/storage from/in fractured platform carbonates pertaining to fold-and-thrust belts.

4.2 Geological Setting

The southern Apennines fold-and-thrust belt resulted from the compressional tectonics that involved the passive margin of the Adria-Apulian plate since late Oligocene - early Miocene times (Patacca and Scandone, 2007). This belt formed due to the progressive stacking of several thrust sheets (Figure 4. 1a, b), which included deep-water tectono-stratigraphic units such as the Liguride, Sicilide, and Lagonegro units, and shallow-water tectono-stratigraphic units such as the Campania-Lucania carbonates investigated in this work (Piedilato and Prosser, 2005; Vezzani et al., 2010). The whole allochthon units overrode the Apulian platform carbonates by means of thin-skinned tectonics (Shiner et al., 2004; Scrocca et al.,2005). Particularly, the studied Mesozoic platform carbonates were firstly overthrusted during early Miocene by the deep-water Liguride and Sicilide units, and then tectonically overrode the already duplexed Lagonegro units during Tortonian. Thrusting was

accompanied by formation of several thrust top and foredeep basins, which punctuated the eastward propagation of contractional deformation (Wortel and Spakman, 1992; Patacca and Scandone, 2007). The transition from thin- to thick-skinned tectonics, and hence the involvement of the Apulian Platform in contractional deformation, started during early Pliocene due to tectonic inversion of Permian-Triassic extensional structures (Menardi Noguera and Rea, 2000; Shiner et al.,2004), and lasted up to late Pliocene when low-to-high angle transtensional faulting dissected the orogenic wedge (Vezzani et al., 2010). Plio-Quaternary transtension was interpreted as a consequence of the gravitational collapse of the orogen, and/or of the aperture of the Tyrrhenian Basin (Cello and Mazzoli, 1998; Doglioni et al., 1996; Vezzani et al., 2010; Bucci et al.,2012; Novellino et al., 2015).

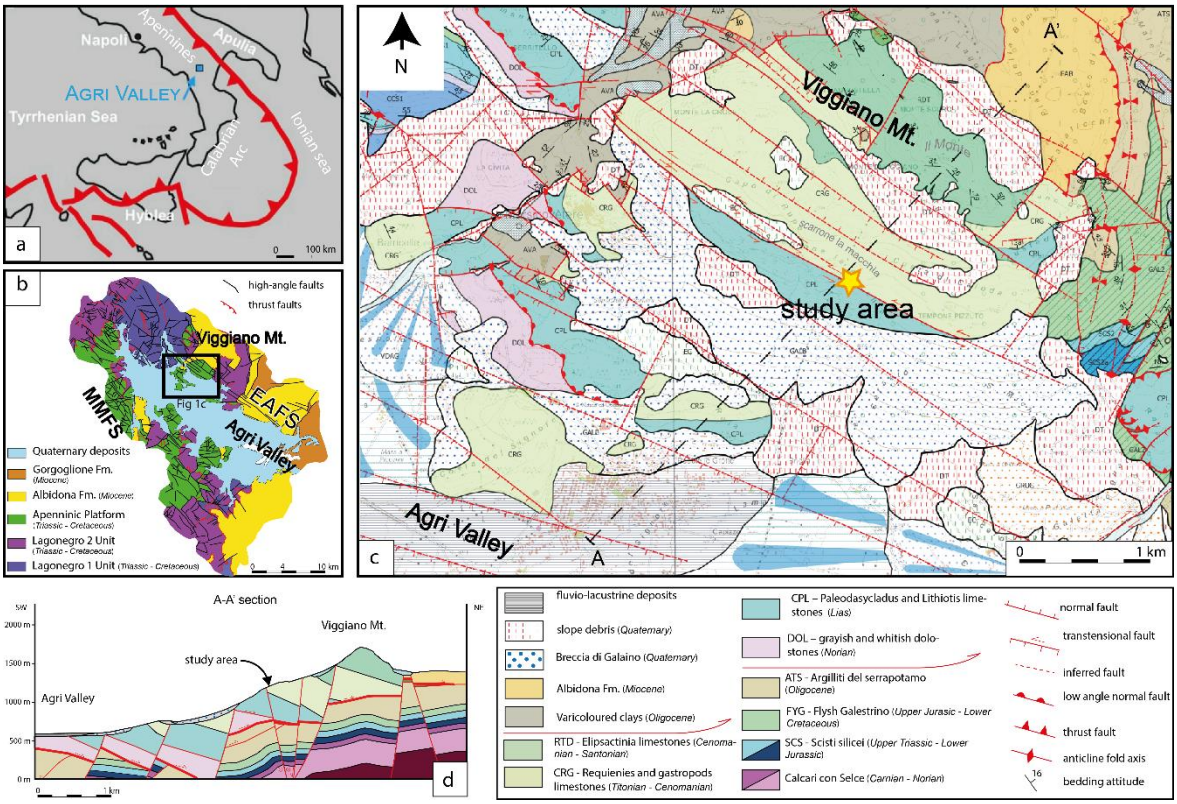

Figure 4. 1 Geological map of the study area. a) Sketch map of the southern Apennines ftb, and location of the Agri Valley. b) Schematic geological map of the High Agri Valley. c) Geological map of the Viggiano Mt. area (Palladino et al., personal communication). d) NE-SW trending geological cross-section of the Viggiano Mt. area.

4.2.1 Viggiano Mt.

The Viggiano Mt. is located along the NE margin of the High Agri Valley, which is a WNW-ESE elongated, intramountane tectonic basin infilled with Plio-Quaternary fluvio-lacustrine deposits (Figure 4. 1). The High Agri Valley sedimentary basin is bounded by two main high

angle, transtensional fault systems, which are respectively labelled as East Agri Fault System (EAFS) and Monti della Maddalena Fault System (MMFS), as reported in Figure 4. 1b. The study area of the Viggiano Mt. is crosscut by faults pertaining to EAFS, which includes ca. N120E, N150E, N30E, and N60E striking high-angle faults (Figure 4. 1d). Altogether, these faults form the Plio-Quaternary transtensional fault network (Cello and Mazzoli, 1998). Late-orogenic strike-slip kinematics occurred along the EAFS faults, which dissected and, in part, re-sheared the pre-existing NNW-SSE-striking thrusts (Monaco et al., 1998; Cello et al., 2000). The late orogenic strike-slip faulting was followed by post-orogenic, dip-slip extensional tectonics that mainly involved the formation of NW-SE high-angle faults (Giano et al., 2000; Maschio et al., 2005; Barchi et al., 2007; Zembo et al., 2009 and 2011; Brozzetti, 2011). The work of Palladino and co-authors (personal communication), who mapped the whole study area of the High Agri Valley at a 1:10.000 scale, showed that the Viggiano Mt. is part of the hanging wall block of a Miocene regional-scale thrust with a top to NE-ENE transport direction (Figure 4. 1c, d).

The present work focuses on the Scarrone la macchia outcrop (40° 22.4840 N, 15° 50.3830 E), which is located along the southern cliff of the Viggiano Mt. (Figure 4. 2). The outcropping carbonate succession is constituted by two informal stratigraphic units, which are respectively labeled as oolithic carbonates and well-layered carbonates (Manniello et al., 2022). The oolithic carbonates, Toarcian in age, are made up of bed packages containing amalgamated beds of oolithic grainstone carbonates. Those carbonates are grain-supported, well-sorted, cemented, and include bed package interfaces made up of mm-thick terrigenous laminae. This unit was originally deposited in a ramp rimmed by sand shoals (Lechler, 2012; Manniello et al, 2022). The well-layered carbonates, Sinemurian - Pleisbachian in age, include grain-to- mud-supported beds separated by laterally continuous bed interfaces. The carbonate grainstones and packstones contain biogenic clasts, pisoids, and oncoids embedded in a carbonate muddy matrix and in carbonatic cements. The carbonate mudstones and wackestones contain sparse fragmented biogenic clasts embedded in a carbonate muddy matrix. The carbonate beds are organized in single bed packages separated by cm-thick interfaces containing clayish materials (Figure 4. 2). The well-layered carbonates were originally deposited in a low energy, open lagoonal depositional setting, protected by sand shoals (Manniello et al., 2022).

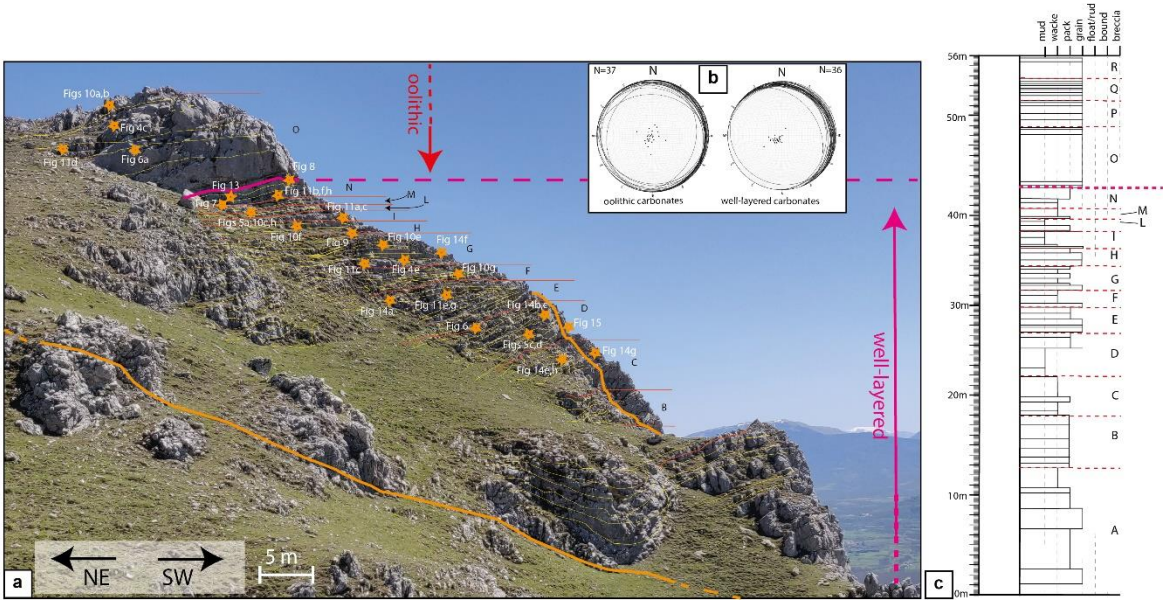

Figure 4. 2 Stratigraphy of Scarrone la macchia platform carbonates. a) Outcrop view of the study succession. The two exposed bed packages associations are labelled as oolithic and well-layered carbonates, respectively. The single bed packages are labelled with capital letters (B-O). The localities of analyzed outcrops are also labelled with the corresponding figure numbers b) Bedding attitude of the main stratigraphic units. c) Detailed stratigraphic log of the studied succession. The carbonate lithofacies are classified according to Dunham (1971). Results are reported at the top of the stratigraphic log as follows: mud=mudstone, wacke=wackestone, pack=packstone; grain=grainstone; float/rud=floatstone/rudstone, bound=boundstone, breccia= carbonate breccia.

4.3 Methods

We deciphered the geometry of the fracture network, the nature of single structural elements, and the abutting/crosscutting relations among the fracture sets, by means of a multidisciplinary investigation including 3D digital outcrop modeling, and mesoscale and microscale structural analyses. The 3D modeling followed a drone-based photogrammetric acquisition performed with a DJI® Mavic pro 2 zoom drone equipped with the stock camera, which ensured an image overlap of ca. 90%. The digital model was built using a surface-from-motion analysis included in the Agisoft Metashape® software, which allowed the merging of the entire dataset of images, and subsequently the building of a geo-referenced point cloud with a minimum investigation resolution of 50 cm. The point cloud was subsequently imported in Cloud Compare®, an open-source software that allowed the manual picking of the structural heterogeneities. There, the minimum considered length of the depicted structural elements was ca. 150 cm.

The qualitative, field-based mesoscale structural analysis was performed at specific outcrops aiming at documenting the nature (failure mode), dimension, attitude (right-hand rule), and both crosscutting and abutting relations of single structural elements. To achieve these goals,

we produced detailed structural maps of single outcrops by using high resolution outcrop images as base maps, and manually drawing of fracture traces in the field. The outcrops were selected based upon the quality of the exposure, and lack of vegetation. The oolithic-well-layered unit interface was investigated in detail by producing multiple outcrop-scale structural maps. All study outcrops were selected away from the large outcropping faults.

In the laboratory, the line drawing of the outcrops was digitalized by means of the Adobe Illustrator® software. Within selected bed packages (A, B, G, H, I, L, M and N, cf. Figure 4. 2), in correspondence of outcrops not totally obliterated by fault-related fracturing, we conducted bed-orthogonal linear scanline measurements aiming at measuring the spacing variations and trace length of bed-parallel, intra-bed solution surfaces. The measured spacing values were employed to calculate the P10 values (linear intensity) by means of the following equation:

$$P10 = n/L$$

where n represented the number of structural elements measured over 30 cm, which corresponded to unit length, L. The calculated P10 values were then plotted vs. the trace length of the pressure solution seams and reported in the stratigraphic column of the studied carbonate succession together with both thickness and lithology of single beds.

The collected rock specimens were oriented in the field by reporting both stratigraphic up and strike direction. In the sawing laboratory, 21 rock specimens were cut perpendicular to bedding to produce polished slabs, which were then used for thin section preparation. Both stratigraphic up and strike direction were reported on each thin section. Microstructural analysis was performed by using a Nikon Eclipse E600 optical microscope equipped with a digital camera. Thin section observation was carried out under cross-polarized light. Microphotographs were taken at different magnifications, as reported in the accompanying figures.

4.4 Results

4.4.1 Digital structural analysis

After photogrammetric acquisition, a 60mx45mx15m digital model of the Scarrone la macchia outcrop was built. There, a total of 123 structural heterogeneities, with traces longer than 150 cm, were recognized (Figure 4. 3). These heterogeneities consist of high-angle

fractures with negligible amounts of throw, and small faults with throws up to a few tens of cm. In the digital model, a large-scale, NE-SW striking, sub-vertical fault is depicted; this fault displaces the contact between the oolithic and well-layered carbonate unit showing ca. 3.5 m of predominantly horizontal (right lateral) offset (Figure 4. 3a, d). Unfortunately, no kinematic markers such as abrasive striae, slickenfibers, and small-scale grooves are visible in the field along the slip surfaces. Altogether, fractures and small faults form two main high-angle sets respectively striking NE-SW and WNW-ESE (Figure 4. 3b). We note that a similar geometry is displayed by the large-scale faults reported in the 1:10.000 scale geological map of the study area (cf. Figure 4. 1c). Minor fractures and small faults sets respectively striking NW-SE, N-S, and ENE-WSW are also documented (Figure 4. 3b, c). Most of them show mutual crosscutting relations, likely due to Quaternary carbonate exhumation from depth, and concomitant re-shearing of the pre-existing heterogeneities as documented for the platform carbonate exposed in the nearby area of Monte Alpi (La Bruna et al., 2018). Nevertheless, we take advantage of the results of digital outcrop analysis to define the dimensions of the fault-bounded carbonate blocks in which detailed field and microscale structural analyses are carried out (Figure 4. 3c, d).

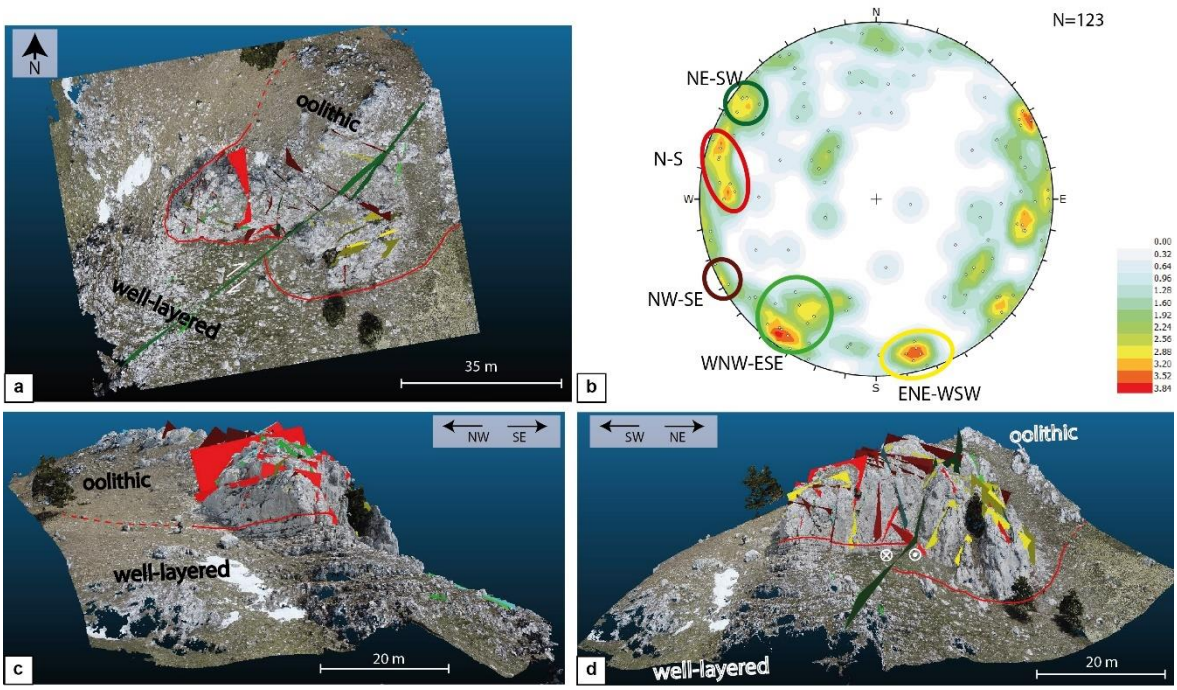

Figure 4. 3 Different perspectives captured from the 3D digital outcrop model of the topmost portion of the Scarrone la macchia carbonates. a) Top view of the digital outcrop. b) Lower hemisphere, equal area projection of the poles of the fault planes. Contour intervals are 0.32% per 1% area as shown in the legends. The main fault planes are reported. c) and d) Section views of the digital outcrop.

4.4.2 Field and microscale structural analyses

Field structural data regard small-scale thrust faults, solution surfaces, and bed-parallel veins. Solution surfaces are described according to the cut-off angles with the bedding interfaces. We report their morphologies according to the classification originally proposed by Park and Shot (1968), and subsequently revised by Koehn et al. (2016). Results of microscale structural analysis are related to thin sections obtained from rock specimens collected from the bed package interfaces bounding the top portion of the G, H, and I bed packages (cf. Figure 4. 2) respectively, and from single carbonate beds pertaining to either the well-layered or oolithic carbonate units.

"Thrust faults"

The carbonate succession is dissected by small-scale thrust faults ca. ENE-WSW striking and SSE dipping (Figure 4. 4). These faults show a ca. NNW-directed transport direction. Minor NNW-dipping thrust faults are also observed. The thrust faults show up to several cm of throw and caused formation of open antiformal folds at their hanging wall blocks (Figure 4. 4). At a close view, the thrust faults display flat-ramp-flat geometries. The ramps localize along low angle-to-bedding slip planes crosscutting either single or multiple carbonate beds (Figure 4. 5 and 6). The flats, instead, localize along the bed-parallel interfaces bounding single bed packages (Figure 4. 7 and 8).

In detail, focusing on the SSE dipping ramps, they commonly form cut-off angle comprised between 25° and 35° with the bedding interfaces (Figure 4. 5). The ramps consist of oblique-to-bedding slip planes crosscutting either mud- or grain-supported carbonates. In the former carbonates, the oblique slip planes solve throws up to a few cm (Figure 4. 5a, b). There, the smooth, laterally continuous oblique slip planes are encompassed by very thin and discontinuous fractured rock volumes (Figure 4. 5a, b). By contrast, in the grain-supported carbonates the oblique slip planes show throws up to ca. 15 cm (Figure 4. 5c), and include closely spaced, multiple shear fractures oriented almost parallel to each other. At a close view, the single shear fractures bound mm-thick volumes of poorly cohesive, laminated, clayish carbonates (Figure 4. 5c). These laminated carbonates are sandwiched by tens of cm-thick fractured rock volumes, in which both bed-parallel and bed-oblique structural heterogeneities are present (Figure 4. 6a, b). The bed-oblique structural elements contain 5 to 10 cm-long slickolites with sub-horizontal teeth. The teeth of those solution surfaces are

oriented ca. parallel to the ramps and abut against the bed-parallel pressure solution seams and veins.

The flat geometry ©s provided by bed-parallel slip of the bed package interfaces, which include laterally continuous, up to ca. 15 cm-thick carbonate volumes containing dm-scale, elongated, lenticular-shaped carbonate lithons (Figure 4. 6d, 7). The lithons form very low cut off angles with the bedding interfaces (up to ca. 10°), are in close contact with each other, and include oblique-to-bedding solution surfaces. These oblique solution surfaces are described in detail in the classification of solution surfaces proposed further on, and are labelled as PS3b (cf. Ch. 4.2.2.). Around the lithons, mm-thick films of clayish material and karst-related voids are documented (Choquette and James, 1988). The oolithic-well-layered interface also includes cm-scale, sigmoidal-shaped carbonate lithons. The latter lithons are enclosed by bed-parallel slip surfaces including N310E trending striae, and by SSE-dipping solution surfaces forming 30-35° cut-off angles with the bedding interfaces. The latter surfaces include mm-thick films of clayish material. Both bed-parallel and bed-oblique planes are crosscut by low-angle, NNW-dipping shear surfaces forming cutoff angles <18° with the bedding interfaces. Altogether, the aforementioned elements form S-C and S-S-C' structural fabrics (Figure 4. 8). The C-planes are those parallel to bedding, the S-planes include the SSE-dipping solution surfaces, and the C'-planes include the NNW-dipping shear discontinuities. Based upon kinematic markers such as abrasive striae documented along the C-planes, and considering the overall geometry of the S-C and S-C-C' fabrics, a NNW-directed transport direction is assessed for the outcropping thrust faults.

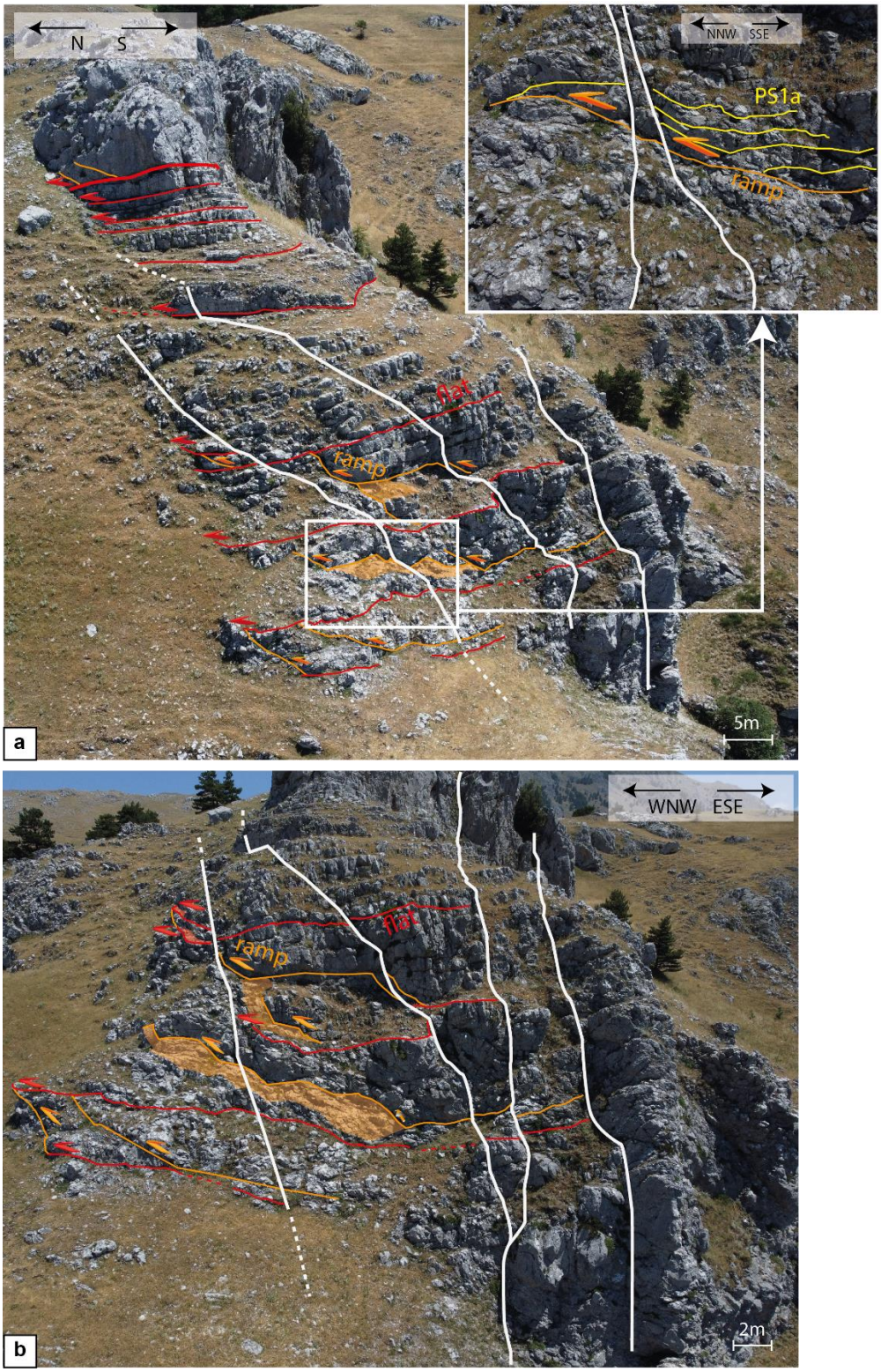

Figure 4. 4 Scarrone la macchia outcrop. a) N-S view of the outcrop. b) WNW-ESE view of the outcrop. The inset of (a) shows a detail of an intra-formational thrust fault (orange). There, the fault hanging wall is gently folded forming small-scale antiform folds.

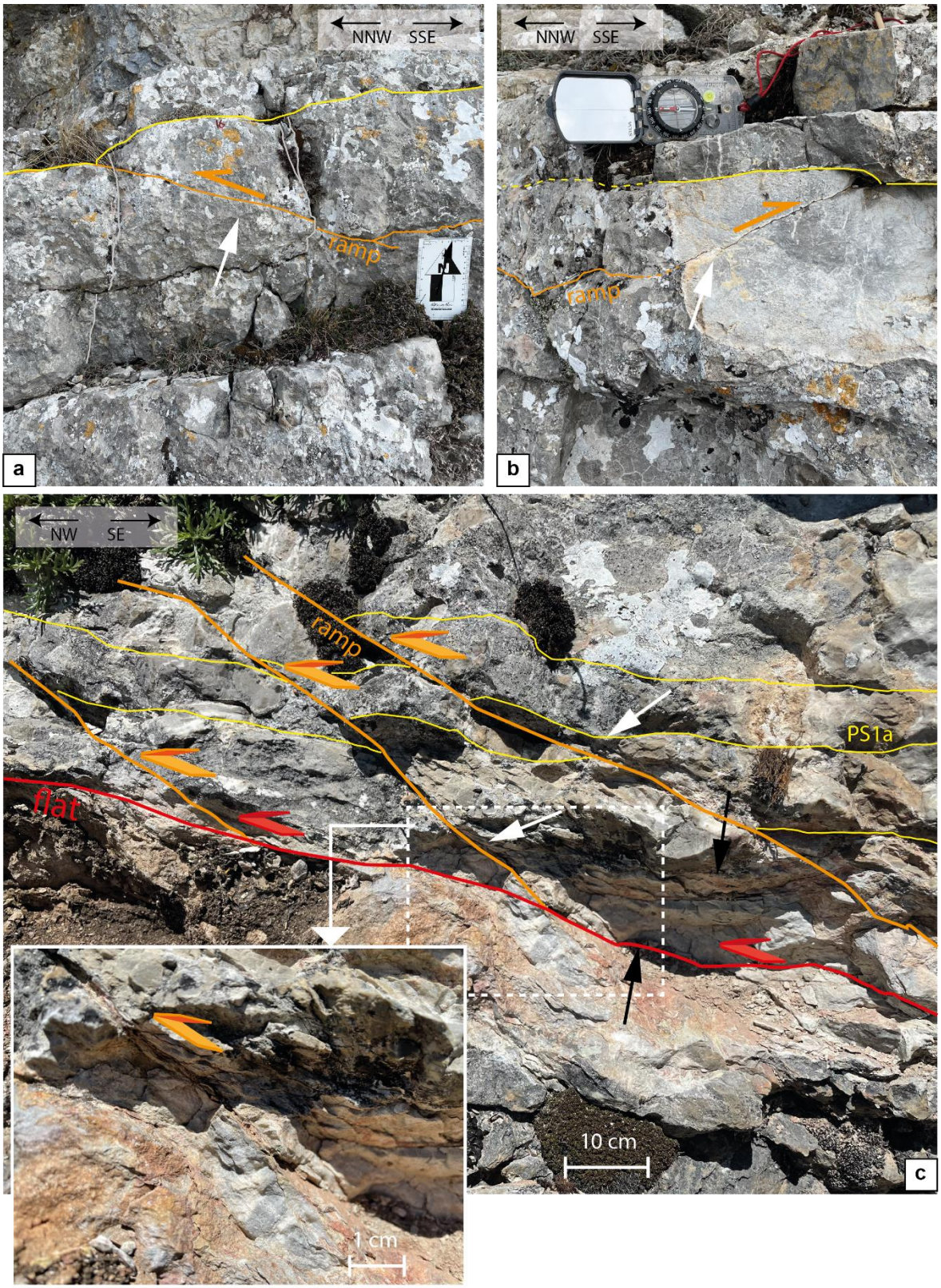

Figure 4. 5 Outcrop view of back thrust faults characterized by flat-ramp-flat geometries. a) Intra-formational back thrust faults dislocating a single mud-supported carbonate bed showing top-to-NNW transport direction. b) Synthetic intra formational thrust fault dislocating a single mud-supported carbonate bed showing top-to-SE transport direction. c) Grain-supported carbonate bed dislocated by multiple thrust surfaces (orange lines) and delimited by a flat surface at the bottom (red line). The inset of©) is the close-up view of a single reverse fault containing mm-thick, iso-oriented, scaly argillaceous materials.

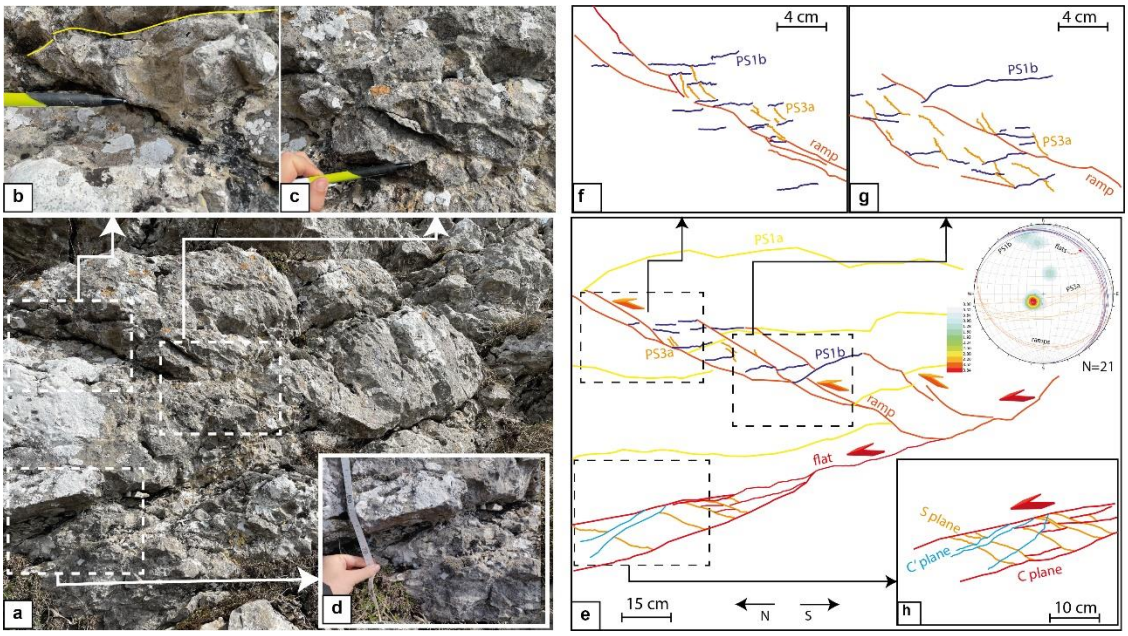

Figure 4. 6 Internal architecture of a well-developed flat-ramp-flat thrust fault dissecting multiple carbonate beds. a) to d) outcrop view of the thrust fault; the b) to d) figures show close-up views of the outcrop. e) to h) line drawings of the main structural elements dissecting the carbonate rock volume. In particular, f) and g) are details of the reverse fault forming the ramp geometry, h) is a detail of the bed-parallel slip zone. The former planes are reported with the same color in the lower-hemisphere, equal-area projection (contour intervals are 0.32% per 1% area, as shown in the legends). In f), The S-C-C' fabric is shown.

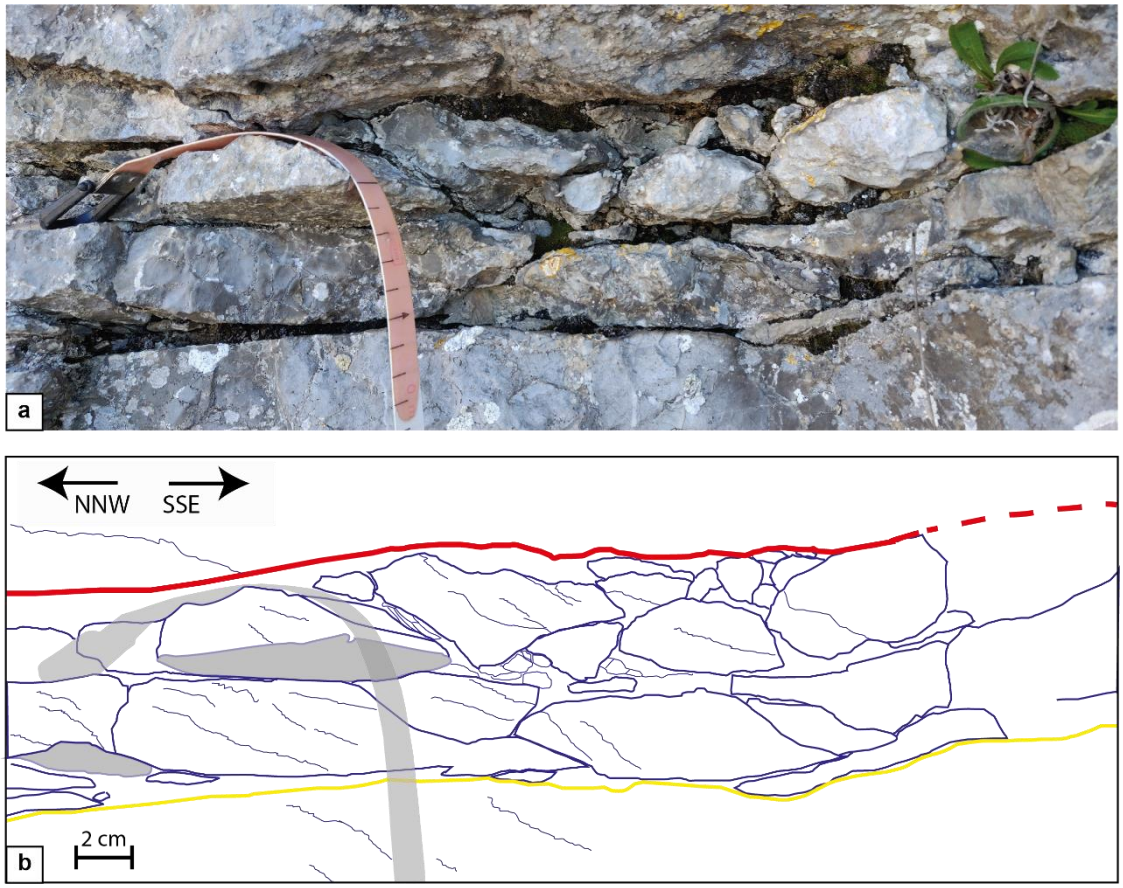

Figure 4. 7 Bed package interface containing elongated, isolated carbonate lithons bounded by bed-parallel and bed-oblique solution surfaces enlarged by karstic processes. The single lithons are crosscut by bed oblique PS3b slickolites. a) Outcrop view of the bed package interface. b) Line drawing reporting the main bounding interfaces

and intrabed discontinuities: the package interface (red), the single bed interface (yellow), and the intra-bed solution surfaces (blue). The metric tape is for scale.

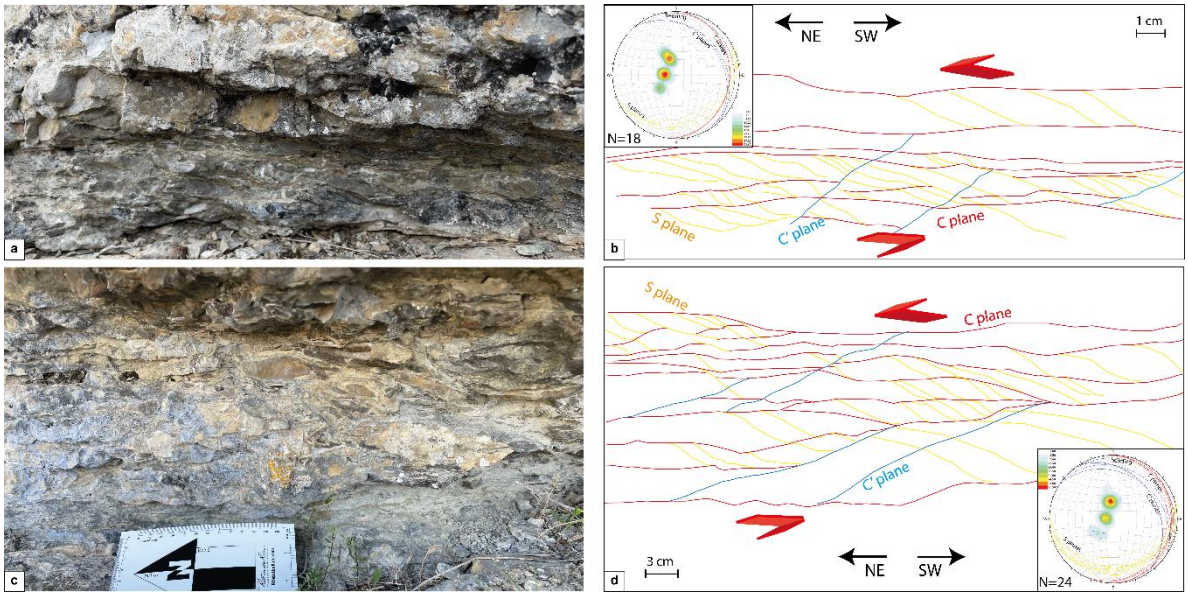

Figure 4. 8 a), c) Bed packages associations interfaces including elongated, sigmoidal-shaped carbonate lithons forming a S-C-C' fabric. The traces of single surfaces are reported in the line drawings in b), d) as follows: C-planes in red, S-planes in yellow, and C'-planes in cyan. The transport direction is towards NNW. The former planes are reported with the same color in the lower-hemisphere, equal-area projection (Contour intervals are 3.40% per 1% area, as shown in the legends) with the same colors

"Interbed solution surfaces"

The bed packages interfaces bounding m-scale, fining-up sedimentary sequences (Manniello et al., 2022) include a few cm-thick, mud-supported carbonate rock volumes with anastomosed, mm- to cm- spaced, bundles of bed-parallel stylolites with clayish residual material (Figure 4. 9). Altogether, these bundles of stylolites form a disjunctive cleavage (Powell, 1979; Engelder and Marshak, 1985). Combined with the bed-oblique slickolites later described in the text (cf. Ch. 4.2.3), this disjunctive cleavage bound elongated, single carbonate lithons forming ca. 10° cut off angles with the bed package interfaces.

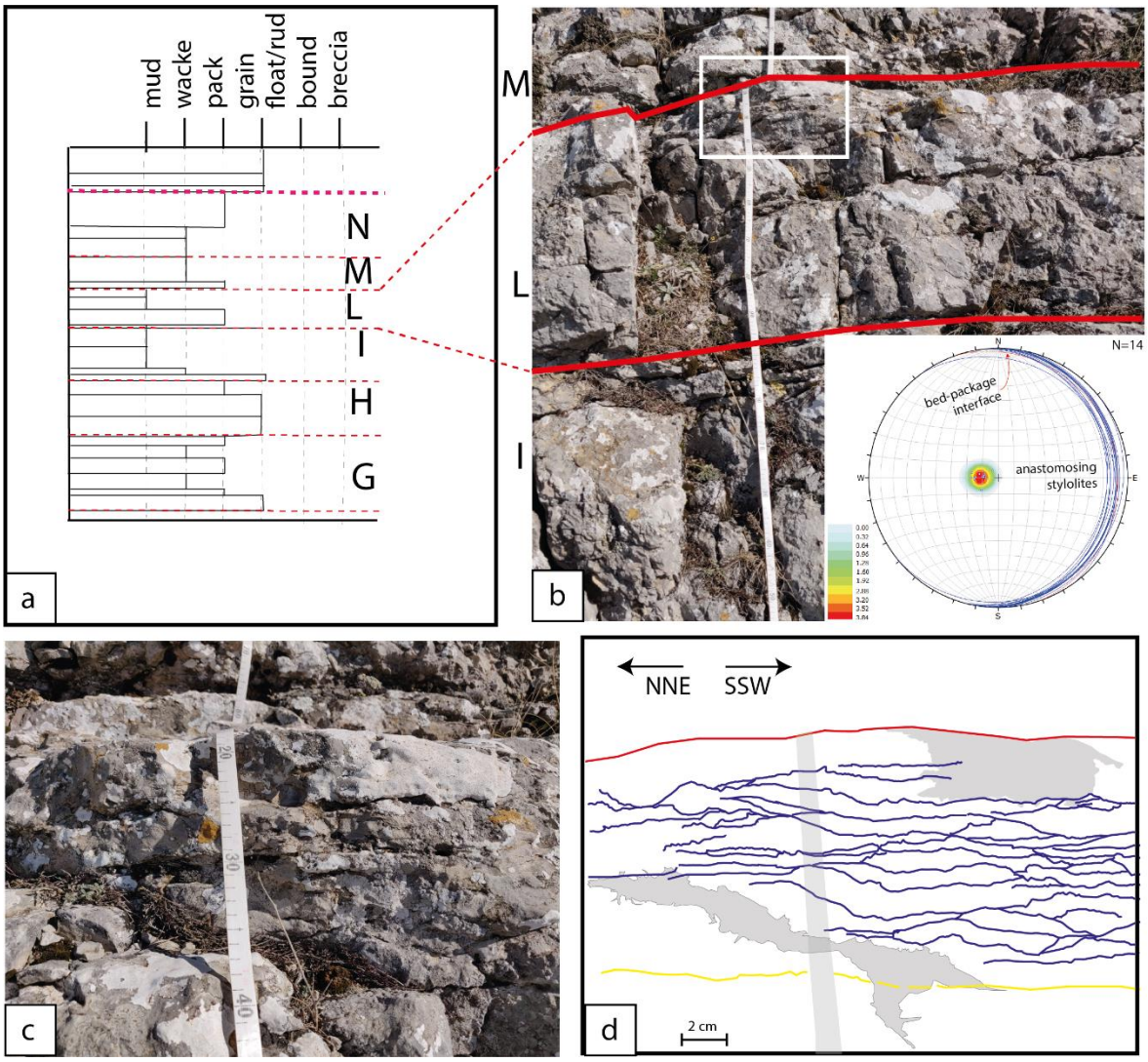

Figure 4. 9 Anastomosed bed-parallel solution surface localized at a L-M bed package interface. a) portion of the stratigraphic column of Scarrone la macchia (from Figure 5. 2). b) Outcrop view of the L bed package. c) Close up view of the L-M bed package interface. d) Line drawing of the anastomosed solution surfaces (blue), bed interface (yellow), and bed package interface (red). d) The attitudes of the anastomosing, intrabed stylolites (blue) and bed package interface (red) are reported in the lower-hemisphere, equal-area projection (contour intervals are 0.32% per 1% area).

The interbed, bed-parallel solution surfaces are labelled as PS1a solution surfaces, dissolve single bed interfaces, and show a lateral continuity that might exceed the extent of single outcrops. In the oolithic carbonates, PS1a solution surfaces are very thin and are associated to bed amalgamation (Figure 4. 10a, b). Differently, in the well-layered carbonate PS1a solution surfaces include mm-thick films of terrigenous material (Figure 4. 10d, g), and show wave-type morphologies (Koehn et al., 2016), with dissolution teeth orthogonal to the solution surfaces. In particular, we note that the PS1a solution surfaces encompassed by grain-supported carbonate beds exhibit sharp morphologies and large teeth. On the contrary, those in between mud-supported carbonate beds show smooth morphologies and tiny

irregular teeth, that are also partially obliterated by karst-related dissolution (Figure 4. 10c) (Pontes et al., 2022).

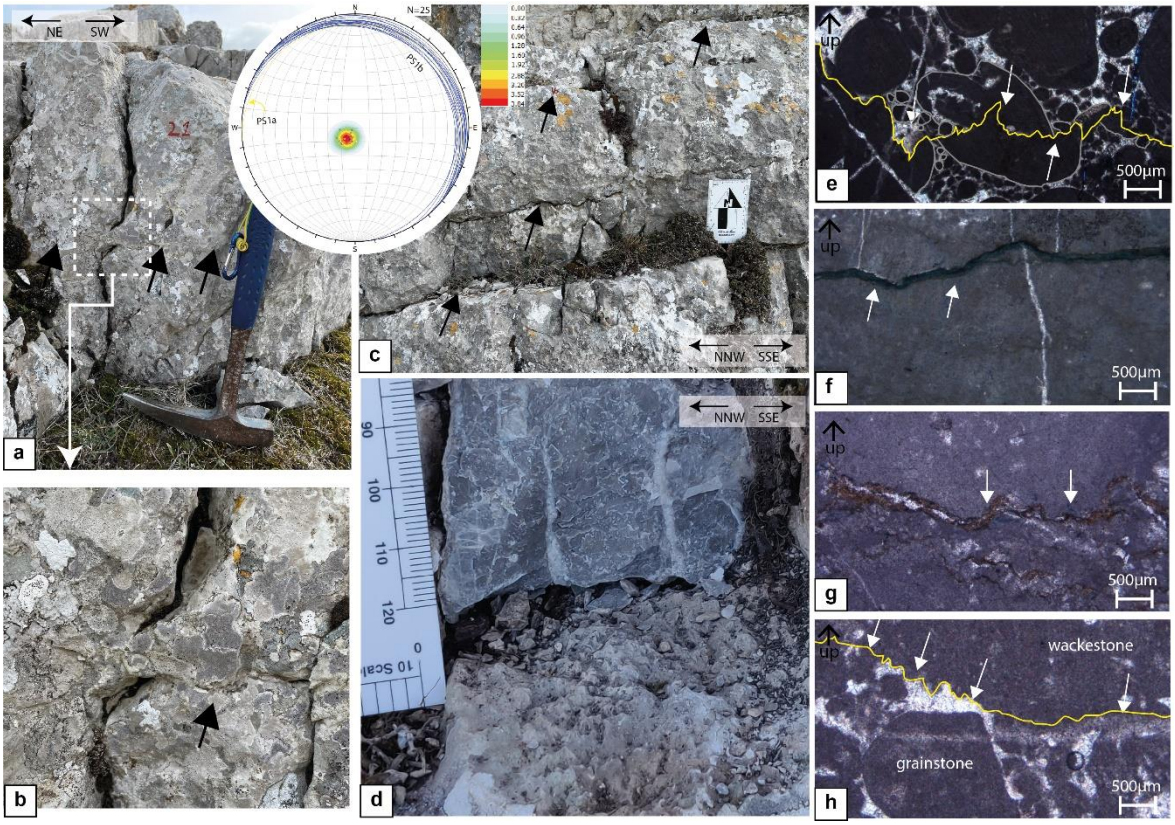

Figure 4. 10 a) Outcrop view of PS1a solution surfaces in oolithic carbonates. b) Close up view of a PS1a surface in the oolithic carbonates. c) Outcrop view of PS1a surfaces in well-layered carbonates. These surfaces are often enlarged due to karst-related dissolution. d) Close up view of a PS1a surface in well-layered carbonates. Terrigenous material accumulates within the small troughs. Microphotographs taken under cross-polarized light showing: e) PS1a solution surfaces in oolithic carbonates; f) PS1a solution surfaces in carbonate mudstones; g) PS1a solution surface in a carbonate wackestone; h) PS1a solution surface at the contact between grain- and mud-supported carbonates. The attitude of the PS1a solution surfaces localized along the oolithic - well-layered contact are reported in the lower-hemisphere, equal-area projection (contour intervals are 0.32% per 1% area).

At the micro-scale, the dissolution teeth associated to pressure solution surfaces localized within the mud-supported carbonate lithofacies are characterized by height values varying between 0.18 mm and 0.01 mm, and amplitude values varying between 0.1 mm and 0.01 mm. In the grain-supported carbonate lithofacies, the pressure solution teeth have height values comprised between 0.5 mm and 0.1 mm, and amplitude values that varies between 0.2 mm and 0.05 mm. Moreover, the PS1a solution surfaces within grain-supported carbonate beds generally do not include any infilling material (Figure 4. 10e). Differently, those within mud-supported carbonates include brownish-to-reddish infills (Figure 4. 10f, g). In the latter ones, sparse pods of fibrous calcite minerals elongated orthogonal to the enlarged dissolution surfaces are also documented. The teeth of PS1a solution surfaces

juxtaposing carbonate beds with dissimilar rock textures mainly extend towards the bed with a larger grain size (Figure 4. 10h).

"Intrabed solution surfaces"

Data are reported for one set of bed-parallel (cut-off angle < 12°), three sets of bed-perpendicular (cut-off angle > 80°), and two sets of bed-oblique (12° < cut-off angle < 80°) solution surfaces.

Parallel to bedding

The intrabed bed-parallel solution surfaces are labelled as PS1b. They show a limited lateral persistence (length in the order of a few tens of cm), and very often a seismogram-type morphology (Figure 4. 11a, b). In fact, the single surfaces show a rough morphology with teeth 0.8 mm to 0.3 mm-high, and 0.3 mm to 0.2 mm-wide. These solution surfaces crosscut the high-angle, WNW-ESE striking hairline veins (Figure 4. 11b), interpreted as due to burial-related deformation of the Viggiano Mt. carbonates (Manniello et al., 2022). The P10 values computed for the PS1b solution surfaces refer to the rock volumes located below the oolithic/well-layered carbonate interface, and at the base of the Scarrone la macchia outcrop (Figure 4. 12). At the former site, the results of a 11 m-long linear scanline survey show that the PS1b length values vary between 100 cm and 10 cm, with a calculated average of 31 cm. Independently from the bed thickness, the longest PS1b surfaces are documented within the mud-supported carbonate beds topping single bed packages. The P10 values vary between 1 and 7; the highest values are calculated for the PS1b surfaces dissolving grain-supported carbonate beds. The P10 values are hence inversely correlated with the PS1b length values. At the base of the outcrop, the results of a 9 m-long linear scanline show that the PS1b length values vary between 20 cm and 86 cm, with an average value of 46 cm, and the P10 values varies between 1 and 5 independently from the bed thickness. Similar to the previous case, higher P10 values are documented within rock portions containing shorter PS1b solution surfaces.

At the micro-scale, the PS1b solution surfaces localize at the grain contacts in the coarser carbonate beds (Figure 4. 11c, d), whereas they include brownish-to-reddish infill in the mud-supported ones (Figure 4. 11e, f). Occasionally, in the latter carbonate beds the PS1b surfaces localize nearby oblique-to-bedding slickolites, and/or within small pods of calcite cements (Figure 4. 11g). Altogether, these elements form dissolution/precipitation swarms

crosscutting both E-W (Figure 4. 11g) and N-S striking high-angle veins (Figure 4. 11h), and merge with the PS3b elements (cf. text below).

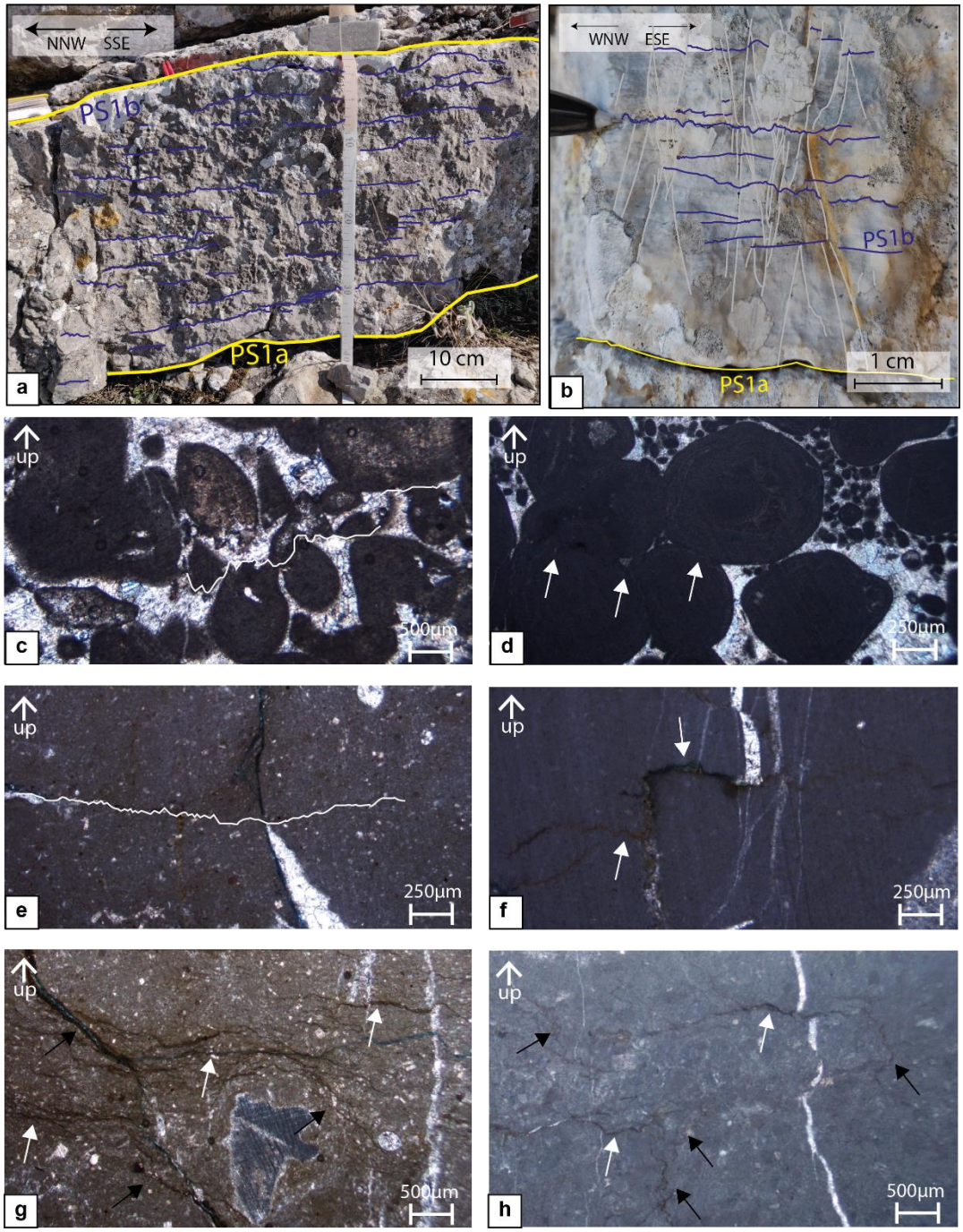

Figure 4. 11 Single carbonate beds crosscut by PS1b solution surfaces. a) Grain-supported carbonates with seismogram-type PS1b. b) Mud-supported carbonates with PS1b at very low angles (<12°) to bedding interfaces. The PS1b show seismogram-type morphologies and postdate the high-angle to bedding veins. Microphotographs taken under cross-polarized light showing: c) oolithic carbonates with intergranular blocky cements containinga PS1b solution surface dissolving both carbonate grains and cements (white line); d) oolithic carobnates containing stylolites at grain contacts(see white arrows), and blocky cements that infills intergranular space which is not affected by any dissolution. e) PS1b solution surface localized in a carbonate wackestone; f) PS1b solution surface localized in a carbonate mudstone;g) clusters of small-scale PS1b (see white arrows) linked with the bed-oblique slickolites (see black arrow); h) PS1b solution surface linked with the high-angle to bedding solution surfaces.

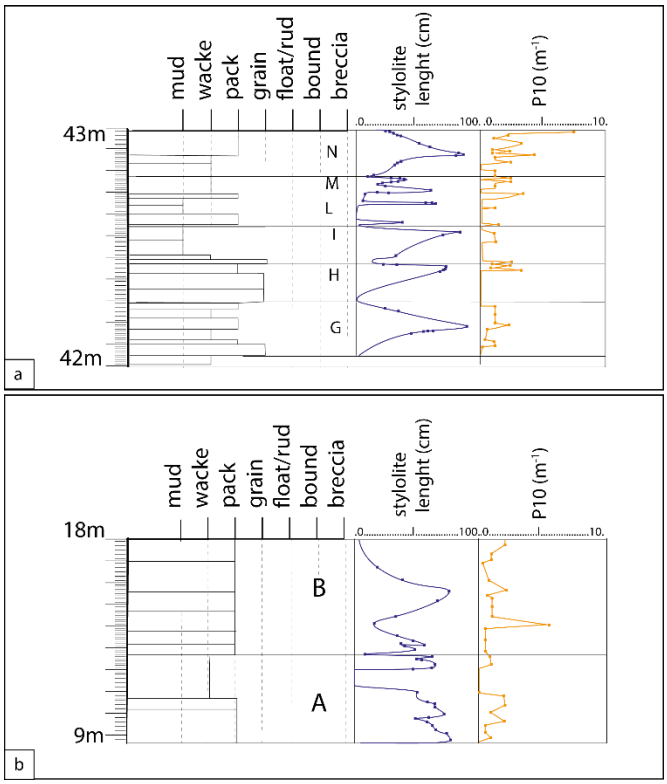

Figure 4. 12 PS1b solution surface length log and P10 log computed for 30 cm-thick intervals surveyed across the a) G-to-N bed packages of the well-layered carbonate unit, and b) across the A-to-B bed packages of the well-layered carbonate unit. See text for details.

Perpendicular to bedding

Three sets of bed-perpendicular surfaces labelled as PS2 elements are present (Figure 4. 13 and 14). The PS2a strike ca. N60E and consist of stylolites up to ca. 10 cm-high abutting against both PS1a and PS1b solution surfaces (Figure 4. 13a, b). At the microscale, the PS2a dissolve high-angle, E-W striking veins, and include sub-horizontal teeth 0.1 to 0.2 mm in height (Figure 4. 13a, b). The PS2b solution surfaces show seismogram-type morphologies (Figure 4. 14a), strike ca. N330-350E, are more than 10 cm-long, and abut against both PS1a and PS1b solution surfaces (Figure 4. 13a, b). Moreover, they dissolve the PS2a surfaces, and bound the bed-parallel calcite veins (Figure 4. 13a to d). At the microscale, the PS2b show seismogram type morphologies with sub-horizontal teeth 0.15 to 0.2 mm in height (Figure 4. 14c). The PS2c solution surfaces, not common along the study outcrops, strike ca. N100E, and are up to ca. 5 cm-long. At the microscale, they show seismogram type morphologies, with sub horizontal teeth ca. 0.1 mm-high (Figure 4. 13e, f). The PS2c abut against both PS1a and PS1b solution surfaces and dissolve the bed parallel veins (Figure 4. 14b).

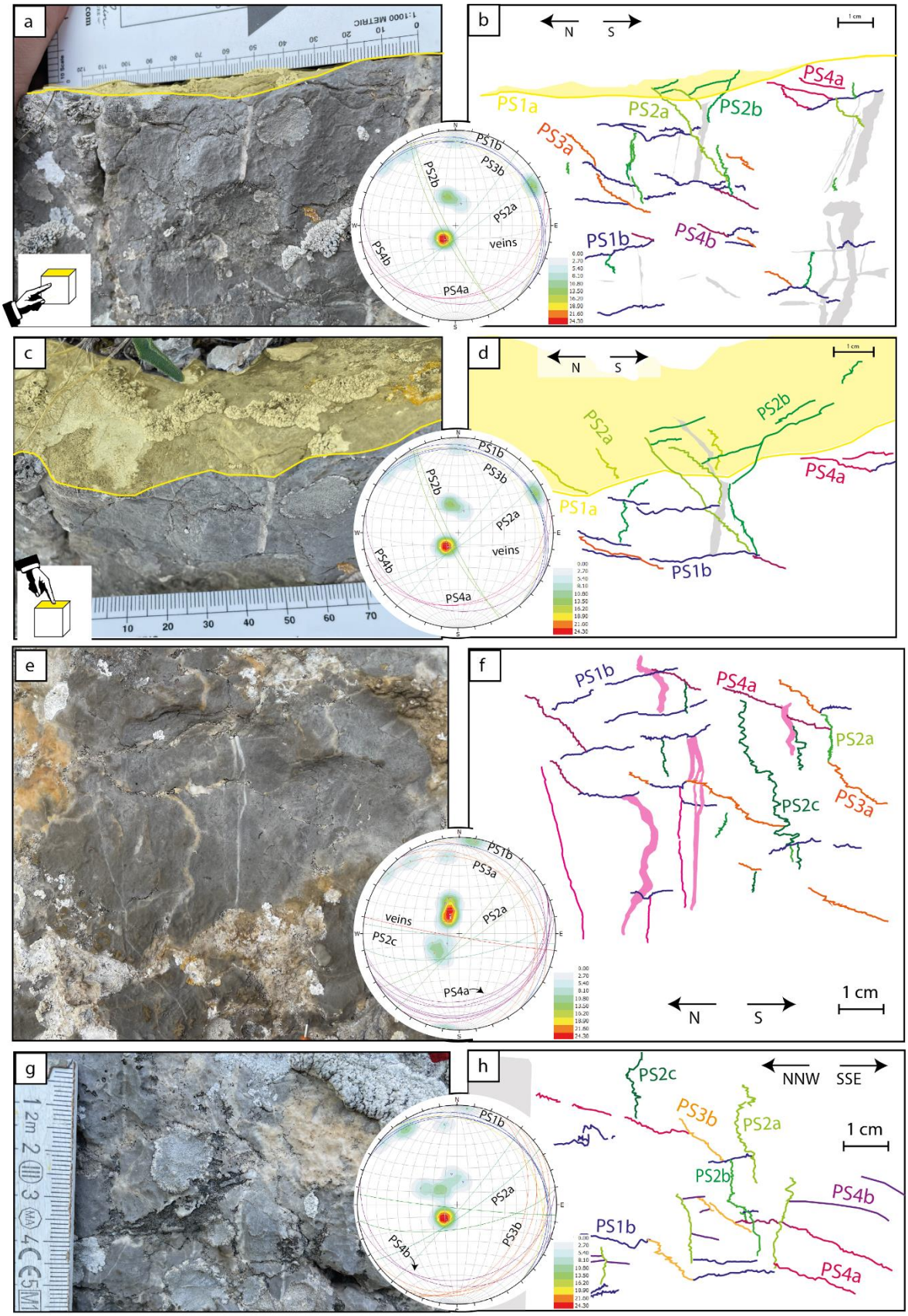

Figure 4. 13 a) Lateral view, and c) top view of a mud-supported carbonate bed of the well-layered carbonate unit. In both figures, the upper side of the bed interface is reported as a yellow surface. b) and d) Structural maps of the outcrop. See text for details. a) and g) Lateral view of two different mud-supported carbonate beds of the well-layered carbonate unit. f) and h) Structural maps of the outcrops. See text for details. The great circles show the

attitudes of solution surfaces and veins in s lower-hemisphere, equal-area projections. The pole contour intervals are of 2.70% per 1% area.

Oblique to bedding

The bed-oblique solution surfaces are classified according to orientation of the dissolution teeth. Those with sub-horizontal teeth are labelled as PS3, whereas the others with sub-vertical teeth are labelled as PS4. The PS3 solution surfaces form two sets of slickolites labelled as PS3a and PS3b, respectively. The PS3a strike ca. N110E, mainly dip towards SSW, and consist of sharp-peak type slickolites with teeth 0.25 mm to 0.15 mm in height (Figure 4. 13). Rare NNE-dipping PS3a slickolites are also documented. The PS3a surfaces do not contain any infilling material, form cut off angles up to ca. 65° with the bedding interfaces, abut against both PS1a and PS1b solution surfaces, and crosscut the bed parallel veins (Figure 4. 13). The PS3b strike ca. N45E, mainly dip towards SE, and consist of sharp-peak slickolites. They do not contain any infilling material, form ca. 35-40° cut-off angles with the bedding interfaces (Figure 4. 13) and abut against both PS1a and PS1b solution surfaces. At the micro scale, both PS3a and PS3b slickolites are characterized by linkage zones with eye-structure geometries (Figure 4. 14e, f). These geometries are similar to those documented in tight carbonates for overlapping joints (Korneva et al., 2014; Panza et al., 2019), and in porous carbonates for overlapping compactive shear bands (Tondi et al., 2012).

Two sets of PS4 slickolites respectively labelled as PS4a and PS4b crosscut the carbonate beds. The PS4a slickolites strike ca. N70E, dip ca. 20° SSE, form cut-off angles of 25-30° with the bedding interfaces and show tabular shape (Figure 4. 13). The PS4a are diffuse throughout the studied carbonates, and form either isolated elements or bundles of closely spaced surfaces within the disjunctive cleavage reported above (cf. Figure 4. 7). The isolated PS4a surfaces crosscutting grain-supported carbonate beds show sharper morphologies relative to the latter ones. The PS4a surfaces crosscutting mud-supported carbonate beds are generally shorter (length < 20 cm), and more closely spaced (spacing > 3 cm) than those dissolving the grain-supported beds (length < 60 cm, spacing > 10 cm). The PS4a forming a disjunctive cleavage abut against the N-S striking veins and crosscut the WNW-ESE striking veins (Figure 4. 13). The PS4b strike N90-110E, dip at low angles towards south, and form 25-30° cut off angles with the bed interfaces. The PS4b surfaces often show a sharp-peak type morphology, mainly crosscut mud-supported carbonate beds topping the single bed packages (Figure 4. 13), and show lengths < 30 cm. These surfaces crosscut the high-angle,

WSW-ENE and N-S striking hairline veins (Figure 4. 14g, h), and abut against the PS1b surfaces. At the micro-scale, both PS4a and PS4b elements contain brownish-to-reddish infills (Figure 4. 14g, h), and are characterized by wavy irregular surfaces.

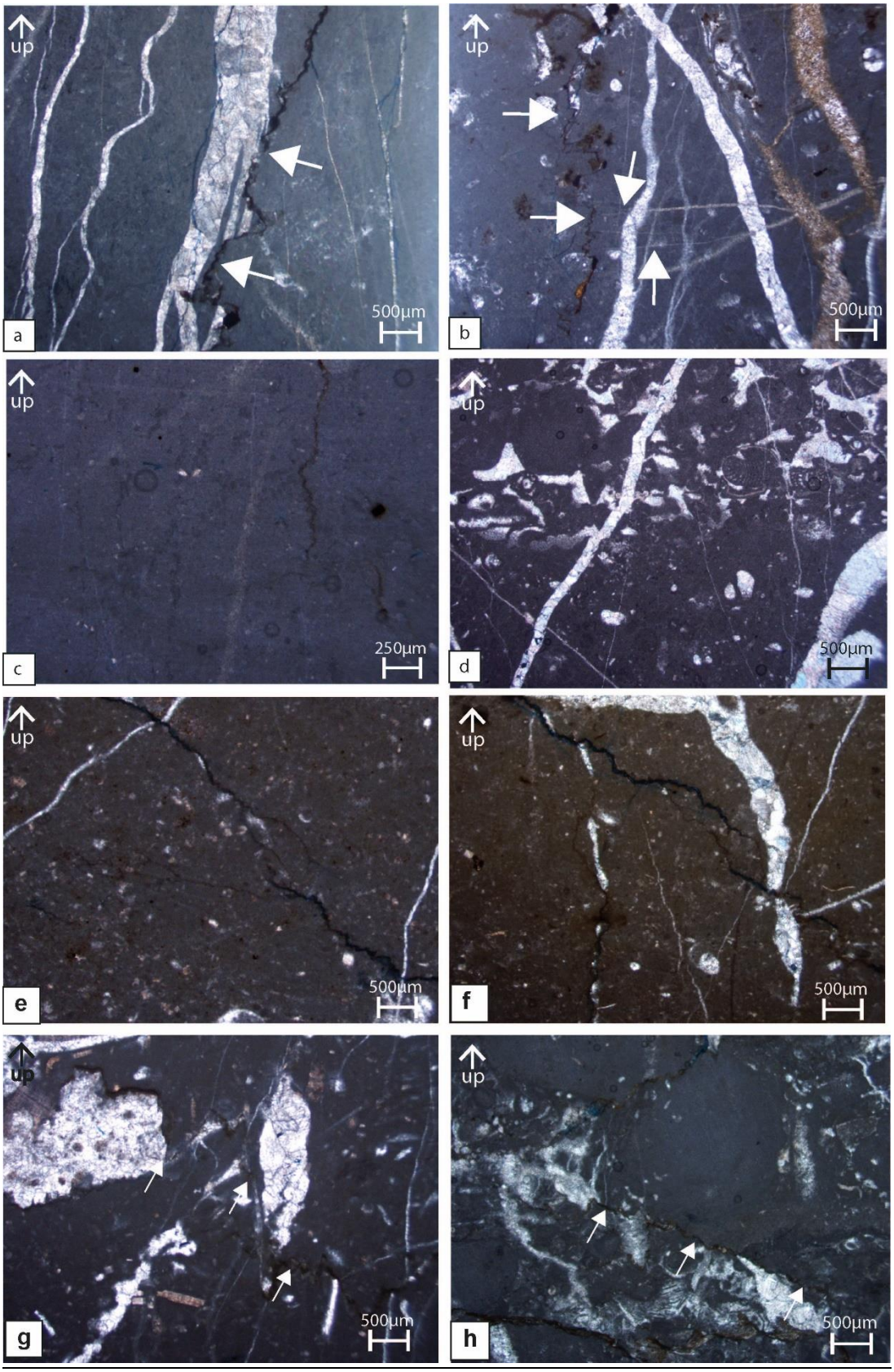

Figure 4. 14 Microphotographs taken under cross-polarized light showing the following structural elements: a) PS2a dissolving preexisting, WNW-ESE, high-angle hairline veins infilled with blocky cements; b) Bed parallel vein (Vparallel) infilled with fibrous cements and abutting against a PS2c solution surface. c) Isolated PS2b solution surface (white arrows) crosscutting a bed parallel PS1b element (black arrows). d) Grain-supported carbonates including both blocky cements and carbonatic mud crosscut by bed-oblique solution surfaces. e) and f) Micro-scale linkage geometries among PS3b solution surfaces. g) PS4a solution surface including thin films of terrigenous

material, and dissolving swarms of WNW-ESE calcite veins. h) PS4b solution surface dissolving swarms of WNW-ESE calcite veins.

"Bed-parallel veins"

The bed-parallel veins, labelled as $V_{parallel}$ elements (Figure 4. 13 to 15), include cm-long, mm-thick calcite veins associated to swarms of bed-oblique veins (Figure 4. 15b, d). The $V_{parallel}$ veins show irregular profiles, have lengths up to ca. 10 cm, and are crosscut by both PS2c and PS3b elements (Figure 4. 13a, 14b). At the micro scale, some of the $V_{parallel}$ elements are also characterized by small amounts of shear, as recorded by the offset of both ooids and veins (Figure 4. 15e, g). Moreover, we document presence of mineralized extensional jogs bounded by interacting, sheared, bed parallel $V_{parallel}$ elements (Figure 4. 14g). We also note that some of the $V_{parallel}$ veins localize along sheared and partially opened PS1b elements (Figure 4. 15d).

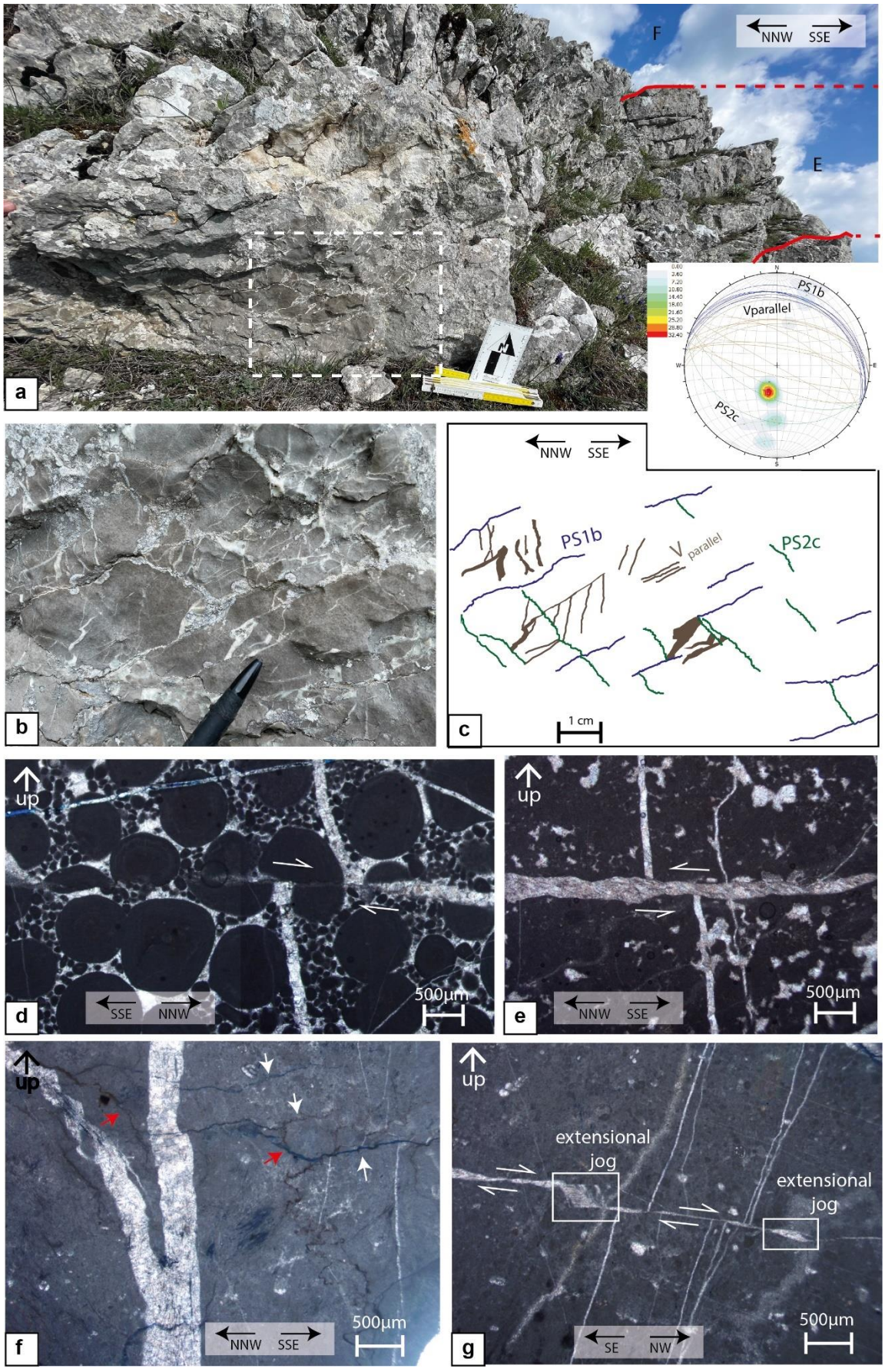

Figure 4. 15 Deformation associated to one of the small-scale back thrust faults crosscutting the Lower Jurassic carbonates. a) Large scale view of the outcrop exposing the E bed package of the well-layered unit. b) Close up of a grain-supported carbonate bed crosscut by calcite veins. c) Structural map of the outcrop. See text for details. d)

Oolithic carbonates, microphotograph taken under cross-polarized light of a sheared, and partially re-opened/cemented, bed-parallel solution surface. The sense of shear is displayed by the offset of the high-angle vein and of the single oolites. e) Sheared bed-parallel vein in oolithic carbonates. See text for details. f) Abutting relations among oblique PS3a (red arrows) and PS1b solution surfaces (white arrows) dissolving high-angle veins. g) Mineralized releasing jogs present at the mode-II termination of sheared bed-parallel veins. The microphotographs were referred to samples coming from the outcrop shown in a). The great circles show the attitudes of measured representative PS and veins in s lower-hemisphere, equal-area projections (contour intervals of 3.60% per 1% area).

4.5 Discussion

4.5.1 Pressure solution-assisted diagenesis

Similar to the Meso-Cenozoic carbonates of the Apulian Platform exposed along the Italian peninsula (Rustichelli et al., 2012, 2015), and to the Cretaceous platform carbonates of Israel (Laronne Ben-Itzhak et al., 2012), we infer that formation of the laterally continuous, 1 m- to 10 m-long, bed-parallel PS1a solution surfaces localized within the primary bed interfaces including a clayish material (Manniello et al., 2022). There, the clayish material likely functioned as a catalyzing factor triggering dissolution (Tada, 1987; Aharonov and Katsman, 2009; Gratier et al., 2015). However, since the PS1a solution surfaces were affected by recent karstic dissolution, we focus on the wave-type, intrabed PS1b solution surfaces to discuss any possible control exerted by the carbonate lithofacies on their morphologies. We document that rougher morphologies characterize coarser grained carbonate beds. Since the roughness of these surfaces can be interpreted as function of the amount of dissolution (Park and Shot, 1968; Alvarez et al., 1976; Toussaint et al., 2018), considering the homogeneous composition of the studied platform carbonates, we assess that the roughening process was controlled by the progressive involvement of grains with dissimilar dimensions. This process in turn influenced the energy regime during dissolution (Koehn et al., 2007; Ebner et al., 2009); in a simplistic view, the larger grain sizes determined more efficient elastic energy-dominated dissolution regimes, and therefore more pronounced peaks and teeth. Moreover, the textural irregularities and heterogeneities characterizing the carbonate grainstones might have also influenced the morphology of the PS1b solution surfaces (Tada et al., 1987; Brouste et al., 2007; Koehn et al., 2007; Ebner et al., 2009; Toussaint et al., 2018).

Considering grain-supported carbonate rocks, the blocky, euhedral, calcite cements filling both primary pores and high-angle veins (cf. Figure 4. 10e, 11c, 11d, 13) are typical of fluid-saturated diagenetic environments (Flugel, 2009). Differently, presence of isopachous cements around the larger grains (cf. Fig 14d) is consistent with phreatic diagenetic environments (Flugel, 2009) typical of early diagenesis (Tucker and Wright, 2009). We note

that the very tiny, µm-scale stylolites that localize at the grain contacts do not propagate through the surrounding blocky cements (cf. Figure 4. 11d). Accordingly, we assess that an incipient bed-parallel dissolution occurred during early diagenesis (Beaudoin et al., 2020), prior to blocky cements precipitation due to an initial surface energy-dominated regime that characterized the lithifying rock subjected to a sub-vertical load. As the pressure solution processes proceeded, determining the chemical compaction of the lithifying rock, the primary pores were then progressively infilled with the blocky cements due to diffusion/precipitation processes (Todaro, personal communication). We also assess that cementation therefore determined the gradual transition from surface energy- to elastic-energy-dominated diagenetic environments (Tada et al., 1987, Koehn et al., 2007; Ebner et al., 2009 Toussaint et al., 2018).

Of course, possible episodes of early embrittlement of the carbonates due to precipitation of the isopach cement rims around the carbonate grains might have determined jointing (and veining) at very shallow depths prior to any pressure solution processes (Lamarche et al., 2012; Lavenu et al., 2014, 2015; La Bruna et al., 2020). To further investigate the diagenetic conditions of dissolution throughout the studied carbonate succession, we consider the mud-supported carbonates. We note that most of the WNW-ESE striking hairline veins abut against the micro-scale, wave-type PS1b surfaces (cf. Figure 4. 10f). Accordingly, we interpret that the development of these wave-type solution surfaces occurred during burial diagenesis (Agosta and Aydin, 2006; Agosta et al., 2009; Korneva et al., 2014; Panza et al., 2016; 2018; Giuffrida et al., 2019), prior to the Oligo-Miocene peripheral foreland bulging of the platform carbonates (Tavani et al., 2015; Corradetti et al., 2018).

During burial diagenesis, dissolution of the blocky cements along the bed-parallel surfaces took place within cohesive carbonates also subjected to fracturing processes (Carrio-Shaffhauser et al., 1990). In fact, we document that many of the WNW-ESE striking hairline veins were dissolved by the microscale wave-type stylolites (cf. Figure 4. 10e). Taking the present-day thickness of the overlaying sedimentary units into account, hence considering the thickness of both Middle Jurassic-Upper Cretaceous platform carbonates and Oligo-Miocene Bifurto Fm., a burial depth of at least 1.4 - 1.6 km is computed for the study platform carbonates (Bruno et al., 2014). In order to assess the maximum burial conditions, we now consider the seismogram-type solution surfaces, and their crosscutting relations with the surrounding structural elements. These surfaces dissolve most of the high-angle veins, and the PS3 slickolites (Figure 4. 11f, 11h, 13b, 15f), and therefore formed after thrusting-related deformation. Focusing on their morphology, the dissolution teeth of the seismogram-

type stylolites are ca. 30% higher than those of the wave-type stylolites, suggesting that a greater amount of chemical compaction was solved by these elements (Park and Shot, 1968; Koehn et al., 2016; Toussaint et al., 2018). Previous XRD analyses of clayish samples collected from the Viggiano Mt. bed package interfaces (Manniello et al., 2022) documented that the mixed layers illite/smectite with R1 and R3 ordering are respectively characterized by 80% and 90% of illite contents. This evidence was interpreted with ca. 120-130 °C of thermal maturity (Merriman, 2005), and assuming 20-25 °C temperature gradients (Doglioni et al.,1996) with a ca. 4 km of burial depth. Following early diagenesis, we hence infer that the studied platform carbonates underwent to two distinct burial stages (Figure 4. 16). A first stage of sedimentary burial, recorded by the wave-type stylolites, which took place during the Jurassic - Lower Miocene time period at a maximum depth of 1.4 – 1.6 km. Then, during Late Burdigalian - Early Langhian (Patacca and Scandone, 2007), the studied carbonates were gradually incorporated into the foreland-foredeep domains of the evolving southern Apennine fold-and-thrust belt (Vezzani et al., 2010), and then stacked in the tectonic wedge reaching a maximum depth of ca. 4 km forming seismogram-type stylolites. Considering the cross-cutting relations documented both in the field and at the microscale, we ascribe at this latest stage also the formation of PS4 oblique slickolites with vertical teeth.

4.5.2 Pressure solution-assisted thrusting

Throughout the studied Lower Jurassic carbonate succession, we document the presence of small-scale thrust faults with a NNW transport direction (cf. Figure 4. 4). According to the large-scale structural setting of the platform carbonates (cf. Figure 4. 1), they are interpreted as back thrust faults associated to the flexural slip (Ramsay, 1967) of the carbonates at the forelimb of a wide antiform fold localized at the hanging wall block of the main, NE-verging thrust fault. The back thrust faults include both bed-parallel and bed-oblique slip planes, forming altogether flat-ramp-flat thrust geometries (Twiss and Moores, 1992). Hereafter, we will discuss the deformation mechanisms associated to these slip planes, and their possible controlling factors.

According to the results of field and microstructural analyses, the following three main structural architectures characterize the bed package interfaces: (i) bundles of clay-containing anastomosed stylolites, (ii) elongated carbonate lithons, and (iii) S-C and S-C-C’ fabrics. The former architecture is interpreted as a diagenetic load structure (Engelder and Marshak, 1985), the second one as associated to small amounts of shear strain, the latter one

as due to localized shear strain. Focusing on the shear-related structural architecture, we consider the interfaces containing elongated carbonate lithons including relicts of the anastomosed stylolites and bed-oblique PS3 solution surfaces (cf. Fig 6). We interpret these structures as due to the strain localization along pre-existing bundles of anastomosed stylolites (Twiss and Moores, 1992). During the bed-tilting and coeval contractional deformation, then, those shear structures formed weak interfaces (Byerlee, 1968; Cooke and Underwood, 2001; Smeraglia et al., 2017; Collettini et al., 2019) and acted as efficient mechanical anisotropies throughout the whole carbonate succession (Donath, 1964; Pollard and Aydin, 1990; Jing et al., 1992; Rawling et al.,2001; Baud, 2005).The S-C and S-C-C' fabrics are also associated to thrusting tectonics (Schweigl and Neubauer, 1997) due to pressure solution-assisted creeping mechanisms that localized within the platform carbonates at relatively low temperatures (Alvarez et al., 1978; Schmid et al., 1982, Bigi, 2006; Curzi et al., 2021).

Focusing on the ramp geometries, we note that the simplest structural elements solving reverse components of slip are the slickolites with sub-horizontal teeth (PS3a and PS3b solution surfaces). They formed as hybrid shear structures due to concomitant simple shearing and pressure-solution of the carbonates (Stockdale, 1921; Ebner 2010; Toussaint, 2018). Differently, the bed-perpendicular stylolites (PS2 solution surfaces) are interpreted as due to the layer-parallel shortening of the platform carbonates (Nickelsen, 1966; Engelder and Engelder, 1977; Alvarez et al., 1978; Holl and Anastasio, 1995; Agosta and Aydin, 2006; Agosta et al., 2009, 2010; Quintà and Tavani, 2012; Tavani et al., 2015). Formation of the bed-oblique slickolites, and their interaction with the pre-existing bed-parallel and bed-perpendicular stylolites hence produced the structural array associated to the small-scale reverse faults displacing the single bed interfaces (cf. Fig 13). The PS3 surfaces nucleated either as isolated structural elements, or as swarms localizing at the tips of bed-parallel solution surfaces. Accordingly, we interpret their nucleation as the result of bed parallel shear causing localized contractional deformation at their compressional mode-II quadrants (cf. Figure 4. 15d, e, g), and their subsequent growth due to linkage and tip-zone interactions facilitated by small amounts of overlaps (cf. Figure 4. 14e, f; Fletcher and Pollard, 1981; Katsman et al. 2006; Gratier, 2009, Zhou and Aydin, 2010; Aharonov and Karcz, 2019). Similar structural architectures associated to pressure solution were documented by Graham et al. (2003) and Antonellini et al. (2008) in the platform and slope carbonates of central Italy, respectively. Overall, in this work we document that ramp development within the coarser carbonates was accompanied by up to 30 cm-thick fragmented damage zones

surrounding the slip surfaces. On the contrary, ramp-related slip surfaces are not surrounded by any fractured damage zone in the mud-supported carbonates.

4.5.3 Conceptual model of pressure solution-assisted deformation

In this section, we synthetize our observations and findings in a time-dependent conceptual model based on the evolution of the Southern Apennines ftb (Patacca and Scandone, 2007). The model includes six main stages of pressure solution-assisted deformation associated to sedimentary burial and thrusting-related deformation of the platform carbonates:

a) The first stage is referred to early diagenesis (Figure 4. 16, 17a). It takes place at very shallow depths within a not totally lithified carbonate rock volume with formation of bed-parallel pressure solution surfaces. The greatest principal stress axis, σ_1, is vertically oriented (Figure 4. 16), and proportional to the very shallow burial depth < 500 m (Beaudoin et al., 2020). At this stage, the rock is subject to pure shear deformation forming incipient, bed-parallel solution surfaces (PS1a, PS1b). Bed-parallel solution surfaces mainly localize at the grain contacts and are associated to pure-shear deformation (Figure 4. 17a).
b) The second stage occurs as the burial depth gradually increases, and likely involved the carbonate rocks up to the late Oligocene. During burial diagenesis, both physical-chemical compaction and cementation processes produce stiffer carbonate rocks, in which bed-parallel solution surfaces form along bed interfaces (PS1a) and within single carbonate beds (PS1b). Pure shear deformation hence occurs, and wavy-type, bed-parallel solution surfaces form. The greatest principal stress axis, σ_1, is vertical, and proportional to the increasing lithostatic loading (Figure 4. 16). Considering that a maximum depth of ca. 1.4-1.6 km (Patacca and Scandone, 2007; Bruno et al., 2014), a value of σ_1 up to ca. 35 MPa is envisioned assuming an average pressure gradient of ca. 25 MPa/km (Mavko et al., 1998). Bed-perpendicular hairline fractures and veins also form in the grain-supported carbonates (Figure 4. 17b).
c) The third stage takes place during Late Burdigalian - Early Langhian foreland bulging and/or along-foredeep stretching, and Langhian layer-parallel shortening of the carbonates (Figure 4. 16 and 17c). Foreland and foredeep-related deformation promotes mode-I fracturing, which partially overprints the pre-existing network of hairline veins. Layer-parallel shortening, instead, marks the very beginning of

thrusting tectonics forming bed-perpendicular solution surfaces, PS2b, and bed-parallel veins, $V_{parallel}$ due to pure shear deformation. During this stage, the orientation of the greatest principal stress axis, σ_1, switches from vertical to horizontal (Figure 4. 16).

d) The fourth stage occurs during post Early Serravallian times, when the Apenninic Platform overthrusts the already structured Lagonegro units. (Figure 4. 16, 17d). At a larger scale, flexural slip-folding and shearing of the bed package interfaces cause formation of low angle-to-bedding reverse faults (Figure 4. 17d). This deformation is therefore due to a hybrid contraction-shearing mechanism. The inferred yield cap is consistent with formation of oblique to bed slickolites, along which both shear and contraction takes place, determining a sub-simple shear deformation. The greatest principal stress axis, σ_1, is horizontal, and characterized by values > 35 Mpa (Figure 4. 16).

e) The fifth stage is also related to flexural slip and sub-simple shearing of the platform carbonates (Figure 4. 16, 17e). Small-scale back thrust faults propagate throughout the carbonates and show flat-ramp-flat geometries due to linkage of the previously mentioned structural elements. The S-C and S-C-C' fabrics localize along the main flats. The yield cap of this stage represents an evolution of the previous stage and is consistent with formation of shear zones due to simple shear deformation. In fact, during this stage the shearing component is significantly predominant and reverse faults form. This stage takes place under a horizontal greatest principal stress axis, $\sigma 1$ and characterized by values >> 35 MPa.

f) The sixth stage takes place during Late Miocene tectonic burial of the carbonates (Figure 4. 16, 17f). At this stage, the PS4 oblique slickolites with vertical teeth also form under a vertical σ_1. The maximum tectonic burial stage is associated to the formation of new seismogram-type bed parallel stylolites. At depths of ca. 4 km, those stylolites form at very low angles with the bedding interfaces, dissolving the pre-existing elements. The tectonic load determines a predominant pure shear deformation, under a vertical principal stress axis, σ 1 (Figure 4. 16).

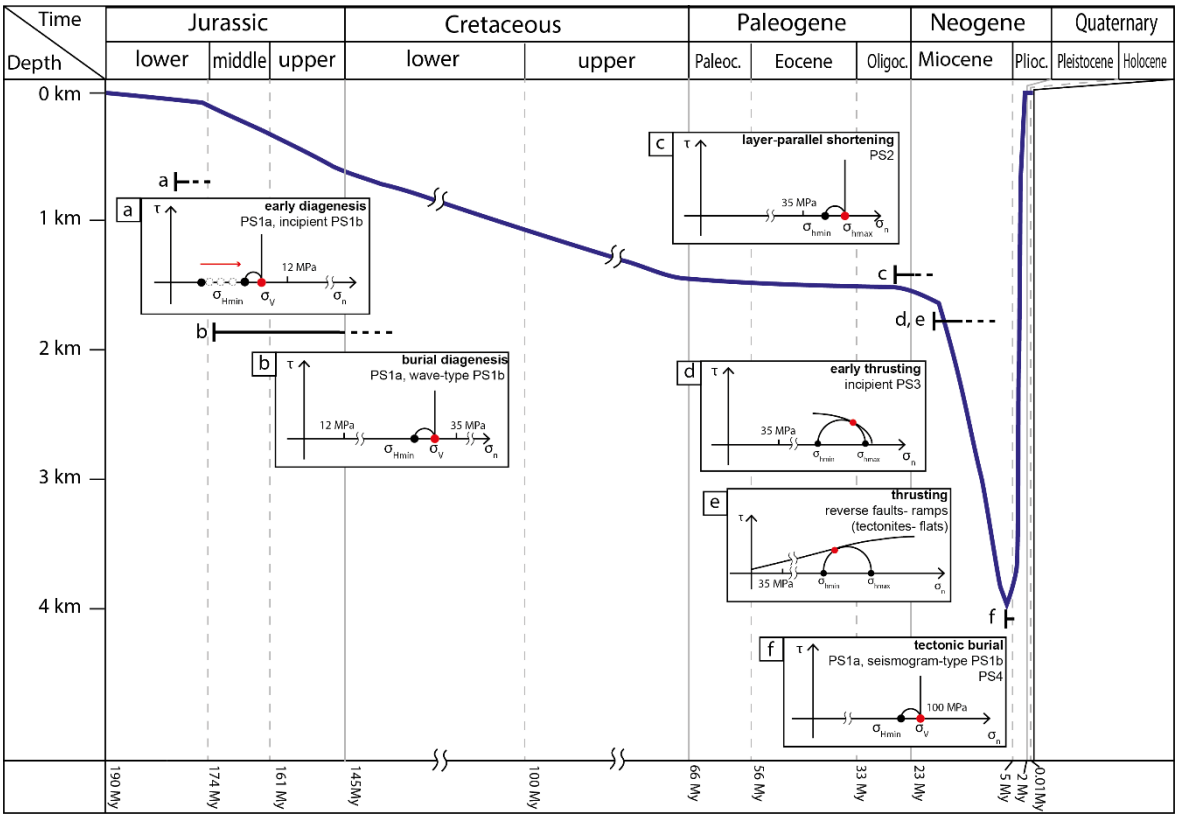

Figure 4. 16 Schematic burial history of the Lower Jurassic carbonates. The main tectonic stages are reported: a) early diagenesis; b) burial diagenesis; c) layer-parallel shortening due to thrusting tectonics; d) early thrusting and oblique slickolites formation; e) intra-formational flats and ramps due to thrusting tectonics; f) tectonic burial. See text for details.

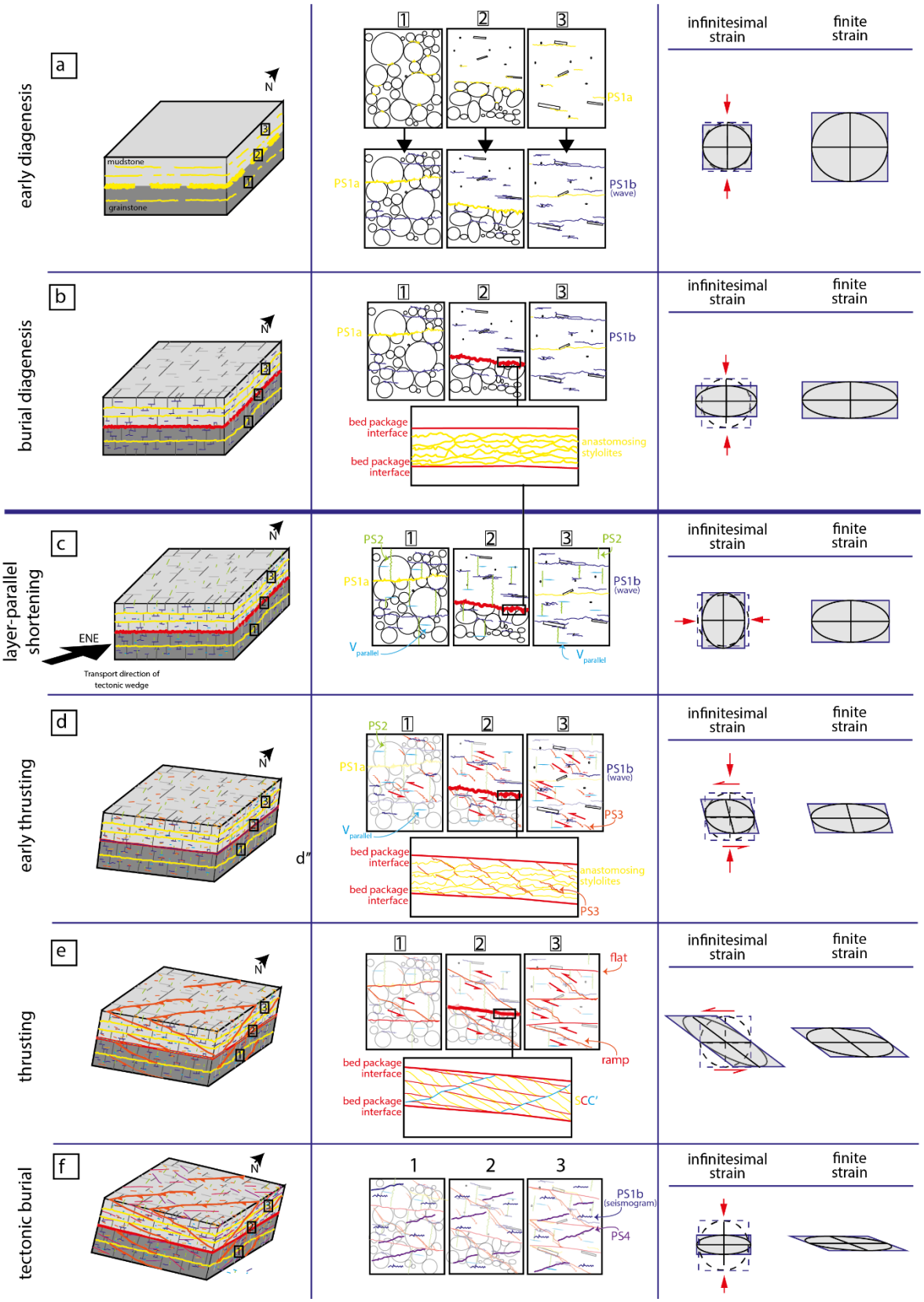

Figure 4. 17 Schematic sketch of the main deformation mechanisms that took place within the early to burial diagenesis of platform carbonates since Early Jurassic, and Middle-Upper Miocene thrusting tectonics. The left column shows a representative sketch of the deformation stages occurring through the carbonate multilayer: a) early diagenesis; b) burial diagenesis; c) layer-parallel shortening; d) early thrusting; e) late thrusting; f) tectonic burial. The central column represents the deformation observed within the single carbonate beds through the different stages. The right column shows both infinitesimal and finite strain ellipses through the stages. See text for details.

4.6 Conclusions

This work focused on the structural evolution of Mesozoic platform carbonates exposed in southern Italy. The results of combined field and microscale structural analyses allowed to document the modalities of pressure-assisted diagenesis and thrusting deformation. In particular, we first defined the control exerted by the primary heterogeneities on pressure solution by showing that the bed-parallel solution surfaces mainly localized within the coarser grained carbonate beds. These observations were explained invoking that a greater elastic energy-dominated regime characterized the grain-supported carbonates with respect to the mud-supported carbonates promoting their dissolution. The relations among blocky cements and bed-parallel solution surfaces documented at the microscale were useful to establish the environmental conditions at which pressure solution occurred. As end members, we assessed that the wave-type stylolites either bounding or localizing within the single carbonate beds formed during burial diagenesis at depth not greater than 1.4.-1.6 km. Differently, we interpreted the seismogram-type solution stylolites as due to a more recent tectonic burial of the platform carbonates, at depths of ca. 4 km.

In the time interval between the sedimentary and tectonic burial conditions, the carbonates were subjected to Middle-Late Miocene thrusting tectonics, which caused formation of small-scale back thrust faults including both bed-parallel and bed-oblique slip planes. Altogether, the coalescence of these planes produced flat-ramp-flat geometries along the single thrust faults. The bed-parallel flat localized along primary heterogeneities already affected by pressure solution, which formed bundles of anastomosing, elongated carbonate lithons oriented oblique to bedding, and eventually discrete shear zones characterized by S-C and S-C-C' fabrics. Focusing on intrabed pressure solution surfaces, we documented that bed-orthogonal stylolites and bed-oblique slickolites interacted with the pre-existing bed-parallel solution surfaces forming small-scale, NNW-verging reverse faults.

The main results of this work were synthesized in a synoptic scheme including six main deformation stages. This scheme reported a deformation that took place within platform carbonates subjected to varying burial conditions and stress regimes. As a main outcome, the results emphasized the need of combined field and laboratory analyses to unravel the role of primary carbonate architectures on the time-dependent structural evolution of the platform carbonates. Further laboratory analyses may shed more lights on the controlling factors affecting the formation of single structural elements, and possible shed lights into the

role exerted by these elements on subsurface fluid flow during thrusting tectonic and subsequent downfaulting of the platform carbonates.

CHAPTER 5 - PORE SPACE PROPERTIES ASSOCIATED WITH SOLUTION SURFACES IN MESOZOIC PLATFORM CARBONATES, SOUTHERN ITALY

5.1 Introduction

Carbonates display some of the most complex porosity networks in reservoir rocks. Diagenetic and tectonic processes significantly affect the texture and petrophysical properties of carbonate rocks, due to the partial or complete overprinting the depositional features, and hence modify the original pore space and vary the mechanical behavior of these rocks (Jardine et al., 1985; Lucia, 2003; Ehrenberg et al.,2006, 2012; Baud, 2016; Dernaika et al., 2019, Vasudevan, 2020). Specifically, the dissolution processes including the precipitation of different generations of calcite cements during continuous burial due to diagenetic fluids, and the formation of dissolution surfaces such as pressure solution seams and stylolites associated to the reverse solubility of calcite minerals with temperature (Carrio-Schaffhauser et al., 1990; Koehn et al., 2007, Toussaint et al., 2018) may occur at the same time determining an antagonistic dissolution-precipitation effect (Rustichelli et al., 2015; La Bruna et al., 2020). As a results, not only the interplay between the two aforementioned mechanisms makes difficult to predict the pore space of carbonate rocks, but additional uncertainties are associated to presence of a variety of carbonate lithofacies affecting the relative extent of mineral precipitation and dissolution.

Focusing on pressure solution seams and stylolites, they are commonly considered to form isolated baffles and/or barriers to subsurface flow. However, several recent works have shown that they may form a new pore space, influencing the storage properties of the carbonates and possibly affecting the modalities of fluid flow (Raynaud et al., 1992; Heap et al., 2014, 2018; Rustichelli et al., 2015; Koehn et al., 2016; Toussaint et al., 2018; Bruna et al., 2019; Araùjo et al., 2021, Cortes-Pontes et al., 2022). Result showed that the morphology of solution surfaces is a key controlling factor for the pore space properties of carbonates. It is known that stylolites and pressure solution seams (cf. Ch. 3.1) are recognized according to their morphology, which include very smooth profiles (wave type), rectangular profiles, sharp-peaked profiles (sharp-peak or seismogram type) and anastomosed patterns (Park and Schot, 1968; Koehn et al., 2016). The morphology can be parametrized through the “roughness”, a geometrical parameter that follows the laws of fractal geometry, and gives an estimate for the amount of dissolution (Ebner et al., 2010;

Laronne Ben-Itzhak et al., 2012; Toussaint et al., 2018; Beaudoin et al., 2016, 2019, 2020; Labeur et al., 2021; Zhou et al., 2022). Furthermore, the structure of the carbonate rocks containing burial pressure solution seams and stylolites may significantly evolve during time, due to the imposition of specific tectonic regimes. For example, the involvement of those rocks in a fold-and-thrusts belt may determine the shearing of the pre-existing stylolites, forming microfractures within the immediate proximity of the stylolites , enhancing the porosity and permeability associated with them (Manniello et al., 2023).

In this work, we consider the bed parallel pressure solution seams and stylolites that, together with the high-angle to bedding stylolites and oblique slickolites, crosscut the Mesozoic platform carbonates cropping out within the Southern Apennines fold-and-thrusts belt (Manniello et al., 2022, 2023). Focusing on bed-parallel, both interbed and intrabed wave-type pressure solution seams, they were interpreted as due to a sedimentary burial during diagenesis. Differently, the younger, intrabed seismogram-type stylolites were interpreted as either newly formed structures or reactivate, pre existing wavy-type stylolites, and due to the tectonic burial (cf. Ch 3.5) associated to the stacking of a thick shell of allochthonous thrust sheets (Patacca and Scandone, 2007; Palladino et al., 2023). High-angle to bedding stylolites and oblique slickolites formed, at different stages, during thrusting tectonics. Aiming at assessing the control exerted by solution surfaces on the pore space properties of specific carbonate lithofacies, we conduct microstructural and experimental laboratory analyses on selected samples collected away from meso-scale fault zones. The result of this work contribute to the better understanding the processes that govern the properties of the matrix during the exploration and production of carbonate reservoirs.

5.2 Geological setting

The study focuses on the Mesozoic platform carbonates cropping out at the Viggiano Mt, within the Southern Apennines fold-and-thrusts belt of Italy. Southern Apennines consist of a pile of thrust sheets emplaced since the late Oligocene – early Miocene, forming a multi-duplex structure due to the collision between the Adria-Apulian plate and the Eurasian plate (Patacca and Scandone, 2007; Vezzani et al., 2010). The compressional tectonic involved the sedimentary covers of the Adria-Apulian platform, represented by the basinal Liguride-Sicilide and Lagonegro units, and the shallow-water platform carbonates of the Apenninic Platform and of the Apulian Platform units. During the early Miocene, the basinal Liguride and Sicilide units started to overthrust the Apenninic Platform. Subsequently, during

Tortonian, the tectonic wedge overthrusted the already duplexed basinal Lagonegro units in an out-of-sequence thrust. The platform carbonates experienced a maximum burial depth of ca. 4 km during this period (Manniello et al., 2022). The whole tectonic wedge overrode the Apulian Platform due to mixed thin-skinned and thick-skinned tectonics (Menardi Nouguera and Rea, 2000; Shiner et al., 2004). The thrust front's migration steps were marked by the formation of several foredeep basins and thrust-top basins (Wortel and Spankman, 1992; Patacca et al., 1992; Palladino et al., 2008). Since late Pliocene, the contractional wedge was subjected to extensional tectonics, due to the concomitant action of the Tyrrhenian back-arc basin and the gravitational collapse of the contractional belt (Mostardini & Merlini, 1986; Hippolyte et al. 1995; Cello and Mazzoli, 1998; Doglioni et al., 1996; Giano et al. 2000; Scrocca et al., 2005; Vezzani et al., 2010; Bucci et al., 2012; Novellino et al., 2015). The belt was firstly dissected by low-angle normal faults, formed along pre-existing thrust faults due to gravity-driven reactivation (Mazzoli et al. 2006, 2014). During the Quaternary, the belt was dissected by high-angle transtensional faults.

The Viggiano Mt. is the easternmost outcropping portion of the Apenninic platform carbonates and is located in the High Agri Valley (Fig 1a), a tectonic, intra-montane basin in which fluvial-lacustrine sediments deposited during Quaternary bounded by high angle WNW-ESE and NE-SW high angle transtensional faults belonging to the East Agri Fault System (EAFS) (Figure 5. 1b). The carbonate massif lies on top of a buried, regional-scale thrust front that juxtaposes the Viggiano Mt. carbonates with the Lagonegro II Unit. Multiple WNW-ESE and NW-SW-striking, transtensional faults crosscut both the Viggiano MT. succession and the thrust, reaching the buried Lagonegro units. (Fig 1c, d, Palladino et al., 2023).

The lowermost portion of the Viggiano Mt. succession is characterized by Triassic dolostones, topped by Lower Jurassic limestones. The limestones include Pleinsbachian-aged wackestones, packstones, and grainstones initially deposited in a low-energy, lagoonal environment, informally labeled as “well-layered carbonates”, and by Toarcian oolithic grainstones, originally deposited in a carbonate ramp rimmed by sand shoals, characterized by higher energy, informally labeled as “oolithic carbonates” (Lechler et al., 2012; Manniello et al., 2022). The diagenetic evolution of the carbonates includes multiple phases of burial with episodes of cementation and pressure solution. The first cementation episode was not very pervasive and took place during Mesozoic early diagenesis, in a marine phreatic environment, where isopachous calcite cements started precipitating and likely determined early embrittlement (Todaro et al., *pers. comm.*). During this phase, pressure solution seams

nucleated within the lithifying carbonate rocks (Manniello et al., 2023). The second stage of pervasive cementation occurred as the burial increased, in a freshwater phreatic environment, with precipitation of blocky calcite types of cement that occluded the primary pore space (Todaro, *pers. comm.*). During this phase, the layered architecture of the carbonates started forming due to the formation of laterally continuous wave-type pressure solution seams (Manniello et al., 2023). A distinct burial episode took place later, during Miocene thrusting tectonics when the piling of allochthonous units determined a tectonic burial (ca. 4 km of depth) (Manniello et al., 2023; Todaro, *pers. comm.*). At this stage, the rock was yet pervasively cemented and intrabed seismogram-type, bed parallel stylolites formed pervasively through the carbonate succession due to the new loading conditions. Thrusting tectonics also played pivotal role in the structural evolution of those carbonates, determining the formation of a dense array of bed-perpendicular stylolites and bed-oblique slickolites that controlled the formation of intra-formational thrust faults (Manniello et al., 2023).

The highest portion of the Viggiano Mt. is characterized by Cretaceous (Albian-Cenomanian) limestones that include mainly carbonate grainstones, rudstones, boundstones, and sporadic mudstones originally deposited in a high-energy shelf environment close to the platform margin, informally labeled as “massive carbonates (Lechler et al., 2012; Manniello et al., 2022). This portion of the platform experienced a different diagenetic evolution; indeed, the grains were reworked in situ before being cemented by marine types of cement (Todaro., *pers. comm*.). Early Mesozoic burial was characterized by open moldic pores due to some primary intergranular pores that were still open and due to aragonite fossils that were being dissolved. Subsequently, during intermediate burial, most of those residual primary and moldic pores were pervasively cemented by blocky calcite cement types. Within this portion of the succession, the formation of bed parallel pressure solution seams and stylolites generally postdated the calcite cement precipitation (Todaro, *pers. comm.*).

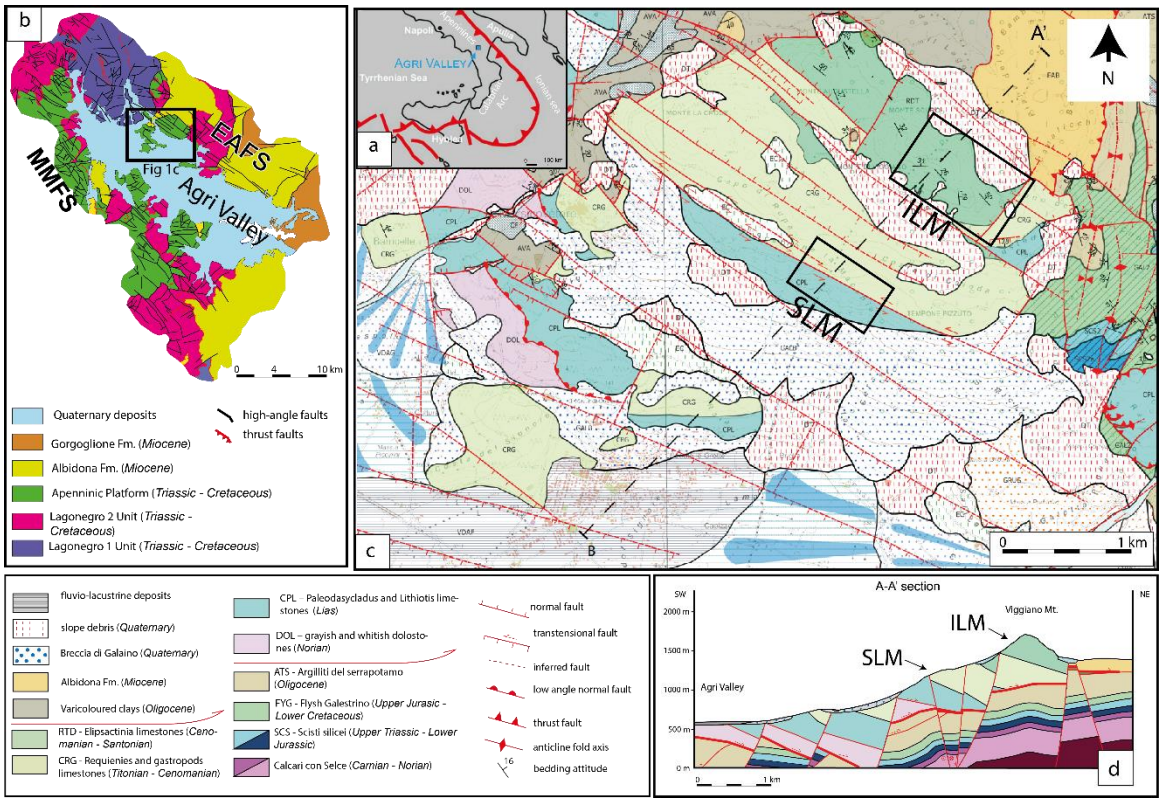

Figure 5. 1 Geological map of the study area. a) schematic map of the southern Apennines FTB, with the Agri Valley location. b) Structural map of the Agri Valley. c) Geological map of the Viggiano Mts. area (Palladino et al., personal communication), with the locations of the SLM (Scarrone la Macchia) and ILM (Il Monte) study sites. d) NE-SW trending geological cross-section of the Viggiano Mts. area.

5.3 Methods

In this work, we perform petrographic analyses, thin section 2D digital analyses, and NMR (Nuclear Magnetic Resonance) analyses of 21 carbonate rock samples collected at the Viggiano Mt., representative of the lower Jurassic and the Cretaceous carbonate succession. The sampling sites are located far away from large fault zones, to avoid as much as possible the extensional deformation and hence to better focus our attention on the pressure solution seams. The sampled rock volumes included both intra-bed and inter-bed solution surfaces (i.e., stylolites and pressure solution seams, from now on identified also as PS). We pay particular attention on the different morphologies that characterize the solution surfaces (according to what documented by Manniello et al., 2023). The lower Jurassic portion of the succession includess two informal stratigraphic units labelled respectively “well-layered” and “oolithic” carbonates. The well-layered carbonates samples are made up of mud-supported carbonates labelled *Yn* and grain-supported carbonated lithofacies labelled X*n*. The oolithic carbonates samples include exclusively oolithic, cemented grainstones labelled

as Z*n*. The Cretaceous succession includes a single informal stratigraphic unit labelled as “massive carbonates”, and the samples include grain-supported carbonates and bioclastic, matrix-supported carbonate grainstones labelled as J*n*, and coarse bioclastic rudstones and sedimentary breccia (labelled as L*n*).

The 2D pore properties of the carbonate rocks are deciphered by petrographic analysis of oriented thin sections obtained in the proximity of the cored plugs used for petrophysical analyses, and by digital analysis of selected 24x36 mm-wide images obtained using a “PathScanner Enabler 5 thin section scanner”. Samples for thin sections are impregnated with a blue epoxy under vacuum overnight, and then a total of 26, 26x39 mm, 30µm-thick, thin sections oriented perpendicularly to bedding are obtained. The “PathScanner Enabler 5 thin section scanner” allows to acquire the 85% of the thin section area (which is ca. 26x39 mm). The goal is to measure of the geometrical and dimensional properties of the pore space and the pore distribution within the thin section. For the purpose, we employed both GIMP and ImageJ softwares. GIMP allows to select and isolate, by a specific tool, the blue-dyed portions of the image, corresponding to the blue epoxy-saturated pore space. Subsequently, a black and white binary image is created, in which the pore space is represented in black, and the host rock is entirely white (Figure 5. 2a, b). ImageJ allows the execute the quantitative analysis on the pore space using "Particle Analysis” and “Fractal box count” commands value. We use the former command to compute the 2D porosity, that represents the percentage of area covered by pore space over the entire image, and the aspect ratio, that is the ratio between the longest axis and shortest axis of each pore (Figure 5. 2c). Using the latter tool, instead, we compute the Box-counting Dimension (D_0), obtained by superimposing a square grid on each binary image and then counting the boxes including at least one pore (filling frequency). The counting procedure is repeated, varying the size of grid boxes (2 to 1024). The number of boxes that contain pores is plotted versus the corresponding box size in a log-log plot. If the relation among the two parameters shows a good power-law correlation, the pore space distribution is fractal, and the angular coefficient of the best fit line represents the D_0 value (Figure 5. 2c, d) (Mandelbrot, 1985; Falconer, 2003).

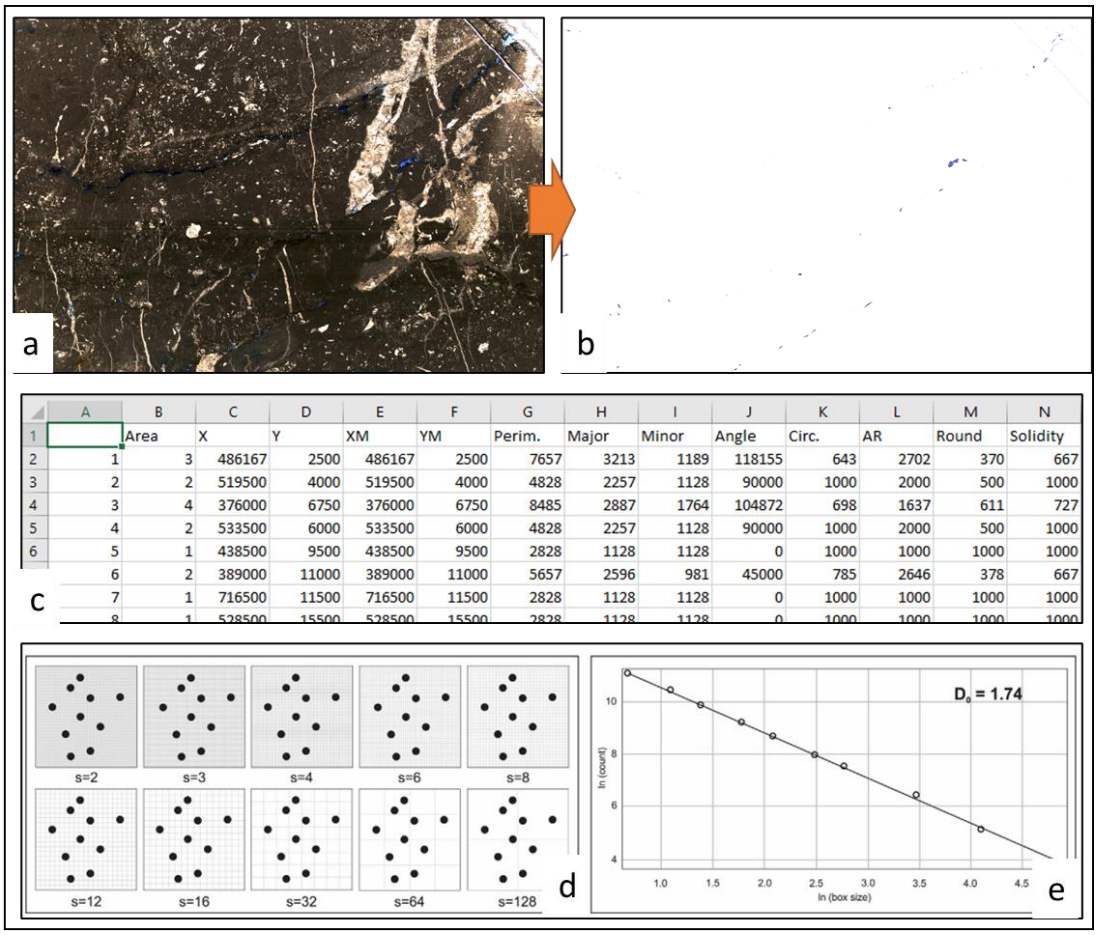

	A	B	C	D	E	F	G	H	I	J	K	L	M	N
1		Area	X	Y	XM	YM	Perim.	Major	Minor	Angle	Circ.	AR	Round	Solidity
2	1	3	486167	2500	486167	2500	7657	3213	1189	118155	643	2702	370	667
3	2	2	519500	4000	519500	4000	4828	2257	1128	90000	1000	2000	500	1000
4	3	4	376000	6750	376000	6750	8485	2887	1764	104872	698	1637	611	727
5	4	2	533500	6000	533500	6000	4828	2257	1128	90000	1000	2000	500	1000
6	5	1	438500	9500	438500	9500	2828	1128	1128	0	1000	1000	1000	1000
	6	2	389000	11000	389000	11000	5657	2596	981	45000	785	2646	378	667
	7	1	716500	11500	716500	11500	2828	1128	1128	0	1000	1000	1000	1000
	8	1	528500	15500	528500	15500	2828	1128	1128	0	1000	1000	1000	1000

Figure 5. 2 Example of 2D pore space analysis on a thin section scan. a), b) isolation of pore space; c) output of the 2D pore space analyses ; d) e) Box-counting dimension and D value calculation.

NMR (Nuclear Magnetic Resonance) analyses are carried out at the Laboratory of Physical Properties of Rocks (LPFR) in the Department of Geophysics (DGEF) of the Federal University of Rio Grande do Norte (UFRN). NMR data were obtained using the MesoMr12-060H-I (Niumag) equipment. The technique is based upon the resonance of the hydrogen nuclei in the water in an external magnetic field. For this reason, the samples need to be saturated with water. Specifically, the saturation process is made with water at 20,000 ppm of KCl in a vacuum, with a capacity of 60 cmHg, and with a water saturator operating at a pressure of 2,000 psi. After the saturation process, the mass (m_{sw}) of the sample is measured. In this process, it is possible to esimate the effective porosity using the Equation 1. The samples, then, are prepared for measurements in the NMR equipment and are wrapped individually in PTFE tape (Teflon) to avoid water drainage during the measurement.

$$\varphi = \frac{\frac{(m_{sw} - m) * 100}{0{,}99}}{V}$$

Equation 1 – Porosity via water saturation.

The equipment is calibrated using the FID (*free induction decay*) sequence to obtain the best central induction frequency. The relaxation times (T_2) are obtained using the CPMG[2] sequence (Carr-Purcell-Meiboom-Gill), and the distribution curves of T_2 are obtained by Laplace transform inversion, using the *Data Analysis* software provided by Niumag [TM], with 128 points and range from 0.01 to 10,000 milliseconds (ms). The profile for each plug is obtained following the sequence SE-SPI[3] (Spin-Echo Single-Point-Image), a sequence of pulses that intercalates the marking of the times T_1 and T_2. The measurement was performed in *slices* with thicknesses between 7.57 mm and 8 mm. From the distribution curve of T_2 is possible to estimate the distribution of pore sizes. The volumetric fraction of water associated with clay (*Clay Bound Water* - CBW[4]) can therefore be calculated in the sample, as the result of the area (A_{CBW}) of the curve lower than 3 ms (Figure 5.3), over the total area (A_{TOTAL}) of the curve, according to Equation 2:

$$CBW = {\sum A_{CBW}}/{\sum A_{TOTAL}}$$

Equation 2 – Associated volumetric fraction of water in clay.

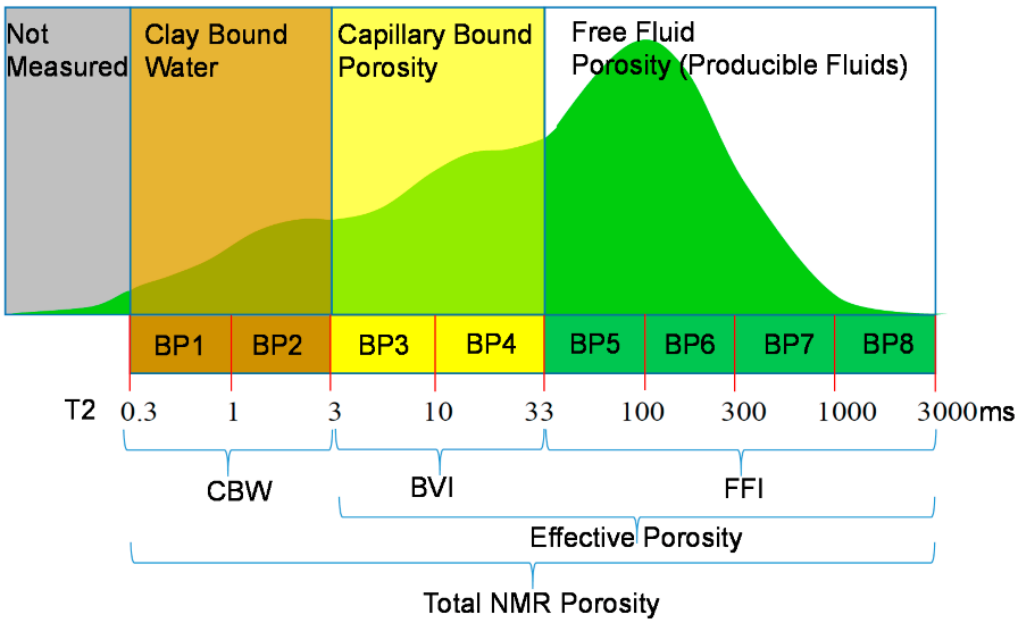

Figure 5. 3 T2 distribution and the limits used to determine the total and effective porosity, the clay bounded water, capillary bound porosity and free fluid.

5.4Results

5.4.1 Morphology of solution surfaces

According to their morphologies, the bed-parallel solution surfaces are classified as wave-type or seismogram-type (cf. Ch. 3.1, and as documented by Manniello et al., 2023, according to the classification proposed by Koehn et al., 2016). Differently, bed perpendicular stylolites and bed oblique slickolites are generally characterized by a seismogram-type morphology. The wave-type pressure solution seams are characterized by a smooth morphology, and often localize in between textural heterogeneities such as grain contacts (Figure 5. 4a, b, d, f), and at rock portions where there is a relative abundance of muddy matrix (Figure 5. 4c, e). Small-scale, high-angle open fractures and veins, when present, abut against the wave type, bed-parallel solution surfaces. Nonetheless, large open fractures and veins cut across them.

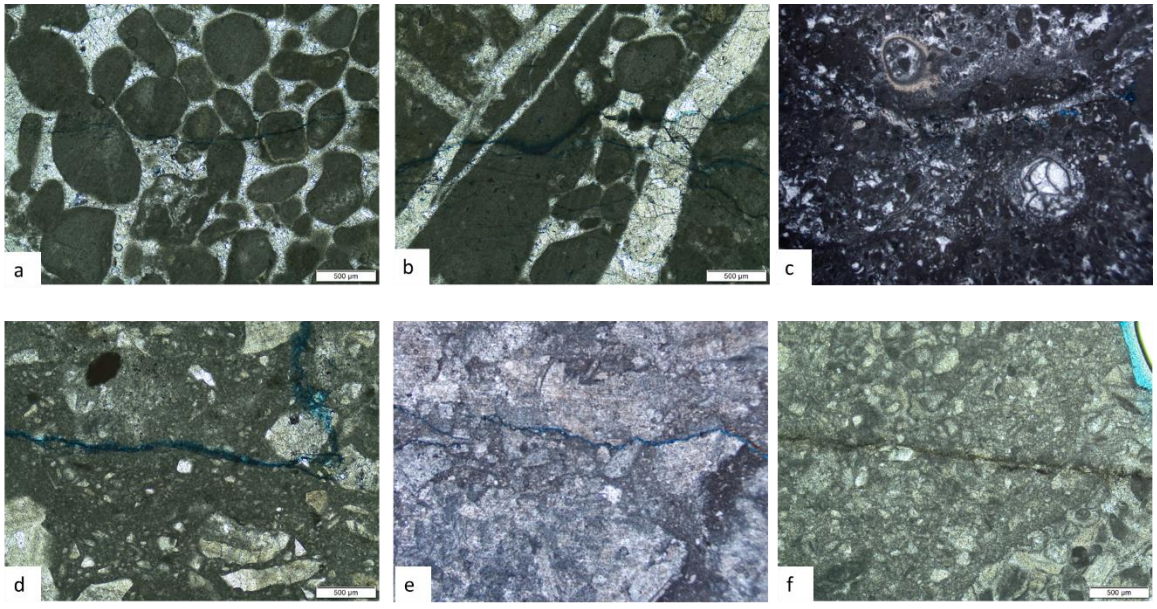

Figure 5. 4 Wave-type stylolites through the different lithofacies. a) Toarcian oolithic carbonates, b) Pleinsbachian grain-supported carbonates, c) Pleinsbachian mud-supported carbonates, d) Cretaceous sedimentary breccia, e)Cretaceous floatstone/rudstone; f) Cretaceous grainstone

The seismogram-type, bed parallel stylolites are characterized by a rough morphology, made up of sharp dissolution teeth (Figure 5. 5). In grain-supported limestones, these solution surfaces localize mainly at the grain contacts (Figure 5. 5a, d, f). In mud-supported limestones, these solution surfaces often include films of undissolved residual material. Regarding abutting and crosscutting relations with the high-angle open fracture and veins,

the seismogram-type solution surfaces consistently dissolve the high-angle structural heterogeneities (Figure 5. 5b, c, e).

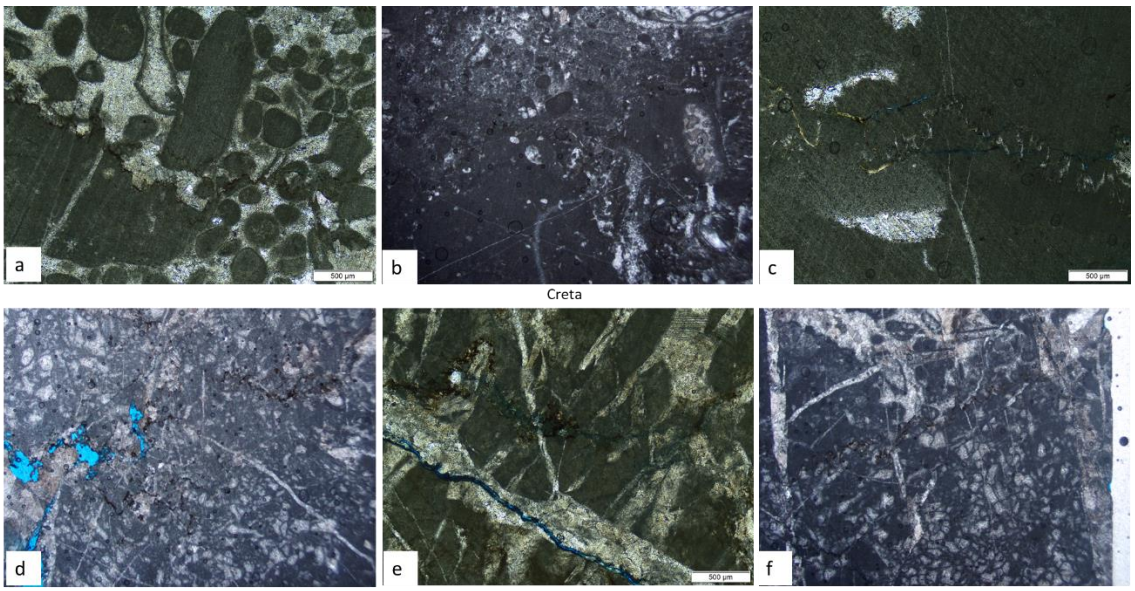

Figure 5. 5 Seismogram-type stylolites through the different lithofacies. a) Toarcian oolithic carbonates, b) Pleinsbachian grain-supported carbonates, c) Pleinsbachian mudstone, d) Cretaceous grainstone, e)Cretaceous floatstone/rudstone; f) Cretaceous grainstone

The oblique slickolites are also diffuse throughout the studied carbonate outcrops (Figure 5. 6). Particularly, the ones characterized by sub-horizontal teeth, which are oblique to the slickolite, are characterized by cut-off angle up to 65° and abut against the bed parallel solution surfaces. We note that in grain-supported limestones, these slickolites might localize along the grains border and at the grain contacts (Figure 5. 6a, b, e, f). In the mud-supported limestones, we often note small-scale linkage zones that often involve high-angle stylolites (Figure 5. 6c, e). The oblique slickolites characterized by sub-vertical teeth, differently form very low cut-off angles with the bedding, up to 25°-30°. These slickolites are diffuse through the entire succession and dissolve all the high-angle and oblique structural heterogeneities. We also note that oblique slickolites with sub-horizontal teeth may include films of undissolved, clayish residual material (Figure 5. 6d).

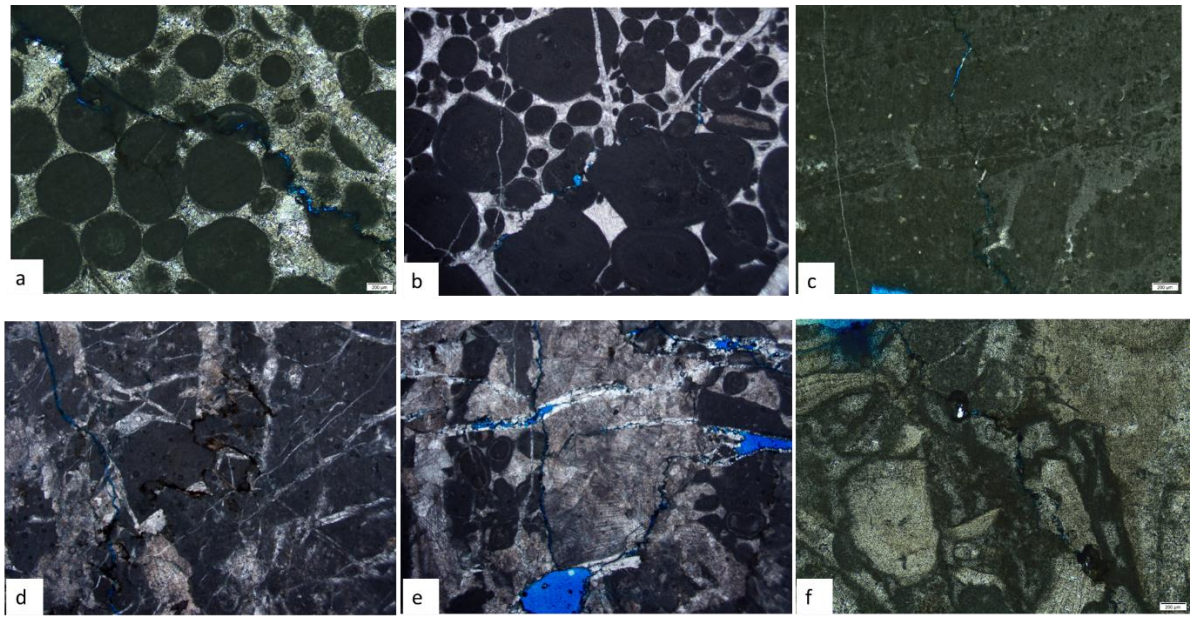

Figure 5. 6 Oblique slickolites through the different lithofacies. a) Toarcian oolithic carbonates, b) Pleinsbachian grainstone, c) Pleinsbachian mudstone, d) Cretaceous mudstone, e) Cretaceous floatstone; f) Cretaceous rudstone

5.4.2 Pore space along solution surfaces

Petrographic analyses are aimed at the qualitative description of the pore space according to the classification proposed by Lucia (2007), while 2D digital image analyses are aimed at the quantitative description of pore space in term of percentage of area, shape and distribution. At a thin section scale, the pore space is displayed by blue-dyed epoxy resin. From a qualitative point of view, the porosity of the lower Jurassic mud-supported and grain-supported limestones is mainly associated to solution-enlarged bed-parallel stylolites/pressure solution seams and bed-oblique slickolites. The bed-parallel solution interfaces are often associated with poorly connected/separated vug pores (Figure 5. 7). However, the wave-type surfaces in some cases form a very tight channeled porosity, which is displayed by the laterally continuous blue epoxy saturation (Figure 5. 7a, b). We note that these cases often occur in the presence of re-opened and subsequently partially mineralized bed parallel structures (Figure 5. 7a). The seismogram-type surfaces localize voids along the side walls of the single dissolution teeth (Figure 5. 7c), producing isolated vugs. Microfractures are likely to occur near the seismogram-type stylolites, significantly increasing the overall porosity, and also promoting the connectivity among pores, and forming a channeled porosity (Figure 5. 7d). Within grain-supported carbonate lithofacies, euhedral blocky calcite cement type is very common and pervasive (Manniello et al., 2023;

Todaro et al., pers. comm.) and within the cemented portions we also document intercrystal microporosity as shown in Figure 5. 7 a,b.

In the Cretaceous rocks, the porosity is due to the presence of intra-fossil moldic porosity, solution-enlarged bed-parallel and bed perpendicular stylolites/pressure solution seams, and bed-oblique slickolites, the carbonate grainstones and rudstones often include wave-type, bed-parallel pressure solutions seams, oblique slickolites, and high-angle to bedding microfractures which generally do not localize significant amounts of effective porosity (Figure 5. 8a, b). Enlarged solution surfaces that form a localized channel porosity do exist but are sporadic (Figure 5. 8e). Differently, the bed-parallel, seismogram-type surfaces are the main structures that can localize porosity in the form of vuggy pore space (Figure 5. 8c), similarly to what is documented in the lower Jurassic limestones. Within these rocks, significant amounts of porosity is represented by, intrafossil voids forming moldic porosity (Fig 8d), and intercrystal pores (Figure 5. 8f) in which the pore space sometimes exceeds the single crystal dimensions.

The 2D pore space characterization is obtained by means of digital analysis of 24x36 mm-wide images selected from the study thin sections. Aiming at deciphering the amount of porosity due to diagenetic and tectonic solution surfaces, we avoided highly fractured and faulted rock portions. The results of 2D pore analysis are summarized in Table 4. The 2D porosity values (% of thin section area) vary between 0.1% (lower Jurassic, mud-supported limestones) and 4.5% (Cretaceous carbonate rudstones). Considering all measurements (n= 18), the mean 2D porosity value is 1.09%, the median value is 0.59%, and the standard deviation is 1.18%. The computed circularity values of single pores vary between 0.85 and 0.96. The mean value is 0.89, the median value is 0.88, and the standard deviation is 0.03. The mean aspect ratio value of the pore space ranges from 1.41 (lower Jurassic, grain-supported limestones) and 1.76 (lower Jurassic, oolithic carbonate grainstones). Considering the different pore types associated with the structural elements that crosscut the studied carbonates, we calculate the aspect ratio of pores and determined a range of values representative of the pore type. In the Lower Jurassic carbonate grainstones, we noted that the aspect ratio of pores associated to oblique slickolites and high angle microfractures often exceeds the value of 2. Remarkably, within these rocks, the aspect ratio of the pores related to microfractures varies between 2 and 10. Differently, the intercrystal micropores are associated with aspect ratio values close to 1. The pores associated to the bed parallel stylolites are often characterized by aspect ratio values varying between 1 and 1.9. In the Lower Jurassic mud-supported carbonate lithofacies, the pores due to microfractures are

characterized by aspect ratio values between 2 and 9.5. In those pores are also included the bed-parallel, enlarged wave type structures. The generally isolated pores associated with bed-parallel seismogram-type solution surfaces are close to 1.5. In the Lower Jurassic oolithic grainstones we note the presence of diffuse, intracrystal micropores with aspect ratios close to 1, of microfractures with aspect ratios varying between 2 and 12.3, and of pores associated mainly to oblique slickolites and occasionally to bed parallel stylolites with aspect ratios ranging between 1.2 and 1.9.

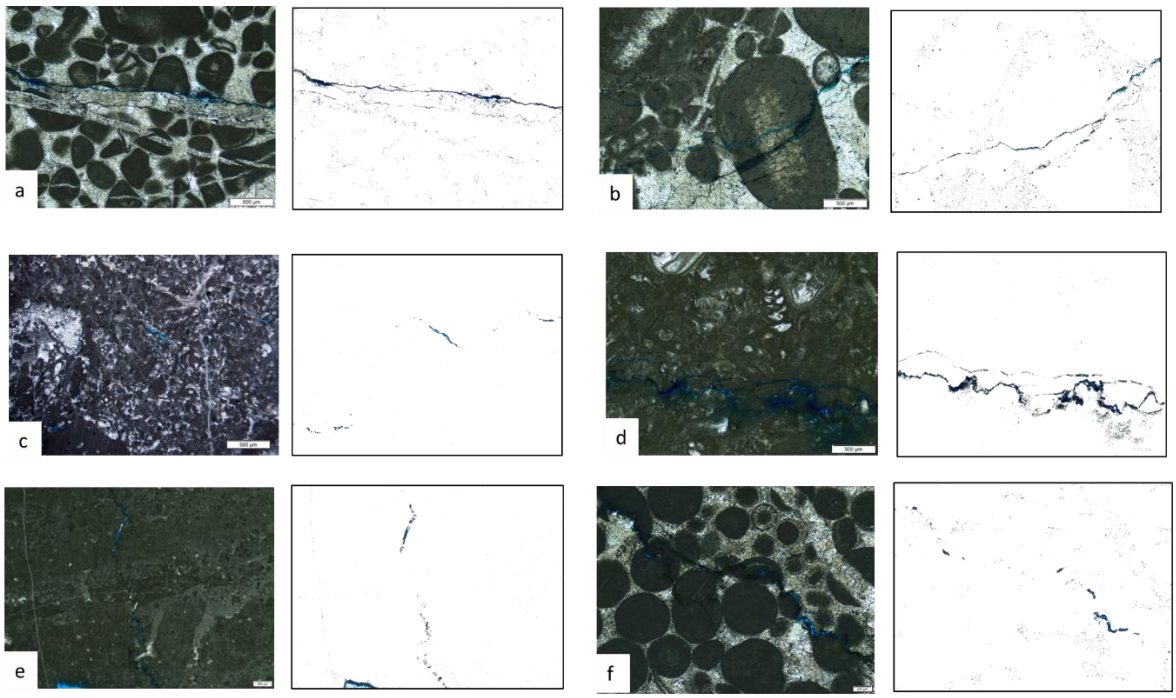

Figure 5. 7 Representative pore space associated to the different stylolites morphologies through Lower Jurassic carbonates. a), b) Wave type; c), d) seismogram type; e) high angle pressure solution seams; f) oblique slickolites.

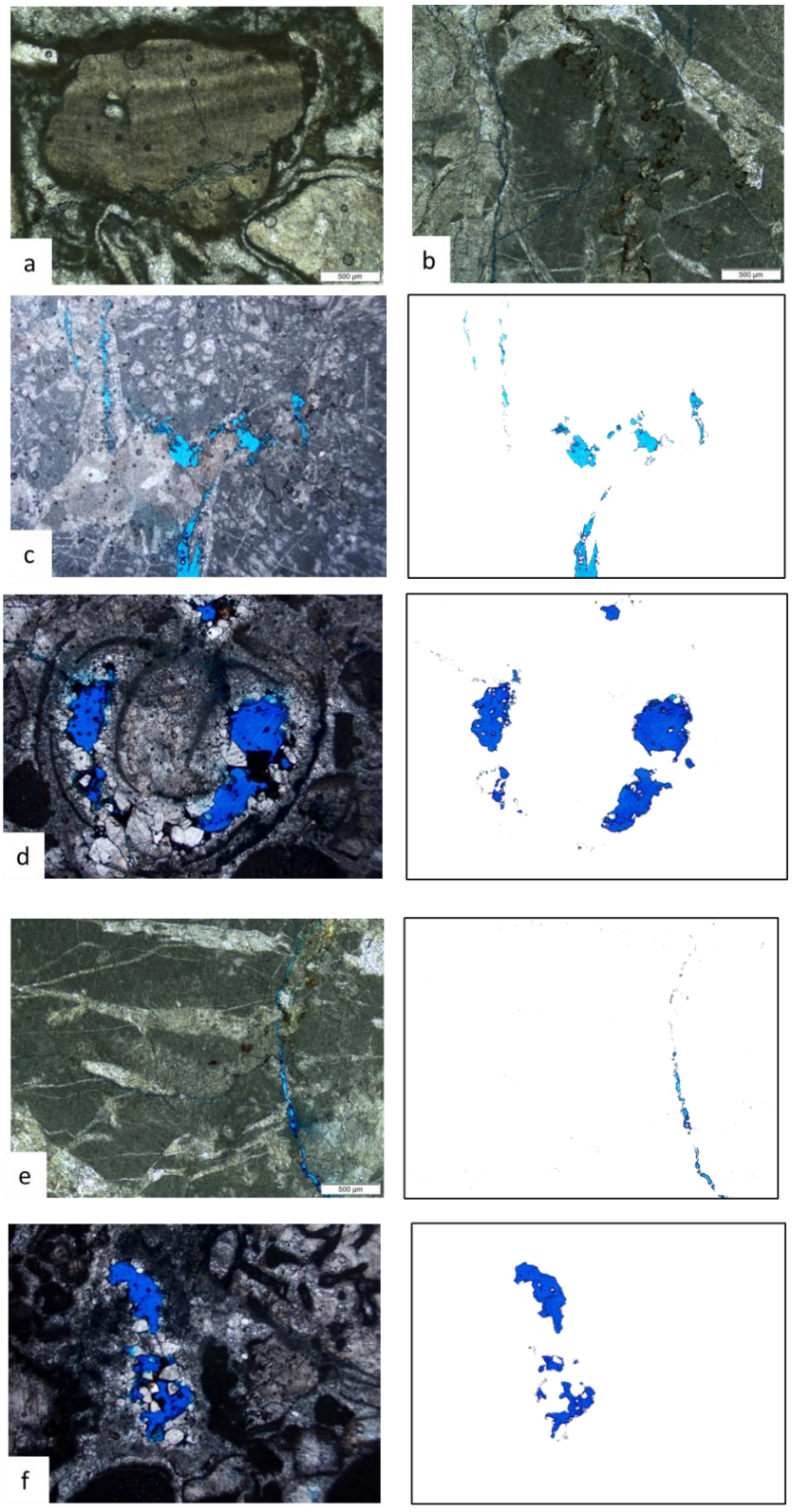

Figure 5. 8 Representative pore space within Cretaceous carbonates. a) b) bed parallel wave type styolites with no pore space; c) seismogram type stylolites; d) intrafossil molds; e) high angle pressure solution seams; f)intrecrystal molds.

Table 4 results of the 2D digital analysis.

Thin section	Unit/Age	Lithofacies	2D porosity (%)	2D porosity reduct. (AR>=2)	Mean Aspect ratio	D0(pores)
X1	well-layered carbonates/lower Jurassic	grain-supported carbonates	0.27	0.12	1.408	1.1813
X2	well-layered carbonates/lower Jurassic	grain-supported carbonates	1.049	0.83	1.466	1.3982
X3	well-layered carbonates/lower Jurassic	grain-supported carbonates	0.68	0.05	1.466	1.1235
X4	well-layered carbonates/lower Jurassic	grain-supported carbonates	0.637	0.04	1.548	1.3176
Y2	well-layered carbonates/lower Jurassic	mud-supported carbonates	0.171	0.14	1.531	1.1084
Y3	well-layered carbonates/lower Jurassic	mud-supported carbonates	2.275	2	1.661	1.3322
Y4	well-layered carbonates/lower Jurassic	mud-supported carbonates	0.322	0.52	1.575	1.3553
Y5	well-layered carbonates/lower Jurassic	mud-supported carbonates	0.111	0.78	1.439	0.6867
Z2	Oolithic carbonates/lower Jurassic	oolithic grainstones	0.423	0.3	1.764	1.151
Z3	Oolithic carbonates/lower Jurassic	oolithic grainstones	0.402	0.3	1.491	1.0863
Z4	Oolithic carbonates/lower Jurassic	oolithic grainstones	2.016	0.28	1.497	1.3484
Z5	Oolithic carbonates/lower Jurassic	oolithic grainstones	0.139	0.08	1.558	1.1165
J1	Massive carbonates/Cretaceous	rudstone	4.159	3.78	1.466	1.4524
J2b	Massive carbonates/Cretaceous	grain-supported carbonates	2.072	0.25	1.531	1.3352
L1	Massive carbonates/Cretaceous	boundstone	2.644	0.27	1.551	1.4336
L2	Massive carbonates/Cretaceous	boundstone	0.541	0.46	1.603	1.0441
L4	Massive carbonates/Cretaceous	boundstone	0.298	0.17	1.589	1.0464
L5	Massive carbonates/Cretaceous	boundstone	0.964	0.44	1.632	1.3377

5.4.3 NMR analyses

For all samples, virtually no water content corresponds to the FFI fraction (Figure 5. 10). Table 5 shows the data obtained by the SE-SPI sequence, showing the porosity and CBW value for each slice in the samples. In Figure 5. 9, we observed the graphs of the amplitude of the signal within the single slice versus relaxation time T_2 for each one of the analyzed samples. To each one of the relaxation time graphs there are associated the pore space distribution graph and the pore throath distribution graph. The main peaks of signal measured in the lithofacies of the Cretaceous carbonates are generally enclosed in the region of the graph with T_2>33ms, corresponding to the effective porosity. Secondary peaks are displayed in the region of the graph with 3ms<T_2<33ms, meaning that part of the porosity is due to capillary porosity. Specifically, the resulting pore space distributions (i.e. the distribution of the radius of the sphere that approximate the pore volume), estimated upon the relaxation time decay, show multi-modal distributions, in which the majority of pores are characterized by radius values ranging between 1 and 10 µm. The secondary peaks are associated to radius values <1µm. The corresponding pore throat (the radius of the circumference that approximate the section of the narrowest pore space where two larger pores meet) distributions generally vary accordingly, suggesting that the pore connectivity is guaranteed by conduits characterized by a section comparable in size with the average cavities. We also note that within the pore throat distributions high peaks are localized at values <2µm, suggesting that capillary conduits are also present and play a significant role in pore connectivity. In the Lower Jurassic carbonates, the main peaks of signal are measured within the region of 3ms<T_2<40ms, with minor peaks at T_2>40ms. The corresponding pore space distributions are generally characterized by tri-modal and quadri-modal distributions. Within the oolithic carbonates, the majority of pores are characterized by radius values of 0.01 µm, and between 0.1 µm and 1 µm, typical of capillary porosity. Minor clusters of data are observed at 1 µm <r<10 µm. Accordingly, the pore throat distributions show that the majority of values are <1 µm. Similarly, within the well layered carbonates, the pore space distribution shows greater peaks at r=0.01 µm, at r=0.1 µm, and at r=1 µm, with minor peaks at r=10 µm. The pore throat distribution varies accordingly, with the majority of the data clustered at r<2 µm (Figure 5. 10). The different lithofacies that characterize the Lower Jurassic carbonates do not play a significant role in pore space and pore throat distribution.

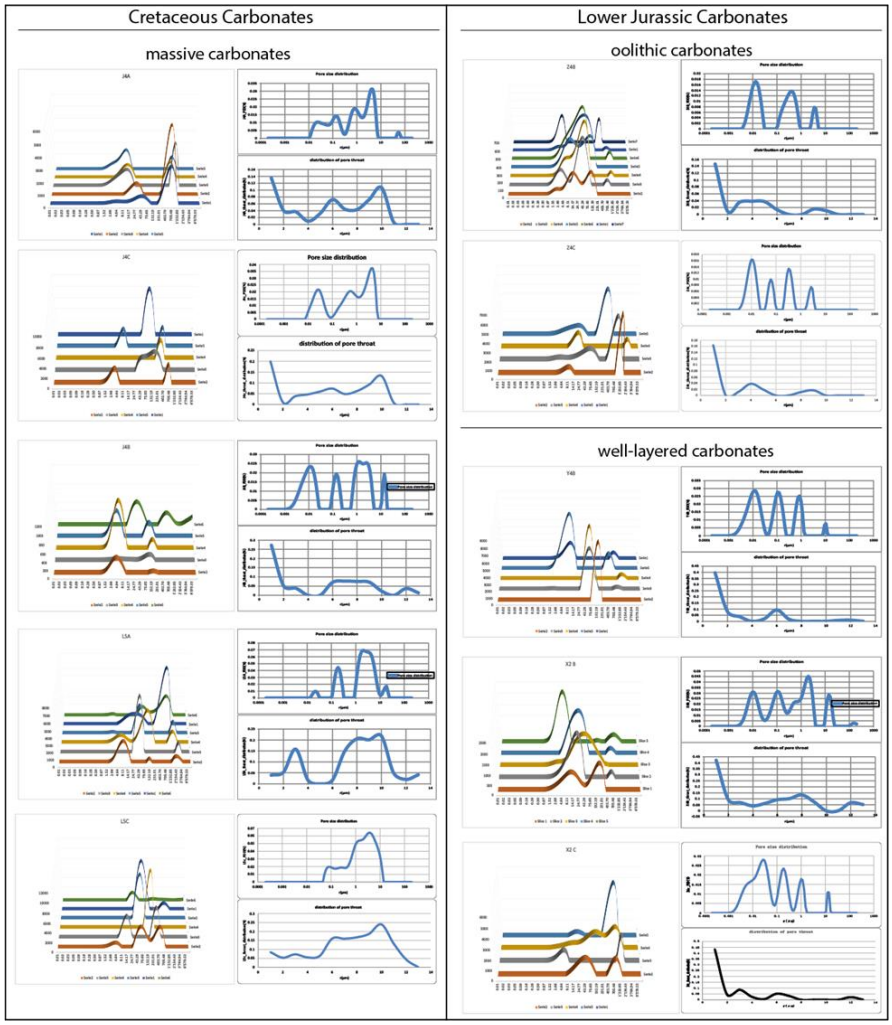

Figure 5. 9 Graphs of the T2 distribution along the slices following the SE-SPI sequence the analyzed samples, and relative pore size distribution and pore throat distribution.

Table 5 porosity and CBW value for each slice within the analyzed samples.

J3A	Slice 1	Slice 2	Slice 3	Slice 4	Slice 5		
Porosity	0,47	0,66	0,61	0,75	0,43		
CBW (%)	0,00	9,21	3,78	0,00	2,75		
J4A	Slice 1	Slice 2	Slice 3	Slice 4	Slice 5		
Porosity	0,30	0,25	0,47	0,84	0,58		
CBW (%)	8,04	0,00	4,33	0,00	1,14		
J4B	Slice 1	Slice 2	Slice 3	Slice 4	Slice 5		
Porosity	1,18	0,51	0,60	0,30	0,33		
CBW (%)	0,00	17,24	12,04	3,51	22,04		
J4C	Slice 1	Slice 2	Slice 3	Slice 4	Slice 5		

Porosity	0,98	0,42	0,43	0,89	0,36		
CBW (%)	0,00	0,00	0,00	0,00	21,17		
L5A	Slice 1	Slice 2	Slice 3	Slice 4	Slice 5	Slice 6	
Porosity	0,86	1,81	0,65	1,17	0,96	0,39	
CBW (%)	1,86	0,00	1,71	1,73	0,00	1,85	
L5B	Slice 1	Slice 2	Slice 3	Slice 4			
Porosity	0,61	0,64	0,66	0,64			
CBW (%)	0,00	4,54	0,00	15,01			
L5C	Slice 1	Slice 2	Slice 3	Slice 4	Slice 5	Slice 6	
Porosity	0,28	1,73	1,20	1,30	1,11	1,49	
CBW (%)	0,00	0,00	0,00	0,00	0,00	2,15	
X2B	Slice 1	Slice 2	Slice 3	Slice 4	Slice 5		
Porosity	0,49	0,65	0,74	0,52	0,59		
CBW (%)	16,26	0,00	1,97	1,57	3,44		
X4C	Slice 1	Slice 2	Slice 3	Slice 4			
Porosity	0,70	0,75	0,21	0,44			
CBW (%)	0,00	0,86	7,08	0,00			
X4B	Slice 1	Slice 2	Slice 3	Slice 4	Slice 5		
Porosity	0,56	0,66	0,69	0,68	0,44		
CBW (%)	7,82	4,83	5,66	0,69	8,47		
Y22	Slice 1	Slice 2	Slice 3	Slice 4	Slice 5		
Porosity	0,36	1,07	1,04	0,40	0,80		
CBW (%)	35,87	10,45	0,00	0,00	0,00		
Y4B	Slice 1	Slice 2	Slice 3	Slice 4	Slice 5		
Porosity	0,23	0,68	0,56	0,63	0,57		
CBW (%)	1,84	4,34	0,00	0,77	0,00		
Z33	Slice 1	Slice 2	Slice 3				
Porosity	0,12	0,30	0,22				
CBW (%)	11,29	0,00	18,22				
Z4A	Slice 1	Slice 2	Slice 3	Slice 4			
Porosity	0,20	0,25	0,07	0,38			
CBW (%)	0,00	0,00	20,18	0,00			

Z4B	Slice 1	Slice 2	Slice 3	Slice 4	Slice 5	Slice 6	Slice 7
Porosity	0,13	0,29	0,32	0,27	0,31	0,28	0,27
CBW (%)	20,75	2,72	2,44	2,43	1,92	8,57	6,06
Z4C	Slice 1	Slice 2	Slice 3	Slice 4			
Porosity	0,28	0,06	0,28	0,15			
CBW (%)	0,94	0,00	1,46	0,07			

5.5 Preliminary discussion and conclusions

The Lower Jurassic and the Cretaceous carbonates show dissimilar characteristics of the pore space, whose main properties can be summarized as follows in light of the study lithofacies:

- the primary pores, mainly sub-circular in shape after 2D analysis, was completely occluded by pervasive cementation of blocky calcite within the Lower Jurassic oolithic and well-layered carbonates;
- all Lower Jurassic carbonates show a present-day pore space that localize along bed-parallel and low-angle stylolites, pressure solution seams and slickolites, and along the high-angle microfractures forming the greatest amount of secondary porosity;
- the Cretaceous massive carbonates, the amount of porosity associated to pressure solution-related features and microfractures form a negligible amount of porosity due to perveasive remnants of large intrafossil and intercystal moldic porosity.

Different types of stylolites, pressure solution seams and slickolites classified according to their morphology (Park and Schot, 1968; Koehn et al., 2016). The wave-type stylolites, formed during an early burial stages, in which the chemical-physical compaction was predominant. During this stage, the compaction determined the obliteration of primary porosity (Ehrenberg, 2006; Rustichelli et al., 2015, Manniello et al. 2023). Differently, the seismogram-type pressure solution seams can localize porosity, suggesting that also the roughness itself may play a significant role in the circulation of dissolving fluids. The pore space properties associated to the different structures are the following:

- wavy-type stylolites documented within the studied carbonates are very tight and localize negligible amounts of pore space;

- rough seismogram type styloites can localize poorly connected, sub-circular to tubular pores along the spike flanks.
- the pore size is slightly larger within the grain supported carbonate lithofacies, due to larger dissolution teeth.
- microfractures determines the presence of channeled porosity.

Indeed, it has been documented that very smooth, wave-type generally act as barriers for fluid flow. On the contrary, rougher, seismogram-type stylolites may facilitate the circulation of dissolving fluids, especially across spike flanks (Koehn et al., 2016; Toussaint et al., 2018; Zhou et al. 2022).

Based on the petrographic observations, we determined a threshold value for the aspect ratio of pores, that is approximately 2, that subdivides the seismogram type stylolite-related pores and the fracture-related pores. In the lower Jurassic carbonates, our data show that the porosity associated to microfractures represent less than the 30% of the total porosity. This evidence is consistent with the NMR results, in which the fracture pore space is generally represented by the shortest peaks at r>1 μm. These pores are also characterized by small pore throat values (r<3 μm) due to their high aspect ratio. This evidence suggests that in the Lower Jurassic carbonates the porosity is mainly controlled by seismogram type stylolites, but fractures are more likely to enhance pore connectivity. In the Cretaceous carbonates the fracture porosity varies between 45% and 25%, and the remaining amount is due to both seismogram type stylolites and moldic porosity. The NMR analyses show that the seismogram type styolites do not localize significant amounts of pore space (r<1 μm). There, the majority of the pore space is associated to molds and fractures (r>1 μm). Focusing on the pore throat, we note that the pore connectivity depends essentially by large conduits, likely associated to connected large molds, and only occasionally by small conduits, such as fractures. We conclude, that in Cretaceous carbonates the presence of sparse large molds due to the presence of large fossils and intercrystal pores, may be a primary control factor on porosity as displayed by the blue epoxy, and fractures and stylolites operate a minor role, especially within rudstones and floatstones. The quantitative pore space analyses showed that:

- within the Lower Jurassic carbonates, the porosity is mainly controlled by stylolites and secondarily by fractures (that represent no more than the 30% of 2D total porosity);

- the porosity associated to stylolites, within lower Jurassic carbonates, is generally associate to capillary porosity (sub-rounded/sub-spherical to tubular pores characterized by very small pore throat values);
- within Cretaceous carbonates, the porosity is mainly controlled by intrafossil and intercrystal molds, due to their dimensions, even if not very pervasively diffuse (up to 45% of total porosity is associate to moldic porosity);
- in all study rocks, the open fractures form minor amounts of porosity. However, due to their geometry they can significantly control pore connectivity, also among molds (channeled porosity, often localized nearby the dissolution teeth of stylolites).

Our results show that the control exerted by pressure solution on porosity localization is strongly dependent on the carbonate lithofacies and on the specific diagenetic processes. Specifically, the stylolites may become a controlling factor in porosity localization, a) according to their roughness and b) in rocks where the primary porosity destruction due to phisical-chemical compaction was particularly pervasive. These findings may be helpful to develop a predicting tool based on stylolites roughness for the production/storage of fluids from tight cemented platform carbonates.

CHAPTER 6 - CONCLUSIONS

Aiming at gaining new insights into the geological processes associated to pressure solution in shallow-water carbonates made up of limestone rocks with low values of primary porosity, the main goals of the research work carried out in the last three years of activity were the following:

(1) Deciphering the role of the depositional architecture on fracture compartmentalization far away from main fault zones (Chapter 2).
(2) Diagenetic evolution of the different carbonate lithofacies with respect to the main pressure solution processes platform (Chapter 3).
(3) Role of pressure solution processes in the time-dependent evolution of fracture stratigraphy due to bed-parallel and low-angle to bedding mechanical interfaces (Chapter 4).
(4) Assessing the control of the pervasive pressure solution processes on the present-day pore space properties (Chapter 5 and Appendix).

The research work was mainly conducted on the Mesozoic platform carbonates cropping out at the Viggiano Mt., which flanks the eastern side of the Agri Valley along the axial zone of the southern Apennines fold-and-thrust belt of Italy. Specifically, the present Thesis

The research work was conducted on alternations of mud-supported and grain-supported beds organized in 10's of cm-thick and a few m-thick bed-packages respectively separated by cm-thick and several cm-thick, laterally continuous, clay-rich interfaces (well-layered sedimentary unit of Sinemurian-Pleinsbachian in age), oolithic, grain-supported bed-packages with amalgamated, m-thick beds (oolithic sedimentary unit, Toarcian in age) and massive limestone beds made of rudstones, grainstones, packstones, and mud-supported carbonates also characterized by pervasive bed amalgamation (massive sedimentary unit, Cenomanian in age). Overall, these three sedimentary units were originally respectively deposited in low-water energy, inner lagoonal environments (Sinemurian-Pleinsbachian), ramps rimmed by sand shoals (Toarcian), and high-water energy environments close to the paleo-platform margin (Cenomanian).

Focusing on the high angle facture network, the present-day fracture density and intensity properties derive from Meso-Cenozoic sedimentary burial, late Oligocene - Miocene thrusting, and Plio-Quaternary dissection of the fold-and-thrust belt and associated carbonate uplift and exhumation from depth of ca. 4 km. Both fracture density and intensity vary as function of single carbonate lithofacies, and of the presence of clayish bed and bed-package interfaces. In fact, throughout all the studied litho-stratigraphic successions, the higher values of 2D fracture density and intensity were documented within the coarser-grained, grain-supported carbonate beds. These results led to the conclusion that the laterally continuous bed-parallel mechanical interfaces (Sinemurian-Pleinsbachian) determined an original fracture compartmentalization within single mechanical units that consisted on individual bed and bed-packages, and the subsequent control on the vertical growth by linkage of the sheared, high-angle, pre-existing fractures during the multi-phase tectonic activity, and associated localized dilation at their extensional quadrants and within releasing jogs that localized in correspondence of the aforementioned mechanical interfaces.

Focusing on the diagenetic history of the carbonates, the results presented showed that the chemical-physical compaction of the original carbonate sediments started during very early diagenetic stages with calcite cement precipitation at marine phreatic conditions, determining early embrittlement. The cementation processes then continued during sedimentary burial of the carbonates with calcite precipitation under freshwater vadose and marine conditions. Specifically, during this diagenetic stage the Cretaceous carbonates lasted for a longer time at the water-sediment interface with respect to the lagoonal/ramp lower Jurassic carbonates. The latter process was definitely pervasive within the carbonates, with formation of blocky calcite cements that tightened the rocks and determined the mechanical properties of the single carbonate lithofacies. During this diagenetic history of the carbonates, the bed-parallel mechanical interfaces were continuously affected by pressure solution processes, which also occurred within the single carbonate beds, localizing at the grain contacts, and then developed during burial diagenesis forming cm-to-dm long, laterally continuous, wavy type solution surfaces. Differently, pressure solution localized at the bed and bed-package interfaces forming bundles of anastomosing stylolites within the carbonate lithons encompassed by clay-rich matrices.

Studying the pressure solution processes that took place during Miocene thrusting tectonics, the carbonates were involved into compressional stress regimes that caused the activity of regional scale thrust faults characterized by top to E and NE sense of shear, and the tectonic

override of the carbonate onto the basinal sequences of the Lagonegro I and Lagonegro II tectonic units. In the present Thesis Dissertation it was documented that the localization of shear strain along the bed and bed-package interfaces, with formation of 100s' of m-long, bed-parallel shear zones characterized by S-C-C' like fabrics with top to ca. NW sense of shear, and of bed-oblique slickolites with sub-horizontal teeth within the single carbonate beds, which promoted the linkage among the intra-bed, bed-parallel wavy-type solution surfaces, nucleation of bed-parallel veins that formed resulting in ca. NW-verging reverse faults. Altogether, both bed-parallel and low-angle to bedding shear elements composed intra-formational back thrust faults characterized by flat-ramp-flat geometries. These processes occurred at depth down to ca. 4 km, as inferred after XRPD analyses of the clay minerals sampled from the clay-rich bed-package interfaces of the Pleinsbachian-Sinemurian carbonates. These minerals showed a thermal maturity of ca. 100-130 °C, which was therefore compatible with a maximum burial of ca. 4 km according to ca. 20-25 °C/km thermal gradients commonly documented in orogenic wedges. At those conditions, during tectonic burial of the Mesozoic carbonates, a new generation of seismogram-type, bed parallel stylolites formed together with a generation of low-angle to bedding slickolites with sub-vertical teeth. These structural elements crosscut all previous contractional, shearing and opening-mode elements, forming a new mechanical layering of the carbonate rocks due to their later extent and pervasiveness.

After the burial diagenesis, the carbonates were involved in thrusting tectonics, with a first stage of layer parallel shortening occurred. Then, with incorporation of the carbonates in the tectonic wedge, intra-bed, oblique slickolites, started forming and also localizing at the intra bed, bed-parallel structural elements, bed interfaces and bed package interfaces. As a result of the linkage of those strucutres, NW- verging thrust faults formed. At the same time, some of the the bed-parallel interfaces formed the bed-parallel shear zones. With the reaching of the maximum tectonic burial, there formed the seismogram-type stylolites.

The chemical-physical compaction and cementation determined a complete obliteration of the primary porosity within the studied lithofacies. Far away from large fault zones, the matrix porosity is comprised between 2% and 5%, and those values are widely associated to the presence of stylolites. Specifically, within the Lower Jurassic carbonates, the porosity is mainly controlled by stylolites, that form mostly capillary porosity, and secondarily by fractures, as shown by the NMR results. Within Cretaceous carbonates, the porosity is mainly controlled by intrafossil and intercrystal molds, due to their dimensions. In all study

rocks, the open fractures form minor amounts of porosity. However, due to their geometry they can significantly control pore connectivity (channeled porosity, often localized nearby the dissolution teeth of stylolites). Wavy-type stylolites are generally very tight and localize negligible amounts of pore space. Differently, the seismogram type stylolites and oblique slickolites, characterized by a rougher porosity, can localize sub-circular to tubular pores along the flanks of the dissolution teeth. The resulting pore size is slightly larger within the grain supported carbonate lithofacies, due to larger dissolution teeth.

Preliminary results deriving from porosity and permeability measurements conducted at room pressure by means of gas as a circulating fluid showed that the poro/perm relation along the bed-perpendicular direction is consistently not linear in all studied carbonate lithofacies consistent with a poorly connected system. On-going activites related to bed-parallel and bed-perpendicular permeability measurements conducted at increasing effective pressure, will likely help to better assess the role exerted by bed-parallel solution surfaces on the 3D permeability properties of the studied carbonate lithofaacies. In fact, aiming at excluding the role of open fractures during permeability measurements due to their high aspect ratio, which will cause their closure at increasing confining pressures (soft porosity), the control exerted by the low aspect ratio pores that localize within the solution surface, mainly seismogram-type stylolites (stiff porosity) will be deciphered. The preliminary results show that, within the samples that include open fractures, the permeability decreases up to a threshold value around 15-20 MPa of effective pressure, and beyond this value the permeability remains almost constant. This preliminary evidence suggests that the effect of microfractures on pore connectivity is limited at relatively shallow depths (<1 km). Current laboratory activites will then hopefully help to decipher the shape and magnitude of the 3D permeability ellipsoids for the individual carbonate lithofacies subjected to pressure solution processes.

According to the main outcomes of the present PhD Thesis dissertation reported above, the following unsolved issues remain to be investigated, and hopefully will provide research topics in the near future for a deeper understanding of the fracture stratigraphy properties of the studied Mesozoic carbonate successions:

- A better knowledge of the Plio-Quaternary tectonic-structural evolution of the studied area of the Agri Valley Basin is required. In this work, new structural elements associated to burial diagenesis (both sedimentary and tectonic) and thrusting tectonics were documented for the studied rocks. These elements were not

previously reported in the literature, and hence improved the current understanding of the structural complexity of the area. However, the time-space development of the fracture network, the precise assessment of the timing of formation and possible re-activation of the single fracture sets, and the large-scale evolution settings of the transtensional Monti della Maddalena and East Agri fault systems should be better addressed. This new knowledge will permit to better explain the vertical fracture growth processes that occurred by rupturing the pre-existing bed-parallel mechanical interfaces, and hence affected the modalities of fluid circulation and accumulation within the shallow-water carbonates.

- Both absolute timing of the different generations of calcite cements, and origin of the mineralizing fluids were not addressed in the present PhD Thesis Dissertation. Following the aforementioned goal, these data will be key to better constrain the time-space modalities of fluid circulation through the fractured carbonates. Specifically, the new knowledge will be helpful to assess the specific burial depths at which specific processes were triggered (such as the nucleation of early, wavy-type stylolites), the role played by individual structural elements in the paleo-fluid flow patterns, and the age of formation and possible re-activation of single fracture and vein sets.
- The maximum burial at which the different types of styolites formed was extrapolated upon information such as the relative timing among the different structural elements and the maximum burial experienced by the rocks. Further quantitative analysis on the stylolite roughness could be useful to determine the amount of dissolution associated to the different generations of solution surfaces. Moreover, specific analyses on the circulating paleo-fluids can shed lights the specific rock-fluid interactions that controlled the dissolution. The dissolution of calcite, in fact, is strongly linked to the amount of dissolved CO_2 and by the fluid temperature. These parameters can also be useful to determine the origin of the circulating fluids and, hence shed lights on the fluid pathways through the evolution of the fold and thrusts belt.
- The pore space properties within these rocks may be also controlled by both exhumation and weathering processes. A detailed analysis on the karstic features at both micro scale and outcrop scale, coupled with the analysis of samples from sub-surface, can shed lights on the overall intensity of the weathering processes, and also on the control exerted by the nature of structural elements on the localization of

dissolution. Karst dissolution cavities generally follow high angle structural discontinuities such as bed-perpendicular fractures. However, stylolites (isolated or anastomosing) can contribute to fluid percolation and the dissolution can increase the pore connectivity degree along the stylolite resulting in the formation of channeled porosity.

Aknowledgements

The past three years mark, without a doubt, one of the most important transition phases of my life to date. During the course of my doctorate, which I like to define as "my journey into Middle-earth" (just so we don't miss a few quotes), I had to deal with many of my limitations and in some cases it may have learned to overcome them. If it had happened, it must certainly have been thanks to the people who supported me throughout the adventure, but also thanks to all the "wayfarers" with whom I shared short sections of the journey. All those who, ultimately, gave me a part of themselves and who, in turn, agreed to welcome a part of me in exchange.

I thank my friend Dr. Vincenzo La Bruna, who made my trip to Brazil possible, one of the most significant experiences of my entire journey, both on a human and scientific level. To this I add an equally special thanks to Prof. Hilario Bezerra, Dr. Renata Araùjo and all the people who in some way enriched my research period at the Federal University of Rio Grande do Norte. I thank my friends Carola Candeloro, Gianbattista Restelli, Leone Vernazza and, last but not least, Prof. Fabrizio Balsamo for sharing part of their work with me during our stay in Brazil and giving me the opportunity to expand my horizons.

The first thanks goes to my tutor, Prof. Fabrizio Agosta. The results that I am proud of having obtained today are largely due to his guidance which, to be honest, was not limited to just the three-year period of the doctorate, but influenced my entire course of study. As a good mentor, he ensured that, over the years, I developed awareness and a critical sense, and that I did not lose the way to follow. I also thank my co-tutor, Prof Giacomo Prosser. Thanks to the support of both of them, I was able to get to know the world and take in everything good that a doctoral path has to offer.

I thank Dr. Emma Michie for making my research period at the University of Liverpool possible, Prof. Daniel Faulkner and Dr. Michael Allen for welcoming me into their laboratories and to all the professors and doctoral students for making me feel part of their research group. A special thank you, in this case, goes to my friend Dr. Piercarlo Giacomel who helped and supported me in every way and in every situation, and from whom I had the pleasure of learning a lot.

I thank my friends and fellow doctoral students: Ian Abdallah, with whom I shared a lot of work, but also a lot of achievements, Filippo Zummo, Fabio Olita, Giammarco Guidetti, Nicoletta Sgarro and Faith Obasuy, for the constant discussion they provided me.

I thank Dr. Simona Todaro for having contributed to a large and very important part of this thesis.

I also thank my friend Alessia Pietragalla for having contributed, with her work, to the success of this thesis.

I thank Giulia Schirripa Spagnolo for sharing long days in the field with me.

I thank Dr. Luca Smeraglia for the interesting scientific discussions, for the time spent in the countryside during our fieldtrip in Greece and, last but not least, for his extremely constructive comments and observations regarding this thesis. Regarding this last point, I cannot help but also thank Prof. Andrea Brogi for his equally constructive comments.

I thank the students of the geology degree course and the guys from the Geobas association for the affection shown to me over the years.

I thank all those, teachers and researchers, who contributed with their teachings, suggestions and comments to the success of this work, especially Prof. Stefano Tavani.

I thank my friends Francesco Pio Ramunno, Antonello Menchise, Antonio Polosa, Michele Lioi, Mattia Pepe and Donatello Marone for their moral support during this journey.

Special thanks go to my family, my mother, my father, and my brother, who have always believed in me and who supported me in every possible way during my doctorate. Without them, all this would not have been possible.

Finally, I thank my girlfriend Grazia. Her support during the hardest moments was crucial, and her presence during moments of great satisfaction was the most important added value.

Ringraziamenti

Il triennio appena trascorso segna, senza alcun dubbio, una delle fasi di transizione più importanti della mia vita fino ad oggi. Durante il percorso del dottorato, che mi piace definire "il mio viaggio all'interno della Terra di Mezzo" (tanto per non farci mancare qualche citazione), ho dovuto fare i conti con molti dei mei limiti e in alcuni casi può essere che abbia imparato a superarli. Se fosse successo, dev'essere stato certamente grazie alle persone che mi hanno affiancato durante tutta l'avventura, ma anche grazie a tutti i "viandanti" con cui ho condiviso brevi tratti del cammino. Tutti coloro che, in definitiva, mi hanno donato una parte di sé e che, a loro volta, hanno acconsentito ad accogliere in cambio una parte di me.

Il primo ringraziamento va al mio tutor, il Prof. Fabrizio Agosta. I risultati che oggi mi fregio di aver ottenuto sono in gran parte dovuti alla sua guida che, a onor del vero, non è stata limitata al solo triennio del dottorato, ma ha segnato tutto il mio percorso di studi. Da buon mentore ha fatto sì che, negli anni, sviluppassi consapevolezza e senso critico, e che non smarrissi la via da seguire. Ringrazio anche il mio co-tutor, il prof Giacomo Prosser. Grazie al supporto di entrambi ho potuto conoscere il mondo e prendere tutto ciò che di buono un percorso di dottorato ha da offrire.

Ringrazio il mio amico Dott. Vincenzo La Bruna, che ha reso possibile il mio viaggio in Brasile, una delle esperienze più significative di tutto il mio percorso, sia sul piano umano che scientifico. A questo aggiungo un ringraziamento altrettanto speciale al Prof. Hilario Bezerra, alla Dott.ssa Renata Araùjo ed a tutte le persone che in qualche modo hanno arricchito il mio periodo di ricerca presso l'Unversità Federale del Rio Grande do Norte. Ringrazio i miei amici Carola Candeloro, Gianbattista Restelli, Leone Vernazza e, non ultimo, il Prof. Fabrizio Balsamo per aver condiviso con me, durante il nostro soggiorno in Brasile, parte del proprio lavoro ed avermi dato la possibilità di espandere i miei orizzonti.

Ringrazio la Dott.ssa Emma Michie per aver reso possibile il mio periodo di ricerca presso l'Università di Liverpool, il Prof. Daniel Faulkner e il Dott. Michael Allen per avermi accolto all'interno dei loro laboratori e a tutti i docenti e dottorandi per avermi fatto sentire parte del proprio gruppo di ricerca. Un ringraziamento speciale, in questo caso, va al mio amico Dott. Piercarlo Giacomel che mi ha aiutato e supportato in ogni modo ed in ogni situazione, e dal quale ho avuto il piacere di imparare molto.

Ringrazio i miei amici e colleghi dottorandi: Ian Abdallah, con cui ho condiviso parecchio lavoro, ma anche parecchi risultati, Filippo Zummo, Fabio Olita, Giammarco Guidetti, Nicoletta Sgarro e Faith Obasuy, per il confronto costante che mi hanno fornito.

Ringrazio la Dott.ssa Simona Todaro per aver contribuito a una parte ampia ed importantissima di questa tesi.

Ringrazio anche la mia amica Alessia Pietragalla per aver contribuito, col proprio lavoro, alla riuscita di questa tesi.

Ringrazio Giulia Schirripa Spagnolo per aver condiviso con me lunghe giornate in campagna.

Ringrazio il Dott. Luca Smeraglia per le interessanti discussioni scientifiche, per il tempo trascorso in campagna durante il nostro lavoro in Grecia e, non ultimo, per i suoi commenti ed osservazioni estremamente costruttivi in merito a questa tesi. Riguardo a quest'ultimo punto, non posso non ringraziare anche il Prof. Andrea Brogi per i suoi commenti altrettanto costruttivi.

Ringrazio tutti i coloro, docenti e ricercatori, che a vario titolo hanno contribuito con i loro insegnamenti, suggerimenti e commenti alla buona riuscita di questo lavoro, in particolar modo il Prof. Stefano Tavani.

Ringrazio gli studenti e le studentesse del corso di laurea di geologia e i ragazzi dell'associazione Geobas per l'affetto mostratomi negli anni.

Ringrazio i miei amici Francesco Pio Ramunno, Antonello Menchise, Antonio Polosa, Michele Lioi, Mattia Pepe e Donatello Marone per il supporto morale durante questo percorso.

Un ringraziamento speciale va alla mia famiglia, mia madre, mio padre e mio fratello, che hanno creduto in me da sempre e che mi hanno supportato in tutti i modi possibili durante il dottorato. Senza di loro, tutto questo non sarebbe stato possibile.

Infine, ringrazio la mia fidanzata Grazia. Il suo sostegno durante i momenti più difficili è stato cruciale, e la sua presenza durante i momenti di grande soddisfazione è stato il valore aggiunto più importante.

REFERENCE LIST

Agosta, F. & Aydin, A. 2006. Architecture and deformation mechanism of a basin-bounding normal fault in Mesozoic platform carbonates, central Italy. Journal of Structural Geology 28(8), 1445–1467.

Agosta, F., Alessandroni, M., Antonellini, M., Tondi, E., Giorgioni, M., 2010. From fractures to flow: A field-based quantitative analysis of an outcropping carbonate reservoir. Tectonophysics 490, 197–213. https://doi.org/10.1016/j.tecto.2010.05.005

Agosta, F., Alessandroni, M., Tondi, E., Aydin, A., 2009. Oblique normal faulting along the northern edge of the Majella Anticline, central Italy: Inferences on hydrocarbon migration and accumulation. Journal of Structural Geology 31. https://doi.org/10.1016/j.jsg.2009.03.012

Agosta, F., Aydin, A., 2006. Architecture and deformation mechanism of a basin-bounding normal fault in Mesozoic platform carbonates, central Italy. Journal of Structural Geology 28, 1445–1467. https://doi.org/10.1016/j.jsg.2006.04.006

Agosta, F., Kirschner, D.L., 2003. Fluid conduits in carbonate-hosted seismogenic normal faults of central Italy. Journal of Geophysical Research: Solid Earth 108, 1–13. https://doi.org/10.1029/2002jb002013

Agosta, F., Manniello, C., Cavalcante, F., Belviso C., Prosser, G., 2021. Late Cretaceous transtensional faulting of the Apulian Platform, Italy. Marine and Petroleum Geology. 127, 104889.

Agosta, F., Wilson, C. & Aydin, A. 2015. The role of mechanical stratigraphy on normal fault growth across a Cretaceous carbonate multi-layer, central Texas (USA). Italian Journal of Geosciences 134(3), 423–441.

Aharonov, E., Karcz, Z., 2019. How stylolite tips crack rocks. Journal of Structural Geology 118, 299–307. https://doi.org/10.1016/j.jsg.2018.11.002

Aharonov, E., Katsman, R., 2009. Interaction between pressure solution and clays in stylolite development: insights from modeling. American Journal of Science 309, 607–632. https://doi.org/10.2475/07.2009.04

Al-Fahmi, M.M., Hooker, J.N., Al-Mojel, A.S., Cartwright, J.A., 2020. New scaling of fractures in a giant carbonate platform from outcrops and subsurface. Journal of Structural Geology 140, 104142. https://doi.org/10.1016/j.jsg.2020.104142

Allmendinger, R. W., Cardozo, N., & Fisher, D. M. 2011. Structural geology algorithms: Vectors and tensors. Cambridge University Press.

Alvarez, W., Engelder, T., Geiser, P.A., 1978. Classification of solution cleavage in pelagic limestones. Geology 6, 263–266. https://doi.org/10.1130/0091-7613(1978)6<263:COSCIP>2.0.CO;2

Alvarez, W., Engelder, T., Lowrie, W., 1976. Formation of spaced cleavage and folds in brittle limestone by dissolution. Geology 4, 698–701. https://doi.org/10.1130/0091-7613(1976)4<698:FOSCAF>2.0.CO;2

Amodio-Morelli L., Bonardi G., Colonna V., Dietrich D., GiunTa G., Ippolito F., Liguori V., Lorenzoni S., Paglionico A., Perrone V., Piccarreta G., Russo M., Scandone P., Zanettin-Lorenzoni E. & Zuppetta A. (1976). L'Arco calabro-peloritano nell'orogene appenninico-maghrebide. Mem. Soc. Geol. Ital., 17, 1-60

Amrouch, K., Lacombe, O., Bellahsen, N., Daniel, J.M. & Callot, J.P. 2010. Stress and strain patterns, kinematics and deformation mechanisms in a basement-cored anticline: Sheep Mountain Anticline,

Wyoming. Tectonics 29(1), 1–27.

Andreo, B., Vías, J., Durán, J.J., Jiménez, P., López-Geta, J.A. & Carrasco, F. 2008. Methodology for groundwater recharge assessment in carbonate aquifers: Application to pilot sites in southern Spain. Hydrogeology Journal 16(5), 911–925.

Antonellini, M., Tondi, E., Agosta, F., Aydin, A., Cello, G., 2008. Failure modes in deep-water carbonates and their impact for fault development: Majella Mountain, Central Apennines, Italy. Marine and Petroleum Geology 25, 1074–1096. https://doi.org/10.1016/j.marpetgeo.2007.10.008

Araújo, R.E.B., La Bruna, V., Rustichelli, A., Bezerra, F.H.R., Xavier, M.M., Audra, P., Barbosa, J.A., Antonino, A.C.D., 2021. Structural and sedimentary discontinuities control the generation of karst dissolution cavities in a carbonate sequence, Potiguar Basin, Brazil. Marine and Petroleum Geology 123. https://doi.org/10.1016/j.marpetgeo.2020.104753

Aydin, A. & Berryman, J.G. 2010. Analysis of the growth of strike-slip faults using effective medium theory. Journal of Structural Geology 32(11), 1629–1642.

Aydin, A., Antonellini, M., Tondi, E. & Agosta, F. 2010. Deformation along the leading edge of the Maiella thrust sheet in central Italy. Journal of Structural Geology 32(9), 1291–1304.

Aydin, A., Borja, R.I. & Eichhubl, P. 2006. Geological and mathematical framework for failure modes in granular rock. Journal of Structural Geology 28(1), 83–98.

Bai, T. & Pollard, D.D. 2000. Fracture spacing in layered rocks: A new explanation based on the stress transition. Journal of Structural Geology 22(1), 43–57.

Bai, T., Maerten, L., Gross, M.R. & Aydin, A. 2002. Orthogonal cross joints: Do they imply a regional stress rotation? Journal of Structural Geology 24(1), 77–88.

Barattolo, F. & Romano, R. 2005. Shallow carbonate platform bioevents during the Upper Triassic-Lower Jurassic: An evolutive interpretation. Bollettino della Societa Geologica Italiana 124(1), 123–142.

Barattolo, F. 1991. Mesozoic and Cenozoic Marine Benthic Calcareous Algae with Particular Regard to Mesozoic Dasycladaleans. In Calcareous Algae and Stromatolites, pp. 504–540. , Berlin, Heidelberg: Springer Berlin Heidelberg.

Baud, P., Louis, L., David, C., Rawling, G.C., Wong, T.-F., 2005. Effects of bedding and foliation on mechanical anisotropy, damage evolution and failure mode. Geological Society, London, Special Publications 245, 223–249. https://doi.org/10.1144/GSL.SP.2005.245.01.11

Baud, P., Rolland, A., Heap, M., Xu, T., Nicolé, M., Ferrand, T., Reuschlé, T., Toussaint, R., Conil, N., 2016. Impact of stylolites on the mechanical strength of limestone. Tectonophysics 690, 4–20. https://doi.org/10.1016/j.tecto.2016.03.004

Beaudoin, N., Gasparrini, M., David, M.E., Lacombe, O., Koehn, D., 2019. Bedding-parallel stylolites as a tool to unravel maximum burial depth in sedimentary basins: Application to Middle Jurassic carbonate reservoirs in the Paris basin, France. Bulletin of the Geological Society of America 131, 1239–1254. https://doi.org/10.1130/B32064.1

Beaudoin, N., Koehn, D., Lacombe, O., Lecouty, A., Billi, A., Aharonov, E., Parlangeau, C., 2016. Fingerprinting stress: Stylolite and calcite twinning paleopiezometry revealing the complexity of

progressive stress patterns during folding—The case of the Monte Nero anticline in the Apennines, Italy. Tectonics 35, 1687–1712. https://doi.org/10.1002/2016TC004128

Beaudoin, N., Lacombe, O., Koehn, D., David, M.E., Farrell, N., Healy, D., 2020. Vertical stress history and paleoburial in foreland basins unravelled by stylolite roughness paleopiezometry: Insights from bedding-parallel stylolites in the Bighorn Basin, Wyoming, USA. Journal of Structural Geology 136. https://doi.org/10.1016/j.jsg.2020.104061

Becker, A. & Gross, M.R. 1996. Mechanism for joint saturation in mechanically layered rocks: An example from southern Israel. Tectonophysics 257(2-4 SPEC. ISS.), 223–237.

Bellani, S., Brogi, A., Lazzarotto, A., Liotta, D. & Ranalli, G. 2004. Heat flow, deep temperatures and extensional structures in the Larderello Geothermal Field (Italy): Constraints on geothermal fluid flow. Journal of Volcanology and Geothermal Research 132(1), 15–29.

Ben-itzhak, L.L., Aharonov, E., Toussaint, R., Sagy, A., Ben-itzhak, L.L., Aharonov, E., Toussaint, R., Sagy, A., Life, T., 2012. The Life and Death of Stylolites : stylolite roughness as indicator for the duration and amount of dissolution. Earth and Planetary Science Letters 337–338, 186–196.

Bense, V.F., Gleeson, T., Loveless, S.E., Bour, O., Scibek, J., 2013. Fault zone hydrogeology. Earth-Science Reviews 127, 171–192. https://doi.org/10.1016/j.earscirev.2013.09.008

Bentivenga, M., Palladino, G., Prosser, G., Guglielmi, P., Geremia, F. & Laviano, A. 2017. A Geological Itinerary Through the Southern Apennine Thrust Belt (Basilicata—Southern Italy). Geoheritage 9(1), 1–17.

Berry, M.D., Stearns, D.W., Friedman, M., 1996. the Development of a Fractured Reservoir Model for the Palm Valley Gas Field. The APPEA Journal 36, 82. https://doi.org/10.1071/aj95005

Bigi, S., 2006. An example of inversion in a brittle shear zone. Journal of Structural Geology 28, 431–443. https://doi.org/10.1016/j.jsg.2005.12.012

Billi, A. & Salvini, F. 2003. Development of systematic joints in response to flexure-related fibre stress in flexed foreland plates: The Apulian forebulge case history, Italy. Journal of Geodynamics 36(4), 523–536.

Bonnet, E., Bour, O., Odling, N.E., Davy, P., Main, I., Cowie, P. & Berkowitz, B. 2001. Scaling of fracture systems in geological media. Reviews of Geophysics 39(3), 347–383.

BouDagher-Fadel, M.K. & Bosence, D.W.J. 2007. Early Jurassic benthic foraminiferal diversification and biozones in shallow-marine carbonates of western Tethys. Senckenbergiana Lethaea 87(1), 1–39.

BouDagher-Fadel, M.K., 2008. Chapter 6 The Cenozoic larger benthic foraminifera: the Palaeogene. In: Boudagher-Fadel, M.K.B.T.-D. in P. and S. (Ed.), Evolution and Geological Significance of Larger Benthic Foraminifera. Elsevier, 297–545. https://doi.org/10.1016/S0920-5446(08)00006-X

Brouste, A., Renard, F., Gratier, J.P., Schmittbuhl, J., 2007. Variety of stylolites' morphologies and statistical characterization of the amount of heterogeneities in the rock. Journal of Structural Geology 29, 422–434. https://doi.org/10.1016/j.jsg.2006.09.014

Bruce Railsback, L., Andrews, L.M., 1995. Tectonic stylolites in the "undeformed" Cumberland Plateau of southern Tennessee. Journal of Structural Geology 17, 911–915. https://doi.org/10.1016/0191-

8141(94)00127-L

Bruna, P.O., Lavenu, A.P.C., Matonti, C., Bertotti, G., 2019. Are stylolites fluid-flow efficient features? Journal of Structural Geology 125, 270–277. https://doi.org/10.1016/j.jsg.2018.05.018

Bruno, M.C., Caliri, A., Carbone, S., Chiocchini, M., Di Stefano, A., Giano, S.I., Guarnieri, P., Lentini, F., Martorano, S. & Piccarreta, G., 2014. CARTA GEOLOGICA D'ITALIA, Foglio 505 Moliterno, scala 1: 50.000.

Bucci, F., Novellino, R., Guglielmi, P., Prosser, G., Tavarnelli, E., 2012. Geological map of the northeastern sector of the high Agri Valley, Southern Apennines (Basilicata, Italy). Journal of Maps 8, 282–292. https://doi.org/10.1080/17445647.2012.722403

Bucci, F., Novellino, R., Guglielmi, P., Prosser, G., Tavarnelli, E., 2012. Geological map of the northeastern sector of the high Agri Valley, Southern Apennines (Basilicata, Italy). Journal of Maps 8, 282–292. https://doi.org/10.1080/17445647.2012.722403

Buttinelli, M., Improta, L., Bagh, S. & Chiarabba, C. 2016. Inversion of inherited thrusts by wastewater injection induced seismicity at the Val d'Agri oilfield (Italy). Scientific Reports 6(November), 1–8.

Buxton, T.M. & Sibley, D.F. 1981. Pressure solution features in a shallow buried limestone. Journal of Sedimentary Petrology 51(1), 19–26.

Byerlee, J.D., 1968. Brittle-ductile transition in rocks. Journal of Geophysical Research 73, 4741–4750. https://doi.org/10.1029/jb073i014p04741

Camanni, G., Vinci, F., Tavani, S., Ferrandino, V., Mazzoli, S., Corradetti, A., Parente, M. & Iannace, A. 2021. Fracture density variations within a reservoir-scale normal fault zone: A case study from shallow-water carbonates of southern Italy. Journal of Structural Geology 151(May), 104432.

Carozzi, A. V., Bergen, D. Von, 1987. Stylolitic Porosity in Carbonates: a Critical Factor for Deep Hydrocarbon Production. Journal of Petroleum Geology 10, 267–282. https://doi.org/10.1111/j.1747-5457.1987.tb00946.x

Carrio-Schaffhauser, E., Raynaud, S., Latière, H.J., Mazerolle, F., 1990. Propagation and localization of stylolites in limestones. Geological Society Special Publication 54, 193–199. https://doi.org/10.1144/GSL.SP.1990.054.01.19

Casero P., Roure F. & Vially R., 1991. Tectonic framework and petroleum potential of the southern Apennines. In SPENCER A.M. Ed., Generation, accumulation, and production of Europe's hydrocarbons, Spec. Publ. European Assoc. Petroleum Geosci., 1, 381-387.

Casero P., Roure F., Endignoux L., Moretti I., Müller C., Sage L. & Vially R., 1988. Neogene geodynamic evolution of the Southern Apennines. Mem. Soc. Geol. Ital., 41, 109-120.

Cavalcante, F., Belviso, C., Bentivenga, M., Fiore, S., Prosser G., 2011. Occurence of palygorskite and sepiolite in upper Paleocene – middle Eocene marine deep sediments of the Lagonegro basin (Southern Apennines – Italy): paleoenvironmental and provenante inferences. Sedimentary Geology, 233, 42-52.

Cavalcante, F., Belviso, C., Laurita, S., Prosser, G., 2012. P-T constraints from phyllosilicates of the Liguride Complex of the Pollino area (Southern Apennines, Italy): Geological inferences. Ofioliti, 37, 65-75.

Cavalcante, F., Fiore, S., Lettino, A., Piccarreta, G. & Tateo, F., 2007. Illite-smectite mixed layers in Sicilide shales and piggy-back deposits of the Gorgoglione Formation (southern Apennines): geological inference. Boll. Soc. Geol. It, 126, 241-254

Cavalcante, F., Fiore, S., Piccarreta, G., Tateo, F., 2003. Geochemical and mineralogical approaches to assessing provenance and deposition of shales: a case study. Clay Minerals 38, 383–397.

Cello, G., Gambini, R., Mazzoli, S., Read, A., Tondi, E., Zucconi, V., 2000. Fault zone characteristics and scaling properties of the Val d'Agri Fault system (southern Apennines, Italy). Journal of Geodynamics 29, 293–307. https://doi.org/10.1016/S0264-3707(99)00043-5

Cello, G., Mazzoli, S., 1998. Apennine tectonics in southern Italy: A review. Journal of Geodynamics 27, 191–211. https://doi.org/10.1016/S0264-3707(97)00072-0

Cello, G., Tondi, E., Micarelli, L. & Mattioni, L. 2003. Active tectonics and earthquake sources in the epicentral area of the 1857 Basilicata earthquake (southern Italy). Journal of Geodynamics 36(1–2), 37–50.

Chamley, H., 1989. Clay Sedimentology. Springer-Vergal, Berlin, Heidelberg. 623 pp.

Chiocchini, M.,Farinacci, A.,Mancinelli, A.,Molinari, V.&Potetti, M., 1994. Biostratigrafia a foraminiferi, dasicladali e calpionelle delle successioni carbonatiche mesozoiche dell'Appennino centrale (Italia).In: Mancinelli, A.(ed.)Biostratigrafia dell'Italia centrale. Studi Geologici Camerti, VolumeSpeciale,1994, 9–129

Chiocchini, M., Mancinelli, a., 1977. Microbiostratigrafia del mesozoico in facies di piattaforma carbonatica dei monti aurunci (lazio meridonale).

Choquette PW, Pray LC, 1970. Geologic Nomenclature and Classification of Porosity in Sedimentary Carbonates. American Association of Petroleum Geologists Bulletin 54, 207–250. https://doi.org/10.1306/5d25c98b-16c1-11d7-8645000102c1865d

Choquette, P.W., James, N.P., 1988. Introduction. In: James, N.P., Choquette, P.W. (eds) Paleokarst. Springer, New York, NY. https://doi.org/10.1007/978-1-4612-3748-8_1

Clari, P. 1975. Caratteristiche sedimentologiche e paleontologiche di alcune sezioni dei Calcari Grigi del Veneto. Mem. Sc. Geol., 31, 1-63

Collettini, C., Tesei, T., Scuderi, M.M., Carpenter, B.M., Viti, C., 2019. Beyond Byerlee friction, weak faults and implications for slip behavior. Earth and Planetary Science Letters 519, 245–263. https://doi.org/10.1016/j.epsl.2019.05.011

Cooke, M.L., Underwood, C.A., 2001. Fracture termination and step-over at bedding interfaces due to frictional slip and interface opening. Journal of Structural Geology 23, 223–238. https://doi.org/10.1016/S0191-8141(00)00092-4

Corniello, A., Ducci, D., Ruggieri, G. & Iorio, M. 2018. Complex groundwater flow circulation in a carbonate aquifer: Mount Massico (Campania Region, Southern Italy). Synergistic hydrogeological understanding. Journal of Geochemical Exploration 190(2017), 253–264.

Corradetti, A., Tavani, S., Parente, M., Iannace, A., Vinci, F., Pirmez, C., Torrieri, S., Giorgioni, M., Pignalosa, A., Mazzoli, S., 2018. Distribution and arrest of vertical through-going joints in a seismic-scale carbonate platform exposure (Sorrento peninsula, Italy): insights from integrating field survey and digital outcrop

model. Journal of Structural Geology 108, 121–136. https://doi.org/10.1016/j.jsg.2017.09.009

Cortez Pontes, C.C., Balsamo, F., Pizzati, M., Bezerra, F.H.R., La Bruna, V., Lima, R.S., 2022. Burial Stylolites Enhance Karst Dissolution and Control Cave Geometry in Heterolithic Carbonates, Salitre Formation, Brazil. SSRN Electronic Journal 148, 106029. https://doi.org/10.2139/ssrn.4162706

Croizé, D., Renard, F., Bjørlykke, K. & Dysthe, D.K. 2010. Experimental calcite dissolution under stress: Evolution of grain contact microstructure during pressure solution creep. Journal of Geophysical Research: Solid Earth 115(9), 1–15.

Cruden, D.M. 1977. Describing the size of discontinuities. International Journal of Rock Mechanics and Mining Sciences and 14(3), 133–137.

Cuadros, J. and Altaner, S. P., 1998. Characterization of mixed-layer illite-smectite from bentonites using microscopic, chemical, and X-ray methods: Constraints on the smectite-to-illite transformation mechanism. American Mineralogist, 83, 762–774.

Curzi, M., Aldega, L., Bernasconi, S.M., Berra, F., Billi, A., Boschi, C., Franchini, S., Van der Lelij, R., Viola, G., Carminati, E., 2020. Architecture and evolution of an extensionally-inverted thrust (Mt. Tancia Thrust, Central Apennines): Geological, structural, geochemical, and K–Ar geochronological constraints. Journal of Structural Geology 136, 104059. https://doi.org/10.1016/j.jsg.2020.104059

De Castro, P., 1991. Mesozoic. In:Barattolo, F.,De Castro, P.& Parente,M.(eds)5th International Symposium on Fossil Algae. Field Trip Guide-Book. Giannini, Napoli, 21–38

Demurtas, M., Fondriest, M., Balsamo, F., Clemenzi, L., Storti, F., Bistacchi, A. & Di Toro, G. 2016. Structure of a normal seismogenic fault zone in carbonates: The Vado di Corno Fault, Campo Imperatore, Central Apennines (Italy). Journal of Structural Geology 90, 185–206.

Dernaika, M., Masalmeh, S., Mansour, B., Al-Jallad, O., Koronfol, S., 2019. Modeling Permeability in Carbonate Rocks. SCA Annual Symposium.

Dershowitz, W. S., and H. H. Einstein, 1988. Characterizing rock joint geometry with joint system models, Rock Mech. Rock Eng., 21, 21-51.

Dershowitz, W.S. & Herda, H.H. 1992. Interpretation of fracture spacing and intensity. The 33rd U.S. Symposium on Rock Mechanics (USRMS), ARMA-92-0757.

Di Niro, A., Giano, S.I., Santangelo, N., 1992. Primi dati sull'evoluzione geomorfologica e sedimentaria del bacino dell'alta val d'Agri (Basilicata). Studi Geologici Camerti 1992,1, 257-263.

Di Stefano, P. & Ruberti, D. 2000. Cenomanian rudist-dominated shelf-margin limestones from the panormide carbonate platform (Sicily, Italy): Facies analysis and sequence stratigraphy. Facies 42(1), 133–160.

Di Stefano, P., A. Alessi, and M. Gullo 1996. Mesozoic and Paleogene megabreccias in southern Sicily: New data on the Triassic paleomarginof the Siculo-Tunisian platform. Facies, 34, 101–122

Doglioni, C., Harabaglia, P., Martinelli, G., Mongelli, F., Zito, G., 1996. A geodynamic model of the Southern Apennines accretionary prism. Terra Nova 8, 540–547. https://doi.org/10.1111/j.1365-3121.1996.tb00783.x

Donath, F.A., Parker, R.B., 1964. Folds and Folding*. GSA Bulletin 75, 45–62. https://doi.org/10.1130/0016-

7606(1964)75[45:FAF]2.0.CO;2

Dunham, R.J. 1962. Classification of Carbonate Rocks According to Depositional Texture1 (ed. W. E. Ham). Classification of Carbonate Rocks—A Symposium 1, 0.

Dunnington, H. V 1967. Aspects of Diagenesis and Shape Change in Stylolitic Limestone Reservoirs. 7th World Petroleum Congress, WPC-12129.

Eberli, G.P., Baechle, G.T., Anselmetti, F.S. & Incze, M.L. 2003. Factors controlling elastic properties in carbonate sediments and rocks. Leading Edge (Tulsa, OK) 22(7), 654–660.

Ebner, M., Koehn, D., Toussaint, R., Renard, F., 2009. The influence of rock heterogeneity on the scaling properties of simulated and natural stylolites. Journal of Structural Geology 31, 72–82. https://doi.org/10.1016/j.jsg.2008.10.004

Ebner, M., Toussaint, R., Schmittbuhl, J., Koehn, D., Bons, P., 2010. Anisotropic scaling of tectonic stylolites: A fossilized signature of the stress field? Journal of Geophysical Research 115, B06403. https://doi.org/10.1029/2009JB006649

Ehrenberg, S.N., 2006. Porosity destruction in carbonate platforms. Journal of Petroleum Geology 29, 41–52. https://doi.org/10.1111/j.1747-5457.2006.00041.x

Ehrenberg, S.N., Nadeau, P.H., 2005. Sandstone vs. carbonate petroleum reservoirs: A global perspective on porosity-depth and porosity-permeability relationships. American Association of Petroleum Geologists Bulletin 89, 435–445. https://doi.org/10.1306/11230404071

Ehrenberg, S.N., Walderhaug, O., Bjerlykke, K., 2012. Carbonate porosity creation by mesogenetic dissolution: Reality or illusion? AAPG Bulletin 96, 217–225. https://doi.org/10.1306/05031110187

Embry, A.F. & Klovan, J.E. 1971. A LATE DEVONIAN REEF TRACT ON NORTHEASTERN BANKS ISLAND, N.W.T.1. Bulletin of Canadian Petroleum Geology 19(4), 730–781.

Engelder, T., Engelder, R., 1977. Fossil distortion and décollement tectonics of the Appalachian Plateau. Geology 5, 457–460. https://doi.org/10.1130/0091-7613(1977)5<457:FDADTO>2.0.CO;2

Engelder, T., Marshak, S., 1985. Disjunctive cleavage formed at shallow depths in sedimentary rocks. Journal of Structural Geology 7, 327–343. https://doi.org/10.1016/0191-8141(85)90039-2

Ettinger, N.P., Larson, T.E., Kerans, C., Thibodeau, A.M., Hattori, K.E., Kacur, S.M. & Martindale, R.C. 2021. Ocean acidification and photic-zone anoxia at the Toarcian Oceanic Anoxic Event: Insights from the Adriatic Carbonate Platform. Sedimentology 68(1), 63–107.

Ferraro, F., Grieco, D.S., Agosta, F., Prosser, G., 2018. Space-time evolution of cataclasis in carbonate fault zones. Journal of Structural Geology 110, 45–64. https://doi.org/10.1016/j.jsg.2018.02.007

Ferraro, F., Koutalonis, I., Vallianatos, F., Agosta, F., 2019. Application of Non-Extensive Statistical Physics on the particle size distribution in natural carbonate fault rocks. Tectonophysics 771, 228219. https://doi.org/10.1016/j.tecto.2019.228219

Ferraro, F., Koutalonis, I., Vallianatos, F., Agosta, F., 2019. Application of Non-Extensive Statistical Physics on the particle size distribution in natural carbonate fault rocks. Tectonophysics 771, 228219. https://doi.org/10.1016/j.tecto.2019.228219

Fletcher, R.C., Pollard, D.D., 1981. Anticrack model for pressure solution surfaces. Geology 9, 419–424. https://doi.org/10.1130/0091-7613(1981)9<419:AMFPSS>2.0.CO;2

Flügel, E., 2004. Carbonate Depositional Environments. In: Microfacies of Carbonate Rocks. Springer, Berlin, Heidelberg. https://doi.org/10.1007/978-3-662-08726-8_2

Fu, Y., Hao, Q., Peng, S., Markovic S. B., Gao X., Han L., Wu X., Namier, N., Zhang, W., Gavrilov, M. B., Markovic, R., Guo, Z., 2021. Clay mineralogy of the Stari Slankamen (Serbia) loess-paleosol sequence during the last glacial cycle d Implications for dust provenance and interglacial climate. Quaternary Science Reviews, 263, 106990

Fugagnoli, A. 2004. Trophic regimes of benthic foraminiferal assemblages in Lower Jurassic shallow water carbonates from northeastern Italy (Calcari Grigi, Trento Platform, Venetian Prealps). Palaeogeography, Palaeoclimatology, Palaeoecology 205, 111–130.

Gale, A.S., Kennedy, W.J., Voigt, S. & Walaszczyk, I. 2005. Stratigraphy of the Upper Cenomanian-Lower Turonian Chalk succession at Eastbourne, Sussex, UK: Ammonites, inoceramid bivalves and stable carbon isotopes. Cretaceous Research 26(3), 460–487.

Ghisetti, F., Vezzani, L., 1999. Depth and modes of Pliocene-Pleistocene crustal extension of the Apennines (Italy). Terra Nova 11, 67–72. https://doi.org/10.1046/j.1365-3121.1999.00227.x

Giano, S.I., Maschio, L., Alessio, M., Ferranti, L., Improta, S., Schiattarella, M., 2000. Radiocarbon dating of active faulting in the Agri high. Journal of Geodynamics 29, 371–386.

Gillespie, P.A., Howard, C.B., Walsh, J.J. & Watterson, J. 1993. Measurement and characterisation of spatial distributions of fractures. Tectonophysics 226(1–4), 113–141.

Giuffrida, A., Agosta, F., Rustichelli, A., Panza, E., La Bruna, V., Eriksson, M., Torrieri, S., Giorgioni, M., 2020. Fracture stratigraphy and DFN modelling of tight carbonates, the case study of the Lower Cretaceous carbonates exposed at the Monte Alpi (Basilicata, Italy). Marine and Petroleum Geology 112, 104045. https://doi.org/10.1016/j.marpetgeo.2019.104045

Giuffrida, A., La Bruna, V., Castelluccio, P., Panza, E., Rustichelli, A., Tondi, E., Giorgioni, M. & Agosta, F. 2019. Fracture simulation parameters of fractured reservoirs: Analogy with outcropping carbonates of the Inner Apulian Platform, southern Italy. Journal of Structural Geology 123, 18–41.

Graham, B., Antonellini, M. & Aydin, A. 2003. Formation and growth of normal faults in carbonates within a compressive environment. Geology 31(1), 11–14.

Graham, B., Antonellini, M., Aydin, A., 2003. Formation and growth of normal faults in carbonates within a compressive environment. Geology 31, 11–14. https://doi.org/10.1130/0091-7613(2003)031<0011:FAGONF>2.0.CO;2

Gratier, J.-P., Guiguet, R., Renard, F., Jenatton, L., Bernard, D., 2009. A pressure solution creep law for quartz from indentation experiments. Journal of Geophysical Research 114, 1–16. https://doi.org/10.1029/2008jb005652

Gratier, J.P., Noiriel, C., Renard, F., 2015. Experimental evidence for rock layering development by pressure solution. Geology 43, 871–874. https://doi.org/10.1130/G36713.1

Gratier, J.P., Renard, F. & Vial, B. 2014. Postseismic pressure solution creep: Evidence and time-dependent

change from dynamic indenting experiments. Journal of Geophysical Research: Solid Earth 119(4), 2764–2779.

Gross, M.R. 1993. The origin and spacing of cross joints: examples from the Monterey Formation, Santa Barbara Coastline, California. Journal of Structural Geology 15(6), 737–751.

Gross, M.R., Fischer, M.P., Engelder, T. & Greenfield, R.J. 1995. Factors controlling joint spacing in interbedded sedimentary rocks: Integrating numerical models with field observations from the Monterey Formation, USA. Geological Society Special Publication 92, 215–233.

Gross, M.R., Gutiérrez-Alonso, G., Bai, T., Wacker, M.A., Collinsworth, K.B. & Behl, R.J. 1997. Influence of mechanical stratigraphy and kinematics on fault scaling relations. Journal of Structural Geology 19(2), 171–183.

Hager, B.H., Dieterich, J., Frohlich, C., Juanes, R., Mantica, S., Shaw, J.H., Bottazzi, F., Caresani, F., Castineira, D., Cominelli, A., Meda, M., Osculati, L., Petroselli, S. & Plesch, A. 2021. A process-based approach to understanding and managing triggered seismicity. Nature 595(7869), 684–689.

Heap, M., Reuschlé, T., Baud, P., Renard, F., Iezzi, G., 2018. The permeability of stylolite-bearing limestone. Journal of Structural Geology 116, 81–93. https://doi.org/10.1016/j.jsg.2018.08.007

Heap, M.J., Baud, P., Reuschlé, T., Meredith, P.G., 2014. Stylolites in limestones: Barriers to fluid flow? Geology 42, 51–54. https://doi.org/10.1130/G34900.1

Hippolyte, J.C., Angelier, J., Barrier, E., 1995. Compressional and extensional tectonics in an arc system: example of the Southern Apennines. Journal of Structural Geology 17, 1725–1740. https://doi.org/10.1016/0191-8141(95)00066-M

Hoffman, J. and Hower, J., 1979 Clay mineral assemblages as low grade metamorphic geothermometers: Application to the thrust faulted disturbed belt of Montana: in Aspects of Diagenesis. P. A. Scholle and P. S. Schluger, eds., SEPM Spec. Publ. 26, 55-79.

Holl, J.E., Anastasio, D.J., 1995. Cleavage development within a foreland fold and thrust belt, southern Pyrenees, Spain. Journal of Structural Geology 17, 357–369. https://doi.org/10.1016/0191-8141(94)00062-5

Hughes, T.P. & Tanner, J.E. 2000. Recruitment Failure, Life Histories, and Long-Term Decline of Caribbean Corals. Ecology 81(8), 2250.

Humphrey, E., Gomez-Rivas, E., Koehn, D., Bons, P.D., Neilson, J., Martín-Martín, J.D., Schoenherr, J., 2019. Stylolite-controlled diagenesis of a mudstone carbonate reservoir: A case study from the Zechstein_2_Carbonate (Central European Basin, NW Germany). Marine and Petroleum Geology 109, 88–107. https://doi.org/10.1016/j.marpetgeo.2019.05.040

Improta L., Iannaccone G., Capuano P., Zollo A. & Scandone P., 2000. Inferences on the upper crustal structure of Southern Apennines (Italy) from seismic refraction investigations and subsurface data. Tectonophysics, 317 (3-4), 273-297.

Jing, L., Nordlund, E., Stephansson, O., 1992. An experimental study on the anisotropy and stress-dependency of the strength and deformability of rock joints. International Journal of Rock Mechanics and Mining Sciences & Geomechanics Abstracts. Elsevier, 535–542.

Kastens, K. & Mascle, J. 1990. The geological evolution of the Tyrrhenian Sea: an introduction to the scientific results of ODP Leg 107. Proc., scientific results, ODP, Leg 107, Tyrrhenian Sea 107(1986), 3–26.

Katsman, R., Aharonov, E., Scher, H., 2006. A numerical study on localized volume reduction in elastic media: Some insights on the mechanics of anticracks. Journal of Geophysical Research: Solid Earth 111, n/a-n/a. https://doi.org/10.1029/2004JB003607

Koehn, D., Renard, F., Toussaint, R., Passchier, C.W., 2007. Growth of stylolite teeth patterns depending on normal stress and finite compaction. Earth and Planetary Science Letters 257, 582–595. https://doi.org/10.1016/j.epsl.2007.03.015

Koehn, D., Rood, M.P., Beaudoin, N., Chung, P., Bons, P.D., Gomez-Rivas, E., 2016. A new stylolite classification scheme to estimate compaction and local permeability variations. Sedimentary Geology 346, 60–71. https://doi.org/10.1016/j.sedgeo.2016.10.007

Korneva, I., Tondi, E., Agosta, F., Rustichelli, A., Spina, V., Bitonte, R., Di Cuia, R., 2014. Structural properties of fractured and faulted Cretaceous platform carbonates, Murge Plateau (southern Italy). Marine and Petroleum Geology 57, 312–326. https://doi.org/10.1016/j.marpetgeo.2014.05.004

La Bruna, V., Agosta, F., Lamarche, J., Viseur, S., Prosser, G., 2018. Fault growth mechanisms and scaling properties in foreland basin system: The case study of Monte Alpi, Southern Apennines, Italy. Journal of Structural Geology 116, 94–113. https://doi.org/10.1016/j.jsg.2018.08.009

La Bruna, V., Lamarche, J., Agosta, F., Rustichelli, A., Giuffrida, A., Salardon, R. & Marié, L. 2020. Structural diagenesis of shallow platform carbonates: Role of early embrittlement on fracture setting and distribution, case study of Monte Alpi (Southern Apennines, Italy). Journal of Structural Geology 131(June 2019), 103940.

Lamarche, J., Lavenu, A.P.C., Gauthier, B.D.M., Guglielmi, Y., Jayet, O., 2012. Relationships between fracture patterns, geodynamics and mechanical stratigraphy in Carbonates (South-East Basin, France). Tectonophysics 581, 231–245. https://doi.org/10.1016/j.tecto.2012.06.042

Laronne Ben-Itzhak, L., Aharonov, E., Karcz, Z., Kaduri, M. & Toussaint, R. 2014. Sedimentary stylolite networks and connectivity in limestone: Large-scale field observations and implications for structure evolution. Journal of Structural Geology 63, 106–123.

Laronne Ben-Itzhak, L., Aharonov, E., Toussaint, R., Sagy, A., 2012. Upper bound on stylolite roughness as indicator for amount of dissolution. Earth and Planetary Science Letters 337–338, 186–196. https://doi.org/10.1016/j.epsl.2012.05.026

Larsen, B., Gudmundsson, A., Grunnaleite, I., Sælen, G., Talbot, M.R. & Buckley, S.J. 2010. Effects of sedimentary interfaces on fracture pattern, linkage, and cluster formation in peritidal carbonate rocks. Marine and Petroleum Geology 27(7), 1531–1550.

Laubach, S.E., Olson, J.E., Cross, M.R., 2009. Mechanical and fracture stratigraphy. AAPG Bulletin 93, 1413–1426. https://doi.org/10.1306/07270909094

Lavenu, A.P.C., Lamarche, J., 2018. What controls diffuse fractures in platform carbonates? Insights from Provence (France) and Apulia (Italy). Journal of Structural Geology 108, 94–107. https://doi.org/10.1016/j.jsg.2017.05.011

Lavenu, A.P.C., Lamarche, J., Salardon, R., Gallois, A., Marié, L. & Gauthier, B.D.M. 2014. Relating background fractures to diagenesis and rock physical properties in a platform-slope transect. Example of the Maiella Mountain (central Italy). Marine and Petroleum Geology 51, 2–19.

Lavenu, A.P.C., Lamarche, J., Texier, L., Marié, L., Gauthier, B.D.M., 2015. Background fractures in carbonates: Inference on control of sedimentary facies, diagenesis and petrophysics on rock mechanical behavior. Example of the Murge Plateau (southern Italy). Italian Journal of Geosciences 134, 535–555. https://doi.org/10.3301/IJG.2014.58

Lechler, M., Frijia, G., Mutti, M., Palladino, G., Prosser, G., 2012. Stratigraphic setting of a segment from the Eastern margin of the Apennine platform (Monte di Viggiano, Southern Apennines). Rendiconti Online Societa Geologica Italiana 21, 1012–1013.

Lucia, F., Kerans, C., Jennings, J., 2003. Carbonate Reservoir Characterization. Journal of Petroleum Technology 55. https://doi.org/10.2118/82071-ms

Lucia, F.J. & Fogg, G.E. 1990. Geologic/stochastic mapping of heterogeneity in a carbonate reservoir. JPT, Journal of Petroleum Technology 42(10), 1298–1303.

Lucia, F.J. 1983. Petrophysical Parameters Estimated From Visual Descriptions of Carbonate Rocks: a Field Classification of Carbonate Pore Space. JPT, Journal of Petroleum Technology 35(3), 629–637.

Lucia, F.J., 2007. Petrophysical rock properties. Carbonate Reservoir Characterization: An Integrated Approach 1–27.

M. B. Rohrbaugh Jr., 1 W. M. Du 2002. Estimating fracture trace intensity, density, and mean length using circular scan lines and windows. AAPG Bulletin 86.

Malinverno, A. & Ryan, W.B.F. 1986. Extension in the Tyrrhenian Sea and shortening in the Apennines as result of arc migration driven by sinking of the lithosphere. Tectonics 5(2), 227–245.

Mallet R., 1862. Great Neapolitan Earthquake of 1857. The First Principles of Observational Seismology. London, 2 voll.

Mancinelli, A., Chiocchini, M., Chiocchini, R.A. & Romano, A. 2005. Biostratigraphy of Upper Triassic-Lower Jurassic carbonate platform sediments of the central-southern Apennines (Italy). Rivista Italiana di Paleontologia e Stratigrafia 111(2), 271–283.

Mandelbrot, B.B. & Wheeler, J.A. 1983.The Fractal Geometry of Nature. American Journal of Physics 51(3), 286–287.

Manniello, C., Abdallah, I.B., Prosser, G., Agosta, F., 2023. Pressure solution-assisted diagenesis and thrusting-related deformation of Mesozoic platform carbonates. Journal of Structural Geology 173, 104906. https://doi.org/10.1016/j.jsg.2023.104906

Manniello, C., Agosta, F., Todaro, S., Cavalcante, F., Prosser, G., 2022. Fracture stratigraphy of Mesozoic platform carbonates, Agri Valley, southern Italy. Geological Magazine 1–23. https://doi.org/10.1017/s0016756822000322

Manniello, C., Agosta, F., Todaro, S., Cavalcante, F., Prosser, G., 2022. Fracture stratigraphy of Mesozoic platform carbonates, Agri Valley, southern Italy. Geological Magazine 1–23. https://doi.org/10.1017/s0016756822000322

Marchegiani, L., Van Dijk, J.P., Gillespie, P.A., Tondi, E., Cello, G., 2006. Scaling properties of the dimensional and spatial characteristics of fault and fracture systems in the Majella Mountain, central Italy. Geological Society Special Publication 261, 113–131. https://doi.org/10.1144/GSL.SP.2006.261.01.09

Marín, A.I. & Andreo, B. 2015. Vulnerability to Contamination of Karst Aquifers, 251–266p.

Maschio, L., Ferranti, L., Burrato, P., 2005. Active extension in Val d'Agri area, southern Apennines, Italy: Implications for the geometry of the seismogenic belt. Geophysical Journal International 162, 591–609. https://doi.org/10.1111/j.1365-246X.2005.02597.xMavko G, Mukerji T, Dvorkin J (1998) The Rock Physics Handbook. Cambridge University Press, Cambridge, 329 pp.

Mauldon, M., Dunne, W.M. & Rohrbaugh, M.B. 2001. Circular scanlines and circular windows: New tools for characterizing the geometry of fracture traces. Journal of Structural Geology 23(2–3), 247–258.

Mazzoli, S., D'Errico, M., Aldega, L.,Corrado S., Invernizzi C., Shiner P. & Zattin M., 2008. Tectonic burial and "young" (<10 Ma) exhumation in the southern Apennines fold-and-thrust belt (Italy). Geology, 36, 243-246.

McCubbin, D. G. and Patton, J.W., 1981. Burial diagenesis of illite/smectite: The kinetic model: Amer. Assoc. Petrol. Geol. Bull. 65, 956.

Mei, M. & Gao, J. 2012. Giant Induan oolite: A case study from the Lower Triassic Daye Formation in the western Hubei Province, South China. Geoscience Frontiers 3(6), 843–851.

Mercuri, M., Carminati, E., Tartarello, M.C., Brandano, M., Mazzanti, P., Brunetti, A., McCaffrey, K.J.W. & Collettini, C. 2020. Lithological and structural control on fracture frequency distribution within a carbonate-hosted relay ramp. Journal of Structural Geology 137(May).

Merriman RJ, 2005. Clay minerals and sedimentary basin history. European Journal of Mineralogy 17, 7–20.

Monaco C., Tortorici L. & Paltrinieri W., 1998. Structural evolution of the Lucanian Apennines, southern Italy. Journ. Struct. Geol., 20, 617-638.

Moore, C.H. 2002. Carbonate Reservoirs Porosity Evolution and Diagenesis in a Sequence Stratigraphic Framework. Marine and Petroleum Geology 19(10), 1295–1296.

Moore, D.M. & Reynolds, R.C., Jr., 1997. X-ray Diffraction and Identification and Analysis of Clay Minerals, 2nd ed. Oxford University Press: Oxford, UK; New York, NY, USA, 378p.

Mosca, F., Wavrek, D. A., 2002. Petroleum System Characteristics Of Val D'Agri Region, Southern Apennines, Italy. In: AAPG Annual Conference And Exhibition (Abstract Book).

Mostardini F. & Merlini S. 1986. Appennino centro-meridionale. Sezioni geologiche e proposta di modello strutturale. Mem. Soc. Geol. Ital., 35, 177-202.

Myers, R. & Aydin, A. 2004. The evolution of faults formed by shearing across joint zones in sandstone. Journal of Structural Geology 26(5), 947–966.

Nelson, R., 2001. Geologic analysis of naturally fractured reservoirs. Elsevier.

Nickelsen, R.P., 1966. Fossil Distortion and Penetrative Rock Deformation in the Appalachian Plateau, Pennsylvania. The Journal of Geology 74, 924–931. https://doi.org/10.1086/627220

Noguera, A.M., Rea, G., 2000. Deep structure of the Campanian-Lucanian Arc (Southern Apennine, Italy). Tectonophysics 324, 239–265. https://doi.org/10.1016/S0040-1951(00)00137-2

Novellino, R., Prosser, G., Spiess, R., Viti, C., Agosta, F., Tavarnelli, E., Bucci, F., 2015. Dynamic weakening along incipient low-angle normal faults in pelagic limestones (Southern Apennines, Italy). Journal of the Geological Society 172, 283–286. https://doi.org/10.1144/jgs2014-091

Nur, A. & Israel, M. 1980. The role of heterogeneities in faulting. Physics of the Earth and Planetary Interiors 21(2–3), 225–236.

Odling, N.E., Gillespie, P., Bourgine, B., Castaing, C., Chilés, J.P., Christensen, N.P., Fillion, E., Genter, A., Olsen, C., Thrane, L., Trice, R., Aarseth, E., Walsh, J.J. & Watterson, J. 1999. Variations in fracture system geometry and their implications for fluid flow in fractured hydrocarbon reservoirs. Petroleum Geoscience 5(4), 373–384.

Palladino, G., Parente, M., Prosser, G., Di Staso, A., 2008. Tectonic control on the deposition of the lower Miocene sediments of the Monti della Maddalena ridge (Southern Apennines): Synsedimentary extensional deformation in a foreland setting. Bollettino Della Societa Geologica Italiana. 317–335.

Panza, E., Agosta, F., Rustichelli, A., Vinciguerra, S.C., Ougier-Simonin, A., Dobbs, M. & Prosser, G. 2019. Meso-to-microscale fracture porosity in tight limestones, results of an integrated field and laboratory study. Marine and Petroleum Geology 103(November 2018), 581–595.

Panza, E., Agosta, F., Rustichelli, A., Zambrano, M., Tondi, E., Prosser, G., Giorgioni, M. & Janiseck, J.M. 2016. Fracture stratigraphy and fluid flow properties of shallow-water, tight carbonates: The case study of the Murge Plateau (southern Italy). Marine and Petroleum Geology 73, 350–370.

Park, W.C., Schot, E.H., 1968. Stylolites; their nature and origin. Journal of Sedimentary Research 38, 175–191.

Parrino, N., Agosta, F., Di Stefano, P., Napoli, G., Pepe, F., Renda, P., 2019. Fluid storage and migration properties of sheared Neptunian dykes. Marine and Petroleum Geology 102, 521–534. https://doi.org/10.1016/j.marpetgeo.2019.01.008

Patacca E., Sartori R. & Scandone P., 1990. Tyrrhenian basin and Apenninic arcs: kinematic relations since Late Tortonian times. Mem. Soc. Geol. Ital., 45, 425-451.

Patacca E., Scandone P., Bellatalla M., Perilli N. & Santini U. 1992°. The Numidian-sand event in the Southern Apennines. Mem. Sci. Geol. già Mem. Ist. Geol. Mineral. Univ. Padova, all. 43, 297-337.

Patacca, E., Scandone, P., 2007. Geology of the Southern Apennines. Bollettino Della Societa Geologica Italiana, Supplemento 7, 75–119.

Peacock, D.C.P., Sanderson, D.J., 1995. Pull-aparts, shear fractures and pressure solution. Tectonophysics 241, 1–13. https://doi.org/10.1016/0040-1951(94)00184-B

Perri, F., Caracciolo, L., Cavalcante, F., Corrado, S.; Critelli, S., Muto, F., Dominici, R., 2016. Sedimentary and thermal evolution of the Eocene-Oligocene mudrocks from the southwestern Thrace Basin (NE Greece). Basin Res. 28, 319–339.

Petrella, E., Aquino, D., Fiorillo, F. & Celico, F. 2015. The effect of low-permeability fault zones on groundwater flow in a compartmentalized system. Experimental evidence from a carbonate aquifer

(Southern Italy). Hydrological Processes 29(6), 1577–1587.

Piedilato, S., Prosser, G. 2005. Thrust sequences and evolution of the external sector of a fold and thrust belt: An example from the Southern Apennines (Italy). Journal of Geodynamics 39, 386–402.

Pollard, D.D. & Aydin, A. 1990. Progress in understanding jointing over the past century. Special Paper of the Geological Society of America 253, 313–336.

Pollastro R. M., 1993 - Consideration and applications off the illite/smectite geothermometer in hydrocarbon-bearing rocks of Miocene to Mississippian age. Clays and Clay Min., 41, 119-133.

Powell, C.M., 1979. A morphological classification of rock cleavage. Tectonophysics 58, 21–34. https://doi.org/10.1016/0040-1951(79)90320-2

Priest, S. D., and J. A. Hudson, 1981. Estimation of disconitinuity spacing and trace length using scanline surveys. International Journal of Rock Mechanics and Mining Sciences and Geomechanics Abstracts, v. 18, p. 183–197.

Prosser, G., Palladino, G., Avagliano, D., Coraggio, F., Bolla, E.M., Riva, M. & Catellani, D.E. 2021. Stratigraphic and tectonic setting of the liguride units cropping out along the southeastern side of the agri valley (Southern apennines, Italy). Geosciences (Switzerland) 11(3).

Quintà, A., Tavani, S., 2012. The foreland deformation in the south-western Basque-Cantabrian Belt (Spain). Tectonophysics 576–577, 4–19. https://doi.org/10.1016/j.tecto.2012.02.015

Ramsay, J. G. 1967. Folding and fracturing of rocks. Mc Graw Hill Book Company, 568.

Rawling, G.C., Goodwin, L.B., Wilson, J.L., 2001. Internal architecture, permeability structure, and hydrologic significance of contrasting fault-zone types. Geology 29, 43–46. https://doi.org/10.1130/0091-7613(2001)029<0043:IAPSAH>2.0.CO;2

Rispoli, R., 1981. Stress fields about strike-slip faults inferred from stylolites and tension gashes. Tectonophysics 75, 29–36. https://doi.org/10.1016/0040-1951(81)90274-2

Rustichelli, A., Tondi, E., Agosta, F., Cilona, A., Giorgioni, M., 2012. Development and distribution of bed-parallel compaction bands and pressure solution seams in carbonates (Bolognano Formation, Majella Mountain, Italy). Journal of Structural Geology 37, 181–199. https://doi.org/10.1016/j.jsg.2012.01.007

Rustichelli, A., Tondi, E., Korneva, I., Baud, P., Vinciguerra, S., Agosta, F., Reuschlé, T., Janiseck, J.M., 2015. Bedding-parallel stylolites in shallow-water limestone successions of the Apulian carbonate platform (central-Southern Italy). Italian Journal of Geosciences 134, 513–534. https://doi.org/10.3301/IJG.2014.35

Rustichelli, A., Torrieri, S., Tondi, E., Laurita, S., Strauss, C., Agosta, F. & Balsamo, F. 2016. Fracture characteristics in Cretaceous platform and overlying ramp carbonates: An outcrop study from Maiella Mountain (central Italy). Marine and Petroleum Geology 76, 68–87.

Salvini, F., Billi, A. & Wise, D.U. 1999. Strike-slip fault-propagation cleavage in carbonate rocks: The Mattinata Fault zone, southern Apennines, Italy. Journal of Structural Geology 21(12), 1731–1749.

Sartoni S. & Crescenti U. 1961. Ricerche biostratigrafiche nel Mesozoico dell'Appennino meridionale. G. Geol., s. 2, 29, 161- 302.

Schettino, A., Turco, E., 2011. Tectonic history of the Western Tethys since the Late Triassic. Bulletin of the Geological Society of America 123, 89–105. https://doi.org/10.1130/B30064.1

Schmid, S. M. 1982. Laboratory experiments on rheology and deformation mechanisms in calcite rocks and their application to studies in the field. Geologisches Institut der Eidg. Technische Hochschule und der Universität Zürich.

Schöpfer, M.P.J., Arslan, A., Walsh, J.J. & Childs, C. 2011. Reconciliation of contrasting theories for fracture spacing in layered rocks. Journal of Structural Geology 33(4), 551–565.

Schweigl, J., Neubauer, F., 1997. Semiductile deformation in pelagic limestones at diagenetic conditions. Geologica Carpathica 48, 361–370.

Scrocca, D., Carminati, E., Doglioni, C., 2005. Deep structure of the southern Apennines, Italy: Thin-skinned or thick-skinned? Tectonics 24, 1–20. https://doi.org/10.1029/2004TC001634

Selli R., 1962. Il Paleogene nel quadro della geologia dell'Italia Meridionale, Mem. Soc. Geol. Ital., 3, 733-7.

Shiner, P., Beccacini, A., Mazzoli, S., 2004. Thin-skinned versus thick-skinned structural models for Apulian carbonate reservoirs: Constraints from the Val d'Agri Fields, S Apennines, Italy. Marine and Petroleum Geology 21, 805–827. https://doi.org/10.1016/j.marpetgeo.2003.11.020

Smeraglia, L., Billi, A., Carminati, E., Cavallo, A., Di Toro, G., Spagnuolo, E., Zorzi, F., 2017. Ultra-thin clay layers facilitate seismic slip in carbonate faults. Scientific Reports 7. https://doi.org/10.1038/s41598-017-00717-4

Smeraglia, L., Giuffrida, A., Grimaldi, S., Pullen, A., La Bruna, V., Billi, A., Agosta, F., 2021. Fault-controlled upwelling of low-T hydrothermal fluids tracked by travertines in a fold-and-thrust belt, Monte Alpi, southern apennines, Italy. Journal of Structural Geology 144, 104276. https://doi.org/10.1016/j.jsg.2020.104276

Smeraglia, L., Mercuri, M., Tavani, S., Pignalosa, A., Kettermann, M., Billi, A. & Carminati, E. 2021a. 3D Discrete Fracture Network (DFN) models of damage zone fluid corridors within a reservoir-scale normal fault in carbonates: Multiscale approach using field data and UAV imagery. Marine and Petroleum Geology 126(December 2020), 104902.

Spalluto, L. 2008. Sedimentology and high -resolution sequence stratigraphy of a Lower Cretaceous shallow-water carbonate succession from the western Gargano Promontory (Apulia, Southern Italy). GeoActa, Spec. Publ. 1(1991), 77–96.

Spalluto, L. 2012. Facies evolution and sequence chronostratigraphy of a 'mid'-Cretaceous shallow-water carbonate succession of the Apulia Carbonate Platform from the northern Murge area (Apulia, southern Italy). Facies 58(1), 17–36.

Stockdale, P.B., 1921. Stylolites: their nature and origin. Bloomington, Ind.: sn.

Tada, R. & Siever, R. 1989. Pressure solution during diagenesis. Annual review of earth and planetary sciences. Vol. 17, 89–118.

Tada, R., Maliva, R., Siever, R., 1987. A new mechanism for pressure solution in porous quartzose sandstone. Geochimica et Cosmochimica Acta 51, 2295–2301. https://doi.org/10.1016/0016-7037(87)90282-1

Tavani, S., Storti, F., Lacombe, O., Corradetti, A., Muñoz, J.A., Mazzoli, S., 2015. A review of deformation pattern templates in foreland basin systems and fold-and-thrust belts: Implications for the state of stress in the frontal regions of thrust wedges. Earth-Science Reviews 141, 82–104. https://doi.org/10.1016/j.earscirev.2014.11.013

Tavani, S., Storti, F., Muñoz, J.A., 2010. Scaling relationships between stratabound pressure solution cleavage spacing and layer thickness in a folded carbonate multilayer of the Northern Apennines (Italy). Journal of Structural Geology 32, 278–287. https://doi.org/10.1016/j.jsg.2009.12.004

Thiry, M., 2000.. Palaeoclimatic interpretation of clay minerals inmarine deposits: an outlook from the continental origin. Earth Sci. Rev. 49, 201–221.

Todaro, S., Di Stefano, P., Zarcone, G. & Randazzo, V. 2017. Facies stacking and extinctions across the Triassic–Jurassic boundary in a peritidal succession from western Sicily. Facies 63(3), 1–21.

Todaro, S., Rigo, M., Randazzo, V. & Di Stefano, P. 2018. The end-Triassic mass extinction: A new correlation between extinction events and δ13C fluctuations from a Triassic-Jurassic peritidal succession in western Sicily. Sedimentary Geology 368, 105–113.

Tondi, E., Cilona, A., Agosta, F., Aydin, A., Rustichelli, A., Renda, P., Giunta, G., 2012. Growth processes, dimensional parameters and scaling relationships of two conjugate sets of compactive shear bands in porous carbonate grainstones, Favignana Island, Italy. Journal of Structural Geology 37, 53–64. https://doi.org/10.1016/j.jsg.2012.02.003

Toussaint, R., Aharonov, E., Koehn, D., Gratier, J.P., Ebner, M., Baud, P., Rolland, A., Renard, F., 2018. Stylolites: A review. Journal of Structural Geology 114, 163–195. https://doi.org/10.1016/j.jsg.2018.05.003

Tucker, M.E. 1985. Shallow-marine carbonate facies and facies models. Sedimentology: recent developments and applied aspects (January 1985), 147–169.

Tucker, M.E., Wright, V.P., 2009. Carbonate sedimentology. John Wiley & Sons.

Twiss, R.J., Moores, E.M., 1992. Structural geology .Stress Distribution. Chapters 4, 5, 6, 7, 9 and 10, section 10.9, pp. 202-205.. Macmillan.

Vasudevan, K., 2020. Conquering Carbonate Complexities: Understanding Geological Processes that Control Poro-Perm Relationships. Petro-Physics and Rock Physics of Carbonate Reservoirs. Springer Singapore, Singapore, 15–27. https://doi.org/10.1007/978-981-13-1211-3_2

Vezzani, L., Festa, A., Ghisetti, F.C., 2010. Geology and tectonic evolution of the Central-Southern Apennines, Italy. Special Paper of the Geological Society of America 469, 1–58. https://doi.org/10.1130/2010.2469

Volatili, T., Zambrano, M., Cilona, A., Huisman, B.A.H., Rustichelli, A., Giorgioni, M., Vittori, S. & Tondi, E. 2019. From fracture analysis to flow simulations in fractured carbonates: The case study of the Roman Valley Quarry (Majella Mountain, Italy). Marine and Petroleum Geology 100(July 2018), 95–110.Waliczek, M., Machowski, G., Poprawa, P., Świerczewska, A. & Więcław D., 2021.. A novel VRo, Tmax, and S indices conversion formulae on data from the fold-and-thrust belt of the Western Outer Carpathians (Poland). International Journal of Coal Geology, 234, 103672.

Wennberg, O.P., Svånå, T., Azizzadeh, M., Aqrawi, A.M.M., Brockbank, P., Lyslo, K.B. & Ogilvie, S. 2006.

Fracture intensity vs. mechanical stratigraphy in platform top carbonates: The Aquitanian of the Asmari Formation, Khaviz Anticline, Zagros, SW Iran. Petroleum Geoscience 12(3), 235–245.

Willemse, E.J.M., Peacock, D.C.P., Aydin, A., 1997. Nucleation and growth of strike-slip faults in limestones from Somerset, U.K. Journal of Structural Geology 19, 1461–1477. https://doi.org/10.1016/S0191-8141(97)00056-4

Wong, P.K., Oldershaw, A., 1981. Burial cementation in the Devonian, Kaybob reef complex, Alberta, Canada. Journal of Sedimentary Research 51, 507–520.

Wortel, R., Spakman, W., 1992. Structure and dynamics of subducted lithosphere in the Mediterranean region. Proc. Kon. Ned. Akad. v. Wetensch 95, 325–347.

Wu, H. & D. Pollard, D. 1995. An experimental study of the relationship between joint spacing and layer thickness. Journal of Structural Geology 17(6), 887–905.

Zarcone, G., Petti, F.M., Cillari, A., Di Stefano, P., Guzzetta, D. & Nicosia, U. 2010. A possible bridge between Adria and Africa: New palaeobiogeographic and stratigraphic constraints on the Mesozoic palaeogeography of the Central Mediterranean area. Earth-Science Reviews 103(3–4), 154–162.

Zhang, X. & Spiers, C.J. 2005. Compaction of granular calcite by pressure solution at room temperature and effects of pore fluid chemistry. International Journal of Rock Mechanics and Mining Sciences 42(7-8 SPEC. ISS.), 950–960.

Zhou, L., Wang, G., Hao, F., Xu, R., Jin, Z., Quan, L., Zou, H., 2022. The quantitative characterization of stylolites in the limestone reservoirs of the Lower Triassic Feixianguan Formation, northeastern Sichuan Basin: Insights to the influence of pressure solution on the quality of carbonate reservoirs. Marine and Petroleum Geology 139, 105612. https://doi.org/10.1016/j.marpetgeo.2022.105612

Zhou, X., Aydin, A., 2012. Mechanics of the formation of orthogonal sets of solution seams, and solution seams and veins and parallel solution seams and veins. Tectonophysics 532–535, 242–257. https://doi.org/10.1016/j.tecto.2012.02.013

APPENDIX – PERMEABILITY MEASUREMENTS IN LOW-POROSITY, SHALLOW-WATER CARBONATES: INSIGHTS ON THE EFFECT OF PRESSURE SOLUTION-RELATED PORES ON THE FLUID FLOW PROPERTIES OF LIMESTONE ROCKS

Poro/perm assessment

The results of petrophysical analyses of 21 carbonate rock samples collected from the Viggiano Mt., southern Italy, are briefly reported hereafter. The samples were collected as representative of the lower Jurassic and Cretaceous carbonate successions exposed in that area (cf. Chapters 2 and 3). The sampling sites were selected to avoid as much as possible the fault-related deformation associated to the main tectonic structures dissecting the carbonate successions. The goal of this laboratory work is the porosity and permeability (in direction orthogonal to the bedding surfaces) characterization of the carbonate lithofacies comprised of both mud- and grain-supported carbonate rocks including bed-parallel and low-angle to bedding solution surfaces.

Specifically, the carbonate rock volumes were sampled due to the presence of both intra-bed and inter-bed, bed-parallel stylolites and pressure solution seams, which actually form the main target for this analysis. Moreover, a particular attention was paid to select samples including the solution surfaces representative of the various morphologies assessed in the Chapter 4 of the present PhD Thesis Dissertation. The lower Jurassic carbonates include two informal sedimentary units, which are labelled respectively as “well-layered” and “oolithic” carbonates. The well-layered carbonate samples consist of mud-supported carbonates (mudstone and wackestone, labelled Y*n*, and of grain-supported carbonated lithofacies (packstones and grainstones, labelled X*n*. The oolithic carbonates samples include exclusively cemented grainstones, which are labelled Z*n*. The Cretaceous succession includes a single informal sedimentary unit labelled as “massive carbonates”. The samples consist of grain-supported carbonates (packstones and grainstones, labelled J*n*), and of coarse bioclastic rudstones and sedimentary breccia, which are labelled L*n*).

The petrophysical analyses were carried out on cylindrical plugs characterized by 1 inch of diameter, and 3 to 5 cm of height. The plugs were cored orthogonal to the bedding. In the adjacent portion of the individual samples, thin sections were cut also orthogonal to bedding. The petrophysical analyses consisted in both porosity and permeability measurements.

These measurements were performed at room pressures and very shallow confining pressure conditions. by means of the unsteady-state gas technique, using a Coreval 700 N/He-permeameter/porosimeter. The analyses were performed at the Laboratory of Engineering of Petroleum Reservoirs (LABRES-UFRN). The experimental work, as said both atmospheric conditions and at confining pressure of 600 psi (≈160 m of depth), allowed us to measure the values of porosity, expressed both as void volume (cm^3) and as volume percentage (%) of the total rock, and the bed-perpendicular gas-permeability (parallel to the coring direction), at which the Klinkenberg correction was applied (Klinkenberg, 1941).

The results of petrophysical analyses are summarized in Table 1, and also plotted in Fig 1. The void volume (cm^3) at atmospheric conditions varies from 0.3294 cm^3 to 0.8184 cm^3, with an average of 0.4896 cm^3, a median value of 0.4700 cm^3, and a standard deviation of 0.117872. At higher confining pressures, the void volume (cm^3) varies from 0.3085 cm^3 to 0.7843 cm^3, with an average of 0.4669 cm^3, a median value of 0.4484 cm^3, and a standard deviation of 0.113639. Comparing the two datasets, we note that the volume loss due to the increasing confining pressure is comprised between 4.2% and 5.2%, with an average of 4.7% of the total void volume. Reporting the aforementioned data as % values of the total rock volume, the porosity values at atm conditions ($\phi 0\%$) vary between 1.6824% and 4.7314%, with an average of 3.1564%, a median value of 2.9296%, and a standard deviation of 0.941589%. At higher confining pressure, the porosity values ($\phi\%$) vary from 1.5968% and 4.5437%, with a mean value of 3.0164%, a median of 2.7945%, and a standard deviation of 0.910818%.

Table 6 Results of N-porosimetry and permeametry. Vp0(cc) = void volume (atm conditions); Vp(cc) = void volume (confining conditions); ϕ0(%) = Porosity (atm conditions); ϕ(%) = Porosity (confining conditions); K[n2](mD) = Gas Permeability (not corrected); K∞(mD) = Corrected Permeability (Klinkenberg); ρb(g/cc) = Bulk density (confining conditions); Vb0(cc) = Bulk volume (atm conditions); Vb(cc) = Bulk volume (confining conditions); Vg(cc) = Grain volume; ρg(g/cc) = Grain density; ρb0(g/cc) = Bulk density (atm conditions); Weight = weight of the sample (g).

Name	Vp0(cc)	Vp(cc)	ϕ0(%)	ϕ(%)	K[n2](mD)	K∞(mD)	ρb(g/cc)	Vb0(cc)	Vb(cc)	Vg(cc)	ρg(g/cc)	ρb0(g/cc)	Weight(g)
J1a	0.5425	0.5169	3.0047	2.8670	0.0115	0.0022	2.6784	18.0551	18.0295	17.5126	2.7574	2.6746	48.2896
J1b	0.4516	0.4282	1.6824	1.5968	0.0140	0.0030	2.6565	26.8391	26.8158	26.3876	2.6996	2.6542	71.2367
J3a	0.6578	0.6287	3.9106	3.7442	0.0087	0.0015	2.7099	16.8203	16.7912	16.1625	2.8153	2.7052	45.5022
J4a2	0.4758	0.4528	2.6727	2.5468	0.0084	0.0014	2.6971	17.8012	17.7782	17.3254	2.7676	2.6936	47.9499
J4b	0.4359	0.4150	2.7765	2.6468	0.0080	0.0013	2.6870	15.6996	15.6786	15.2637	2.7601	2.6835	42.1292
J4c	0.4048	0.3848	2.3840	2.2691	0.0076	0.0012	2.3861	16.9794	16.9594	16.5746	2.4414	2.3832	40.4660
L1	0.6057	0.5804	4.6635	4.4774	0.0673	0.0269	2.6603	12.9876	12.9623	12.3819	2.7850	2.6551	34.4836
L2	0.4030	0.3833	2.5695	2.4475	0.0076	0.0013	2.6616	15.6825	15.6629	15.2795	2.7284	2.6583	41.6881
L4b	0.4243	0.4037	2.6687	2.5430	0.0169	0.0039	2.6650	15.8974	15.8769	15.4731	2.7346	2.6616	42.3124
L4C	0.3249	0.3085	2.0728	1.9704	0.0064	0.0010	2.7017	15.6739	15.6575	15.3490	2.7560	2.6989	42.3020
L4d	0.3443	0.3269	2.0101	1.9103	0.0087	0.0015	2.6942	17.1297	17.1123	16.7854	2.7467	2.6915	46.1047
L5a	0.4103	0.3905	2.6847	2.5584	0.0079	0.0013	2.6512	15.2832	15.2634	14.8729	2.7208	2.6477	40.4660
L5B	0.3300	0.3132	1.9729	1.8747	0.0075	0.0012	2.6773	16.7252	16.7085	16.3952	2.7284	2.6746	44.7336
L5C	0.3879	0.3688	2.4092	2.2933	0.0110	0.0021	2.6764	16.1000	16.0809	15.7121	2.7392	2.6732	43.0382
X1	0.5662	0.5420	4.3641	4.1854	0.0094	0.0017	2.7283	12.9742	12.9500	12.4080	2.8475	2.7232	35.3319
X2A	0.3422	0.3248	1.9454	1.8484	0.1522	0.0692	2.6751	17.5902	17.5728	17.2480	2.7255	2.6724	47.0088
X2B	0.3931	0.3740	2.6138	2.4901	0.0101	0.0019	2.6626	15.0378	15.0187	14.6448	2.7306	2.6592	39.9888
X2C	0.3807	0.3630	3.1880	3.0440	0.0062	0.0009	2.6723	11.9417	11.9239	11.5610	2.7562	2.6683	31.8639
X3A	0.4642	0.4441	4.1692	3.9957	0.0850	0.0332	2.6646	11.1341	11.1140	10.6699	2.7755	2.6598	29.6139
X3B	0.4804	0.4603	4.6202	4.4351	0.0061	0.0009	2.6433	10.3979	10.3778	9.9175	2.7659	2.6381	27.4313
X4A	0.7178	0.6874	4.4612	4.2801	0.0299	0.0084	2.6473	16.0903	16.0599	15.3725	2.7657	2.6423	42.5160
X4B	0.8184	0.7843	4.7314	4.5437	0.4973	0.2977	2.6416	17.2963	17.2623	16.4780	2.7673	2.6364	45.6001
Y2	0.6230	0.5948	3.5857	3.4290	0.0283	0.0078	2.6102	17.3740	17.3458	16.7510	2.7029	2.6060	45.2759
Y4A	0.5007	0.4769	2.9207	2.7859	0.2800	0.1520	2.6431	17.1428	17.1191	16.6422	2.7188	2.6394	45.2472
Y4B	0.5333	0.5084	3.1917	3.0475	0.4367	0.2566	2.6928	16.7087	16.6838	16.1754	2.7774	2.6888	44.9257
Z2a (Ir1)	0.5813	0.5541	3.1620	3.0189	0.0098	0.0018	2.6198	18.3828	18.3557	17.8016	2.7013	2.6159	48.0881
Z2b (Ir2)	0.4243	0.4034	2.4106	2.2946	0.0072	0.0012	2.6459	17.6019	17.5810	17.1776	2.7080	2.6427	46.5172
Z2c (Ir3)	0.4340	0.4124	2.2772	2.1665	0.0095	0.0017	2.6596	19.0577	19.0361	18.6237	2.7185	2.6566	50.6287
Z3 (Ir4)	0.5844	0.5595	4.3864	4.2071	0.0164	0.0037	2.5953	13.3227	13.2978	12.7384	2.7093	2.5905	34.5122
Z4a (Ir5)	0.4949	0.4736	4.2752	4.0988	0.0110	0.0021	2.6534	11.5758	11.5545	11.0809	2.7668	2.6485	30.6584
Z4b(Ir6)	0.6230	0.5934	2.9386	2.8032	0.0082	0.0014	2.6890	21.1998	21.1703	20.5768	2.7666	2.6853	56.9270
Z4c (Ir7)	0.5056	0.4838	4.2820	4.1054	0.0133	0.0028	2.6212	11.8069	11.7852	11.3014	2.7334	2.6163	30.8908

The vertical permeability, K (Klinkenberg corrected), ranges from 0.0009 mD and 0.2977 mD. Considering all measurements, we compute a mean value of 0.0280 mD, a median value of 0.0018 mD, and a standard deviation of 0,071697 mD. - The poro –perm (bed-perpendicular) relations shown in Fig. 1 are characterized by a pronounced non-linearity. However, not considering the four samples with a Klinkenberg permeability values of ca. 10-s mDarcy, all the others lie in a low-angle best fit line consistent with a poor connectivity of the pore system associated to the bed parallel solution surfaces. As expected, the cross-solution surface fluid flow properties are not enhanced by these surfaces, which actually might inhibit the bed-orthogonal fluid flow. However, a few samples show a higher degree of pore connectivity (cf. the aforementioned four data points), suggesting either the role played by the high-angle to bedding microfractures on the cross-solution surface fluid flow,

and/or the presence of larger and well-connected pore space within the bed-parallel surfaces. Unfortunately, direct inspection of the thin section obtained in the nearby sample volumes did not allow us to decipher the driving mechanism. For this reason, we decided to visit a different laboratory to perform permeability tests t increasing confining pressure conditions.

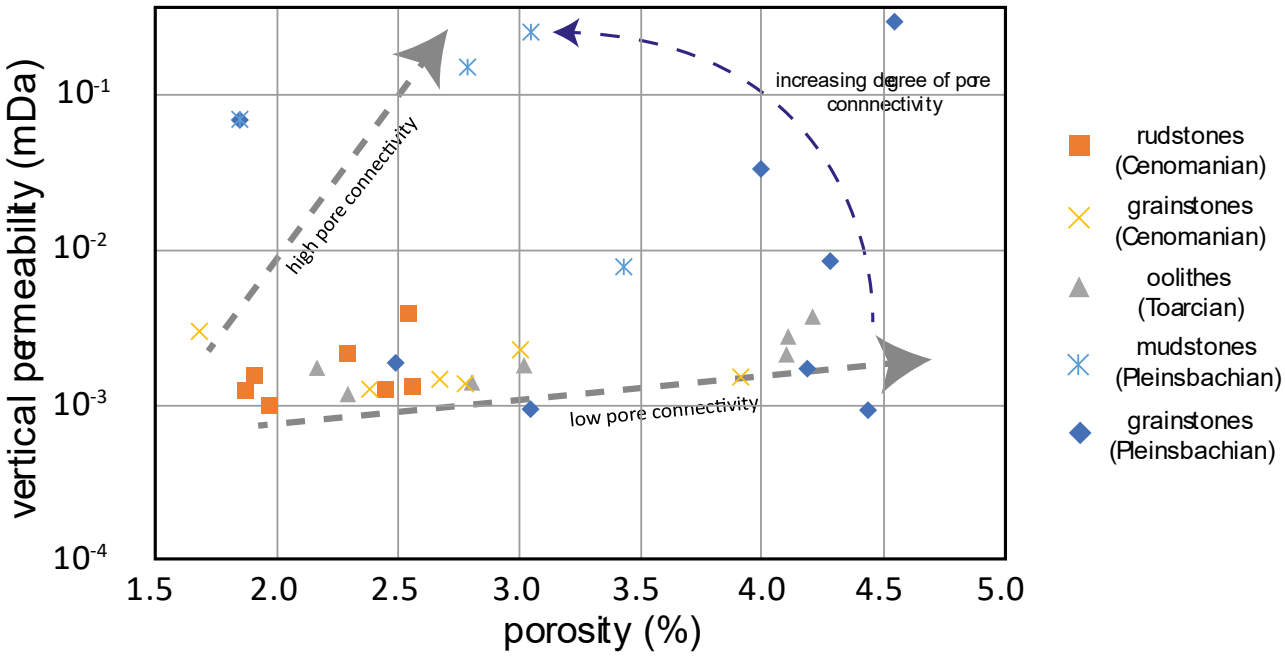

Figure 1 Poro/perm relations of the analyzed samples. The relation is non-linear, and the majority of the samples are characterized by a low pore connectivity (samples clustered along a horizontal line). The presence of outliers characterized by relatively high permeability is due to the presence of a higher connectivity degree.

Permeability at increasing confining pressure.

Laboratory tests were conducted on samples derived from hand specimens collected from the Viggiano Mt., labeled according to the previous classification, and the Raparo Mt., labeled as RA*n*, RB*n*, RC*n*. The Raparo Mt. is located along the SW portion of the Agri Valley, in southern Italy, and also exposes the inner portion of the Apenninic Platform. The stratigraphic succession exposed at the study sites of the Raparo Mt. consists of Cretaceous to Eocene carbonates. Aiming at deciphering the specific role of the seismogram type stylolites on the permeability values measure both across and along these structural element, we first conducted a detailed petrographic analysis of the selected samples to clearly decipher the microstructural setting of the chosen carbonate samples.

First, we conducted gas permeability measurements at room pressure, and then water permeability measurements at increasing confining pressures (from 5 MPa to 70MPa) by

means of pulse transient method. The pulse transient method is applied with a pulse upstream pressure increment to discharge fluid through the sample to downstream fluid reservoir. Permeability is calculated when the upstream reservoir and downstream reservoir reach a new equilibrium pressure. The governing equation for the pressure pulse through the sample is written as follows:

Ep. 1 $$P_{up}(t) - P_{dn}(t) = (P_{up}(t_0) - P_{dn}(t_0))\, e^{-at}$$

Eq. 2 $$\alpha = (kA / \mu bL)(1/V_{up} + 1/V_{dn})$$

Where $P_{up}(t) - P_{dn}(t)$ is the pressure difference between the upstream and downstream reservoirs at time t; and$(P_{up}(t0) - P_{dn}(t0))$ is the initial pressure difference between the upstream and downstream reservoirs at time t0. α is the slope of the line when plotting the pressure decay $P_{up}(t) - P_{dn}(t)$ on semilog paper against time (Figure 2). In the equations above, A and L are the cross sectional area and the length of each sample, respectively. In the same equations, μ, β, V_{up}, and V_{dn} are the dynamic viscosity and compressibility of the gas, and the volume of the upstream reservoir and downstream reservoir, respectively. Permeability k is then calculated from Eq. 2 because it is the only unknown parameter after the run of single experiments.

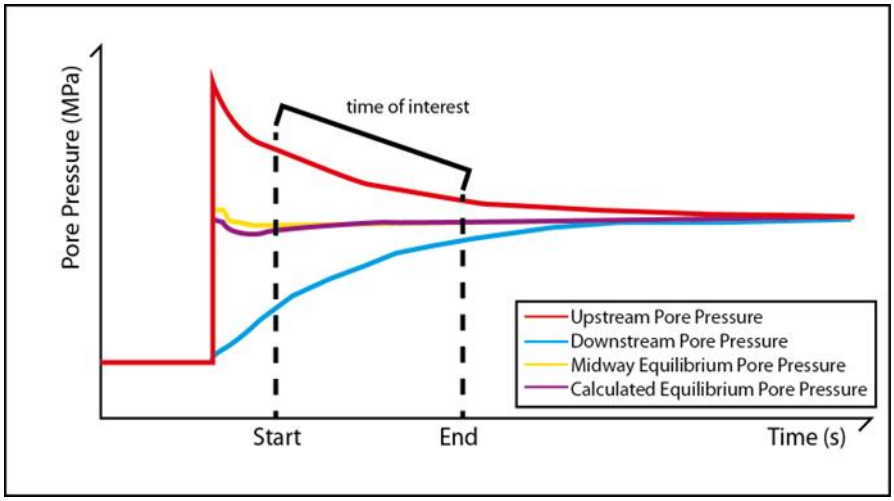

Figure 2 Typical pressure decay plot of upstream and downstream pressure vs time.

The results of the permeability measurements through pulse transient method are summarized in Table 2, and plotted in Figure 3. These results were achieved in the days before the preparation of the present PhD Thesis Dissertation, and hence were not reported and described in detail. At a first sight, we observe that the data varies between 10^{-19} and 10^{-22} m^2, corresponding to a range comprised between 10^{-3} and 10^{-6} mDa. The data roughly cluster into two regions of the graph (Figure 3), an upper cluster and a lower cluster. The

upper cluster include mostly bed-perpendicular plugs that include high angle microfractures and bed-parallel stylolites. Within those samples the decrease of permeability associated to increasing confining pressure is of one order of magnitude. We note that generally the permeability deceases at a lower rate after 25 MPa. Differently, the lower cluster include mostly bed-parallel plugs, containing single stylolite surfaces and the permeability does not decrease significantly with the increasing confining pressure. Considering the relatively higher values of permeability associated to the bed-perpendicular plugs, we note that the decease of permeability is likely associated to the presence of open fractures, and the stylolites do not act as barriers to fluid flow. Further X-ray tomography analyses will shed more lights on the internal structure of the plugs and on the specific structure of the zones where fracture intersect/abut against stylolites, in order to gain more information on the microstructures that the control fluid flow through different structural elements.

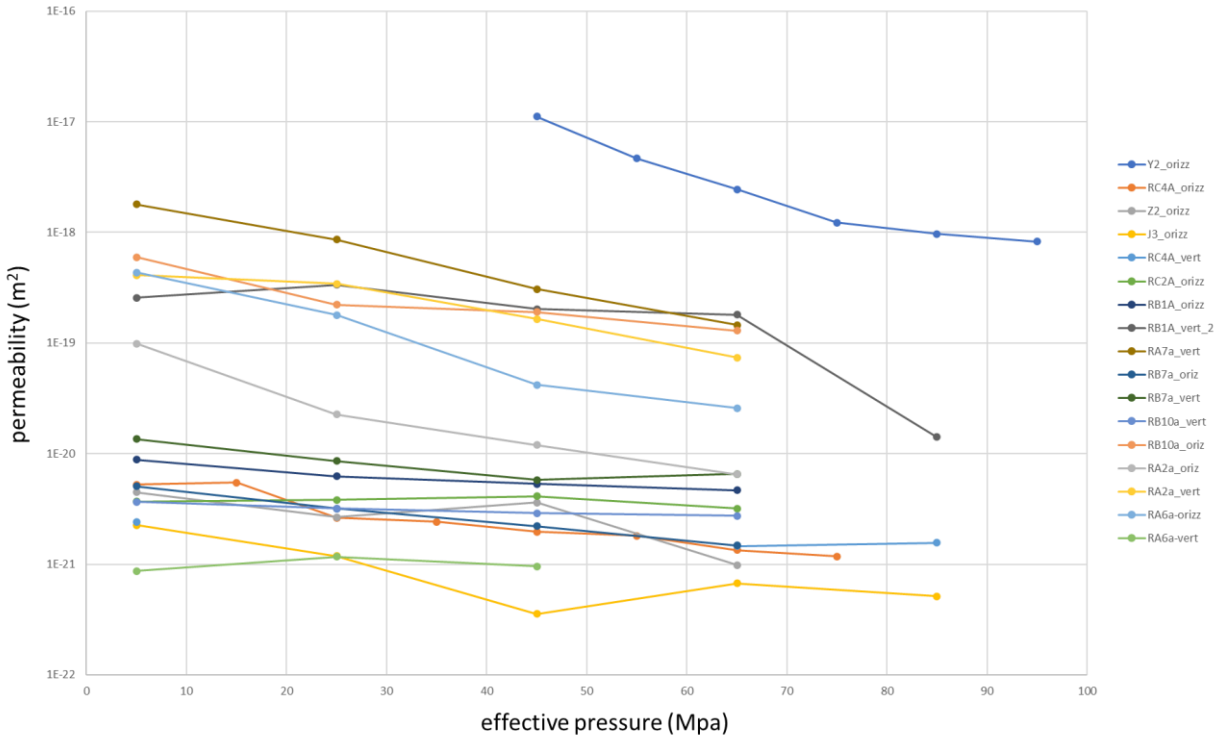

Figure 3 Permeability variation as a function of the increasing effective pressure within the samples.

Table 7. Summary of the permeability values calculated with the pulse transient method.

Y2_orizz			RC4A_orizz			Z2_orizz			J3_orizz	
Effective Pressure	Permeability		Effective Pressure	Permeability		Effective Pressure	Permeability		Effective Pressure	Permeability
MPa	m2		MPa	m2		MPa	m2		MPa	m2
			5	5.23229E-21						
45	1.11066E-17		15	5.45699E-21		5	4.47813E-21		5	2.25382E-21
55	4.64579E-18		25	2.62392E-21		25	2.66244E-21		25	1.18734E-21
65	2.4542E-18		35	2.42424E-21		45	3.61836E-21		45	3.55767E-22
75	1.22477E-18		45	1.96497E-21		65	9.81343E-22		65	6.72245E-22
85	9.68668E-19		55	1.80218E-21					85	5.13003E-22
95	8.24415E-19		65	1.33957E-21						
			75	1.18021E-21						

RC4A_vert			RC2A_orizz			RB1A_orizz				
Effective Pressure	Permeability		Effective Pressure	Permeability		Effective Pressure	Permeability			
MPa	m2		MPa	m2		MPa	m2			
5	2.39911E-21		5	3.69098E-21		5	8.81619E-21			
25			25	3.80958E-21		25	6.21785E-21			
45			45	4.12175E-21		45	5.30847E-21			
65	1.46124E-21		65	3.18874E-21		65	4.65562E-21			
85	1.56441E-21									

RA7a_vert			RB1A_vert_2			RB7a_oriz			RB7a_vert	
Data Effective Pressure	**Permeability**		Data Effec	Permeability		Data Effect	Permeability		Data Effect	Permeability
MPa	m2		MPa	m2		MPa	m2		MPa	m2
5	1.79E-18		5	2.56049E-19		5	5.05605E-21		5	1.35877E-20
25	8.64E-19		25	3.36138E-19		25	3.19596E-21		25	8.59356E-21
45	3.08E-19		45	2.03285E-19		45	2.20437E-21		45	5.79165E-21
65	1.46E-19		65	1.79681E-19		65	1.48239E-21		65	6.55597E-21
			85	1.40782E-20						

RA7a_oriz			RB10a_vert			RB10a_oriz			RA2a_oriz	
Data Effective Pressure	**Permeability**		Data Effec	Permeability		**Data Effective Pressure**	**Permeability**		Data Effect	Permeability
MPa	m^2		MPa	m2		MPa	m^2		MPa	m2
5	0.00E+00		5	3.66181E-21		5	5.97E-19		5	9.89394E-20
25	0.00E+00		25	3.19291E-21		25	2.22E-19		25	2.26009E-20
45	0.00E+00		45	2.88754E-21		45	1.90E-19		45	1.19848E-20
			65	2.73041E-21		65	1.29E-19		65	6.49189E-21

RA2a_vert			RA6a-orizz			RA6a-vert				
Data Effective Pressure	**Permeability**		Data Effec	Permeability		**Data Effective Pressure**	**Permeability**			
MPa	m2		MPa	m2		MPa	m^2			
5	4.09E-19		5	4.33722E-19		5	8.69E-22			
25	3.42E-19		25	1.79124E-19		25	1.17E-21			
45	1.64E-19		45	4.17164E-20		45	9.58E-22			
65	7.36E-20		65	2.56882E-20		65	1.01E-20			